Design and synthesis of micellar nanocarriers for internal radiotherapy

Conception et synthèse de nanovecteurs micellaires pour la radiothérapie interne

Thèse de doctorat de l'Université Paris-Saclay et de l'institut de chimie et de technologies nucléaires (ICHTJ)

École doctorale n° 571 : Sciences chimique : molécules, matériaux, instrumentation et biosystèmes (2MIB)
Spécialité de doctorat : Chimie
Graduate School : Chimie. Référent : Faculté des sciences d'Orsay

Thèse préparée dans l'unité de recherche **Médicament et Technologies pour la Santé** (Université Paris-Saclay, CEA) et l'équipe **Radiopharmaceutiques** (NOMATEN, NCBJ) sous la direction d'**Eric Doris**, Directeur de recherche et la co-direction de **Marek Pruszynski**, Professeur des Universités

Thèse soutenue à Paris-Saclay, le , par

Mathilde PONCHELLE

Composition du Jury

Membres du jury avec voix délibérative

Beata BRZOZOWSKA Chercheuse, Université de Varsovie	Rapportrice
Elena ISHOW Professeure, Nantes Université	Rapportrice
Cyrille RICHARD Directeur de recherche, Université Paris-Cité	Rapporteur
Simona MURA Professeure, Université Paris-Saclay	Examinatrice
Anna LANKOFF Professeure, Institut de chimie et de technologie nucléaires	Examinatrice

THÈSE DE DOCTORAT

NNT : 2025UPASF001

Mathilde Ponchelle

Design and synthesis of micellar nanocarriers for internal radiotherapy

Supervisor: Eric Doris PhD

Supervisor: Marek Pruszyński PhD, DSc

Center of Radiochemistry and Nuclear Chemistry

Institute of Nuclear Chemistry and Technology

NOMATEN Center of Excellence

National Center for Nuclear Research

Doctoral School

Warsaw, 2025

Mathilde Ponchelle

Projektowanie i synteza nanonośników micelarnych do radioterapii wewnętrznej

Promotor: Eric Doris PhD

Promotor: Marek Pruszyński PhD, DSc

Centrum Radiochemii i Chemii Jądrowej

Instytut Chemii i Techniki Jądrowej

Centrum Doskonałości NOMATEN

Narodowe Centrum Badań Jądrowych

Doctoral School

Warszawa, 2025

Acknowledgment

First of all, I would like to thank the jury members for accepting to evaluate my work.

I would like to thank Frédéric Taran, the head of the *Service de Chimie Bioorganique et de marquage* in CEA who allowed to do my PhD in his laboratory. I also would like to thank Łukasz Kurpaska for letting me be part of the NOMATEN research group in NCBJ.

I also would like to thank my two co-directors, Eric Doris and Marek Pruszyński, for trusting me with this project during the past three years. Thanks to you I had the opportunity to be part of this cotutelle program, to work in two different institutes and two different countries. I learned a lot during those three years on a professional but also on a personal aspect. I would like to thank Edmond Gravel; your advice and your support were very helpful all along the way, it was a great pleasure to work with you.

I would like to thank people from the SCBM labs, including the analytical team for your support. Of course, I would like to specifically thank people from the tritium lab and the Nanosciences Team, past and present. It was a pleasure to work with you all, during those three years. Thank you for the nice coffee and crosswords break, we're getting good at this! A special thanks to Céline, I had a nice time with you in the lab and at the coffee break, and great memories of us fixing vacuum pumps for days… Thank you Aurore for supporting me anytime the chemistry was not on my side, I'll miss your daily singing in the lab. Thanks to Killian, for your support (was it really support though?) during the gold nanoparticle crisis.

Then, I have a thought for my colleagues in the Radiopharmaceutical research group in NOMATEN. It was a great pleasure meeting you all and follow a part of the journey to open this lab (finally!). A special thanks to Marcin Zieliński who run the biological experiment, I know I gave you a lot of work but we finally did it! Anna, Karolina, you were with me all the time, since I landed in Warsaw until I left few months ago. You taught me a lot, on a professional side of course, but I'll mostly miss all our moments outside, chatting around a drink and a pizza. Thanks for everything girls.

A huge thank you to Barbara Paprocka and Natalia Cacko, you helped me anytime I needed it, especially with the polish administration. Thanks to you my arrival in NOMATEN was easy and smooth.

I also would like to thank Izabela Cieszykowska for giving access to her lab in Polatom and for training me. Thanks to Urszula Karczmarczyk for your wise advices, and Agnieszka Kulesza, for running the animal experiment.

Je vais finir par un petit mot en français, pour mes proches, mes amis qui ont été des soutiens inconditionnels pendant ces 3 ans, même à 1500 km. Merci à mes oncles et tantes de cœur, *pour avoir été là depuis le tout début et à chaque instant. À mes quatre gardiens, je sais que vous vous reconnaîtrez, qui ont vécu avec moi chaque étape de ce projet, toujours prêt à me proposer des sorties pour vider la tête ou tout simplement à papoter des heures au téléphone sur nos projets respectifs.*

À ma famille, pour vos petits mots et vos petites attentions tout au long de ces trois ans. Grâce à vous, j'ai une collection de cartes immense ! Ces trois années n'ont pas été de tout repos pour vous aussi, je le sais et je mesure la chance que vous m'avez donnée. Pour tout cela un grand merci ! (en attendant le voyage en Polynésie, ou ailleurs !)

CONTENT

List of abbreviations

AuNP	Gold nanoparticle
CMC	Critical micellar concentration
CT	Computed tomography
DEF	Dose enhancement factor
DFO	Desferrioxamine
DLS	Dynamic light scattering
DMF	Dimethylformamide
DMR	Dose-modifying ratio
DOTA	2,2′,2′′,2′′′-(1,4,7,10-Tetraazacyclododecane-1,4,7,10-tetrayl)tetraacetic acid
EMA	European Medicines Agency
EPR	Enhanced permeability and retention
FBS	Fetal bovine serum
FDA	Food and Drug Administration
IC50	Half maximal inhibitory concentration
ICP-MS	Inductively coupled plasma mass spectroscopy
iTLC	instant Thin Layer Chromatography
kVP	kiloVoltage peak
LC-MS	Liquid chromatography mass spectroscopy
LET	Linear energy transfer
MRI	Magnetic resonance imaging
NIR	Near infra red
NMR	Nuclear magnetic resonance
OER	Oxygen enhancement factor
PBS	phosphate buffer saline
PDT	Photodynamic therapy
PEG	Poly(ethylene glycol)
PET	Positron emission tomography
PFC	Perfluorocarbon
PFMC	Perfluoromethylcyclohexan
PFSH	Pferluorooctodecan thiol
RAD	Radiation absorbed dose
RCP	Radiochemical purity
RCY	Radiochemical yield
RER	Radiation enhancement ratio
RES	Reticuloendothelial system
ROS	Reactive oxygen species
SA	Specific activity
SAXS	Small-angle X-ray scattering
SD	Standard deviation

SERS	Surface-enhanced Raman scattering
SF	Survival fraction
SPECT	Single photon emission computed tomography
SPR	Surface plasmon resonance
TEM	Transmission electron microscopy
THF	tetrahydrofuran
TOAB	Tetraoctylammonium bromide
TRT	Targeted radiation therapy
UPLC-MS	Ultra performance liquid chromatography mass spectroscopy

General introduction

I. Cancer

I. A. Definition

According to the World Health Organization (WHO), cancer is a generic term that refers to a broad group of diseases that can originate in nearly any organ or tissue in the body. It occurs when abnormal cells grow uncontrollably and can invade nearby tissues or spread to distant organs - a process known as metastasis, which is a leading cause of cancer-related deaths. Other common terms for cancer include malignant tumors and neoplasms. Globally, cancer is the second leading cause of death (after cardiovascular diseases), responsible for an estimated 10 million deaths in 2022. Among women, the most common types include breast, colorectal, lung, cervical, and thyroid cancers. In men, lung, prostate, colorectal, stomach, and liver cancers are the most prevalent.

I. B. Main characteristics of cancer

Although cancers can be of different types, they share some common characteristics[1]:

- Sustained proliferation: cancerous cells are insensitive to anti-growth signals and self-sufficient in growth signals, which give them unlimited replication potential.

  Insensitivity to anti-growth signals: in healthy tissues, anti-growth signals help maintain environmental balance (homeostasis) by keeping normal cells in a non-dividing, dormant state. Anti-growth signaling molecules bind to specific receptors on the cell surface, triggering a chain of reactions that ultimately prevent the cell from proliferating. However, cancer cells have developed the ability to evade signaling at various stages, making them unresponsive to anti-growth controls and leading to uncontrolled growth.

  Self-sufficiency in growth signals: in normal cells, growth signals from external sources are required to trigger mitosis. Growth signal molecules bind to receptors on the cell membrane, activating the transition to a proliferative state. In contrast, many cancer cells can produce their own growth signals, allowing them to bypass external signals and promote their own uncontrolled growth.

- Ability to evade apoptosis: apoptosis is a form of programmed cell death that eliminates damaged or unwanted cells. In normal cells, this process is triggered by pro-apoptotic signals, leading to controlled cell degradation and death. Cancer cells, however, often develop mechanisms to resist these signals, allowing them to survive and continue growing despite conditions that would otherwise trigger cell death.

---

[1] Hanahan, D., R.A. Weinberg *Cell* **2011** 144 646-674; Hanahan, D., R.A. Weinberg *Cell* **2000** 100 57-70.

- Tissue migration and metastasis: cancer cells have the possibility to migrate through blood vessels and lymph nodes to reach new areas and colonize them. Those metastases are responsible for most of cancer-related deaths.

- Unlimited proliferation and replication: telomeres protect genetic material by preventing harmful chromosome fusions, which can compromise cell viability. In normal (non-immortalized) cells, telomeres shorten with each cell division, eventually leading to cell death once they become critically short. In contrast, cancer cells exhibit abnormally high telomerase activity, the enzyme responsible for telomere synthesis. This activity counteracts telomere shortening, allowing cells to avoid senescence or apoptosis and enabling unlimited replication.

- Sustained angiogenesis: to grow and survive, cancer cells require a constant supply of oxygen and nutrients that are delivered by blood vessels. To support this need, they disrupt the balance of signals regulating blood vessel formation, promoting angiogenesis. This leads to abnormal growth of vessels within the tumor. These neo-vessels are irregular and porous, contributing to the unstable tumor environment.

- Inflammatory response in the tumor environment: inflammation is a natural defense mechanism that often arises early in cancer development. However, immune cells in the tumor environment can release signals that unintentionally promote cancer cell growth and survival, thereby supporting tumor progression.

- Reprogramming of energy metabolism: unlike normal cells, which primarily rely on glycolysis under low-oxygen (anaerobic) conditions, cancer cells can convert glucose to energy even in the presence of oxygen - a phenomenon known as the Warburg effect. This metabolic shift supports their rapid growth and proliferation.

- Genome instability: cancer cells are highly susceptible to mutations due to increased sensitivity to mutagenic factors. This genomic instability plays a key role in the development of their characteristics and adaptability.

I. C. Cancer diagnosis

Early detection of cancer can help prevent metastasis and increase survival rates. Current diagnostic methods include a range of clinical, biological, and imaging techniques. These methods are essential not only for detecting early signs of cancer but also for assessing its extent and guiding further investigations. These approaches help identify cancer at early stages, thereby increasing chances of effective treatment and long-term survival.

There are three main principles in cancer imaging[2]:

- Detection: find the affected area with the right sensitivity.
- Characterization: determine the phase and the type of tumor.
- Monitoring: watch and observe the progress of the disease.

Clinical examination is the first step in cancer diagnosis. During this initial assessment, the physician checks for visible or palpable abnormalities and evaluates symptoms. Biological tests can reveal tumor markers, substances produced in excess by cancer cells, offering clues about the cancer type and aggressiveness.

Medical imaging for detecting and monitoring cancer evolution:

- X-rays and Computed Tomography scans (CT) use ionizing radiation to produce detailed internal images. X-rays are useful for bone and lung cancers, while CT scans provide cross-sectional views of organs and help determine tumor size and spread.
- Ultrasound uses high-frequency sound waves for real-time imaging of soft tissues.
- Magnetic Resonance Imaging (MRI) uses magnetic fields and radio waves to generate detailed images without radiation. It is particularly effective for the brain, spine, and soft tissues.
- Nuclear imaging uses radioactive tracers to visualize different areas depending on the type of tracer used (e.g., antibody, glucose analog, small molecule).

Yet, biopsy remains the key method to confirm diagnosis of a cancer. It involves collecting a tissue sample for microscopic analysis by a pathologist and allows for determination of the exact nature of abnormal cells. A combined approach using clinical, biological, and imaging assessments is essential to improve treatment outcomes and survival.

Current screening and diagnostic tests are not always accurate, partly due to the often heterogenous structure of tumors, which requires multiple biopsy samples. False negatives can delay care, while false positives may cause unnecessary stress and procedures. These limitations highlight the need for more precise, accessible, and early diagnostic methods to ensure timely and effective cancer care.

---

[2] Pulumati, A., A. Pulumati, B.S. Dwarakanath, A. Verma, R.V.L. Papineni *Cancer Reports* **2023** 6 1-17.

I. D. Treatments

Once cancer is detected and characterized, several treatment options are possible depending on each case and tailored to the cancer type, stage, and location. The main goal is to eliminate or reduce cancer cells while preserving organ functions and minimizing side effects. Various treatments can be used alone or in combination:

- Surgery is often the first option for localized cancers. It may be curative (removing the tumor), palliative (reducing symptoms), or preventive (removing high-risk tissues).
- Chemotherapy uses cytotoxic drugs to kill cancer cells or stop their division, but it often causes severe side effects.
- Immunotherapy boosts the immune system to target cancer, using checkpoint inhibitors or cancer vaccines.
- Hormone therapy is used for hormone-sensitive cancers like breast or prostate cancer. It involves hormone blockers or surgery to remove hormone-producing organs.
- Gene therapy, still in its infancy, aims to correct faulty genes or disable cancer-promoting ones.
- Radiotherapy uses ionizing radiation to expose tumor cells to energy that damages DNA and leads to cell death. It is a part of nuclear medicine and will be explained below.

The three most frequently used methods are surgery, chemotherapy and radiotherapy. In France, 245,000 cancer patients were treated with radiotherapy in 2022[3], either alone or combined with another treatment.

II. Nuclear Medicine

II. A. Definition

In general, “nuclear medicine” refers to the application of a radioisotope in the medical field[4]. Nuclear medicine takes advantage of unique properties of radioactive isotopes. Indeed, unstable atoms have the particularity to decay by emitting different types of particles or electromagnetic radiations that can be used for imaging and/or therapeutic purposes. Interestingly, these isotopes have the same chemical properties as their stable (non-radioactive) analogues[5].

---

[3] Institut National du Cancer **2021** 1-19.

[4] Frey, K.A., H.D. Royal, M.F. Di Carli, G.L. Dillehay, L. Gordon, D.A. Mankoff, J. O'Malley, L. Ramanna, E. Rohren, G.M. Segall, B.L. Shulkin, J.W. Wallis, H.A. Ziessman *Journal of Nuclear Medicine* **2011** 52 994-997.

[5] Zhang, S., X. Wang, X. Gao, X. Chen, L. Li, G. Li, C. Liu, Y. Miao, R. Wang, K. Hu *Signal Transduction and Targeted Therapy* **2025** 10 .

In order to introduce radioactive elements in the body, the radionuclide can either be in the solid state and introduced at the immediate vicinity of the tumor (brachytherapy), or in the liquid state and administered either orally or intravenously (systemic radiotherapy). In the latter case, the radioisotope is linked to a carrier. This carrier can take different forms: small molecules, ligands, antibodies or nanoparticles. Usually, the carrier is chosen according to different criteria to target a specific type of cancer or a certain area in the body. The carrier should behave the same whether it is labeled or unlabeled, without changing the biochemistry of the system. The combination of a carrier and a radioisotope is called a radiopharmaceutical.

II. B. Main types of radiation

Radioactivity comes from an unbalanced number of protons and neutrons in the nucleus of an atom. When the ratio between neutrons and protons becomes unbalanced, the nucleus enters an unstable state. In order to regain stability, it undergoes spontaneous transformations aimed at adjusting this ratio. One common pathway is by changing its atomic number - either by ejecting nucleons (protons or neutrons) or other particles, or by releasing energy in other forms - thereby moving toward a more favorable neutron-to-proton balance. This natural drive toward stability is the fundamental cause of radioactive decay, which gives rise to various forms of nuclear radiation. These radiative processes are generally classified into two main categories: primary and secondary transformations. **Primary transformations** refer to the initial radioactive events that directly change the identity or composition of the nucleus. These processes often result in a daughter nucleus that is either stable or still in an excited state. **Secondary transformations** occur as a consequence of the primary ones. When the daughter nucleus is left in an excited energy state, it may release this excess energy in the form of gamma radiation, or through other mechanisms such as internal conversion or emission of Auger electrons.

The first category of primary transformations is **α-decay**. In this transformation, an α-particle (helium nucleus) is emitted from the nucleus. Due to its relatively large mass, high electric charge, and comparatively low velocity, alpha particle has a high probability of interacting with surrounding atoms as it travels through matter. These frequent interactions cause it to rapidly lose energy, resulting in a short penetration depth in matter. In human tissue, this penetration depth typically ranges 40 – 100 µm. Alpha-particles deliver a high amount of energy upon impact, resulting in pronounced radiocytotoxicity, which makes them good candidates for therapeutic applications. α-emitters are usually atoms with a high atomic number, such as ^{227}Th or ^{225}Ac and ^{211}At, and are usually used in α-therapy.

The second category of primary transformations is **β-emission**. β-particles have a lower energy level but also a higher penetration depth (few mm). There are two types of beta emissions: β^+ and β^-.

> In the case that the nucleus lacks of neutrons, one proton is converted into a neutron, leading to the emission of a positron (electron antiparticle). This is the β^+ emission. The emitted positron diffuses in the surrounding matter until it meets an electron.

Then annihilation occurs, and two gamma photons are emitted with the same energy and in opposite directions. This type of emission is used for Positron Emission Tomography (PET) imaging with isotopes such as ^{18}F, ^{11}C or ^{68}Ga.

The second type of β-radiations happens when the nucleus lacks protons. Then a neutron is converted into a proton and an electron is emitted, corresponding to the β^- emission. The electron interacts directly with the surrounding environment and can potentially damage cells or tissues. The β^--emitters are usually used in therapeutic approaches with radioisotopes such as ^{177}Lu, ^{131}I, or ^{161}Tb.

After the primary decay, the nucleus can still end-up in an excited state. In order to come back to its fundamental state, **secondary transformations** can happen. There are different processes to moderate the energy difference between excited and ground states. They can happen separately or together in one transition.

Among the secondary transformations, the emission of a photon, an electromagnetic radiation, is the most used, especially in imaging techniques. There are two classes of photons depending on their origin. The first type is gamma-ray which is emitted by the nucleus by the de-excitation of an excited state. Gamma-rays have the deepest penetration, which makes them useful in imaging techniques. Among the most used isotopes, we can cite ^{131}I, ^{192}Ir or ^{60}Co. The second type of electromagnetic radiation associated with nuclear processes is the X-ray. X-rays are emitted by the electron shell of the atom; they have longer wavelengths and lower energies than gamma rays. Depending on their penetration range, they are classified as either "soft" ($E < 10$ keV) or "hard" X-rays (10 to 120 keV). They can be used either for imaging or radiation therapy.

In some specific situations, where the difference of energy between the excited state and the ground state is low, and depending on the selection rules for the transition, the excited state of the nucleus can have some form of stability, called metastability. Such nuclei are called nuclear isomers and their half-lives can be even up to few years. An example of such radionuclide for biomedical applications is ^{99m}Tc ($t_{1/2} = 6$ h).

II. C. Production of medical radionuclides

With the development of nuclear medicine, methods to produce and purify radioisotopes were intensely developed. Since most of the radioisotopes used for medical applications are not natural, different production methods were implemented. Usually, the reaction of production of a nuclear isotope is as follows:

$$X + a \rightarrow Y + b$$

With X being the parent atom, Y the produced radionuclide, a the incident particle, and b the emitted particles. It is worth mentioning that this equation can also be written as X(a,b)Y. A focus will be given on the three main methods for radioisotope production: nuclear reactor, cyclotron or particle accelerator and generator.

Radionuclides and emitted radiations or particles are characterized by key parameters[6]:

- Half-life ($t_{1/2}$) – time needed for 50% decay of the initial activity,
- Specific Activity (SA) – radioactivity per mass unit of the product. It is expressed in Bq g^{-1}; similarly, molar specific activity is defined by the radioactivity per mol of matter and is expressed in Bq mol^{-1}.
- Radiation Absorbed Dose (RAD) – amount of energy (from any type of ionizing radiation) deposited to a mass unit of any medium. It is expressed in Gray (Gy) with 1 Gy = 1 J kg^{-1},
- Dose rate – quantity of radiation delivered or absorbed per time unit, expressed in Gray per second (Gy s^{-1}),
- Linear Energy Transfer (LET) – the average energy deposited locally per unit length of an ionizing particle's track, usually expressed in keV μm^{-1}.

LET is an important characteristic in radionuclide therapy. Indeed, a lower LET will induce less ionization inside the cell and make the efficiency of the therapy more dependent on external factors.

II. C. 1. Nuclear Reactor

In a nuclear reactor, isotopes are produced through the collision of neutrons with the nuclei of stationary target atoms. In most cases, the targets used in nuclear reactors are solid (metals or oxide powders), but it is also possible to use liquids or even gases[7]. Such reactions lead to neutron-rich radionuclides, which will decay *via* β^- emission. These isotopes are generally suitable for radiotherapy as they tend to have relatively long half-lives (Table 1).

Most of the reactions that occur in nuclear reactors are (n, γ) type, leading to products that are chemically identical to the target material, *i.e.,* the same chemical element. Therefore, the purification of the product can be difficult if not impossible, leading to generally lower specific activity (SA). Two other types of nuclear reactions can also occur: (n, p) and (2n, γ) reactions. The first one leads to chemically different elements, which facilitate subsequent chemical separation and purification. The (2n, γ) is hard to reach since it requires a high neutron flux to overcome the reaction threshold.

Table 1: Examples of radioisotopes produced in nuclear reactors

Isotope	**$t_{1/2}$**	**Decay**	**Application**
^{67}Cu	61.8 h	β^-	Radiation therapy
^{131}I	8.0 d	$\beta^- + \gamma$	Radiation therapy
^{161}Tb	6.9 d	$\beta^- + \gamma$	Radiation therapy
^{177}Lu	6.6 d	$\beta^- + \gamma$	Radiation therapy

---

[6] Knoll, G.F. **2000** .

[7] Agency, I.A.E. *Manual for Reactor Produced Radioisotopes* **2003** 1-262.

II. C. 2. Cyclotron

Particle accelerators produce radioisotopes *via* accelerating charged particles and directing them on a target material[8]. They are used to produce proton-rich radionuclides, which will decay *via* β^+-emission, applied to PET-imaging (Table 2). Cyclotrons have become the most popular type of accelerators in use for medical radioisotope production due to their compact size.

Cyclotrons can be used to accelerate either positively or negatively charged particles. The acceleration takes place under high vacuum to avoid any molecular collision that could change the particle trajectory, generate a loss of its energy or cause unwanted radioactivation of the cyclotron components. The particles are maintained on a circular path with a magnetic field, and acceleration is achieved through application of an electric potential. Once particles reach the desired energy, they are extracted, and the beam is directed to the target material for nuclear reactions. Target material is mostly in a solid form, but it may also be a liquid or a gas. Excess of beam energy can be used for a chemical reaction with another component of the target material. For example, during the production of ^{11}C, adding dioxygen can lead to the formation of $[^{11}C]CO_2$.

Table 2: Examples of radioisotopes produced in cyclotron

Isotope	**$t_{1/2}$**	**Decay**	**Application**
^{11}C	20.4 min	β^+	PET imaging
^{18}F	109.8 min	β^+	PET imaging
^{64}Cu	12.7 h	β^+mostly, β^-	PET imaging / theranostic
^{89}Zr	78.4 h	β^+	PET imaging
^{123}I	13.2 h	γ	SPECT imaging

II. C. 3. Generators

Generators are usually used to obtain radioisotopes with short half-lives (Table 3). This method exploits the fact that the parent radioisotope is stably absorbed on a resin and decays to a daughter radioisotope that can be washed out selectively. This technique is widely used in hospitals as it allows to obtain short-lived isotopes daily without requiring direct access to a cyclotron or nuclear reactor.

Table 3: Examples of radioisotopes obtained from a generator

Isotope	**$t_{1/2}$**	**Decay**	**Application**
^{68}Ga	67.7 min	$\beta^+ + \gamma$	PET imaging
^{90}Y	64 h	β^-	Radiation therapy
^{99m}Tc	6.0 h	γ	SPECT imaging

---

[8] Humphries, S., D.E. Young *Physics Today* **1988** 41 98-99.

II. D. Nuclear imaging

Nuclear imaging uses the emitted radiations from a radionuclide for diagnosis purposes. The most common methods of nuclear imaging are Positron Emission Tomography (PET) and Single Photon Emission Computed Tomography (SPECT)[9]. Since there is very low natural radioactivity in the body, radiopharmaceuticals accumulated in an organ or tissue can be detected with an excellent contrast compared to other imaging techniques, where all tissues inherently give a signal (MRI or CT). As a result, nuclear imaging usually requires less amounts of tracers to be injected, compared to other techniques. Nuclear imaging is quantitative as there is a direct correlation between the concentration of radiopharmaceutical and the intensity of the detected signal. A variety of radiopharmaceuticals have been developed, which offers multiple options for *in vivo* characterization of physiological and pathological processes.

Both PET- and SPECT-cameras provide functional and metabolic information but fail to provide anatomical information. To circumvent this issue, cameras are usually coupled with another imaging technique that gives morphological information. The most common one is CT, involving an X-ray tube and a row of detectors to measure X-ray attenuation by different tissues. Nowadays, Magnetic Resonance Imaging (MRI) systems are also combined with PET-cameras.

Despite the advantages of nuclear imaging, there are still some shortcomings. The first one is the relatively low spatial resolution of PET and SPECT in clinical studies, *i.e.,* 5 and 15 mm, respectively (this resolution is usually higher in preclinical studies). There is however some efforts put into developing technologies that would allow increased resolution in next generation scanners[10]. The second drawback arises from the radiation exposure associated with these imaging techniques. Although modern techniques have significantly reduced the amount of radioactivity in use, patients are still exposed to non-negligible doses. This raises concerns about cumulative radiation exposure, especially in patients undergoing repeated scans.

The procedure for nuclear imaging requires the administration of a radiopharmaceutical, which is usually done *via* intravenous injection. After administration of the tracer, it is possible to record either static or dynamic images. Static scans are performed after a specific waiting period, allowing the radiopharmaceutical to accumulate in the target tissue. In case of dynamic scans, image acquisitions often begin immediately after tracer administration and consist of a series of imaging (usually with shorter time duration at the beginning of the study and longer at later time points). Such scans can give an excellent representation of the dynamic processes, for example, regional perfusion. Over the last decades, development of whole-body PET scanners drastically increased the sensitivity of PET-imaging. This new type

---

[9] Bockisch, A., L.S. Freudenberg, D. Schmidt, T. Kuwert *Seminars in Nuclear Medicine* **2009** 39 276-289.

[10] Cheng, Z., P. Chen, J. Yan *EJNMMI Physics* **2025** 12 9; Liu, Z., M. Niu, Z. Kuang, N. Ren, S. Wu, L. Cong, X. Wang, Z. Sang, C. Williams, Y. Yang *EJNMMI Physics* **2022** 9 29.

of scanner has the possibility to scan the whole body and contains more detectors to increase the sensitivity[11].

For PET imaging, tracers labelled with positron-emitting radioisotopes are used. When the positron meets the electron, annihilation occurs, leading to the formation of two gamma-photons with energy of 511 keV each emitted in opposite directions, which are detected by the PET scanner to generate 3D images[12]. Common isotopes used in clinical studies are ^{11}C and ^{18}F, useful for labelling small molecules and realizing brain imaging[13], but their short half-lives require on-site cyclotron production. Metallic radionuclides such as ^{89}Zr ($t_{1/2}$ = 3.3 days)[14] offer longer half-lives, making them more suitable for larger molecules and antibodies. Meanwhile, ^{68}Ga, available from generator production, is gaining interest[15], despite its short half-life ($t_{1/2}$ = 68 min).

For SPECT-imaging, the injected radiopharmaceutical contains a gamma-emitting radioisotope. In case of this technique, the gamma camera will detect gamma rays emitted by the radioisotope and give a 2D image of the distribution in the body. To obtain 3D images, the camera takes a series of pictures with different angles, which are later reconstructed into a three-dimensional image. Compared to PET-imaging, the photon emission in SPECT only happens one at a time and in a single direction. Because of this single emission, the spatial resolution of SPECT tends to be lower than for PET-imaging[16]. Despite the lower resolution of SPECT scans compared to PET, the selection of radioisotopes used in this technique (usually with longer half-lives or generator-based as ^{99m}Tc) makes SPECT more popular and more accessible[17].

III. Radiotherapy

III. A. Definition

Radiotherapy is the application of ionizing radiation for therapeutic purpose[18]. When exposed to high-energy radiation, tumor cells undergo irreversible damages, leading to cell death. There are two types of radiotherapy depending on the origin of the irradiation source, external or internal radiotherapy.

External radiotherapy is the most used in ambulatory treatment as it consists in external irradiation of the tumor area. Most of the time, X-rays are used, but also gamma-rays or

---

[11] Katal, S., L.S. Eibschutz, B. Saboury, A. Gholamrezanezhad, A. Alavi *Diagnostics* **2022** 12 .

[12] Surti, S. *Journal of Nuclear Medicine* **2015** 56 98-105; Cherry, S.R., *R.D. Badawi, J.S. Karp, W.W. Moses, P. Price, T. Jones Science Translational Medicine* **2017** 9.

[13] Wang, J., *et al., Alzheimer's & Dementia* **2025** 21 70563.

[14] Wang, T., *et al., Journal of Medicinal Chemistry* **2025** 68 14843-14858.

[15] N'Guessan, *et al., EJNMMI Radiopharmacy and Chemistry* **2025** 10 54.

[16] Mark W. Groch, W.D.E. **2000** 233-244; Ritt, P. *Seminars in Nuclear Medicine* **2022** 52 276-285.

[17] Li, C., X. Li, Y. Wang, Z. Bai, Y. Wang, R. Gao, B. Jia *ACS Pharmacology & Translational Science* **2025** 8 2673-2682.

[18] Giraudet, A.L. *Cancer/Radiotherapie* **2023** 27 754-758.

electron beams. Radiations can be directly ionizing when charged particles (e.g., heavy ions, protons, electrons) are used, or indirectly ionizing with electrically neutral photons or neutrons. In the first case, secondary electrons are also responsible for the radiotherapeutic effect. For example, when a photon interacts with an atom in the medium, it collides with the electrons of the valence shell of the atomic nucleus, generating a secondary electron and a lower-energy photon. In order to limit side effects, the radiation should be mostly focused on tumor tissues while sparing healthy ones. External radiotherapy systems have been optimized to deliver radiation beams tailored to the three-dimensional geometry of the target volume. In early treatments, simple 2D irradiation was used but a large volume of healthy tissues was also irradiated together with the tumor. Nowadays, conformational radiotherapy allows to precisely match the irradiated volume with the tumor volume using multiple small X-ray beams[19]. This method allows to modulate the delivered dose and better protect healthy tissues.

The second approach is internal radiotherapy in which the radiation source is administered into or nearby the tumor. In this case, the emitted radiation should be ionizing with a short penetration depth such as with β^- (moderate linear energy transfer (LET) around 0.2 $keV \cdot \mu m^{-1}$) or α particles (high LET around 50-230 $keV \cdot \mu m^{-1}$). This allows to increase the dose locally near the tumor while protecting the healthy surroundings.

There are two main types of internal radiotherapy: sources can be either in the solid state and introduced in the vicinity of the tumor, or in the liquid state and administered either orally or intravenously. The former method is called Curie therapy or brachytherapy. Depending on where and how the source is introduced, different types of brachytherapy can be considered:

- directly into the tumor, interstitial brachytherapy,
- in a body cavity close to the tumor, such as the uterus or vagina, intracavitary brachytherapy,
- at the surface of the skin, surface brachytherapy.

The source used in brachytherapy approaches is classically ^{192}Ir ($t_{1/2}$ = 73.8 days), a β^- emitter[20]. This strategy allows to reach high doses in the tumor area.

An alternative to brachytherapy is the injection of radiopharmaceuticals in the blood stream (systemic radiotherapy). Targeted radionuclide therapy (TRT) was developed in order to improve the delivery of radiation in secondary cancer lesions. The main advantage is that tumor area does not need to be precisely defined as the radiopharmaceuticals can target cancer cells. Systemic administration offers the possibility of reaching deep areas in the body with no *a priori* on the precise localization of the tumor. In fact, pharmacokinetics and

---

[19] Choi, W.H., J. Cho *Journal of Korean Medical Science* **2016** 31 S75.

[20] Ciurlia, E., B. Santo, M.C. Barba, E. Cavalera, P. De Franco, S. De Matteis, G. Di Paola, A. Leone, A. Papaleo, D. Rubini, D. Russo, G. Rubini, A. Sardaro *Frontiers in Oncology* **2025** 14 1525926.

targeted biodistribution are mainly driven by physicochemical properties of the carrier platform and by the physiological environment of the cancerous tissue[21]. This aspect is important to consider in the treatment of spreading metastatic cancers whose precise diagnosis remains problematic in the early stages of the disease. Such an effect cannot be expected with external radiotherapy or brachytherapy since irradiation is applied only locally.

One of the first example of systemic internal radiotherapy exploited the high affinity of iodine for thyroid to reach this area selectively and deliver ^{131}I for thyroid cancer or hyperthyroidism[22]. The most commonly used radioisotopes in internal radiotherapy are ^{131}I and ^{177}Lu, conjugated with a carrier system. One can mention, Lutathera® a radiopharmaceutical for Peptide Receptor Radionuclide Therapy (PRRT) that was first approved in 2017 by European Medical Agency (EMA) and the following year by the Food and Drug Administration (FDA)[23]. Lutathera® is composed of a somatostatin analogue radiolabeled with ^{177}Lu through a DOTA chelating unit. It is used in the treatment of cancers which express somatostatin receptors, as gastroenteropancreatic neuroendocrine tumors.

III. B. Design of a radiopharmaceutical

The efficacy of the systemic injection of radiopharmaceuticals relies mostly on selectivity of the carrier for the tumor and choice of the appropriate radioisotope, which depends on many factors[24]. The type of emission needed is directly correlated with the desired penetration depth of the irradiation. To treat small tumors, α particles are more efficient since they have short penetration depth and high energy level. On the other hand, β-particles have deeper penetration, rationalizing their use against larger tumors. Such considerations become important when distribution of the radiopharmaceutical inside tumor is inhomogeneous. In that case, the therapeutic response can be improved by using radionuclides with extended range of emission. This is called the "cross-fire effect"[25]. It is important to mention that such effect can also impact the surrounding healthy tissues.

Another important point to consider is the half-life of the radioisotope. For therapeutic applications, isotopes with moderately long half-lives such as ^{177}Lu ($t_{1/2}$ = 6.7 days) or ^{90}Y ($t_{1/2}$ = 2.7 days) are preferred, as isotopes with extended half-lives might cause some side effects to healthy organs where they may accumulate transiently.

Finally, daughter radionuclides of the isotope have also to be considered. Indeed, the decay of a parent radionuclide can produce daughter radioactive species. This can induce side effects. One example is ^{225}Ac, an α emitter that decays directly to ^{221}Fr ($t_{1/2}$ = 4.8 min)

---

[21] Gudkov, S., N. Shilyagina, V. Vodeneev, A. Zvyagin *International Journal of Molecular Sciences* **2015** 17 33.

[22] Arnoldo Piccardo, Martina Ugolini, Vania Altrinetti, Sergio Righi, Francesco Fiz, Luca Foppiani, L.G. 6 *Q J Nucl Med Mol Imaging* **2021** 65 132-137.

[23] Das, S., T. Al-Toubah, G. El-Haddad, J. Strosberg *Expert Review of Gastroenterology & Hepatology* **2019** 13 1023-1031.

[24] Volkert, W.A., W.F. Goeckeler, G.J. Ehrhardt, A.R. Ketring *J Nucl Med*. **1991** 32 174-85.

[25] Staudacher, A.H., E. Bezak, A. Borysenko, M.P. Brown *Nuclear Medicine Communications* **2014** 35 1284-1290.

followed by a cascade of decays to ^{213}Bi ($t_{1/2}$ = 45 min), ^{209}Pb ($t_{1/2}$ = 3.2 h) and ending with stable ^{209}Bi isotope. As the first decay daughter isotope ^{221}Fr can be released from the radiopharmaceutical and diffuse to other organs and tissues where it can decay to other radioisotopes. This phenomenon increases the toxicity of ^{225}Ac and limits its application[26]. In such case, a careful dosimetry needs to be performed to assess the dose delivered to healthy tissues to make sure that TRT treatment does not cause damages to the healthy organs.

The efficacy of systemic injection of radiopharmaceuticals relies mostly on the selectivity of a carrier for a tumor. Therefore, design of the appropriate carrier also plays an important part in the success of internal radiotherapy. Small molecules, biomolecules or even nanoparticles can be used as carriers to bring radionuclide to the tumor area. Increasing the selectivity of a carrier allows improving the dose delivered in the tumor area and reducing side effects. Two types of carriers were mainly investigated: biomolecules and nanoparticles. Due to their high selectivity, biomolecules are well suited to target a specific receptor overexpressed in cancer cells[27]. Nanoparticles, on the other hand, benefit from tissue-specific accumulation in tumors through passive targeting, making them very promising platforms[28]. Also, nanoparticles can be decorated with ligands or antibodies to induce active targeting of the cancerous cells. Moreover, different chemical modifications of the nanoparticles can be implemented to improve their pharmacokinetics and biodistribution, as well as to enhance their multi-functionality and applicability.

III. C. Physical principle of radiotherapy

III. C. 1. Interactions between radiation and matter

The radiations applied in radiotherapy are all ionizing, either directly from charged particles, or indirectly from neutral photons or neutrons, which will interact with the matter and create a second wave of electrons.

When ionizing radiations interact with the outer valence shell of an atom, an electron from this shell can be ejected as well as a photon of lower energy. This is the Compton effect and it is one of the most important effects occurring in soft tissues (Figure 1).

---

[26] Dorso, L., E. Bigot-Corbel, J. Abadie, M. Diab, S. Gouard, F. Bruchertseifer, A. Morgenstern, C. Maurel, M. Chérel, F. Davodeau *PLOS ONE* **2016** 11 e0151330.

[27] Chinn, P., G. Braslawsky, C. White, N. Hanna *Cancer Immunology, Immunotherapy* **2003** 52 257-280.

[28] Ehlerding, E.B., P. Grodzinski, W. Cai, C.H. Liu *ACS Nano* **2018** 12 2106-2121.

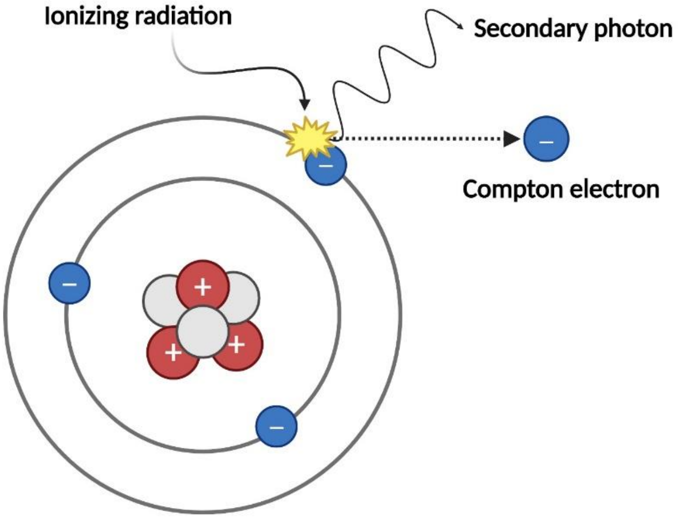

Figure 1: Compton Effect

Another competitive effect is the photoelectric effect. It happens when a photon interacts with an atom. First, an electron from the inner shell is ejected, leading to an excited state of the atom and leaving a vacancy in the electronic shell. In order to fill this vacancy, an electron from the external shell is transferred to the inner one, which releases energy. Then there are two possibilities (Figure 2):

- emission of a photon of lower energy (photoelectric effect),
- transmission of this energy to an electron from the outer shell that is released (Auger electron).

A cascade of Auger electrons can occur, which allows the production of multiple electrons with a single ionizing radiation. The number of Auger electrons released increases with the atomic number (*Z*) of the element.

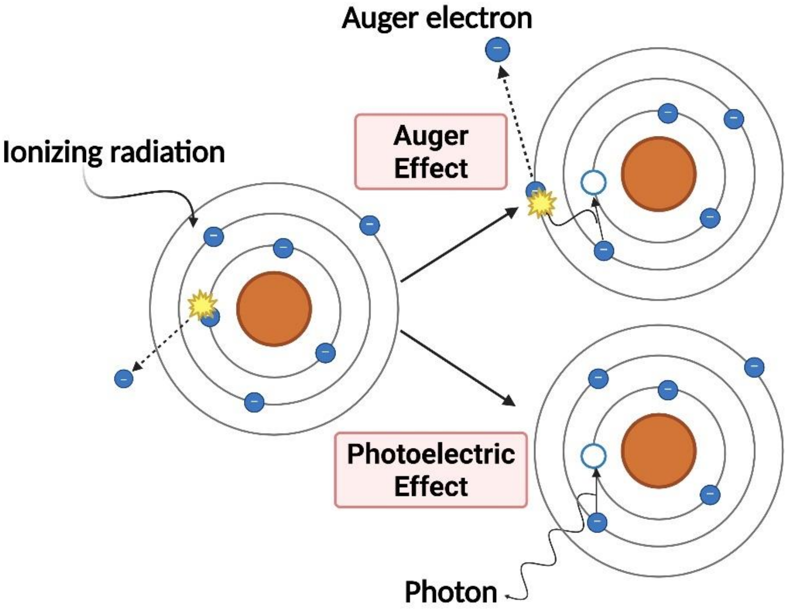

Figure 2: Photoelectric effect and Auger electron

Finally, if the incoming photon has an energy higher than 1022 keV in the surrounding of an atom, a particle-antiparticle (electron-positron) pair is created. Each particle created from the disappearance of the photon has an energy of 511 keV. This phenomenon is called pair production (Figure 3)

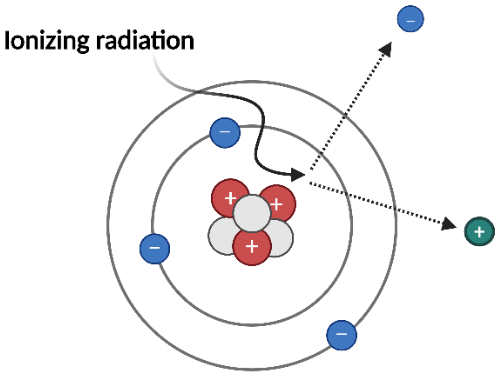

Figure 3: Pair Production

Each of the above phenomena has a different probability of occurrence. As said earlier, the Compton effect is most important in soft tissues and does not depend of the atomic number of the atom (Z). The photoelectric effect probability is proportional to Z and inversely proportional to the energy of incoming photon. Thus, the photoelectric effect will be predominant for heavy atoms and low energy photons. For both, Compton and photoelectric effects, the energy of incoming photon has to be slightly higher than the binding energy of the electron. Finally, pair production probability increases with the energy of incoming photon and according to Z^2.

Furthermore, when a radiation interacts with matter (e.g., tissues), it deposits energy along its entire path. Studies have shown that X-rays release energy continuously until all their initial energy is exhausted, and protons or carbon ions primarily deposit the bulk of their energy at a specific depth within the material. The distribution of energy deposited as radiation penetrates tissues creates a peak known as the Bragg peak (Figure 4) [29].

---

[29] Tinganelli, W., M. Durante *Cancers* **2020** 12 3022.

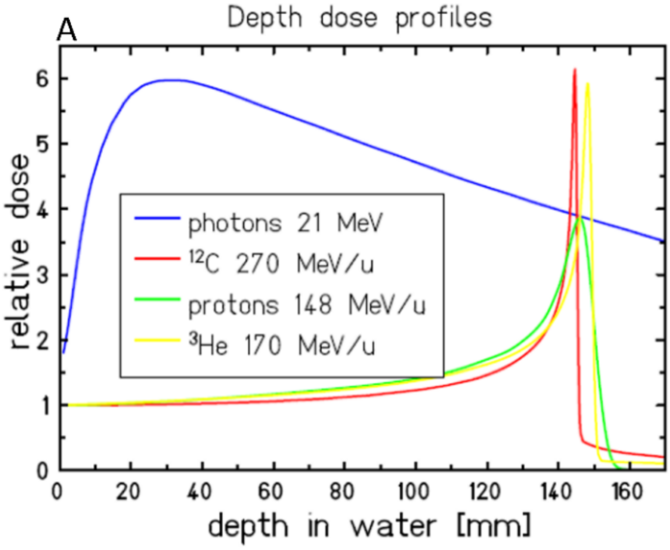

Figure 4: Dose deposition in water[30]

This feature is crucial in radiotherapy, where the objective is to minimize damage to healthy tissue by limiting energy deposition outside the tumor region. Greater penetration depth is particularly beneficial in treating heterogeneous tumors, where the dose distribution may be uneven. In such cases, deeper penetration enables the radiation to reach cells located further within the tumor through the crossfire effect[31].

III. C. 2. Interaction with biological material

In a biological environment, radiations interact with cells or biomolecules, leading to chemical changes. The biological effect can be sorted into two categories: direct and indirect damages.

In the direct pathway, radiations interact directly with cells and especially DNA leading to cell death through different mechanisms: creation of oxidized bases, creation of abasic sites, complex chromosomal rearrangement, simple and double strands breaks, DNA cross-links (Figure 5)[32].

---

[30] Tinganelli, W., M. Durante *Cancers* **2020** 12 3022.

[31] Aghevlian, S., A.J. Boyle, R.M. Reilly *Advanced Drug Delivery Reviews* **2017** 109 102-118.

[32] Lomax, M.E., L.K. Folkes, P. O'Neill *Clinical Oncology* **2013** 25 578-585.

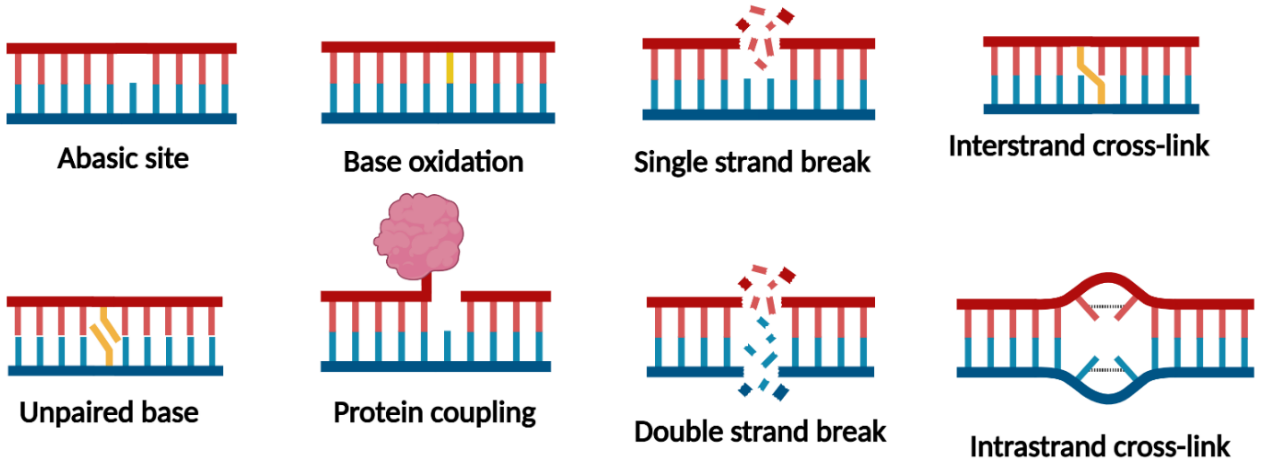

Figure 5: DNA damages

In the indirect pathway, radiations interact with the surrounding environment of the cells leading to the formation of free radicals. A free radical is a chemical species with an unpaired electron on its valence shell giving the species high reactivity. Since living systems are mostly composed of water, most of the radiations will interact with water according to the following equations:

$h\nu + H_2O \rightarrow e^- + H_2O^+$ (*Eq 1*)

$h\nu + H_2O \rightarrow H_2O^*$ (*Eq 2*)

$H_2O^* \rightarrow H^{\cdot} + HO^{\cdot}$ (*Eq 3*)

$H_2O^+ \rightarrow H^+ + HO^{\cdot}$ (*Eq 4*)

$e^- + H_2O \rightarrow H^{\cdot} + HO^-$ (*Eq 5*)

$H^{\cdot} + H_2O \rightarrow H_2 + HO^{\cdot}$ (*Eq 6*)

$H^{\cdot} + O_2 \rightarrow HOO^{\cdot}$ (*Eq 7*)

$e^- + O_2 \rightarrow O_2{}^{\cdot -}$ (*Eq 8*)

$HOO^{\cdot} + H_2O \rightarrow O_2{}^{\cdot -} + H_3O^+$ (*Eq 9*)

$HOO^{\cdot} + H^{\cdot} \rightarrow H_2O_2$ (*Eq 10*)

$HO^{\cdot} + H^{\cdot} \rightarrow H_2O$ (*Eq 11*)

$HO^{\cdot} + HO^{\cdot} \rightarrow H_2O_2$ (*Eq 12*)

$H^{\cdot} + H^{\cdot} \rightarrow H_2$ (*Eq 13*)

The irradiation of water leads to the formation of different species, and the intracellular oxygen level has a strong impact on the nature and yield of formed species. In the presence of oxygen, the hydrogen radical ($H^\bullet$) can react to form the hydroxyperoxyl radical $HOO^\bullet$ (eq. 7), a highly unstable and reactive intermediate. It is easily deprotonated and leads to the superoxide radical $O_2^{\bullet-}$ (eq. 9). Superoxide radicals can also be produced by the reaction of an electron with molecular oxygen (eq. 8). These oxygen-derived radicals have a large number of recombination possibilities leading to the formation of ions (H^+, OH^- or H_3O^+), other radicals ($H^\bullet$, $OH^\bullet$, $O_2^{\bullet-}$, or $HOO^\bullet$), or molecular species (H_2, H_2O_2). The free radicals produced are usually called ROS (Reactive Oxygen Species).

Among the different products of water radiolysis, the $OH^\bullet$ radical plays an important part in the efficacy of radiotherapy since it is involved in DNA damages[33]. The $OH^\bullet$ radicals behave like electrophilic species which can oxidize DNA bases. These reactions can lead to the formation of intra- and inter-strand adducts. Additionally, ROS can damage other cellular structures (cell membrane or mitochondria) that also leads to cell death.

Cells have the capacity to repair DNA damages to some extent but damages can be irreversible. When irreversible damage occurs to the DNA or key organelles, the cell is driven toward either apoptosis or mitotic catastrophe. Apoptosis is a process in which the cell and its damaged DNA are systematically broken down and eliminated. Mitotic catastrophe, on the other hand, arises from DNA damage that disrupts proper chromosome segregation during cell division, leading to the formation of an enlarged cell with multiple micronuclei. This abnormal cell ultimately dies through apoptosis, necrosis, or enters a state of senescence.

III. D. Radiosensitivity

The effects of radiations on cells and tissues vary depending on the type of radiation involved. When exposure causes toxicity - most commonly by inhibiting cell proliferation - the cell or tissue is considered radiosensitive[34]. In contrast, radioresistance refers to cell or tissue ability to withstand the effects of ionizing radiation, reducing the effectiveness of radiotherapy. The biological mechanisms underlying radioresistance are complex. The correlation between radiosensitivity and the properties of the tissues (cell division rate, cell differentiation) has been investigated. It is therefore useful to distinguish between:

- compartmentalized tissues (e.g., bone marrow, skin) which contain a compartment of radiosensitive stem cells capable of self-reproduction that can compensate for cell loss and a compartment of mature, radioresistant differentiated cells incapable of dividing,
- Non-compartmentalized tissues that do not contain stem cells exhibit a delayed onset of functional impairment after irradiation, depending on the lifespan of their differentiated cells, and in which cell renewal depends on the considered cell type.

---

[33] Breen, A.P., J.A. Murphy *Free Radical Biology and Medicine* **1995** 18 1033-1077.

[34] El-Nachef, L., *et al.*, *International Journal of Molecular Sciences* **2021** 22 7158.

An important aspect of radiosensitivity is the differential effect: not all cells have the same ability to repair radiation-induced damage. Healthy cells generally possess more effective repair mechanisms than cancer cells, making them less susceptible to radiation. This difference underlies the selective action of ionizing radiation on tumors. In addition, several other biological and physiological factors influence the overall effectiveness of radiotherapy.

III. D. 1. Biological phenomenon of radiosensitization

One key factor influencing radiosensitivity is the stage of the cell cycle. During the cell cycle, a cell duplicates its genetic material and divides into two identical daughter cells. This cycle consists of four main phases: i) G1 phase – cell growth and preparation for DNA replication, ii) S phase – DNA replication, iii) G2 phase – further growth and preparation for mitosis, iv) M phase (mitosis) – the actual process of cell division. Cells in the late S phase tend to be more radioresistant, while those in the G2 and M phases are the most radiosensitive.[35]

Each type of tissue has an inherent level of radiosensitivity, largely determined by its ability to repair radiation-induced damage. The radiobiological response of a tissue depends on both lethal damage, which causes immediate cell death, and sub-lethal damage, which may accumulate over time and eventually lead to cell death. Tissues with a strong repair capacity can manage sub-lethal damage more effectively and are generally considered radioresistant. In contrast, tissues with limited repair capacity are more radiosensitive.

In recent years, dose fractionation has become a widely adopted approach in radiotherapy[36]. This technique involves delivering the total radiation dose over multiple sessions spaced out over time. It has proven effective in distinguishing between cancerous and healthy tissues due to differences in their biological responses. The success of dose fractionation is based on the four "R"s of radiobiology: i) Repopulation – surviving cells begin to proliferate after radiation, ii) Redistribution – tumor cells shift into more radiosensitive phases of the cell cycle, iii) Re-oxygenation – improved oxygen availability enhances radiation effectiveness, iv) Repair – healthy tissues repair sub-lethal damage more efficiently than tumor tissues[37].

Between treatment sessions, these four processes occur simultaneously. For example, tumor cells may move into more radiosensitive phases, making subsequent treatments more effective. At the same time, the stress of irradiation may accelerate tumor cell repopulation, which may require adjusting the total radiation dose. Re-oxygenation also plays a key role. As radiation kills tumor cells, oxygen consumption decreases, allowing more oxygen to reach the remaining cells - making them more susceptible to future radiation.

Overall, the effectiveness of dose fractionation depends on the differential effect and the repair capacity of the tissues. Fractionated doses let normal tissues recover while tumor cells accumulate damage, enhancing cancer control with less harm for surrounding healthy

---

[35] Pawlik, T.M., K. Keyomarsi *International Journal of Radiation Oncology*Biology*Physics* **2004** 59 928-942.

[36] Hennequin, C., S. Guillerm, L. Quero *Cancer/Radiothérapie* **2019** 23 500-502.

[37] Withers, H.R. *Advances in Radiation Biology* **1975** 5 241-271.

tissues. However, some cancers (e.g., carcinomas, lymphomas) may repopulate under fractionation, reducing efficacy and requiring higher total doses. Additionally, early-responding tissues are generally less affected by fractionation, limiting its benefit in certain contexts.

Another strategy to enhance radiosensitivity is hyperthermia - raising the temperature of tumor tissues above 42 °C. At this elevated temperature, the ability of tumor cells to repair radiation-induced DNA damage is inhibited, making them more vulnerable to radiation therapy[38].

III. D. 2. Role of oxygen in tumor radiosensitivity

Since the late 1940s, the role of oxygen in influencing tumor radiosensitivity has been extensively studied[39]. This phenomenon, known as the oxygen effect, refers to the enhanced effectiveness of radiation in the presence of oxygen. The mechanism involves the formation of reactive oxygen species (ROS), which causes additional damage to cellular structures and DNA. Higher oxygen levels in tumor tissues promote greater ROS production and, consequently, more extensive radiation damage. Tumors with reduced oxygen levels are referred to as hypoxic, in contrast to normoxic tumors with normal oxygenation. Hypoxic tumors tend to be more radioresistant due to the reduced generation of ROS.

Moreover, irradiation of cancer cells can create radicals directly on DNA ($R^\bullet$). In normoxic conditions, those radicals react with molecular oxygen to form peroxyl radicals ($ROO^\bullet$) that will become organic peroxides (ROOH), which are difficult for cells to remediate. Dioxygen stabilizes radiation-induced damages and increases the toxicity of the radiation towards cells. This effect is more important for radiations with lower Linear Energy Transfer values (X rays) since they have lower ionization capacity. To characterize the oxygen effect, the Oxygen Enhancement Ratio (OER) was introduced[40].

$$OER = \frac{irradiation\ dose\ in\ hypoxic\ condition}{irradiation\ dose\ in\ normoxic\ conditions}$$

The OER highlights the importance of oxygen supply during tumor cell irradiation by establishing the ratio between the irradiation dose under hypoxic conditions and the irradiation dose under aerobic conditions required to achieve the same biological effect. It was demonstrated that the OER decreases when the LET increases. Therefore, for radiations with a low LET value, the OER is usually high, between 2 and 3 while radiations with higher LET show a low OER, around 1 for α radiations.

The volume of tumor also plays an important part of the radiosensitivity of the tissue. Indeed, the chaotic vascularization of tumor tissues can create hypoxic areas, where the level of

---

[38] Genet, S.C., *et al.*, *Journal of Cellular Physiology* **2013** 228 1473-1481.

[39] Thoday, J.M., J. Read *Nature* **1947** 160 608-608; Liu, C., Q. Lin, Z. Yun *Radiation research* **2015** 183 487-496.

[40] Rockwell, S., I. Dobrucki, E. Kim, S. Marrison, V. Vu *Current Molecular Medicine* **2009** 9 442-458.

oxygen is low. In those areas, the radiosensitivity of the tumor is also lower. It is well documented that oxygen can diffuse only 75 µm around the blood vessels, Therefore, the smaller the volume of tumor, the higher the oxygen perfusion and radiosensitivity.

III. E. Radioresistance

Even though different tumor tissues have varying sensitivities to radiations, cancer cells can also develop radioresistance. Several mechanisms contribute to this:

- Inflammation and fibrosis: repeated exposure to radiation can trigger an inflammatory response within the tumor. This inflammation can lead to fibrosis, an abnormal growth of fibrous connective tissue in the tumor. Tumor fibrosis is often linked to cancer-associated fibroblasts, which are known to promote radioresistance.
- Blood vessel damage and hypoxia: ionizing radiation can also damage blood vessels, particularly the small microvasculature within the tumor. A lower density of blood vessels increases the risk of hypoxia (low oxygen levels) in the cancer cells. Hypoxia is a significant factor in increasing tumor radioresistance[41].

Tumors become radioresistant by altering their microenvironment to combat the oxidative stress from radiation and reactive oxygen species. They achieve this by creating a more reductive medium or by inducing chronic hypoxia, a state of low oxygen (1-3% compared to 4-9% in normal tissues). In this hypoxic state, ATP production is hindered, forcing cells to rely on glycolysis, which overproduces lactate. Lactate then acidifies the tumor pH and acts as an antioxidant, enhancing radioresistance.

Hypoxia also influences signaling pathways involved in tumor proliferation and cell cycle regulation. The overexpression of certain proteins, like p53, due to hypoxia can induce radioresistance. Furthermore, hypoxia can modify cancer cell characteristics, notably through epithelial-mesenchymal transition (EMT), a process linked to radioresistance. The resulting mesenchymal phenotype is highly invasive and can lead to metastasis. Finally, hypoxia can over-activate transcription factors crucial for cell survival, such as Hypoxia-Inducible Factor-1 (HIF-1). HIF-1 plays a key role in tumor cells' response to oxidative stress by controlling genes involved in angiogenesis, glucose metabolism, cell proliferation, and metastatic invasion. Overexpression of HIF-1 can led to increased angiogenesis, radioresistance, and a poorer clinical prognosis.

Given these mechanisms, counteracting hypoxia is a critical strategy to improve radiation therapy effectiveness. Current approaches include breathing hyperbaric oxygen, which aims to increase overall oxygen levels, but can cause side effects like nephrotic toxicity or hypertension. Another strategy involves injecting oxygen carriers like hemoglobin or nanoparticles to deliver oxygen directly to the tumor site.

---

[41] Richard P. Hill, PhD,*,‡,§ Robert G. Bristow, MD, P., P. Anthony Fyles, MD,†,§ Marianne Koritzinsky, P. Michael Milosevic, MD,†,§ and Bradly G. Wouters *Seminars in Radiation Oncology* **2015** 25 260-272.

IV. Nanoparticles

IV. A. Definition

Nanoparticles are defined as particles with at least one of their dimensions comprised between 1 and 100 nm. The nanometric scale provides unique properties to the particles. They show a higher surface area per volume unit, compared to larger particles, allowing a higher functionalization degree. Nanoparticles can be made of different materials and come in different sizes and shapes that give them different properties. They find applications in many fields such as manufacturing, material sciences, environment, energy and nanomedicine.

IV. B. Classification

Nanoparticles are usually classified according to their shape and the material they are made of. In terms of material, a distinction is generally made between organic, inorganic, and carbon-based nanoparticles (Figure 6).

Carbon-based nanoparticles are usually classified depending on the structuration of the carbon atoms they are made of, e.g., fullerenes, carbon nanotubes, nanodiamonds and graphene oxide[42]. Fullerenes and carbon nanotubes are made of sp^2 carbon atoms arranged in spherical or tubular shapes[43,44]. They are used in nanomedicine for exploiting, for example the photophysical properties of fullerenes that can be excited by photons, leading to the production of reactive oxygen species. Nanodiamonds are sp^3 carbon crystallized in cubic shape. Improving the water solubility and stability is a current challenge in order to use nanodiamonds in nanomedicine.

Organic nanoparticles include dendrimers, polymeric nanoparticles, micelles and liposomes[45]. Dendrimers are highly ordered, branched polymeric macromolecules that consist in the repetition of the same chemical pattern from a single core. Dendrimers have a lipophilic cavity and are usually coated with hydrophilic motifs increasing their solubility. On the other hand, amphiphiles or amphiphilic units are molecules with a hydrophilic head and a lipophilic tail. Polymeric nanoparticles are made of a polymer with hydrophilic coating wrapped up around itself, forming cavity to load drugs or any type of product. Polymeric vesicles or polymersomes consist in an auto-assembly in aqueous medium of amphiphilic copolymer units, forming an artificial vesicle. The polymers are assembled in bilayers creating an aqueous cavity in its core. Similarly, liposomes are made of lipidic bilayers, forming artificial vesicles and have an aqueous cavity. On the contrary, micelles are made of a monolayer of amphiphilic units. The term polymeric micelles is used to describe micelles

---

[42] Patel, K.D., R.K. Singh, H.-W. Kim *Materials Horizons* **2019** 6 434-469.

[43] M. Pérez, E., N. Martín *Chemical Society Reviews* **2015** 44 6425-6433.

[44] Gobre, V.V., A. Tkatchenko *Nature Communications* **2013** 4 2341.

[45] Mitragotri, S., S. Patrick *MRS Bulletin* **2014** 39 219-223.

made of block copolymers. To form micelles, the amphiphilic units are self-assembled in water into a spherical structure with a lipophilic central cavity. The cavity formed inside organic nanoparticles is of primary use for drug delivery[46].

Finally, inorganic nanoparticles are made of metal or metal oxides. Almost any metal can be used to form nanoparticles but some of them are better suited for nanomedicine. The most common are gold (Au), nickel (Ni), silver (Ag), iron oxides (FeO, Fe_2O_3, Fe_3O_4), platinum (Pt), silicon oxide (SiO_2) or titanium dioxide (TiO_2). These nanoparticles have different compositions, sizes and shapes. They can form nanospheres, nanorods, nanostars, and are usually coated with an organic molecule to increase their biological compatibility.

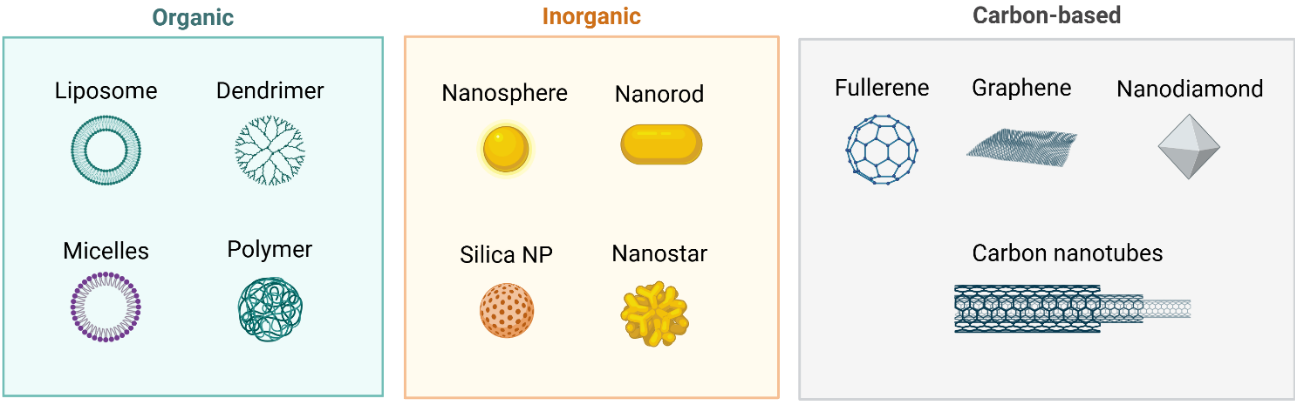

Figure 6: Different types of nanoparticles

Each type of nanoparticle has a different surface chemistry that allows a variety of transformations and modifications[47].

IV. C. *In vivo* behavior

Depending on the intended application, the behavior of nanoparticles can be optimized. As an example, for therapeutic application, an extended circulation time in the blood stream and slower excretion are required to leave enough time to the system to reach the targeted area, after injection.

When introduced into the body, nanoparticles can be taken up by the reticuloendothelial system (RES)[48], more precisely by the mononuclear phagocyte system, the first line of defense of the body against unidentified circulating objects. In fact, foreign objects are detected by a circulating protein family known as opsonins that are able to recruit macrophages. Once an opsonin binds to an object, a configuration change induces the recruitment of macrophages. Then, phagocytic cells from liver and spleen will quickly engulf the opsonized antigen and eliminate it from the circulation.

---

[46] Farokhzad, O.C., R. Langer *ACS Nano* **2009** 3 16-20.

[47] Lin, G., M. Zhang *Accounts of Chemical Research* **2023** 56 1578-1590.

[48] M. Christopher, A.M.L.S. *Physiology & behavior* **2016** 176 100-106.

The interaction between opsonin and nanoparticles depends on their surface charge, hydrophobicity and their hydrodynamic diameter. It was demonstrated that charged particles or very lipophobic particles are rapidly cleared from blood circulation. The behavior of nanoparticles is also correlated to their size[49]. According to the literature, small particles below 5 nm usually go through renal excretion with a fast clearance. Larger particles tend to accumulate in the liver and spleen and show a longer circulation time. Particles larger than 15 nm have slow elimination rates and high retention[50]. Finally, the flexibility of the particles seems to play a part as well. Indeed, soft nanoparticles seems to show longer blood circulation compared to solid ones.

The above properties can be modulated especially by modifying the surface of the particles. For example, polyethylene glycol (PEG) is known as a stealth polymer that can extend the circulation time of the particles in the body. Addition of biomolecules at the surface of the nanoparticle can also increase its circulation time and avoid uptake by the RES. Finally, the addition of targeting moieties at the surface of the particles can increase their accumulation in the desired area.

IV. D. Nanoparticles for cancer treatment

Nanoparticles are widely studied to create an innovative therapeutic formulation against cancer. In this context, nanoparticles have to escape the blood vessels to reach the tumor area. This is called extravasation and is mediated by the tumor micro-environment. In fact, the chaotic growth of tumors leads to the formation of abnormal vessels that are more dilated, irregular, disorganized and porous. This increased porosity comes from the loose junctions between endothelial cells constituting the walls of the blood vessels. These specificities allow nanoparticles to escape the circulation, diffuse outside of the blood vessels and passively accumulate in the tumor area. This is called the Enhanced Permeability and Retention (EPR) effect (Figure 7) [51].

---

[49] Hoshyar, N., S. Gray, H. Han, G. Bao *Nanomedicine* **2016** 11 673-692.

[50] Sonavane, G., K. Tomoda, K. Makino *Colloids and Surfaces B: Biointerfaces* **2008** 66 274-280.

[51] Wu, J. *Journal of Personalized Medicine* **2021** 11 .

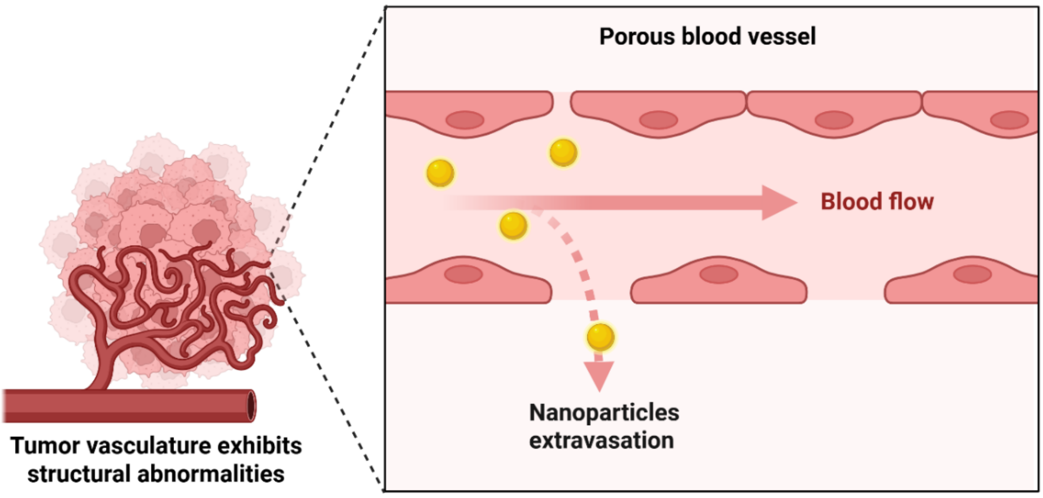

Figure 7: EPR effect

Healthy tissues do not have porous blood vessels; therefore, nanometric platforms extravasate only in the tumor area thanks to the defective vascularization. Nowadays, micelles are widely used for drug delivery of anti-cancer agents to the tumor area thanks to the EPR effect.

It has been shown that the average size of the pores in neo blood vessels is in the micrometer range[52], which allows extravasation of nanoparticles. To take advantage of the EPR effect, nanoparticles should have a molecular weight higher than 40 kDa since smaller compounds suffer from a faster clearance[53]. Biocompatibility is also required for the particles to circulate in the body.

IV. E. Nanoparticles for radiotherapy

In internal radiotherapy approaches, in order to target efficiently the tumor, a therapeutic radionuclide has to be combined with a carrier system such as a nanoparticle.

In the specific field of radiotherapy, nanoparticles present some advantages[54] compared to small molecules:

- it is possible to have more than one radionuclide per nanoparticle[55], which increases the amount of carried activity,
- it is also possible to combine radionuclides with other payloads to get access to multimodal platforms[56]. Such platforms can induce synergy between radiotherapy and other treatments such as chemotherapy, photodynamic therapy, etc.,

---

[52] Hashizume, H., P. Baluk, S. Morikawa, J.W. McLean, G. Thurston, S. Roberge, R.K. Jain, D.M. McDonald *American Journal of Pathology* **2000** 156 1363-1380.

[53] Maeda, H. *Proceedings of the Japan Academy Series B: Physical and Biological Sciences* **2012** 88 53-71.

[54] Liu, W., B. Chen, H. Zheng, Y. Xing, G. Chen, P. Zhou, L. Qian, Y. Min *Pharmaceutics* **2021** 13 1-31.

[55] Ancira-Cortez, A., *et al., Materials Science and Engineering C* **2020** 117 111335.

[56] Luna-Gutiérrez, M., *et al., Journal of the Mexican Chemical Society* **2013** 57 212-219.

- surface modification of the nanoparticle allows the grafting of targeting units to increase local accumulation and selectivity of the particle towards tumor cells[57].
- extended circulation time is beneficial in radiotherapy by allowing increased activity in the area of interest.

Moreover, the choice of the nanoparticle itself can affect the efficiency of radiotherapy. It is indeed possible to exploit the unique properties of some nanoparticles such as magnetism that can be used to guide drug delivery[58]. Another well-known strategy is to combine high atomic number (Z) metal with radiotherapy as it boosts the effect of irradiation by a radio-amplification phenomenon.

Radio-amplification or radio-enhancement are expressions that describe the capacity of certain element to increase the effect of ionizing radiation thanks to several physical phenomena. The radiation is absorbed by high atomic number metallic nanoparticles (e.g., gold nanoparticles[59]) which generates additional species that will increase the effect of the dose. The processes behind the radioenhancement effect by gold is complex and can be divided into three main stages: i) physical, with the activation and ionization of gold; ii) chemical, with the production of new chemical entities mostly from water and molecular oxygen; and finally, iii) biological, with directly or indirectly induced damages. The mechanism of radio-enhancement is different whether the source of irradiation is charged or neutral.

Gold nanoparticles are used in internal radiotherapy for their radio-enhancement properties. They can be combined with different radioisotopes such as Lutetium-177 (^{177}Lu) a low energy β^- (electron) and γ emitter. In that case the radiations can interact either with the biomolecules from the cell, with the surrounding environment (water radiolysis) or with the metal to produce other reactive species. Generally, low energy photons interact with gold mostly through the photoelectric effect. This interaction releases photoelectrons, X-rays and can generate multiple Auger electrons. These secondary electrons have a short range and their energy is deposited locally.

Another application of nanometric carrier systems for radiotherapy is their application to counterbalance hypoxia. As discussed earlier, hypoxia is a phenomenon that limits the efficiency of radiotherapy. The general idea is to restore the level of oxygen in the tumor to generate more ROS thanks to reaction with molecular oxygen. Since they can passively target and accumulate into tumors, nanoparticles seem well indicated to transport molecular oxygen to have a localized perfusion. During the past decade, different types of artificial vesicles for oxygen transport have been developed, taking advantages of the cavity inside micelles or polymeric nanoparticles.

---

[57] Yook, S., *et.al., Molecular Pharmaceutics* **2020** 17 1226-1236.

[58] Li, C., L. Li, A.C. Keates *Oncotarget* **2012** 3 365-370.

[59] Kwatra, D., A. Venugopal, S. Anant *Translational Cancer Research* **2013** 2 330-342.

V. Problematic of the PhD work

Among the different strategies available for cancer treatment, two different fields are of interest to our project: nuclear medicine and nanomedicine.

Nanomedicine focusses on the unique properties reached at the nanoscale that allow nanoparticles to passively reach the tumor area thanks to EPR effect. Nanoparticles such as micelles are used as supramolecular carriers for biological applications.

Nuclear medicine focusses on the use of ionizing radiation for treatment or diagnosis. In the context of cancer treatment, internal radiotherapy shows promising properties including the possibility to target deep tissues. However, different radioresistance mechanisms can hamper and limit the efficacy of radiotherapy. Since hypoxia is the source of different radioresistance phenomena, developing therapeutic agents that can restore the oxygen perfusion is sought.

The objective of my Ph.D. thesis was to develop a micellar nanocarrier formulation applied to internal radiotherapy. The designed carrier was intended to integrate multiple functionalities, including tumor targeting, radiotherapeutic delivery, re-oxygenation and radio-enhancement properties. The association of gold nanoparticles with micelles is expected to provide the radio-enhancement effect due to the high atomic number of gold, while simultaneously utilizing the micelles as oxygen carriers addressing the tumor hypoxia. Moreover, micelles further functionalized with a chelating moiety allow radiolabeling with a theranostic isotope such as ^{177}Lu. This should enable both the tracking the biodistribution of injected micelles, but also delivering the ionizing radiation source to the tumor.

The first chapter of this thesis presents the development of a fluorinated micellar carrier system combining gold nanoparticles for radioenhancement of external irradiations. The synthesis of an amphiphilic unit, its formulation into micelles and further encapsulation of gold nanoparticles was studied. The potential of the system for radiotherapeutic applications was tested *in vitro* under external electron beam irradiation conditions.

The second chapter focuses on the incorporation of a ^{177}Lu radioisotope to the micellar carrier and *in vitro/in vivo* evaluations. A chelating unit was covalently attached to the amphiphilic units constituting the micelles to allow radiolabeling with ^{177}Lu. The radiotoxicity of this nanohybrid system was evaluated *in vitro,* and biodistribution was performed *in vivo* using healthy mice models. Preliminary therapeutic applications were also evaluated on tumor bearing mice.

Chapter I: Fluorinated micelles encapsulating gold nanoparticles for radiosensitization

I. Objective of the chapter

Nanoparticles offer a versatile approach for targeted delivery of therapeutic agents to tumors, primarily through passive accumulation mediated by the Enhanced Permeability and Retention (EPR) effect. This phenomenon exploits the characteristic leaky vasculature and impaired lymphatic drainage of solid tumors. To maximize EPR-based targeting, nanoparticles must maintain prolonged circulation by evading capture by the reticuloendothelial system (RES), composed mainly of phagocytic cells in organs such as the liver and spleen. Surface modifications, notably PEGylation, enhance nanoparticle stealthiness and bioavailability by reducing opsonization.

Among nanocarriers, micelles have gained prominence due to their small size and customizable surface. Formed by self-assembly of amphiphilic molecules, micelles possess a hydrophobic core, suitable for encapsulating poorly water-soluble drugs, and a hydrophilic shell that confers stability in biological fluids. These characteristics facilitate drug solubility, bioavailability, and tumor-targeted delivery.

Recently, fluorinated nanocarriers have attracted interest for cancer therapy applications due to their high oxygen solubilization capacity. Such carriers can modulate the hypoxic tumor microenvironment (which limits treatments like radiotherapy) by increasing local oxygen concentration. Enhanced oxygen availability promotes ROS generation, crucial for radiation-induced DNA damage, thereby overcoming hypoxia-associated radioresistance.

In this context, our group has developed fluorinated micelles designed for oxygen delivery and radiosensitization. These micelles are expected to amplify radiation-induced ROS production, significantly improving the efficacy of external beam radiotherapy in cancer cells.

Also, gold nanoparticles (AuNPs) are established radiosensitizers due to their high atomic number, which intensifies localized radiation dose *via* secondary electron emission under irradiation.

The objective of this study is to integrate fluorinated micelle–mediated oxygen delivery with AuNP-based radio-enhancement into a single nanoplatform. By encapsulating gold nanoparticles within the hydrophobic core of perfluorinated micelles, we aim to passively co-deliver gold and O_2 to tumors *via* the EPR effect, achieving synergistic enhancement of radiotherapy through concurrent oxygenation and dose amplification.

To this end, we synthesized perfluorinated amphiphiles and induced their self-assembly into stable micelles. Gold nanoparticles were in parallel prepared and encapsulated within the micellar core. The hybrid constructs were characterized for their size, surface charge, colloidal stability, and oxygen-loading capacity. *In vitro* assays permitted to evaluate their cytotoxicity and radiosensitizing potential under external irradiation conditions.

Context

II. Micelles

II. A. Definition and general properties

Micelles are nanoscale colloidal aggregates that have garnered significant attention in the field of biomedical applications, particularly for drug delivery and diagnostic systems. Traditionally, micelles are formed by the self-assembly of amphiphilic surfactant molecules in aqueous solutions, where individual surfactant molecules (also referred to as unimers) spontaneously arrange into spheres, cylinders, or other morphologies above a certain threshold known as the critical micelle concentration (CMC)[60]. The core-shell architecture intrinsic to micelles allows them to encapsulate hydrophobic drugs in their core, while maintaining a hydrophilic shell, a feature that is especially advantageous for enhancing the solubility, stability, and bioavailability of poorly water-soluble therapeutics[61].

The structural paradigm of classical surfactant-based micelles centers around the balance between hydrophobic and hydrophilic moieties within the unimer[62]. Typically, a unimer consists of a hydrophobic tail (composed of long alkyl chains) and a hydrophilic headgroup, which may be ionic, nonionic, or zwitterionic[63]. This dualistic nature drives the segregation of incompatible segments in aqueous media, resulting in the spontaneous assembly into micellar structures once the system surpasses the CMC.

The assembly mechanism of classic surfactant-based micelles is governed by the minimization of the system's free energy[64]. Below the CMC, unimers remain as discrete entities in solution. Upon reaching and exceeding the CMC, the hydrophobic effect drives the aggregation of unimers into micelles, wherein the hydrophobic tails are sequestered within the core, shielded from the aqueous environment by the hydrophilic heads or PEG chains forming the corona. This structural arrangement not only enables the encapsulation of hydrophobic drugs within the core but also permits further functionalization for diagnostic[65] or targeting purposes[66].

The synthesis and the characterization of micelles entail a spectrum of methodologies and analytical tools. Traditional micelles made from small-molecule surfactants are prepared by simply dissolving the surfactant above its CMC in water, often followed by drug

---

[60] Ghezzi, M., S. Pescina, C. Padula, P. Santi, E. Del Favero, L. Cantù, S. Nicoli *Journal of Controlled Release* **2021** 332 312-336.

[61] Shuai, X., T. Merdan, A.K. Schaper, F. Xi, T. Kissel *Bioconjugate Chemistry* **2004** 15 441-448.

[62] Hoffman, H. *Berichte der Bunsengesellschaft für physikalische Chemie* **1978** 82 988-1001.

[63] Kosswig, K. *Ullmann's Encyclopedia of Industrial Chemistry* **2000** a25_747.

[64] Santos, M.S., F.W. Tavares, E.C. Biscaia Jr *Brazilian Journal of Chemical Engineering* **2016** 33 515-523; Nagarajan, R., E. Ruckenstein *Langmuir* **1991** 7 2934-2969.

[65] Kim, K.S., W. Park, J. Hu, Y.H. Bae, K. Na *Biomaterials* **2014** 35 337-343.

[66] Sonali, *et al., Drug Delivery* **2016** 23 1788-1798.

incorporation either by solvent evaporation, direct dissolution, or dialysis. Characterization techniques such as dynamic light scattering (DLS), transmission electron microscopy (TEM), and small-angle X-ray scattering (SAXS) are employed to ascertain micelle size, morphology, and monodispersity[67]. Surface charge (zeta potential)[68] measurements and critical micelle concentration determinations further verify colloidal stability and self-assembly efficiency.

II. A. 1. Nature of the surfactant

The nature of the hydrophilic head of the unimer impacts the intrinsic properties of the corresponding micelles, especially for biomedical applications. Ionic unimers can be anionic or cationic and possess an associated counterion to form a stable salt. The most used ones are anionic surfactant generally known as "soap". From a chemical point of view, they are usually fatty acid based on a linear saturated carbon chain with a terminal anionic group. These surfactants are used in many different fields, but they are not tailored for biological applications, especially due to a high CMC value that leads to low *in vivo* stability and a high nonspecific cytotoxicity. Indeed, such molecules are generally used as detergents and can disrupt the cell walls by dissolving the phospholipids[69]. Similar properties can be observed with cationic surfactants and more rarely with nonionic amphiphiles.

Additionally, the general negative charge at the surface of the micelles can lead to electronic repulsion with the cell membrane, ultimately leading to a lower cellular uptake[70]. Based on this principle, micelles bearing temporary negative charges were developed in the literature. These are acid-sensitive systems that exploit the difference in pH between healthy and tumor tissues, taking advantage of the slightly more acidic environment in the tumor to neutralize charges and be absorbed specifically in the tumor area[71].

Cationic surfactants have opposite properties, as they have higher cellular uptake and clearance due to strong electrostatic interaction with the cell membrane[72]. Similarly, to the anionic surfactants, cationic systems can be tuned to switch on their charge in the tumor area for a better cellular uptake. Most of the cationic unimers used nowadays are composed of an ammonium head, since it is one of the most easily accessible cations.

Another type of ionic surfactants are zwitterions. Zwitterionic amphiphiles exhibit physicochemical properties closer to nonionic surfactant due to their polar head bearing both positive and negative charges resulting in a net neutral charge[73]. Because of the dual charge on their polar head, zwitterions do not need a counter ion as they form their own

---

[67] De Caro, L., T. Stoll, A. Grandeury, F. Gozzo, C. Giannini *Pharmaceutics* **2024** 16 604.

[68] Paruchuri, V.K., A.V. Nguyen, J.D. Miller *Colloids and Surfaces A: Physicochemical and Engineering Aspects* **2004** 250 519-526.

[69] Pang, Z., A. Al-Mahrouki, M. Berezovski, S.N. Krylov *ELECTROPHORESIS* **2006** 27 1489-1494.

[70] Yamamoto, Y., Y. Nagasaki, Y. Kato, Y. Sugiyama, K. Kataoka *Journal of Controlled Release* **2001** 77 27-38.

[71] Zhang, P., D. Chen, L. Li, K. Sun *Journal of Nanobiotechnology* **2022** 20 31.

[72] Deng, H., X. Zhao, J. Liu, L. Deng, J. Zhang, J. Liu, A. Dong *Journal of Materials Chemistry B* **2015** 3 9397-9408.

[73] Seredyuk, V., E. Alami, M. Nydén, K. Holmberg, A.V. Peresypkin, F.M. Menger *Langmuir* **2001** 17 5160-5165.

“inner salt”. One of the best examples of natural zwitterions is phospholipids bearing both ammonium and phosphate groups. Even if they are ionic, zwitterionic amphiphiles exhibit properties similar to nonionic unimers, their CMC is usually lower than that of ionic amphiphiles but higher than nonionic ones. Additionally, the acidic pH of the tumor microenvironment can lead to the protonation of the negative charge of the zwitterion (e.g., carboxylic acids) generating positively charged micelles for a better cellular uptake. This feature, combined with the high stability and ability to reduce opsonization contributed to the popularity of this type of unimer.

Finally, nonionic surfactants are neutral and exhibit lower electrostatic interactions compared to their ionic analogues. They are suitable as coating and hydrophilic agents for biological applications. Additionally, they exhibit lower CMC values due to a lower solubility in water[74]. As a result, they are less likely to be in a monomeric state, which helps to avoid non-specific toxicity. They also feature high steric hindrance that could prevent adsorption of proteins. In biomedical applications, the unimer hydrophilic domain is frequently modified with poly(ethylene glycol) (PEG), a process known as PEGylation, to augment steric stabilization, minimize non-specific protein adsorption, and prolong systemic circulation by evading the mononuclear phagocyte system.

II. A. 2. Advantages for applications in therapy

Micelles are often used as carriers for drug delivery. Drug loading into micelles is typically achieved *via* co-solubilization of the drug and surfactant, or by employing the post-formation loading technique. In both cases, the hydrophobic core of the micelle serves as a reservoir for the therapeutic compound, protecting it from premature degradation and facilitating controlled release. This capacity for solubilizing hydrophobic drugs, together with the ease of surface modification and targeting ligand conjugation, underscores micelles’ utility as drug delivery vehicles[75]. Additionally, micelles can be engineered as diagnostic probes by incorporating imaging agents such as fluorescent dyes, radionuclides, or magnetic nanoparticles, thereby enabling real-time tracking of biological processes[76].

The application of micelles in drug delivery offers several notable benefits. Their nanoscale dimension can promote passive accumulation in tumor tissues *via* the EPR effect. The PEGylated corona reduces opsonization, thereby extending circulation times and improving pharmacokinetics[77]. Furthermore, the modularity of micellar systems allows for co-delivery of multiple agents for combination therapies, or for the integration of stimuli-responsive elements enabling site-specific drug release.

---

[74] Kosswig, K. *Ullmann’s Encyclopedia of Industrial Chemistry* **2000** a25_747.

[75] Almajidi, Y.Q., *et al.*, *Environmental Research* **2023** 227 115722.

[76] Gravel, E., *et al.*, *Chemistry - A European Journal* **2012** 18 400-408.

[77] Fang, Y., J. Xue, S. Gao, A. Lu, D. Yang, H. Jiang, Y. He, K. Shi *Drug Delivery* **2017** 24 22-32.

Despite these amenities, the clinical translation of micelle-based therapeutics is often hindered by several limitations, notably their thermodynamic instability and potential toxicity. Classical surfactant-based micelles can dissociate upon dilution below the CMC in the bloodstream, resulting in premature drug leakage. The toxicity of certain surfactants further complicates their use *in vivo*. To address instability issues, strategies such as chemical crosslinking of the micelle core (as in polydiacetylene micelles) are employed to enhance structural integrity[78]. Additionally, lowering the CMC *via* the rational design of unimers with increased hydrophobic character or optimized chain architecture offers greater stability under physiological conditions. Toxicity can be alleviated by employing biocompatible, biodegradable surfactant molecules[79] or block copolymers, and by rigorous purification to remove residual monomeric surfactant.

In summary, micelles formed from classical surfactants (and to a growing extent, from amphiphilic block copolymers) are versatile and effective nanocarriers for drug delivery and diagnostic imaging. Their self-assembly properties, tunable architecture, and facile functionalization render them highly attractive for biomedical applications, though ongoing efforts to improve their stability and biocompatibility are critical to their broader clinical adoption.

II. B. Specific case of fluorinated micelles

One of the principal barriers to the efficacy of radiotherapy in cancer treatment is tumor hypoxia. Hypoxic conditions, defined by a diminished supply of oxygen within the tumor microenvironment, are prevalent in many solid tumors and drastically constrain the production of reactive oxygen species (ROS) following irradiation. Since ROS are involved in a large part in the cytotoxic effect of radiation therapy, this oxygen deficiency directly compromises the effectiveness of radiotherapy and contributes to poor therapeutic outcomes.

Importantly, molecular oxygen is not only essential for ROS generation but also plays a crucial role in stabilizing DNA damage caused by ionizing radiation. Oxygen reacts with DNA radicals formed during irradiation to sustain strand breaks, preventing their repair and thereby enhancing the lethality of DNA lesions[80]. Consequently, insufficient oxygen levels in tumors also results in more readily reparable DNA damage, further decreasing radiotherapy effectiveness.

Addressing tumor hypoxia to increase radiosensitivity remains an area of intense research. One established approach involves the administration of hemoglobin as an exogenous oxygen carrier. Although hemoglobin can effectively enhance intratumoral oxygenation and

---

[78] Talelli, M., M. Barz, C.J.F. Rijcken, F. Kiessling, W.E. Hennink, T. Lammers *Nano Today* **2015** 10 93-117.

[79] Kalinova, R.G., I.V. Dimitrov, D.I. Ivanova, Y.E. Ilieva, A.N. Tashev, M.M. Zaharieva, G. Angelov, H.M. Najdenski *Journal of Functional Biomaterials* **2024** 15 53.

[80] Srinivas, U.S., B.W.Q. Tan, B.A. Vellayappan, A.D. Jeyasekharan *Redox Biology* **2018** 25 101084.

thereby mitigate hypoxia, its clinical utility is limited by severe adverse effects, including hypertension and liver toxicity[81]. These risks have prompted the search for alternative oxygen delivery systems that are both safer and more effective.

II. B. 1. Properties of perfluorocarbons

Perfluorocarbons (PFCs) have emerged as promising alternatives for oxygen transport due to their exceptional ability to solubilize gases. Perfluorocarbons are molecules made of a carbon backbone where all the hydrogen atoms have been exchanged by fluorine atoms, introducing new properties. Because of the high electronegativity of fluorine, the C-F bond is highly energetic which increases the energy of the C-C bonds *via* a decrease of the size of the carbon atoms orbital. Additionally, since fluorine atoms are bigger than hydrogen, PFC tends to adopt a helicoidal conformation, that is more rigid and more hindered[82]. The strength of the C-F bond also brings high thermal stability and chemical inertness, the best example being polytetrafluoroethylene (PTFE) commercialized under the name Teflon®.

Perfluorocarbons are also used for their high capacity to dissolve gases. This is due to the low polarizability of fluorine that limits the number of van der Waals bonds and thus the number of intermolecular interactions. The low cohesion between molecules leads to the formation of cavities where gas molecules can be included, just like oxygen. As an example, perfluorodecaline can solubilize 403 mL_{O2}/L_{PFC}, while water only solubilizes 10 mL_{O2}/L_{H2O} and blood 200 mL_{O2}/L_{blood}. Additionally, one liter of perfluorodecaline corresponds to 4.2 moles while one liter of water corresponds to 55 moles. From a molar perspective, this further highlights the superior ability of fluorinated phases to carry oxygen. Finally, the solubilization of oxygen in perfluorinated environment follows Henry's law: the gas solubility depends only of its partial pressure[83].

Efforts to clinically translate PFC-based formulations date back to the approval of a perfluorinated nanoemulsion, Fluosol®, by the U.S. Food and Drug Administration in 1989[84]. However, Fluosol® was ultimately discontinued, largely because of the cumbersome requirements for shipping and preparation. This experience illustrates the need for fluorinated oxygen carriers that combine physical stability, ease of use, and clinical practicality.

II. B. 2. Perfluorocarbons for local oxygen perfusion

PFCs present a range of features that make them attractive for biomedical use. Their high thermal stability and chemical inertness enable safe administration and long shelf-life, while their ability to dissolve large quantities of oxygen makes them ideal candidates for oxygen

---

[81] Wang, Q., J.-M. Li, H. Yu, K. Deng, W. Zhou, C.-X. Wang, Y. Zhang, K.-H. Li, R.-X. Zhuo, S.-W. Huang *Biomaterials Science* **2018** 6 3096-3107.

[82] Kirsch, P. **2004** .

[83] Jägers, J., A. Wrobeln, K.B. Ferenz *Pflügers Archiv - European Journal of Physiology* **2021** 473 139-150.

[84] Krafft, M.P., J.G. Riess *Advances in Colloid and Interface Science* **2021** 294 102407.

delivery in medical settings. Beyond serving as inert oxygen carriers, PFCs are known to inhibit platelet activation. This property can profoundly influence tumor physiology by increasing the porosity of tumor vasculature, thereby facilitating greater red blood cell infiltration, an effect that may further relieve hypoxic stress within the tumor. The dual functionality of oxygen delivery and vascular modulation has positioned PFCs at the forefront of research into radiosensitizing nanomedicines.

A recent study by Wu *et al.* exemplifies the innovative application of PFCs for overcoming hypoxia in cancer radiotherapy[85]. The study introduces a two-stage oxygen delivery system that uses perfluorotributylamine (PFTBA) encapsulated in human serum albumin (HSA) matrix, generating nanoparticles of approximately 150 nm in diameter to overcome tumor hypoxia and improve radiotherapy efficacy. In the first stage, physically dissolved O_2 in the perfluorocarbon is rapidly released after the nanoparticles accumulated in the tumor via EPR effect. In the second stage, PFTBA's intrinsic platelet-inhibition disrupts tumor vessel integrity, allowing red blood cells to infiltrate the tumor and supply additional oxygen (Figure 8).

The radiosensitizing potential of PFC@HSA nanoparticles was evaluated in tumor-bearing mice. Compared to control groups receiving radiotherapy alone, mice treated with the nanoparticle formulation exhibited a marked inhibition of tumor growth. Histological and molecular analyses revealed significantly higher levels of necrosis, apoptosis, and DNA double-strand breaks in the combination group, offering compelling evidence for the enhanced efficacy of this dual-action approach.

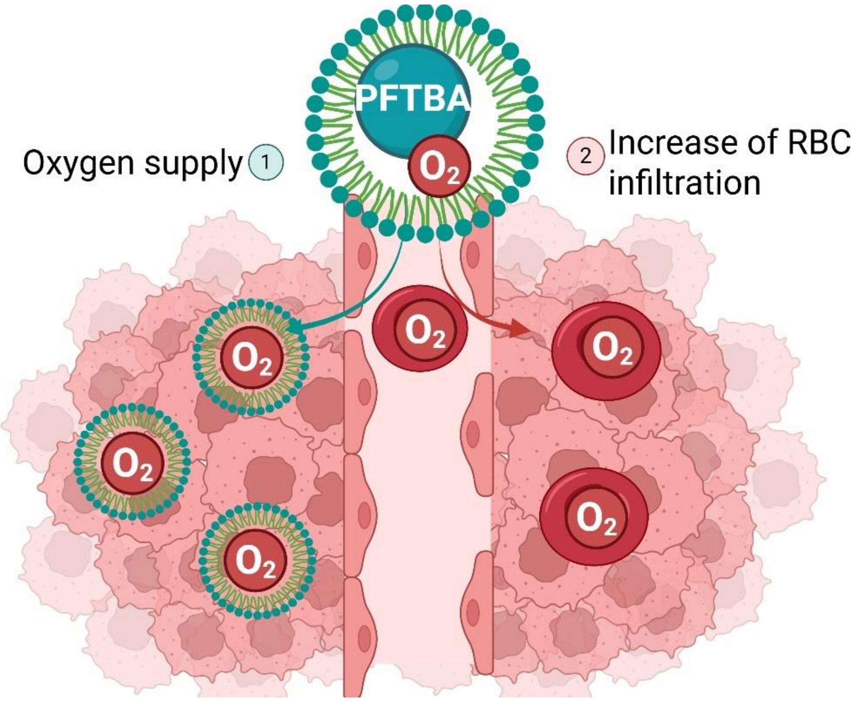

Figure 8: Two-step tumor oxygenation with PFC@HSA

---

[85] Zhou, Z., B. Zhang, H. Wang, A. Yuan, Y. Hu, J. Wu *Theranostics* **2018** 8 4898-4911.

In summary, the dual mechanism of PFC@HSA nanoparticles (immediate oxygen delivery followed by increased vascular permeability/red blood cell infiltration) provides a robust and durable approach to reversing tumor hypoxia and potentiating radiotherapy. By fulfilling the critical role of oxygen in both ROS generation and DNA damage stabilization, these nanoparticles substantially improve the cytotoxic effects of radiation therapy. These findings illustrate the promise of rationally engineered PFC nanocarriers as radiosensitizing agents, capable of overcoming key physiological barriers in the tumor microenvironment and improving outcomes in cancer treatment.

Recent advances in nanomedicine have explored the integration of oxygen delivery properties of PFCs with the drug carrier capabilities of micelles to engineer multifunctional platforms for cancer therapy. Building on this concept, Zheng and colleagues synthesized a cisplatin prodrug (cisPt(IV)) conjugated with lipids capable of encapsulating PFCs, thereby forming nanodroplets designed to simultaneously improve chemotherapy efficacy and alleviate tumor hypoxia during radiotherapy *via* enhanced oxygen transport[86]. The resulting nanoformulation, PFCE@cisPt(IV)Lip, exhibited an average hydrodynamic diameter of approximately 200 nm.

The cytotoxic potency of PFCE@cisPt(IV)Lip was evaluated using cancer cell lines cultured under normoxic and hypoxic conditions. Free cisplatin exhibited an IC_{50} of 1.2 µM in normoxia, increasing to 2.7 µM under hypoxia, consistent with the well-known reduction in efficacy within oxygen-deficient tissues. In comparison, the prodrug nanodroplets showed higher IC_{50} values (*i.e.*, 12 µM in normoxia and 16 µM under hypoxia), but higher double-strand DNA break in hypoxic conditions, suggesting effective reoxygenation. Additionally, the prodrug design conferred reduced intrinsic toxicity relative to free cisplatin, implying a favorable safety profile.

In vivo therapeutic evaluation in tumor-bearing mice involved intravenous injections on days 0 and 3, followed by X-ray irradiation on days 1 and 4. Mice receiving the combined treatment exhibited the most pronounced tumor growth inhibition relative to groups treated with either modality alone, underscoring the synergistic potential of this platform in overcoming tumor hypoxia and enhancing radiochemotherapy outcomes.

The above study presents a nanoformulation that combines oxygen delivery and chemotherapeutic prodrug release within a single micellar nanodroplet. The integrated strategy addresses the dual challenges of hypoxia-induced radioresistance and cisplatin systemic toxicity, thereby significantly improving tumor control in preclinical models. This work exemplifies the promise of engineered PFC-loaded micellar systems as multifunctional radiosensitizers with broad translational potential.

---

[86] Shen, Y., L. Liang, S. Zhang, D. Huang, J. Zhang, S. Xu, C. Liang, W. Xu *Nanoscale* **2018** 10 1622-1630.

II. B. 3. Perfluorocarbons combined with heavy elements

The efficacy of radiotherapy can be significantly enhanced through the use of high atomic number elements, alongside strategies aimed at alleviating tumor hypoxia. This synergistic approach was exemplified in a 2017 study by Song *et al.*, who developed a nanoplatform combining tantalum oxide (TaOx) nanoparticles with PFC-based oxygen carriers[87]. The resulting nanosystem, referred to as TaOx@PFC-PEG, displayed a hydrodynamic diameter of approximately 193 nm, suitable for tumor targeting *via* the EPR effect.

The oxygen loading capacity of the nanoemulsion was investigated and the authors observed that 3.6 ± 0.48 µmol of oxygen could be released per mL of perfluorocarbon under saturation conditions. Subsequently, the radiosensitizing efficacy of this platform was assessed *in vitro* under 6 Gy X-ray irradiation (Figure 9). Cells exposed to the oxygen-saturated TaOx@PFC-PEG@O_2 demonstrated significantly greater cytotoxicity and DNA double-strand breaks than their counterparts treated with the unsaturated formulation, underscoring the critical role of oxygen perfusion in potentiating radiotherapy.

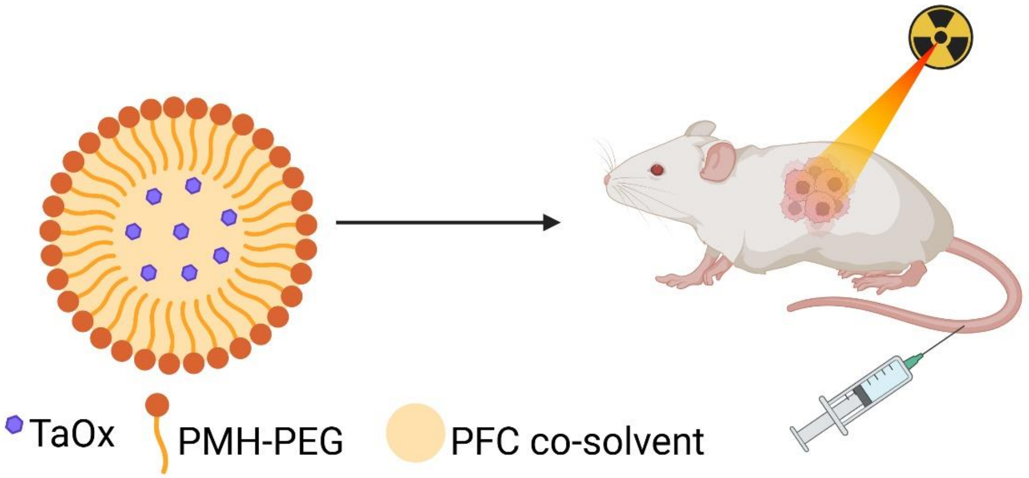

Figure 9: Dual radioenhancement with TaOx@PFC-PEG@O_2

In vivo studies in tumor-bearing animal models corroborated these observations. Mice treated with TaOx@PFC-PEG@O_2 exhibited markedly greater tumor growth inhibition compared to control groups. *Ex vivo* analysis of tumor tissues revealed significantly elevated DNA damage markers following treatment with the oxygen-enriched construct, validating the combined benefit of X-ray attenuation by TaOx and improved oxygen delivery *via* PFC.

This study demonstrates a compelling synergistic interaction wherein fluorocarbon-mediated oxygen perfusion mitigates tumor hypoxia while TaOx nanoparticles enhance local radiation absorption, jointly amplifying the therapeutic impact of radiotherapy. This dual action nanosystem offers a promising avenue for the development of more effective radiosensitizers in cancer treatment.

---

[87] Song, G., C. Ji, C. Liang, X. Song, X. Yi, Z. Dong, K. Yang, Z. Liu *Biomaterials* **2017** 112 257-263.

II. B. 4. Perfluorinated micelles in cancer treatment

While nanoformulations of PFCs have been extensively studied for biomedical applications, their structuring into micellar assemblies offers unique advantages. Perfluorocarbons are both hydrophobic and lipophobic, conferring a strong tendency for phase segregation. This property enhances micelle stability when fluorinated chains replace classical hydrocarbon segments, simultaneously improving their oxygen solubilization capacity. Several reports have exploited fluorinated moieties to stabilize micelles and augment their functional properties[88].

In cancer treatment, fluorinated micelles have predominantly been investigated in the context of photodynamic therapy (PDT). The latter involves systemic administration of a photosensitizer, which upon light activation generates ROS to induce tumor cell death. However, as with radiotherapy, PDT efficacy is frequently limited by tumor hypoxia. Thus, combining photosensitizer delivery with oxygen supply presents a rational strategy to overcome this limitation.

In 2018, Huang *et al.* developed fluorinated polymeric micelles composed of perfluorooctanoic acid conjugated to branched polyethyleneimine (PFOC-PEI)[89]. The micelles exhibited hydrodynamic diameters of approximately 106 nm, increasing to 122 nm upon loading the photosensitizer chlorin e6 (Ce6, a photosensitizer). Compared to non-fluorinated analogues, these micelles demonstrated substantially enhanced oxygen solubilization capacity (up to 11.2 mL O_2 per mg per mL of micelles). *In vitro* studies showed that micelles alone were non-toxic in the absence of irradiation, whereas photoactivation at 630 nm elicited significant cytotoxicity attributable to PDT. The superior efficacy of the Ce6-loaded fluorinated micelles was associated with increased oxygen availability, as evidenced by ROS detection and maintained cytotoxicity under hypoxia. Correspondingly, *in vivo* experiments demonstrated markedly improved tumor growth inhibition and more extensive tumor cell damage relative to non-fluorinated controls, confirming that fluorinated micelles effectively mitigate hypoxia in tumors to enhance PDT outcome.

Although fluorinated micelles have been utilized in PDT, their application in radiotherapy remains underexplored. Recently, our laboratory reported fluorinated micelles synthesized from perfluoroalkyl (PFTD) units functionalized with PEG[90]. These micelles exhibited superior oxygen delivery capabilities compared to other micellar systems, characterized by a notably slower oxygen release profile. Cytotoxicity assays revealed negligible effects even at elevated doses (1 mg mL^{-1}). When tested *in vitro* on B16F10 melanoma cells, the micelles significantly enhanced γ-ray-induced cytotoxicity across a range of doses. This radiosensitization

---

[88] Krafft, M. *Advanced Drug Delivery Reviews* **2001** 47 209-228.

[89] Wang, Q., J.-M. Li, H. Yu, K. Deng, W. Zhou, C.-X. Wang, Y. Zhang, K.-H. Li, R.-X. Zhuo, S.-W. Huang *Biomaterials Science* **2018** 6 3096-3107.

[90] Godel-Pastre, S., E. Porcel, G. Pinna, M. Vandamme, C. Denis, C. Leterrier, E. Doris, C. Truillet, E. Gravel *ACS Applied Materials & Interfaces* **2024** 16 21557-21570.

correlated with a fourfold increase in ROS production at 2 Gy irradiation, indicating efficient augmentation of radiation-induced oxidative stress.

To evaluate pharmacokinetics and tumor accumulation, PFTD-PEG was co-formulated with a fluorinated amphiphile bearing deferoxamine (PFTD-DFO), enabling radiolabeling with ^{89}Zr for positron emission tomography (PET) imaging. Systemic administration resulted in approximately 7% injected dose accumulation within tumors at 24 h post-injection.

Overall, these findings underscore the potential of fluorinated micelles as oxygen carriers to improve radiotherapy efficacy. The intrinsic loading capacity of the micelle core further offers opportunities for synergistic treatments, such as co-delivery of radiosensitizing agents like gold nanoparticles.

III. Gold nanoparticles

III. A. General characteristics

Gold nanoparticles (AuNPs) exhibit unique optical behavior attributable to the collective oscillation of conduction band electrons when excited by electromagnetic radiations. This collective oscillation generates a dipolar moment known as surface plasmon resonance (SPR), which occurs at a characteristic frequency determined by the nanoparticle's size and shape. Importantly, SPR manifests only when the nanoparticle diameter is smaller than the incident light wavelength[91]. For spherical gold nanoparticles, the SPR typically arises near 520 nm, imparting a distinctive red color to their aqueous suspensions. In anisotropic shapes such as nanorods, two SPR modes emerge due to oscillations along transverse and longitudinal axes. The longitudinal SPR, tunable by adjusting the nanorod aspect ratio, generally falls within the near-infrared (NIR) range (650–1300 nm), which is advantageous for biomedical applications owing to minimal tissue absorption in this spectral window[92].

These optical characteristics confer significant value on AuNPs for cancer diagnosis and therapy. Their properties include enhanced Mie scattering, surface plasmon absorption, surface-enhanced luminescence, and surface-enhanced Raman scattering (SERS). Moreover, gold nanoparticle synthesis allows precise control over size, shape, composition, and surface chemistry, including conjugation with biomolecules such as antibodies for targeted applications.

In cancer diagnosis, AuNPs enable specific detection *via* light-scattering imaging and SERS[93]. The excitation of SPR substantially amplifies Rayleigh or Mie scattering signals, facilitating real-time imaging with standard microscopy. By tuning nanoparticle aspect ratios, the scattering intensity and spectral response can be optimized for different imaging modalities, including dark-field microscopy. For example, antibody-functionalized gold nanorods can

---

[91] Huang, X., P.K. Jain, I.H. El-Sayed, M.A. El-Sayed *Nanomedicine* **2007** 2 681-693.

[92] Liu, X.-Y., J.-Q. Wang, C.R. Ashby, L. Zeng, Y.-F. Fan, Z.-S. Chen *Drug Discovery Today* **2021** 26 1284-1292.

[93] Huang, X., P.K. Jain, I.H. El-Sayed, M.A. El-Sayed *Nanomedicine* **2007** 2 681-693.

be selectively targeted to malignant cells, distinguishing them from normal cells through enhanced light scattering. Meanwhile, SERS provides further sensitivity and spectral resolution through plasmon-enhanced fluorescence and Raman scattering of molecules close to the AuNP surface, enabling precise biomarker detection.

Gold nanoparticles also serve as contrast agents in photoacoustic imaging. Upon absorption of pulsed laser light, AuNPs convert optical energy into heat, inducing thermoelastic expansion and generating ultrasonic waves detectable by photoacoustic sensors. Effective photoacoustic contrast depends on strong NIR absorption to facilitate imaging of deep-seated tumors, a criterion well met by elongated (rods) or branched (stars) AuNP morphologies[94].

Therapeutically speaking, AuNPs are active in plasmonic photothermal therapy, wherein resonant light absorption is converted into localized hyperthermia[95]. Cancer cells more sensitive to elevated temperatures, which allows for selective ablation when irradiated at the SPR wavelength of the nanoparticles. Since biological tissues exhibit minimal absorption in the NIR window, nanorods and nanostars, which possess SPR peaks in this range, are favored for clinical photothermal applications due to their high absorption cross-sections and conversion efficiencies.

III. B. Radioenhancement properties of gold nanoparticles.

In the context of cancer treatment using radiotherapy, one of the major challenges is the lack of selectivity due to the similar mass energy absorption properties of both healthy and cancer tissues. Therefore, the use of agents to improve the contrast between the tumor area and the soft tissues appears as a promising strategy to locally enhance the effect of radiation. Because of their high atomic number (Z = 79), AuNPs greatly increase interactions probabilities with ionizing radiation[96]. Indeed, AuNPs absorb more energy per mass unit than soft tissues and therefore enhance the effect of irradiation locally, thus reducing side effects while improving tumor growth control.

The main physical mechanism of interaction between nanoparticles and radiation in the keV range are Compton and photoelectric effects described in the introduction (see section III.B.1). Briefly when radiation interacts with nanoparticles different processes can occur, the Compton effect consists in the collision of a photon with an electron from the atom causing its ejection. The photoelectric process is a competitive phenomenon where the ejected electron photon is from the inner atomic orbital, leaving a vacancy in the electronic shell. This vacancy can be filled by another outer shell electron that will emit a low-energy photons (photoelectric effect) or transfer this energy to another electron that will be released (Auger electron) promoting a cascade of secondary electrons. The Auger cascade is the major contribution to the production of low-energy electrons that have a diffusion range of few

---

[94] Li, W., X. Chen *Nanomedicine* **2015** 10 299-320.

[95] Riley, R.S., E.S. Day *WIREs Nanomedicine and Nanobiotechnology* **2017** 9 .

[96] Her, S., D.A. Jaffray, C. Allen *Advanced Drug Delivery Reviews* **2017** 109 84-101.

micrometers and cause localized ionizing events. However, in the case of gold nanoparticles it appears that chemical and biological processes are also involved in the radiosensitization process

The main mechanisms identified as involved in the biological response of cells to AuNP radiosensitization are the ROS production and oxidative stress. The surface of AuNP appears to be electronically active and catalyzing chemical reactions, thus promoting the production of ROS, especially for small gold nanoparticles (≤ 5 nm) because of their greater surface area-to-volume ratio[97]. One of the mechanisms is the transfer of an electron from the surface of the nanoparticle to oxygen molecules generating superoxide which can lead to ROS production.

III. C. Gold nanoparticles in cancer treatment

The first use of gold nanoparticles as radiosensitizing agents was reported in 2004 by Heinfeld *et al.* who investigated the use of small (1.9 nm) gold nanoparticles to enhance the effects of radiotherapy in mice with subcutaneous EMT-6 mammary carcinomas[98]. They highlighted that intravenous administration of gold nanoparticles, followed by X-ray irradiation, resulted in significant tumor control and improved survival. Specifically, mice receiving a high dose (2.7 g $Au{\cdot}kg^{-1}$) of gold nanoparticles before irradiation had an 86% one-year survival rate, compared to only 20% in the radiation-alone group and 0% in gold-only or untreated groups. The gold nanoparticles preferentially accumulated in tumors, reaching a tumor-to-normal tissue concentration ratio of about 8:1, and were cleared primarily through the kidneys without apparent toxicity. This approach overcame previous limitations of high-*Z* (high atomic number) radioenhancers by achieving uniform and high levels of gold in tumors through intravenous injection. The study concluded that gold nanoparticles show promise for enhancing radiotherapy efficiency and recommended further research into targeted delivery for clinical applications.

More recently, AuroVist^{TM} gold nanoparticles of 1.9 nm of diameter were studied for their interactions (including uptake, toxicity and radiosensitization) with cancer and normal cells under different oxygen levels[99]. Gold nanoparticles uptake was linear over 1–24 h in DU-145, MDA-MB-231, and L132 cells, but the rate and total amount were significantly lower under hypoxia (0.1 % O_2) than under normoxia (21 % O_2) (relative cell uptake ≈ 0.29–0.56). Transmission-electron microscopy showed gold nanoparticles confined to lysosomal aggregates in hypoxic cells, with no free cytosolic or nuclear particles. In hypoxic MDA-MB-231 cells, gold nanoparticles exposure reduced proliferation without affecting colony-forming ability, whereas DU-145 and L132 cells showed no significant proliferation change.

---

[97] Loscertales, E., R. López-Méndez, J. Mateo, L.M. Fraile, J.M. Udias, A. Espinosa, S. España *Nanoscale Advances* **2025** 7 1204-1214.

[98] Hainfeld, J.F., D.N. Slatkin, H.M. Smilowitz *Physics in Medicine and Biology* **2004** 49 N309-N315.

[99] Jain, S., J.A. Coulter, K.T. Butterworth, A.R. Hounsell, S.J. McMahon, W.B. Hyland, M.F. Muir, G.R. Dickson, K.M. Prise, F.J. Currell, D.G. Hirst, J.M. O'Sullivan *Radiotherapy and Oncology* **2014** 110 342-347.

Clonogenic assays revealed that gold nanoparticles enhanced the radiosensitivity in MDA-MB-231 cells under moderate hypoxia (1 % O_2) with a sensitizer enhancement ratio (SER) of 1.39, comparable to normoxia (SER = 1.41). The effect dropped markedly in near-anoxia (0.1 % O_2, SER = 1.1), where the uptake of gold nanoparticles decreases, suggesting that lower uptake under hypoxia limits radiosensitisation.

The authors suggested that gold nanoparticles-mediated radio-sensitization involve both physical dose-enhancement (photo-electric effect) and biological mechanisms (e.g., ROS generation, autophagy), but the exact pathways remain unclear. They observed that hypoxia reduced cellular uptake. The work concluded that gold nanoparticles are taken up by hypoxic cells provide some radiosensitisation under moderate hypoxia.

In 2022, Tudda *et al.* evaluated gold nanoparticles as radiosensitizers for breast-cancer radiotherapy under X-rays[100]. Human MDA-MB-231 breast-cancer cells were incubated with AuNPs (AuroVist™) at 100 µg/mL (4.87 nM) or 200 µg/mL (9.74 nM) and irradiated with 100 kV, 190 kV, or 6 MV X-rays. Cell viability, AuNP internalization, and clonogenic survival were assessed. AuNPs alone showed no toxicity up to 400 µg/mL (19.5 nM). Atomic absorption spectroscopy measured 1.66 µg Au per mg of protein after 24 h exposure to 15 nm AuNPs, confirming intracellular accumulation, primarily in perinuclear endosomal vesicles. Clonogenic assays revealed dose-enhancement factors (DEF) of 1.34 ± 0.02 at 100 kV and 1.33 ± 0.06 at 190 kV for the 200 µg/mL AuNP condition, whereas the 6 MV beam produced a modest DEF of 1.14 ± 0.06. Survival-fraction curves showed greater cell killing with AuNPs, especially at kV energies, and a concentration-dependent effect (higher AuNP dose → lower surviving fraction). The authors concluded that low-nanomolar concentrations of AuNPs significantly enhance kV-radiotherapy of breast cancer while sparing normal tissue.

Owing to the flexibility of synthesis and functionalization, AuNPs are synthesized in various morphologies; nanorods and nanostars are commonly used in NIR-based therapies, while this study that deals with radiotherapy focuses on spherical gold nanoparticles. Their simpler geometry provides a controlled platform to investigate radio-enhancement mechanisms under clinically relevant irradiation conditions.

---

[100] Tudda, A., E. Donzelli, G. Nicolini, S. Semperboni, M. Bossi, G. Cavaletti, R. Castriconi, P. Mangili, A.D. Vecchio, A. Sarno, G. Mettivier, P. Russo *Medical Physics* **2022** 49 568-578.

Results

IV. Synthesis and characterization of perfluorinated micelles

IV. A. PFTD-PEG synthesis and micelles formulation

To develop micelles designed to function both as oxygen carrier to the tumor site and as a carrier for encapsulation of gold nanoparticles, a fluorinated amphiphilic building block was synthesized. The amphiphilic unit consists of a PEG chain (2 kDa) serving as the hydrophilic segment and perfluorotetradecanol (PFTD) as the fluorinated hydrophobic moiety (Scheme 1).

The synthetic route began with the activation of the terminal hydroxyl group of PEG monomethyl ether by converting it into a tosylate (Ts), yielding intermediate **I.1**. The tosylated PEG was subsequently subjected to nucleophilic substitution by PFTD in the presence of sodium hydride (NaH). This two-step reaction sequence afforded the target fluorinated amphiphile (PFTD-PEG) in 64 % overall yield.

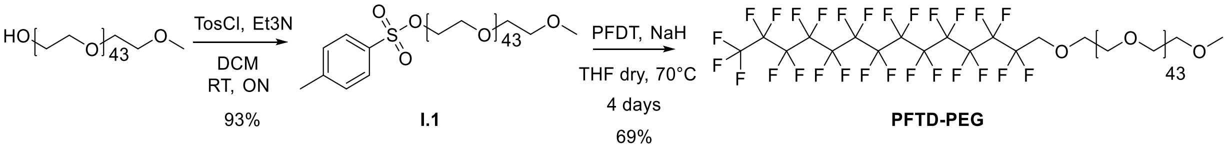

Scheme 1: PFTD-PEG Synthesis

The PFTD-PEG amphiphilic unit was then formulated into micelles in aqueous solution using a probe sonicator[101]. Ultrasonic treatment (300 ms pulses per second, 40% amplitude) of a concentrated (10 mg·mL^{-1}) amphiphiles suspension, yielded a stable colloid corresponding to the micelle. The solution was filtered through a 0.22 µm nylon membrane prior to analysis by Dynamic Light Scattering (DLS), which confirmed the micellar structure with an average hydrodynamic diameter of 11 nm and a polydispersity index (PDI) of 0.20. The ζ-potential measured was approximately zero, reflecting the neutral charge of PEG chains on the micelle surface. Both DLS and ζ-potential are plotted in Figure 10.

---

[101] Cerqueira, P., J. Noro, S. Moura, D. Guimarães, C. Silva, A. Cavaco-Paulo, A. Loureiro *International Journal of Pharmaceutics* **2019** 566 282-290.

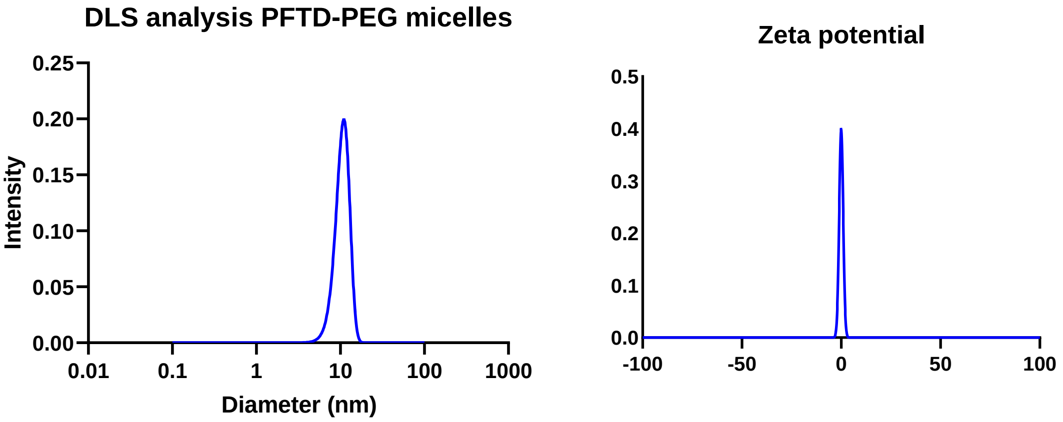

Figure 10: DLS (left) and zeta potential (right) analysis of PFTD-PEG micelles

The amphiphilic units can self-assemble into micelles only after a concentration threshold known as the critical micelle concentration (CMC). This parameter, essential for the micelles' stability, was evaluated for our PFTD-PEG micelles

IV. B. Critical Micellar Concentration

The spontaneous self-assembly of perfluorinated amphiphilic units into micelles occurs only when their concentration exceeds the CMC value. Various techniques can be employed to determine the CMC, including measurements of surface tension, absorbance or fluorescence of an encapsulated probe (e.g., pyrene), DLS to assess micelle size, and conductivity for ionic surfactants. The use of surface tension measurements is widely used due to its sensitivity and relative ease of implementation.

Amphiphiles act as surfactants by reducing the interaction between hydrophobic chains and water, lowering the system's free energy and surface tension. The surface tension decreases with increasing amphiphile concentration until it reaches a plateau at the CMC. Measuring surface tension across varying concentrations thus reveals the CMC value, indicated by the concentration at which surface tension no longer decreases significantly.

Surface tension is commonly measured using either the Wilhelmy plate or Du Noüy ring methods. The Wilhelmy plate is better suited for viscous solutions, while the Du Noüy ring is ideal for aqueous samples[102]. The measurement involves determining the force exerted on a metal probe immersed in the amphiphile solution, which correlates directly with surface tension. Below the CMC, amphiphilic molecules are predominantly organized at the air-water interface, significantly influencing surface tension. When the CMC is exceeded, molecules aggregate into micelles within the volume of dispersant, causing no further changes in surface tension, despite concentration increase.

---

[102] Padday, J.F., A.R. Pitt, R.M. Pashley *Journal of the Chemical Society, Faraday Transactions 1: Physical Chemistry in Condensed Phases* **1975** 71 1919.

To determine the CMC, an adaptation of the Du Noüy-Paday method was used, to suit better for the measurements of small volumes. The strength put on a metallic needle immerged into solutions containing an increasing concentration of PFTD-PEG amphiphilic unit was measured. This strength is mathematically connected to the surface tension and allowed to plot the following graph (Figure 11).

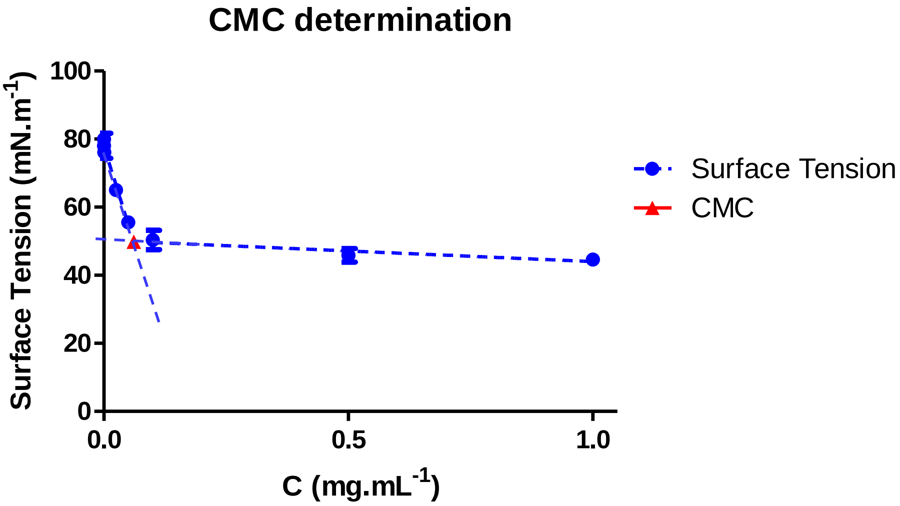

Figure 11: CMC determination for PFTD-PEG

Here, the CMC can be determined at the intersection of the two straight lines. The CMC value obtained by the Du Noüy method gives a CMC value of 0.056 mg mL^{-1} for PFTD-PEG. This CMC value lies at the lower end of the range reported for non-fluorinated surfactants. A low CMC is crucial for *in vivo* applications because it minimizes micelle dissociation upon dilution in the bloodstream, ensuring better stability and effectiveness.

IV. C. Probing oxygen level inside the micelles

One method to probe O_2-micelle interactions is the paramagnetic relaxation enhancement (PRE) effect that can be monitored by NMR spectroscopy[103]. We used $^{19}F/^{1}H$-NMR, exploiting the paramagnetic properties of molecular oxygen, which modulate the relaxation behavior of nearby nuclei by a PRE effect. The unpaired electron in the paramagnetic probe (here O_2) generates a fluctuating magnetic field that interacts with nearby nuclei (here ^{19}F and ^{1}H), enhancing their relaxation rates. This interaction manifests as broader NMR signals or faster decay times, with the effect dependent on the distance between the probe and each nucleus. By analyzing relaxation enhancements, one obtains qualitative information about probe accessibility in the different regions of the micelles.

PFTD-PEG micelles contain two NMR-active nuclei (^{1}H and ^{19}F) while oxygen is paramagnetic. Monitoring the relaxation times of these nuclei under varying oxygen pressures allows

---

[103] Lenard, A.J., F.A.A. Mulder, T. Madl *Progress in Nuclear Magnetic Resonance Spectroscopy* **2022** 132-133 113-139.

assessment of oxygen localization within the micelles. The ^{19}F NMR spectrum of PFTD-PEG shows two signals, the most important one is a broad signal corresponding to the CF_2 groups of the fluorinated chain (*ca.* −120 ppm) and a well-defined signal corresponding to the terminal CF_3 group (*ca.* –80 ppm) that is located deep in the core of the micelle. The latter signal was selected to probe oxygen solubilization in the micelles. On the other hand, ^{1}H-NMR signals between 3.6–3.8 ppm were attributed to the polar PEG protons and will be used to probe the level of oxygen at the periphery of the micelle. This experiment was realized in collaboration with Gaspard Huber.

For the experiment, a 10 mg mL^{-1} solution of PFTD-PEG in D_2O was prepared and placed in a thick-wall NMR pressure tube connected to a stopper valve which allows performing experiments requiring pressurized atmosphere. An initial relaxation measurement was recorded at ambient oxygen pressure (~0.2 bar). The sample was then frozen and degassed under vacuum to fully remove oxygen. Relaxation measurements were recorded again before stepwise introduction of oxygen at controlled pressures was performed, up to 2.5 bar of O_2. Relaxation times for both ^{1}H and ^{19}F nuclei were measured at each oxygen pressure to evaluate oxygen permeation within the micellar structure. The PRE effect was quantified from the slope of the relaxation rate *versus* the oxygen pressure, revealing a significantly elevated PRE in the fluorinated micellar core (1.01 s^{-1} bar^{-1}). This value has to be compared to those measured for the PEGylated domain (0.08 s^{-1} bar^{-1}) interfacing with water, and residual H_2O in D_2O (0.17 s^{-1} bar^{-1}). The experiment results are gathered in Figure 12.

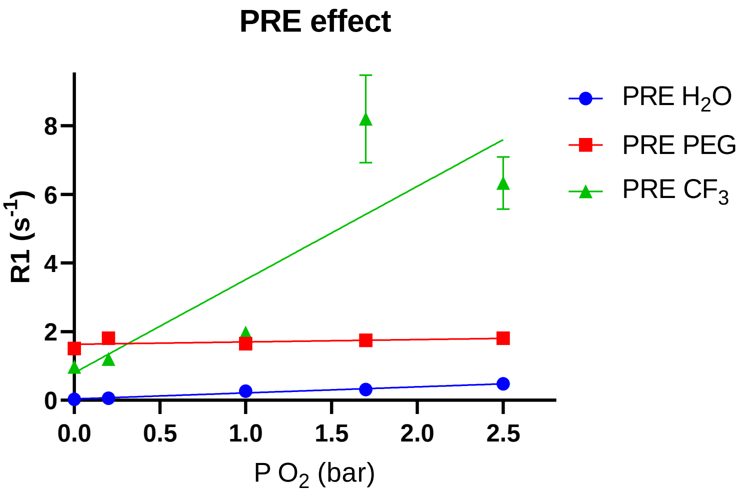

Figure 12: PRE effect on PFTD-PEG micelles in D_2O

As per Henry's law, for experimental pressures below 4 bar the oxygen solubility is directly proportional to the total gas pressure and the molar fraction of oxygen in the gas phase. Since in our experiment, the highest pressure applied is 2.5 bar, the obtained PRE values confirmed the effective oxygen encapsulation in the PFTD-PEG micelles, more precisely by the fluorinated core of the micelles.

V. Gold nanoparticles synthesis and characterization

V. A. Synthetic pathways for spherical nanoparticles

The synthesis of AuNP for biomedical applications demands careful control over several critical parameters to ensure optimal performance and safety. Foremost among these is the particle size, which profoundly influences biodistribution, cellular uptake, and therapeutic efficacy[104]. Equally important is achieving a narrow size distribution to minimize the presence of irregularly sized particles that could provoke undesired biological effects or toxicity.

Chemical reduction remains the predominant method for synthesizing AuNP with precise size and monodispersity. During this process, gold salts (classically $HAuCl_4$) are chemically reduced, inducing nucleation and growth of metallic gold nanoparticles that are simultaneously stabilized by capping agents. Among the well-established synthetic routes are the Turkevich and Brust-Schiffrin methods, each providing distinctive control over particle size and surface chemistry. Additionally, a third approach pioneered by Stellacci offers alternative avenues for tailor-made nanoparticle synthesis. These methods collectively enable reproducible fabrication of AuNP tailored to the stringent demands of biomedical applications.

Maintaining colloidal stability in solutions is another crucial consideration, as aggregation of AuNPs can compromise their functionality and exacerbate toxicity risks. To prevent aggregation, gold nanoparticles are typically stabilized *via* surface modification. This stabilization commonly involves adsorption of small molecules or, more effectively, the incorporation of thiolated ligands, which form strong bonds with the gold surface. These surface ligands not only inhibit particle aggregation but also provide versatile platforms for further functionalization. Such modifications can tune nanoparticle targeting capabilities or extend systemic circulation by reducing opsonization and clearance.

V. B. Functionalization and biocompatibility

V. B. 1. Functionalization

Post-synthetic functionalization of gold nanoparticles is essential to confer colloidal stability and biocompatibility. Functionalization may occur concomitantly with synthesis, as in the case of thiol ligand incorporation during synthesis, or as a subsequent modification step. Depending on the timing and mechanism of ligand attachment, functionalization is categorized as either direct or indirect.

Direct functionalization refers to the grafting of functional ligands directly onto the nanoparticle surface. This can either be performed during nanoparticle formation or *via* ligand exchange after synthesis. Ligand exchange exploits differences in binding affinities;

---

[104] Woźniak, A., A. Malankowska, G. Nowaczyk, B.F. Grześkowiak, K. Tuśnio, R. Słomski, A. Zaleska-Medynska, S. Jurga *Journal of Materials Science: Materials in Medicine* **2017** 28 .

for example, citrate-stabilized nanoparticles can be functionalized by introducing thiol-containing ligands due to the stronger gold-thiol affinity, which displaces citrate ions. In some cases, co-adsorption of thiol and citrate ligands may occur. As bound citrate molecules might resist complete displacement, this could result in mixed ligand shells[105].

Indirect functionalization involves a sequential two-step process. Initially, a molecule bearing a reactive functional group is attached to the nanoparticle surface. In a subsequent step, this reactive handle facilitates conjugation of biomolecules or other functional moieties through highly selective and rapid chemistries, such as azide-alkyne cycloaddition ("click" chemistry) or thiol-maleimide coupling. This modular approach enables the synthesis of complex nanoconjugates, including enzyme-functionalized or targeted nanoparticles tailored for specific biomedical applications.

Additionally, gold nanoparticles can be functionalized non-covalently *via* electrostatic interactions. Proteins, for instance, readily adsorb onto nanoparticle surfaces, forming protective coatings that enhance colloidal stability and biocompatibility without covalent modification[106].

V. B. 2. Biocompatibility

For biomedical applications, gold nanoparticles must exhibit biocompatibility in addition to colloidal stability. Surface functionalization with hydrophilic polymers is commonly employed to achieve this, with PEG being the most widely used. Alternative polymers, including biopolymers[107] and zwitterionic polymers[108], have also been explored. These hydrophilic coatings not only confer water solubility and stability but also modulate circulation time by reducing opsonization. By minimizing protein adsorption and recognition by the mononuclear phagocyte system, such polymer shells effectively impart stealth characteristics to gold nanoparticles, enhancing their *in vivo* performance.

V. C. Brust-Schiffrin method

V. C. 1. Synthesis of gold nanoparticles stabilized with a perfluorinated thiol ligand

The Brust–Schiffrin method, established in 1994, is a widely employed technique for the synthesis of small gold nanoparticles, typically around 5 nm in diameter[109]. This approach produces nanoparticles stabilized by thiol ligands, which exhibit strong affinity for gold surfaces, thereby conferring exceptional colloidal stability. Since its inception, the Brust–Schiffrin synthesis has been extensively studied and modified, enabling improved control

---

[105] Park, J.-W., J.S. Shumaker-Parry *ACS Nano* **2015** 9 1665-1682.

[106] Wang, A., Y.R. Perera, M.B. Davidson, N.C. Fitzkee *The Journal of Physical Chemistry C* **2016** 120 24231-24239.

[107] Ul-Islam, M., K.F. Alabbosh, S. Manan, S. Khan, F. Ahmad, M.W. Ullah *Advanced Industrial and Engineering Polymer Research* **2024** 7 79-99.

[108] Yang, W., L. Zhang, S. Wang, A.D. White, S. Jiang *Biomaterials* **2009** 30 5617-5621.

[109] Brust, M., M. Walker, D. Bethell, D.J. Schiffrin, R. Whyman *J. Chem. Soc., Chem. Commun.* **1994** 0 801-802.

over particle size, monodispersity, and surface functionalization, rendering it highly valuable for biomedical and catalytic applications.

In the classical biphasic synthesis, a gold(III) salt is dissolved in water and combined with a toluene solution of tetraoctylammonium bromide (TOAB), a phase transfer agent. TOAB organizes into reversed micelles (hydrophilic heads oriented inward, lipophilic tails outward) around the gold ions. Electrostatic interactions between the ammonium groups and Au(III) ions facilitate complexation and transfer of gold from the aqueous to the organic phase.

The addition of a thiol (RSH) initiates partial reduction of gold from Au(III) to Au(I), resulting in the formation of soluble and insoluble gold-thiolate species ([Au(I)SR] and polymeric $[Au(I)SR]_n$, respectively). Complete reduction is achieved by introducing sodium borohydride ($NaBH_4$), yielding metallic gold (Au(0)) nanoparticles that are stabilized by thiol ligands. However, the presence of polymeric $[Au(I)SR]_n$ species can increase the polydispersity of particle size[110].

The Au(I) transient species is more accurately described as a complex between Au(I) and TOAB, with thiol ligands binding predominantly after complete reduction[111]. To minimize polymeric byproducts, an improved "reverse" synthesis was developed, wherein $NaBH_4$ is added prior to the thiol. This sequence produces AuNPs initially stabilized by TOAB reversed micelles, which are then displaced by thiols through ligand exchange thanks to the strong gold-sulfur bond (≈50 kcal mol^{-1}). This modification affords better control over particle size compared to the original Brust–Schiffrin procedure.

In our work, the reverse Brust–Schiffrin approach was employed (Figure 13). Chloroauric acid ($HAuCl_4$) was dissolved in ultrapure water, followed by addition of a TOAB solution in toluene. The biphasic system was vigorously stirred to facilitate the phase transfer of gold ions to the organic phase. Next, an aqueous $NaBH_4$ solution was introduced to reduce Au(III) to Au(0), forming TOAB-stabilized AuNPs. After 3 h of stirring, the organic phase was separated, and perfluorooctane thiol (PFSH) was added to induce ligand exchange. The thiol ligand binds to the surface of gold and displaces TOAB. However, due to its low solubility in toluene, the perfluorooctane thiol ligand induces the precipitation of thiol-capped AuNPs in the same solvent.

---

[110] Booth, S.G., A. Uehara, S.-Y. Chang, C.L. Fontaine, T. Fujii, Y. Okamoto, T. Imai, S.L.M. Schroeder, R. a. W. Dryfe *Chemical Science* **2017** 8 7954-7962.

[111] Zhu, L., C. Zhang, C. Guo, X. Wang, P. Sun, D. Zhou, W. Chen, G. Xue *The Journal of Physical Chemistry C* **2013** 117 11399-11405.

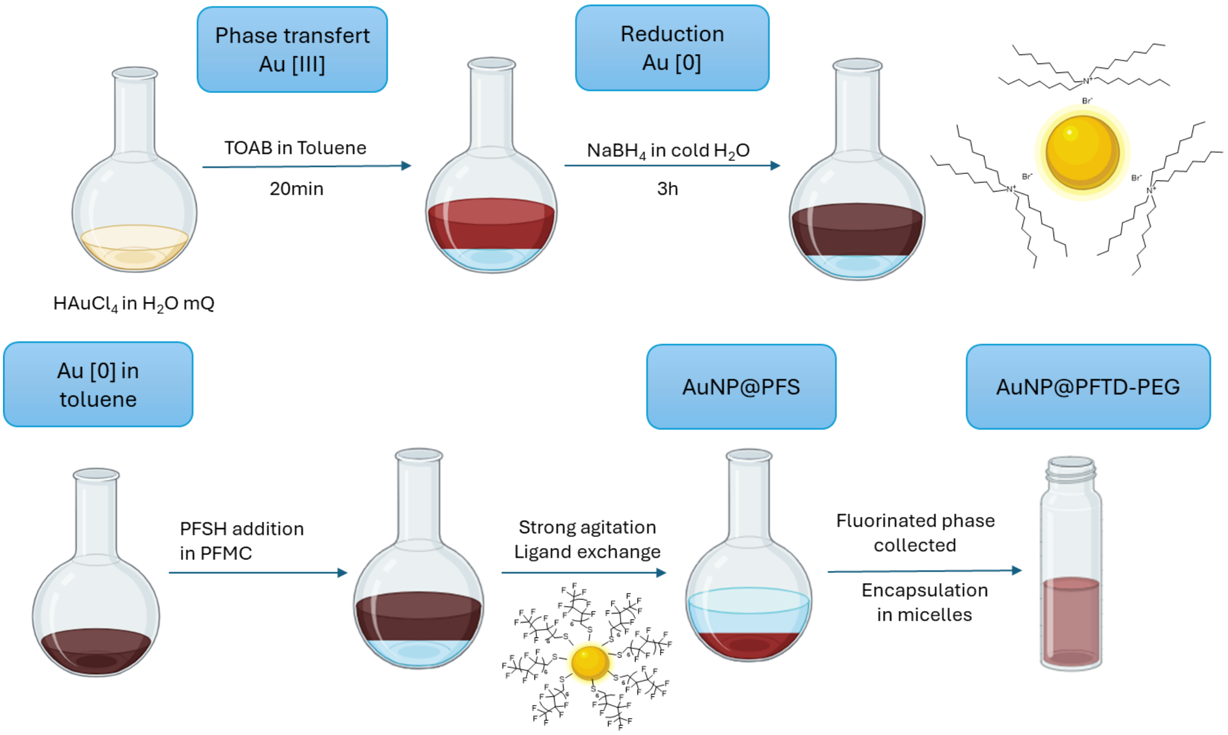

Figure 13: Gold nanoparticles synthesis according to the reversed Brust-Schiffrin method

To ensure effective purification, the solution was divided into aliquots of ~1 mL each. These fractions underwent multiple cycles (minimum of seven) of centrifugation and sonication to remove residual TOAB and solvent traces. Centrifugation was performed at 2000 rpm to form a pellet of gold nanoparticles. The toluene supernatant containing impurities was removed before washing the pellets by sonication in fresh toluene. Finally, the purified nanoparticles were dried under vacuum and redispersed in perfluoromethyl cyclohexane (PFMC) to afford a colloidal suspension of gold nanoparticles stabilized with perfluorooctane thiol ligands (AuNP@PFS). AuNP@PFS was subsequently encapsulated in perfluorinated PFTD-PEG micelles.

V. C. 2. Encapsulation and characterization of the gold nanoparticles in PFTD-PEG micelles

To 1 mL of an aqueous PFTD-PEG solution (10 mg mL^{-1}) was added 0.5 mL of the above gold suspension in PFMC, producing a biphasic mixture. The latter was ultrasonicated three times for 15 min at 40% amplitude. This process permitted the slow evaporation of the perfluoromethyl cyclohexane solvent in which gold nanoparticles were originally dispersed and the concomitant encapsulation of AuNPs in the fluorinated micelles. This process produces a stable burgundy-red aqueous colloid of AuNP@PFTD-PEG.

The colloidal suspension of AuNP@PFTD-PEG was characterized by different methods. DLS analysis of AuNP@PFTD-PEG showed a hydrodynamic diameter of 16 nm with a PDI of 0.28 (Figure 14). The small increase in the size of the particle matches with the encapsulation of the gold nanoparticle inside the micelle. Absorbance spectrum of the construct shows only one absorption band at 515 nm, suggesting spherical gold nanoparticles.

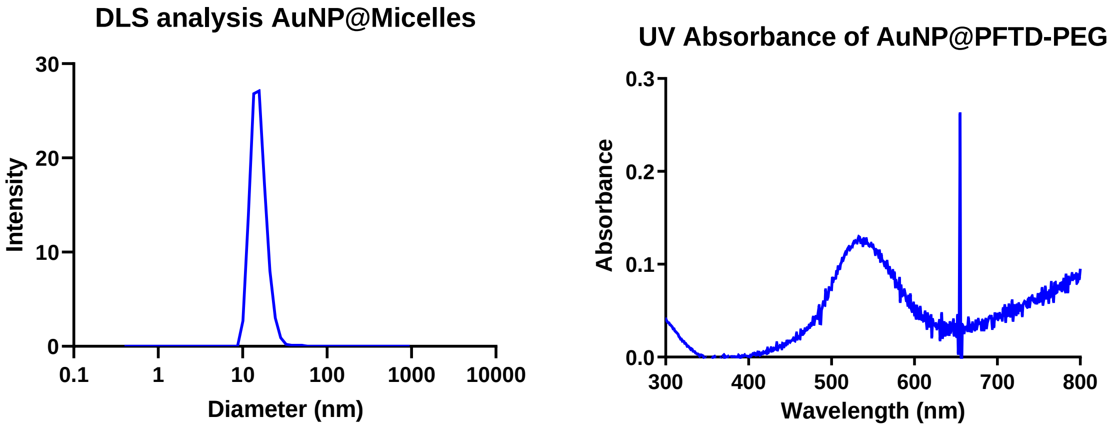

Figure 14: DLS (right) and UV analysis (left) of AuNP@PFTD-PEG

The shape and the size of the gold nanoparticle were later confirmed by Transmission Electron Microscopy (TEM). TEM analysis of the encapsulated gold nanoparticles showed spherical objects with an average diameter of 5 nm (Figure 15).

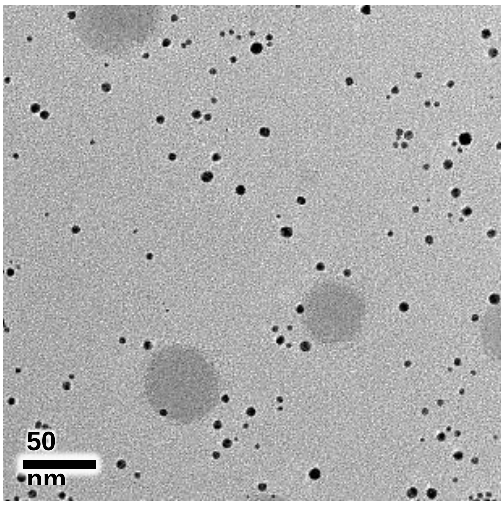

Figure 15: TEM picture of AuNP@PFTD-PEG prepared through the Brust-Schiffrin method

The concentration of gold in the colloidal solution was determined by Inductively Coupled Plasma Mass Spectrometry (ICP-MS), an elemental analysis method. This method consists in ionizing the sample in a plasma. The elements are separated according to the mass of the resulting ions (*m/z*), and a detector gives a signal proportional to the concentration of each species. This technique is very sensitive and allows the quantification of very diluted samples. The gold concentration in the 10 mg mL^{-1} micellar solution is approximately 0.5 mM.

This above synthesis allowed the formation of small spherical gold nanoparticles that could be encapsulated in perfluorinated micelles in such a way to become dispersible in an aqueous medium. Before any further studies, it is important to determine the potential intrinsic cytotoxicity of the sample.

V. C. 3. Evaluation of the cytotoxicity of AuNP@PFTD-PEG

Cytotoxicity of AuNP@PFTD-PEG was investigated on SKBR3 cells (human breast cancer) using the MTS assay (Figure 16). Both "empty" micelles and micelles containing gold nanoparticles were evaluated. To make it easier to read, the concentration in the following graph corresponds to the concentration of the PFTD-PEG amphiphile. Since the concentration of the stock solution is 0.5 mM of gold and 10 mg mL^{-1} of the amphiphile, the highest micelle concentration (1 mg mL^{-1}) studied contains 50 µM of gold and the lowest (0.004 mg mL^{-1}) approximately 0.2 µM.

While simple PFTD-PEG micelles did not show any toxicity, even at the highest amphiphile concentration studied (*i.e.,* 1 mg mL^{-1}), micelles encapsulating gold nanoparticles showed some toxicity starting at 0.25 mg mL^{-1}. After 24 h of incubation, we observed a decrease in the viability of the SKBR3 cells with increasing micelle-gold concentration. At 1 mg mL^{-1} of micelles (50 µM gold) we observed a drastic cytotoxic effect with < 20% of surviving cells. This differentiated result between empty micelles and micelles containing gold nanoparticles indicate that the observed toxicity likely originates from gold nanoparticles.

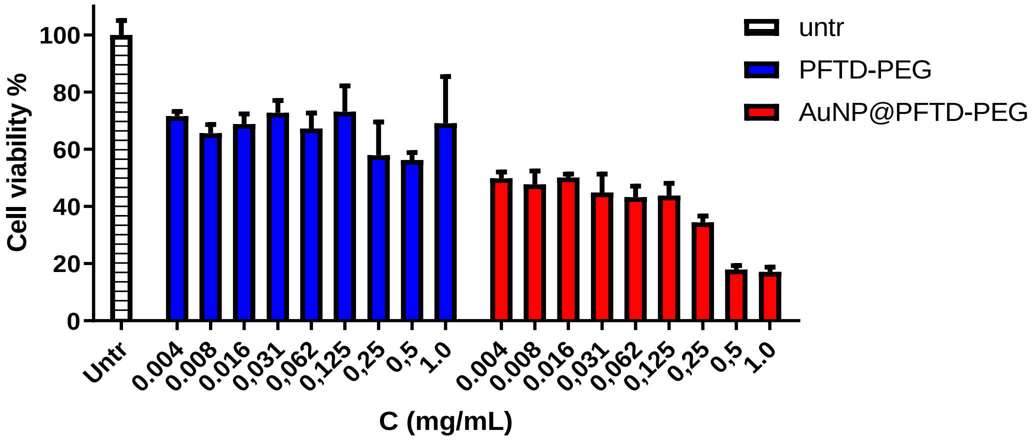

Figure 16: Toxicity study of AuNP@PFTD-PEG prepared through the Brust-Schiffrin method

The observed cytotoxicity of gold nanoparticles encapsulated in micelles can likely be explained by the fact that TOAB, which was used as a temporary ligand in the synthesis of gold nanoparticles, is highly toxic to cells[112]. In fact, long aliphatic chain cationic surfactants agents are toxic due to the fatty acid-effect on cell membranes. Perturbation of the phospholipid-rich cell membrane can result in a cascade of events including activation of phospholipases together with the generation of signaling mediators and increased ROS production. Thus, if traces of TOAB were to remain after the various washing steps during the synthesis of the gold nanoparticles, this could lead to harmful effects observed for SKBR3 cells.

---

[112] Zhang, Y., B. Newton, E. Lewis, P.P. Fu, R. Kafoury, P.C. Ray, H. Yu *Toxicology in Vitro* **2015** 29 762-768.

Our synthesis of gold nanoparticles following the Brust-Schiffrin method showed some reproducibility issues. In fact, during the washing steps to remove TOAB, gold nanoparticles were found to aggregate quickly. So, the first point was to modify the washing steps in order to stabilize gold nanoparticles long enough.

In the original procedure, the toluene fraction containing gold nanoparticles stabilized with fluorinated ligands was treated by seven centrifugation/sonication cycles. We observed that the extended time needed to perform the purification favored nanoparticle aggregation. In order to avoid the latter phenomenon, we reduced the number of centrifugation/sonication cycles. It appeared that performing only one or two cycles was beneficial in avoiding aggregation of gold nanoparticles. However, limiting the number of purification steps resulted in an increase in the amount of TOAB remaining in the final micellar sample.

We also tried in parallel to perform liquid/liquid extraction of the toluene phase containing the coated gold nanoparticles. A perfluorinated solvent (e.g., PFMC) was used for such purpose. In toluene, gold nanoparticles tend to precipitate because of the low solubility of the fluorinated ligands. To try and avoid precipitation, we added PFMC in which fluorinated materials are dispersible. The fluorinated phase containing the coated gold nanoparticles was washed 7 times with toluene to remove TOAB. Although this method prevented aggregation of gold nanoparticles, it was not efficient in removing TOAB from the sample.

Precipitation of gold nanoparticles was also tested by either i) cooling down the colloidal suspension of AuNP@PFS overnight at −18 °C before centrifugation, but no precipitation was observed; or ii) addition of a polar solvent to disturb the suspension in the fluorinated solvent and trigger precipitation of the nanoparticles. Addition of a polar solvent to the medium led to partial precipitation. Because of the difficulties encountered in preparing and purifying the gold nanoparticle by the Brust-Schiffrin method, other strategies were investigated.

V. D. Turkevich synthesis

V. D. 1. Synthesis of gold nanoparticles stabilized with citrate

Considering that the different problems observed with the Brust-Schiffrin synthesis are mostly due to the presence of a toxic additive, another synthetic pathway requiring fewer additives was investigated. The Turkevich method, first reported in 1951, remains one of the simplest and most efficient techniques for synthesizing spherical gold nanoparticles in aqueous solution[113]. The only added reagent to this synthesis is sodium citrate, which is biocompatible. Even if traces of citrate remain in the final sample, it should not bring any toxicity.

---

[113] Dong, J., P.L. Carpinone, G. Pyrgiotakis, P. Demokritou, B.M. Moudgil *KONA Powder and Particle Journal* **2020** 37 224-232.

This approach involves the reduction of chloroauric acid ($HAuCl_4$) by sodium citrate, which serves a dual role as both the reducing agent and the stabilizer of the resulting nanoparticles. Upon reduction, citrate ions adsorb onto the nanoparticle surface, imparting a negative charge that generates electrostatic repulsion and thereby prevents particle aggregation.

The Turkevich synthesis yields gold nanoparticles with tunable diameters typically ranging from 10 to 100 nm. The particle size can be controlled by adjusting the molar ratio of sodium citrate to $HAuCl_4$; higher citrate concentrations generally produce smaller nanoparticles due to increased nucleation sites. Various modifications of this classical synthesis have been developed to achieve enhanced control over particle size distribution and monodispersity, improving reproducibility and suitability for biomedical applications[114].

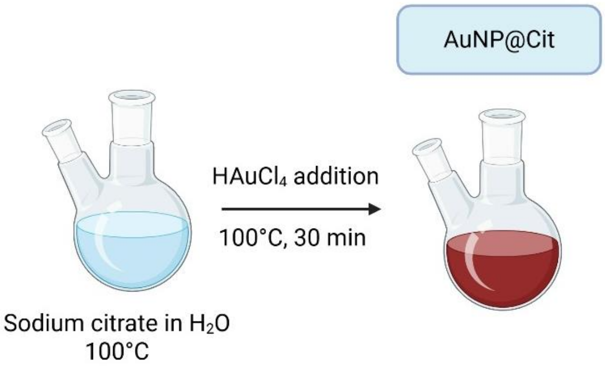

Figure 17: Gold nanoparticle synthesis using Turkevich's method

Since we wanted small gold nanoparticles to be encapsulated into micelles, the synthesis was carried out with 20 equivalents of sodium citrate. Sodium citrate was diluted in ultrapure water and heated up to 100 °C. Then, a solution of tetrachloroauric acid in ultrapure water was added, the resulting mixture heated at 100 °C for 30 min (Figure 17), and the solution was allowed to cool down to room temperature. Citrate-coated gold nanoparticles were obtained as a deep-red suspension. Particles were characterized by TEM and showed a spherical shape and an average diameter of 15 ± 1.5 nm.

V. D. 2. Purification of the gold nanoparticles

Since a large excess of sodium citrate was used during the synthesis, it was first decided to remove the excess of citrate before any ligand exchange. This was done by dialysis which is a separation technique that facilitates the removal of small, unwanted compounds from macromolecules in solution by selective and passive diffusion through a semi-permeable membrane. The sample was loaded into a dialysis bag (cut off = 3500 g mol^{-1}) and put into a large volume of water for a few hours. A progressive color change occurred, the solution went from intense red to purple and then blue before going colorless, suggesting that particles slowly aggregated[115]. It is well documented that the blue color is associated with

---

[114] Sivaraman, S.K., S. Kumar, V. Santhanam *Journal of Colloid and Interface Science* **2011** 361 543-547.

[115] He, Y.Q., S.P. Liu, L. Kong, Z.F. Liu *Spectrochimica Acta Part A: Molecular and Biomolecular Spectroscopy* **2005**

larger gold nanoparticles, while the aggregated ones generally form large dark particles sometimes visible by naked eye. Unfortunately, the latter precipitated to leave a colorless solution.

A ligand exchange was attempted in parallel on the freshly prepared gold nanoparticle colloid. The AuNP suspension in water was treated under vigorous stirring with perfluooctane thiol in PFMC. If ligand exchange were to occur, the characteristic red color of AuNPs should transfer from the aqueous to the fluorinated phase. Yet, no phase transfer of the gold nanoparticles was observed even at high temperatures (*i.e.*, 80 °C).

Since adsorption of the citrate at the surface of the particles occurs mostly through the carboxylate groups, we conceived that protonation could decrease the strength of the interactions and favor the formation of the gold–thiol bond. A diluted solution of hydrochloric acid was thus slowly added to the aqueous suspension of gold capped with citrate ligands. The solution turned rapidly blue before turning translucent. Yet, we could observe some light scattering by suspended particles, using a laser pointer (Tyndall effect). A solution of perfluorinated thiol in PFMC was added, and the mixture was vigorously stirred. The fluorinated phase quickly took the characteristic red color of gold nanoparticles. The fluorinated phase was collected and mixed with PFTD-PEG micelles (10 mg mL^{-1} in ultrapure water). The resulting biphasic mixture was then sonicated 3 times to encapsulate the gold nanoparticle in micelles. The sample was then analyzed by TEM, which showed a mixture of spherical nanoparticles alongside with aggregates, most likely formed before the addition of the thiol. TEM pictures confirmed that this method does not allow for a clean ligand exchange.

Since the ligand exchange did not work properly, it was not possible to cleanly encapsulate gold nanoparticles into micelles. Therefore, this strategy was not investigated further.

V. E. Stellacci synthesis

V. E. 1. Synthesis and purification of gold nanoparticles stabilized by a perfluorinated thiol

More recently, Stellacci and colleagues developed a one-phase synthetic approach for gold nanoparticles in ethanol, addressing limitations inherent to the Brust–Schiffrin method, particularly the restricted solubility of certain ligands in toluene[116]. This methodology permits precise control over the composition of the ligand shell, enabling the use of mixed ligand populations on individual nanoparticles.

In this synthesis, the desired ligand or ligand mixture is dissolved in ethanol and combined directly with an ethanolic solution of the gold precursor. Reduction is achieved through sodium borohydride ($NaBH_4$), yielding monodisperse gold nanoparticles with diameters of

---

61 2861-2866.

[116] Uzun, O., Y. Hu, A. Verma, S. Chen, A. Centrone, F. Stellacci *Chem. Commun.* **2008** 196-198.

approximately 5 nm. A notable advantage of this ethanol-based, single-phase protocol lies in the versatility of purification options, including dialysis and precipitation, facilitating efficient removal of excess reactants and by-products. This method thus provides a streamlined and flexible platform for the preparation of gold nanoparticles with customizable surface chemistry, suitable for various biomedical applications.

Applied to our system, gold salts were solubilized in ethanol, and perfluorooctane thiol was added (Figure 18). Then, a saturated solution of $NaBH_4$ in ethanol was added dropwise to the mixture. After 3 h of stirring, the solution turned brown, which is the characteristic color of small gold nanoparticles. The reaction mixture was stored at 4 °C overnight to allow precipitation of gold nanoparticles. After filtration, particles were washed with ethanol and acetone, but an insoluble (in PFMC) black solid was collected, indicating aggregation.

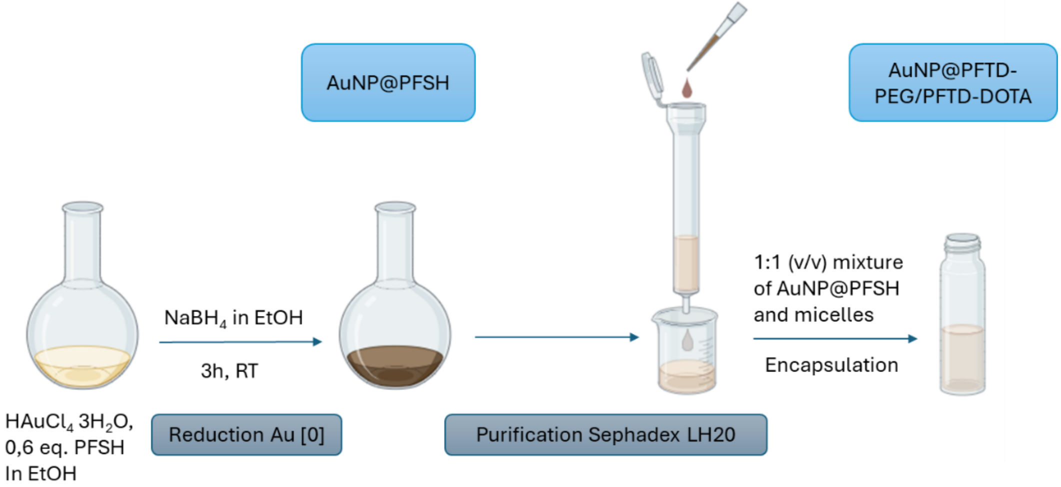

Figure 18: AuNP@PFTD-PEG synthesis using Stellaci's procedure

Since particles aggregated during the washing steps, other purification methods were tested. In their publication, the authors also used dialysis to remove unbound ligands from the medium. Since we are using a fluorinated thiol that is insoluble in water, this method could not be used. However, size exclusion chromatography seemed promising. Therefore, the gold nanoparticles were purified on LH20, a size exclusion resin. Gold nanoparticles could be separated from small molecules, like unbound ligands, and collected as a colloidal suspension in ethanol.

V. E. 2. Encapsulation and characterization of AuNP@PFTD-PEG

The purified particles were encapsulated in PFTD-PEG micelles at 10 mg mL^{-1} (1:1 *v/v*) *via* the ultrasonication treatment (40 % power, 3 x 15 min). Ethanol from the gold nanoparticle suspension slowly evaporated during the ultrasonication process and coated gold nanoparticle became encapsulated in the fluorinated core of the micelle. The mean diameter of the encapsulated gold nanoparticles in micelles was measured by DLS and found to be 18 ± 5 nm. The size of gold nanoparticles was measured from TEM images and displayed a mean diameter of 3.8 ± 1.1 nm (Figure 19). The concentration of the gold nanoparticles in this formulation was determined by ICP-MS and found be 0.5 mM, like the concentration obtained with the Brust-Schiffrin synthesis.

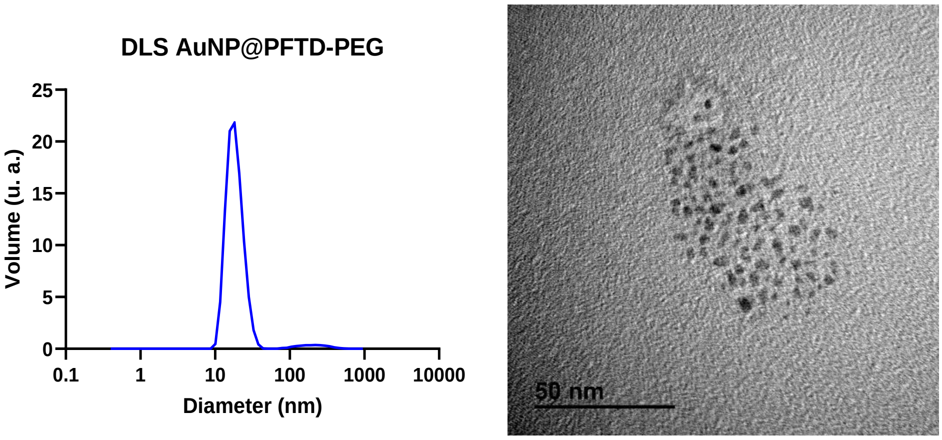

Figure 19: DLS (left) and TEM (right) analysis of AuNP@PFTD-PEG

Finally, the sample underwent thermogravimetric analysis (TGA) to determine the mass of each component in the supra-molecular structure. This method consists in progressively heating the sample to 800 °C while monitoring the evolution of its mass. Over the process, organic compounds will degrade (eventually into carbon dioxide) at specific temperature ranges that depend on their chemical structure. In the end, only gold nanoparticles will remain as they do not decompose and will account for the final mass residue. During the temperature ramp, the evolution of the mass of the sample is recorded to determine the decomposition temperatures of the different components. Results are displayed as a graph showing the evolution of the relative mass of the AuNP@PFTD-PEG sample as a function of the temperature (Figure 20). Two other samples were analyzed: AuNP@PFS (AuNPs with fluorinated ligands) and the PFTD-PEG amphiphile alone to determine its decomposition temperature (250 °C see Annex 1). Since perfluorooctane thiol is a relatively low-boiling-point liquid, it was not used as a reference in TGA. For the nanoparticles with fluorinated coating alone, TGA showed that the gold nanoparticles had an organic layer at their surface corresponding to 76% of their total mass (Annex 1).

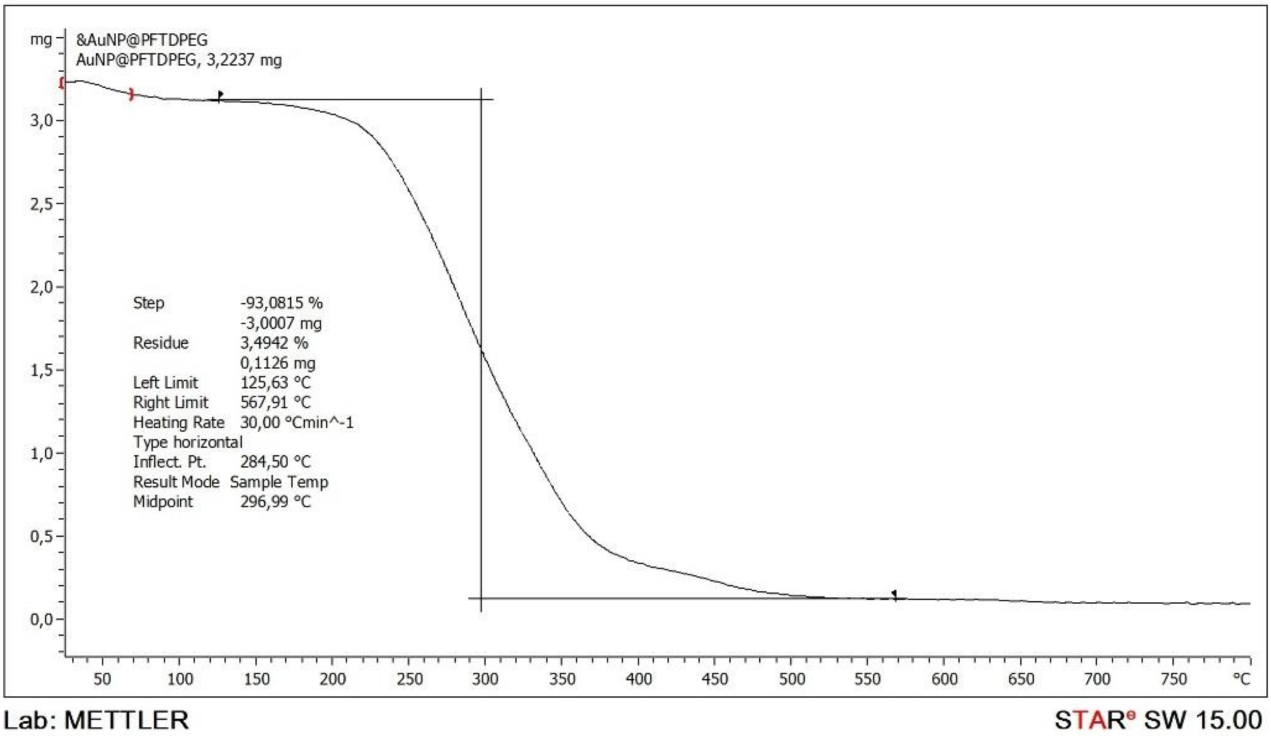

Figure 20: TGA analysis of AuNP@PFTD-PEG

The analysis of AuNP@PFTD-PEG showed a remaining mass after decomposition corresponding to 3% of the starting sample. The amphiphilic PFTD-PEG has a high molecular weight (2600 g·mol^{-1}) and constitutes most of the sample.

V. E. 3. Cytotoxicity of the new formulation of AuNP@PFTD-PEG

The formulation of gold nanoparticles prepared by the Stellacci method in micelles was evaluated as regards its cytotoxicity on the SKBR3 cell line (Figure 21). Micelles without nanoparticles were used as a control. Only the concentration of the amphiphilic unit is reported on the graph, but at the highest micelle concentration (*i.e.*, 1 mg mL^{-1}), the corresponding gold concentration was 50 µM, and 0.2 µM for the least concentrated sample (0.004 mg mL^{-1}). Pleasingly, micelles with and without gold exhibited a similar profile with no signs of major cytotoxicity after 72 h of incubation. This study confirmed the innocuity of gold nanoparticles synthesized using the Stellacci methodology and prompted us to move to the next step, that is, the evaluation of the gold-encapsulated micelles in enhancing radiotherapeutic effect under irradiation.

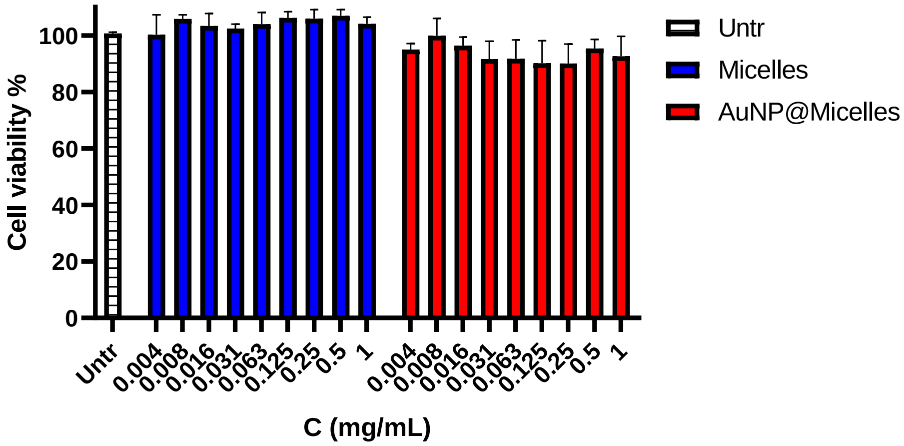

Figure 21: Cytotoxicity study of PFTD-PEG micelles and AuNP@PFTD-PEG on SKBR3 cell line after 72 h incubation

VI. External irradiation studies

Our nanocarriers were designed to have a dual effect: radiosensitization *via* the transported oxygen in the fluorinated core of the micelles, and radioenhancement *via* the encapsulated gold nanoparticles. In an initial step, we wanted to evaluate the effect of the nanoconstructs under external irradiation. To test our micellar systems, two different cell lines were used: SKBR3 (human breast cancer) and B16F10 (murine melanoma), and two types of toxicity were evaluated, *i.e.*, chronic (cells incubated continuously with micelles) and acute (cells exposed only 24 h to the micelles).

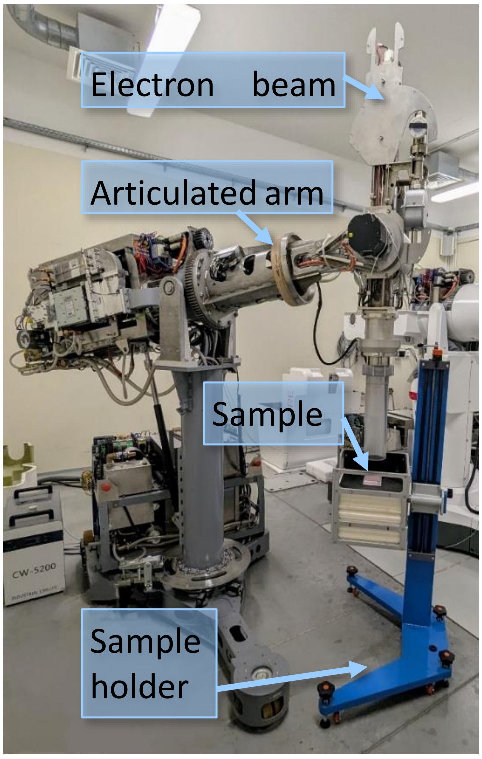

Figure 22: External irradiation setup

The irradiation source that was used to expose the cells is a 9 MV electron beam source delivering 10 Gy min^{-1} and presented in Figure 22. Cells were exposed to either 1, 2, or 4 Gy in order to mimic doses applied in clinical setups. Three concentrations of the micelles were studied w/ and w/o gold: a high concentration of 1 mg mL^{-1} ([Au] = 50 µM) corresponding to the highest concentration tested in cytotoxicity studies, a moderate concentration (0.1 mg mL^{-1}) and a low concentration (0.01 mg mL^{-1}). All following biological experiments were realized in collaboration with Marcin Zieliński.

VI. A. Chronic toxicity

In this experiment, the colloid suspension was first incubated with cells for 24 h on a 96-well plate. The plate was then irradiated by the electron beam source. Exposure time was adjusted to deliver the appropriate dose (*i.e.,* 1, 2, or 4 Gy). The cells were further incubated at 37 °C in a humid environment before the viability was assessed by MTS assay at 24, 48, and 72 h after exposure to the electron beam. Viability of the cells was compared to that of an untreated control group, and a group exposed to electron beam without micelles. Only the results corresponding to samples treated with 1 mg mL^{-1} of micelles are presented. The data corresponding to the other micellar concentrations can be found in annex 2 (B16F10 cell line) and annex 3 (SKBR3 cell line).

VI. A. 1. Chronic toxicity on B16F10 cell line

At 24 h, no detectable effect was observed, as the viability of B16F10 cells treated with either Micelles or AuNP@Micelles was comparable to that of the control group, regardless of the applied dose from 1 to 4 Gy (Figure 23). At 48 h, the highest irradiation dose (4 Gy) induced a general reduction in cell viability, including in untreated controls. Under these conditions, both Micelles and AuNP@Micelles elicited a more pronounced radiotoxic effect, reducing viability to approximately 40%, compared with ~60% in the control group. Nevertheless, no statistically significant difference was observed between the effects of Micelles and AuNP@Micelles, which exhibited similar efficacy in decreasing cell survival. A comparable trend was observed at 72 h with a dose-dependent response, with irradiation effects becoming apparent from 2 Gy onward. The responses induced by Micelles and AuNP@Micelles could not be distinguished at 72 h, as both demonstrated comparable amplification patterns initiated at 1 Gy, resulting in a reduction in cell viability, compared to controls.

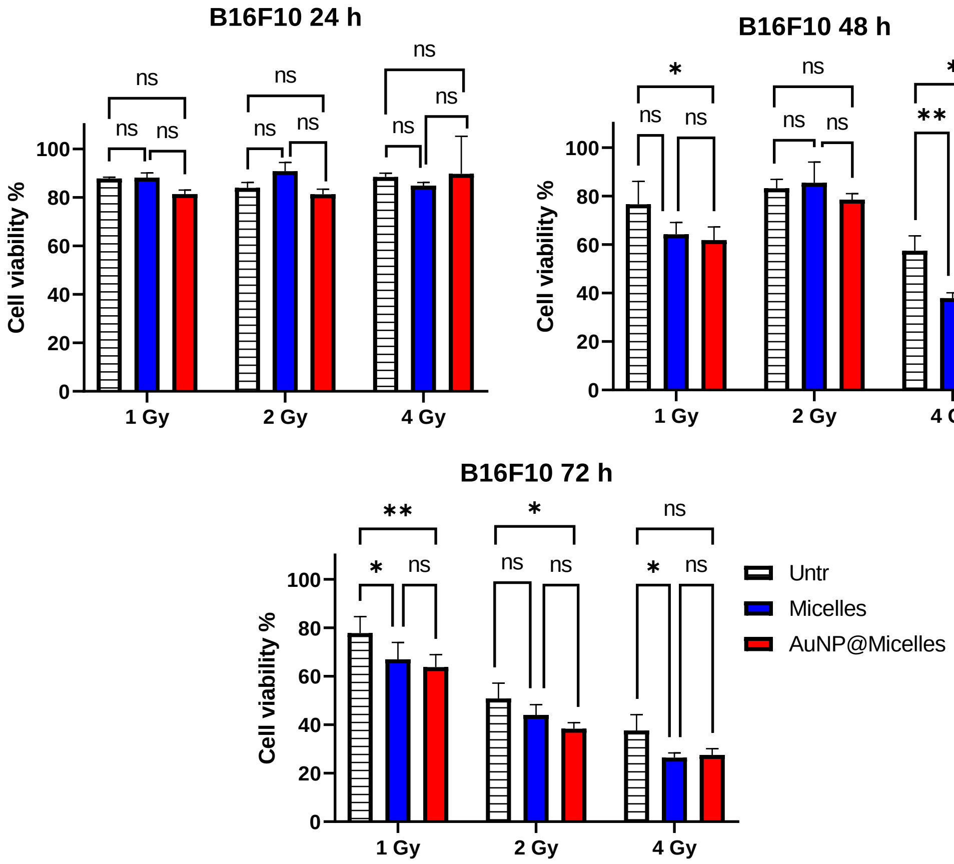

Figure 23: Cytotoxicity study on B16F10 cell line treated with Micelles or AuNP@Micelles (C = 1 mg mL^{-1}*) under external irradiation beam (9 MV, 10 Gy min*$^{-1}$*), ns = non-significant, * p < 0.05, ** p < 0.01, *** p < 0.001, **** p < 0.0001 (two-way ANOVA), results shown as mean ± SD.*

It thus seems that the micellar formulations bring an added value in potentiating the effect of the electron beam irradiations as lower cell viability was evidenced in the presence of the nanocarrier. However, the differences between empty and gold-loaded micelles are negligible, precluding the discrimination of their respective contributions to the observed enhanced radiotoxicity. Given that B16F10 is an inherently radioresistant cell line[117], the cytotoxicity induced by electron beam irradiation alone may have masked potential differences, thereby limiting the ability to assess specific contributions to radiosensitization. It was therefore decided to conduct a new series of radiocytotocicity assays on the SKBR3 cell line which is more radiosensitive (moderate radioresistance)[118].

VI. A. 2. Chronic toxicity on SKBR3 cell line

By selecting the SKBR3 cell line, which is less resistant to radiations than B16F10, we anticipated to be able to better distinguish between the effects induced either by the perfluorinated micelles or the AuNP@Micelles, as potential radiosensitizers. Indeed, if slight

---

[117] Alcaraz, M., A. Olivares, M. Andreu-Gálvez, D.G. Achel, A.M. Mercado, M. Alcaraz-Saura *Antioxidants* **2022** 11 2166.

[118] Wang, L., C. Yuan, K. Lv, S. Xie, P. Fu, X. Liu, Y. Chen, C. Qin, W. Deng, W. Hu *PLoS ONE* **2013** 8 e67373.

differences in radiosensitization were to appear between empty and gold-loaded micelles, this should have a more pronounced effect on a radiosensitive cell line (SKBR3) than on a radioresistant cell line (B16F10).

The radiosensitivity of the SKBR3 cell line was evidenced at the lowest irradiation dose, starting at 24 h (Figure 24). Indeed, at 24 h we observed an effect of the irradiation alone on cellular viability, whatever the applied dose. It has to be noted that micelles had a moderate effect at 24 h but AuNP@Micelles exhibited a stronger radiosensitization. The same trend was observed across the entire range of irradiation dose and time with Micelles and AuNP@Micelles being more potent compared to the control. If we consider the 72 h experiment and the highest dose (4 Gy), AuNP@Micelles induced more than two-fold decrease in cell viability, compared to untreated cells (no micelles), and were approximately 1.5 times more potent than perfluorinated micelles alone. These results, which are statistically relevant, suggests that oxygen perfusion by the micelles, on the one hand, and gold nanoparticles, on the other hand, play a key role in the observed radioenhancement effect which triggers superior biological effects. The two components interact in a synergistic fashion that can be observable at different time points and irradiation doses.

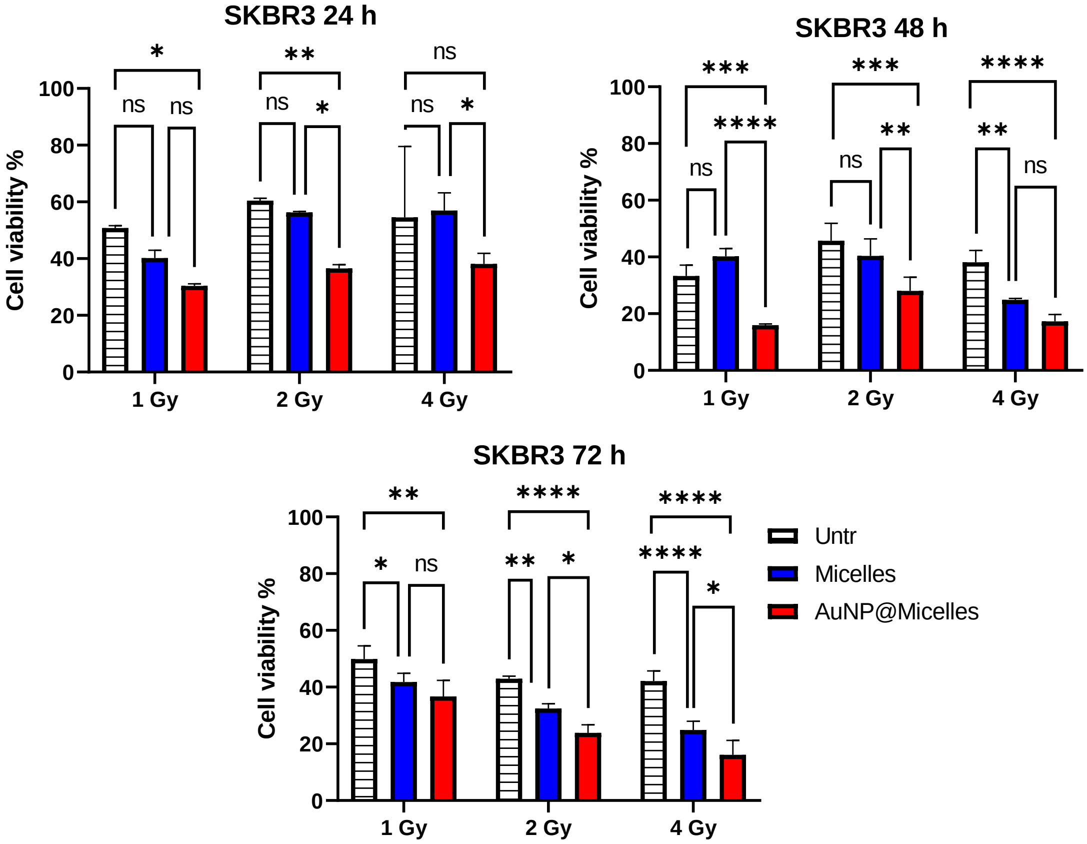

*Figure 24: Cytotoxicity study on SKBR3 cell line treated with Micelles or AuNP@Micelles (C = 1 mg mL^{-1}) and external electron beam irradiation (9 MV, 10 Gy min^{-1}), ns = non-significant, * $p < 0.05$, ** $p < 0.01$, *** $p < 0.001$, **** $p < 0.0001$ (two-way ANOVA), results shown as mean ± SD.*

Based on the above external irradiation studies on B16F10 and SKBR3 cell lines, the radiosensitizing/radioenhancement properties of the nanocarriers was quantified.

VI. A. 3. Radiosensitizing parameters

From these data, it is also possible to look at the effect of the dose for a given concentration of nanoobjects. A polynomial regression can be used to highlight the radioenhancement effect of the nanometric systems by giving access to important parameters:

- The Sensitizing Enhancement Ratio (SER) is used to describe the radiosensitizing effect of a compound. It can be calculated from the area under the curves of the surviving cells (ratio between the control curve and that in the presence of the micelles). This approach is regarded as the most accurate because it incorporates the entire observed radiocytotoxic response rather than relying on a single data point.
- The Dose Modifying Ratio (DMR), defined as the ratio between the dose producing a specific effect in the absence of micelles and the dose required to achieve the same effect in the presence of the same. The DMR is applicable for a specified level of cell survival.
- The Surviving Fraction (SF), which is the ratio between the number of colonies that survive said doses of radiation divided by the cells seeded, is generally determined for a given dose, most of the time 2 Gy, as this is a dose usually in use in clinics[119].
- The Radiation Enhancement Ratio (RER) is also used to describe the nanoparticle sensitizing effect. It corresponds to the ratio between the surviving fraction in the control conditions for a given dose and the surviving fraction in the tested conditions at the same dose[120].

We calculated the different parameters for B16F10 (Table 4) and SKBR3 (Table 5) cell lines with a concentration of 1 mg mL^{-1} of micelles ([Au] = 50 µM). To do so, cell viability was plotted against the irradiation dose for the two samples (Annex 4). All curves follow a polynomial regression that gives access to different parameters.

Table 4: Radiosensitizing parameters of PFTD-PEG and the AuNP@PFTD-PEG on B16F10 cell line

	SER	**DMR$_{50\%}$**	**SF$_{2Gy}$**	**RER$_{2Gy}$**
PFTD-PEG	1.154	1.220	44.05	1.153
AuNP@PFTD-PEG	1.226	1.400	37.21	1.366

Table 5: Radiosensitizing parameters of PFTD-PEG and AuNP@PFTD-PEG on SKBR3 cell line

	SER	**DMR$_{50\%}$**	**SF$_{2Gy}$**	**RER$_{2Gy}$**
PFTD-PEG	1.248	1.161	32.44	1.325
AuNP@PFTD-PEG	1.490	1.263	23.87	1.800

The calculated SER, DMR and RER values were systematically > 1 for the two cell lines.

---

[119] Roach, M.C., J.D. Bradley, C.G. Robinson *Journal of Thoracic Disease* **2018** 10 .

[120] Subiel, A., R. Ashmore, G. Schettino *Theranostics* **2016** 6 1651-1671.

A Sensitizing Enhancement Ratio value > 1 means that the micelles bring a radiosensitizing effect to the cells. The higher SER, the better the radiosensitizing effect. Both Micelles and AuNP@Micelles increase the radiosensitivity of B16F10 and SKBR3 cell lines, with a more important effect for the AuNP-containing micelles. A SER value of 1.49 was calculated for AuNP@Micelles in interaction with SKBR3 cells, which is superior to that of B16F10 (SER = 1.22). These SER values are consistent with data from the literature for AuNP radiosensitization[121]. The higher SER value calculated for SKBR3 cell line indicates that both PFTD-PEG micelles and AuNP@PFTD-PEG have a stronger radiosensitizing effect on this cell line, compared to B16F10.

A Dose Modifying Ratio value > 1 means that a lower dose is needed in the presence of the micelles to achieve the same effect (in this case 50% cell death) and that the applied treatments sensitize the cells. Our two systems, *i.e.*, Micelles and AuNP@Micelles, exhibit radiosensitizing effects, but surprisingly, DMR values were lower for SKBR3 than for B16F10, although SKBR3 is more radiosensitive. $DMR_{50\%}$ values of AuNP@Micelles are superior to those of Micelles.

In this context, SER and DMR provide complementary information: SER characterizes the radiosensitizing potential of a compound, while DMR reflects this effect in the context of the intrinsic radiosensitivity of each cell line.

A Radiation Enhancement Ratio value > 1 corresponds to a lower cell survival in the treated conditions compared to the control. It is thus correlated with the radiosensitizing effect of the treatments. Both cell lines were sensitive to PFTD-PEG micelles and AuNP@PFTD-PEG but with a stronger effect on SKBR3, compared to B16F10. RER_{2Gy} values of AuNP@Micelles are superior to that of Micelles.

Finally, the Surviving Fraction values allow direct comparison between the cell death induced by the micelles and the micelles loaded with gold (here under 2 Gy irradiation). A lower SF value indicates a stronger radiosensitization effect. For both cell lines, the calculated SF_{2Gy} is lower for cells treated with gold nanoparticles in micelles, compared to PFTD-PEG micelles alone.

Most of the previous studies in the literature conducted on gold nanoparticle radioenhancement potential were carried out under gamma or X-ray irradiation, but some were also tested under electron irradiation. A study by Chang *et al.* on B16F10 irradiated by electron beam (6 MV) in the presence of 13 nm gold nanoparticles (10 nM) showed a radioenhancement effect of the gold nanoparticles but only at the highest irradiation doses (> 8 Gy) studied. The authors observed a significant tumor growth delay with tumor-bearing mice[122].

---

[121] Detappe, A., S. Kunjachan, J. Rottmann, J. Robar, P. Tsiamas, H. Korideck, O. Tillement, R. Berbeco *Cancer Nanotechnology* **2015** 6 4.

[122] Chang, M.-Y., A.-L. Shiau, Y.-H. Chen, C.-J. Chang, H.H.-W. Chen, C.-L. Wu *Cancer Science* **2008** 99 1479-1484.

Jain *et al.* studied the radio-sensitizing properties of AuroVist^{TM}, small gold nanoparticles (1.9 nm) developed for computed tomography applications and coated with thiol ligands[123]. The particles were tested on MDA-MB231 breast cancer cells, and with two types of irradiations. With X-ray beams (160 kVp, 6 MV, 15 MV), they calculated a SER value of 1.29 (6 MV) and up to 1.41 under 160 kVp irradiation. Under electron beam (6 MeV and 16 MeV) SER values of 1.04 and 1.35 were measured, respectively. The authors showed that these results also depend on the cell line. The SER value obtained for our gold nanoparticles is in the range of what was previously observed in the literature for small gold nanoparticles.

VI. B. Acute Toxicity

This second set of experiments aims to observe the cytotoxic effect resulting from the particles internalized in the cells and not from the particles in the surrounding medium, under electron beam irradiation. To do so, cells were incubated with nanoparticles for 24 h, before the medium was removed and replaced with fresh cell culture medium. The sample was then irradiated as previously with an electron beam source (1-4 Gy) and cells were further incubated at 37 °C in a humid atmosphere before reading the cell viability after 24 and 48 h. The results are compared with those of the chronic experiments at the same time points, same concentration, and same irradiation dose. The results presented below are for the experiments conducted with 1 mg mL^{-1} of Micelles or AuNP@Micelles. Those of the acute toxicity conducted with 0.01 and 0.1 mg·mL^{-1} of Micelles or AuNP@Micelles are in annex 5 (B16F10) and annex 6 (SKBR3).

VI. B. 1. Acute toxicity on B16F10

As a reminder, B16F10 is a radioresistant cell line. The general trend is that a significantly higher effect is observed in the acute cytotoxicity set of experiments, compared to chronic cytotoxicity (Figure 25). This is particularly true for early times (*i.e.,* 24 h), but differences become less pronounced at 48 h and high doses (e.g., 4 Gy). At 24 h, cellular viability is much lower in the acute set, and differences with the chronic group are striking. This is particularly true for lower doses (1-2 Gy) with a two-fold decrease in cellular viability compared to chronic. Surprisingly, 4 Gy irradiations in the presence of the nanocarriers seem to have lower effects than 1-2 Gy irradiations. Micelles and AuNP@Micelles behaved similarly in potentiating the irradiations at 24 h.

---

[123] Her, S., D.A. Jaffray, C. Allen *Advanced Drug Delivery Reviews* **2017** 109 84-101.

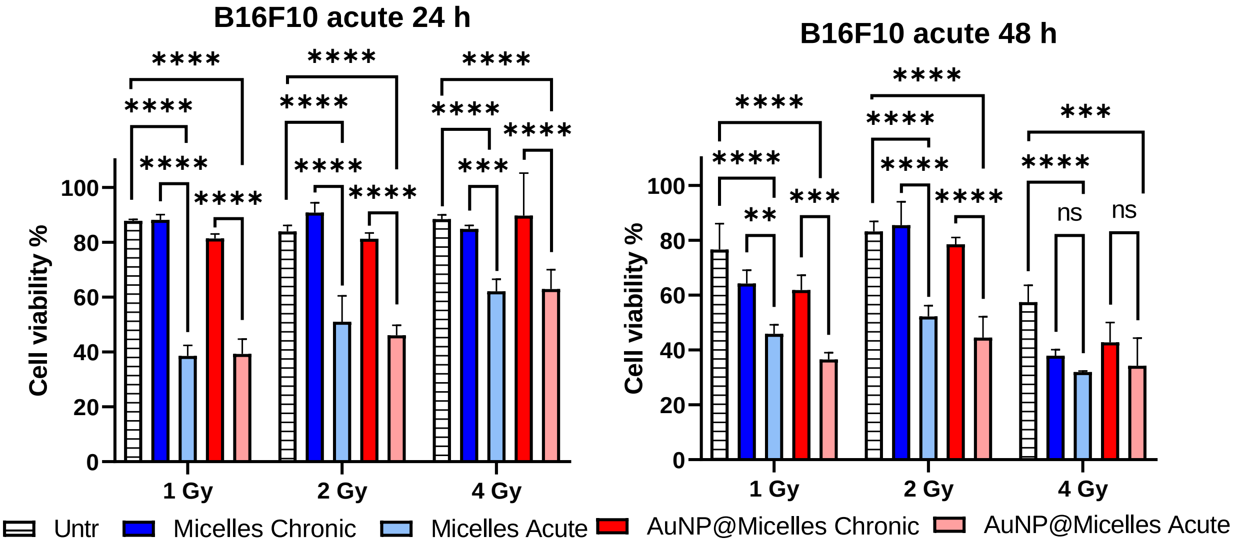

Figure 25: Acute cytotoxicity study on B16F10 cell line treated with Micelles or AuNP@Micelles (C = 1 mg mL^{-1}*) and external irradiation (electron beam, 9 MV, 10 Gy s*$^{-1}$*), comparison with chronic treatment, ns = non-significant, * p < 0.05, ** p < 0.01, *** p < 0.001, **** p < 0.0001 (two-way ANOVA), results shown as mean ± SD.*

At the 48 h time point, lower cell viability was also observed in the acute experiments, compared to chronic, and whatever the applied dose. The highest effects were detected at 4 Gy but the gap between acute/chronic following exposure to Micelles and AuNP@Micelles is minimal. The latter comment applies to the two nanocarriers that had nearly the same effect on B16F10 cellular viability.

VI. B. 2. Acute toxicity on SKBR3

As previously observed in the chronic radiotoxicity experiments, radiosensitizing effects of micelles and gold-micelles are more pronounced on the radiosensitive SKBR3 cell line, compared to radioresistant B16F10 cells. At 24 h, although the cells suffered from the irradiation alone, a beneficial contribution of the nanocarriers could be evidenced, with a 2- to 3-fold decrease in cellular viability. There were however no significant differences in the potentiating effects of micelles and AuNP@micelles.

At 48 h, we had nearly the same trend, but with an overall decrease in cell viability, including w/ and w/o nanocarriers. Although a radioenhancement effect of gold nanoparticles could be detected with a systematically better effect than empty micelles, the gap between the two sets of experiments is small (Figure 26).

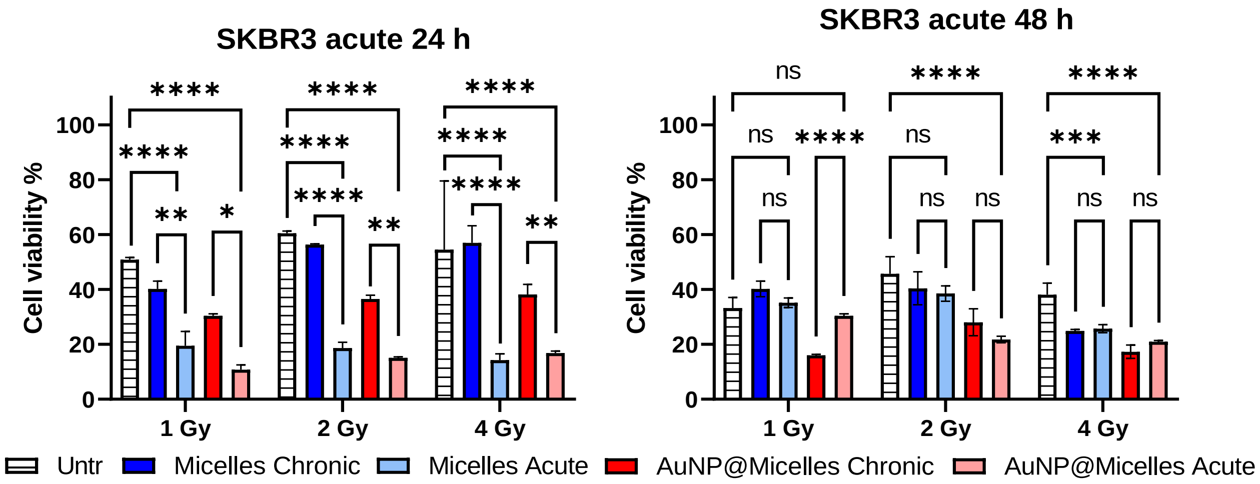

Figure 26: Acute cytotoxicity study on SKBR3 cell line treated with Micelles or AuNP@Micelles (C = 1 mg·mL^{-1}*) and external irradiation (electron beam, 9 MV, 10 Gy·min*$^{-1}$*), comparison with chronic treatment, ns = non-significant, * p < 0.05, ** p < 0.01, *** p < 0.001, **** p < 0.0001 (two-way ANOVA), results shown as mean ± SD.*

The above chronic and acute experiments conducted on less- (SKBR3) and more radioresistant (B16F10) cell lines show a radiosensitizing effect of the nanometric platforms. Differences in radioenhancement between Micelles and AuNP@Micelles could readily be detected in the chronic radiotoxicity study on SKBR3, with a stronger effect of AuNP@Micelles on cell's death. This effect increases with increasing irradiation doses and is always superior to that of empty micelles. On the other hand, chronic exposure of B16F10 cells had a more moderate impact only starting at higher irradiation doses and exposure times. Also, discrimination between the two micellar system was not feasible as cellular viability was almost identical in each of the experiments.

If we consider acute exposure of the cells to the micellar carriers, an overall stronger radiosensitizing effect could be detected on both B16F10 and SKBR3 cells. For example, at 24 and 48 h, Micelles and AuNP@Micelles triggered a two-fold decrease in B16F10 cell viability under 1 or 2 Gy of irradiation, compared to chronic exposure groups. The same trend is valid for the less radioresistant SKBR3 cell line. At an early time point (*i.e.*, 24 h, 1-4 Gy) we measured a two- to four-fold decrease in cellular viability after exposure to Micelles and AuNP@Micelles, compared to chronic groups. These differences are minimized at 48 h. Although AuNP@Micelles appear to behave similarly to micelles on B16F10 (no significant difference in radio-enhancement performance), their effect is superior to that of gold-free micelles interacting with SKBR3 in the acute experiments.

Overall, we observed a more potent effect of the micellar platform in the acute set of experiments. The reduced radiotoxic effect observed under chronic treatment conditions may be explained by a masking effect of nanoparticles present in the supernatant. In both experimental settings, the fraction of nanoparticles internalized by the cells is likely equivalent. However, in the chronic exposure scenario, the majority of nanoparticles remain dispersed in the surrounding culture medium, where they can interact with ionizing radiation. In this context, they act as scavengers, decreasing the amount of radiation that reaches the internalized particles, which in turn reduces toxicity during the initial hours post-irradiation. Over time, this protective effect diminishes due to the increased generation of reactive oxygen species (ROS) in the culture medium, which can compromise the cell membrane or other organelles, ultimately contributing to cell death.

These two external irradiation experiments highlight the dual functional properties of the engineered system. First, oxygen delivery *via* the perfluorinated micelle core markedly enhances radiotoxicity, providing *in vitro* evidence of radiosensitization. Notably, unlike some previous studies, the micelles were not pre-saturated with oxygen prior to cell exposure, demonstrating robust radiosensitizing potential even under atmospheric oxygen levels. Second, the radioenhancement effect of AuNPs, combined with their synergistic interaction with the perfluorinated micelles, was demonstrated under external electron beam radiotherapy. Direct comparison with earlier studies remains difficult due to numerous experimental variables. Radiation type and beam energy, for example, strongly influence nanoparticle–radiation interactions; under X-ray exposure, the radioenhancement efficiency of high-Z nanoparticles is highly dependent on the incident energy. Moreover, as confirmed in our study, the radiosensitizing outcome also varies depending on the specific cell line investigated.

Finally, the acute toxicity analysis of our nanoparticles emphasizes the critical role of the internalized fraction in determining overall toxicity under chronic conditions. The pronounced cytotoxicity observed at the earliest time point underscores the strong contribution of direct DNA damage to the overall toxic effect.

VII. Conclusion

In this chapter, nanocarriers were engineered for the radiosensitization of cancer cells by combining perfluorinated micelles, endowed with oxygen-carrying properties (to favor the production of reactive oxygen species), with gold nanoparticles behaving as radioenhancers (capable of amplifying the effect of irradiations). Micelles were assembled from PFTD-PEG amphiphilic units that were synthesized through a two-step process with satisfactory yield. These micelles exhibited a small size and a low critical micelle concentration, features that are favorable for biomedical applications. *In vitro* evaluation confirmed the biocompatibility of the carrier, with only a very mild intrinsic cytotoxicity detected at the highest concentrations investigated.

Micelles were combined with gold nanoparticles. Several synthetic approaches were evaluated to produce stable nanoparticles. The approach developed by Stellacci was adopted by us to generate gold nanoparticles coated with fluorinated ligands. These particles were successfully encapsulated into the fluorinated micelles to yield the AuNP@PFTD-PEG formulations, which displayed no significant cytotoxicity.

The radio-enhancement capacity of gold-loaded micelles was investigated through external electron beam irradiation studies on two distinct cell lines, B16F10 with higher radioresistance, and less radioresistant SKBR3. Chronic and acute toxicity relative to untreated controls was observed following the irradiation. Quantitative radiosensitization parameters confirmed the increased performances of our formulations with higher sensitizing values for AuNP@Micelles, compared to the empty micelles.

Overall, this *in vitro* proof of concept demonstrates that gold nanoparticles can be effectively integrated with fluorinated micelles to enhance the radiosensitivity of cancer cells. Building on these findings, potential applications in internal radiotherapy may now be envisioned. To enable radioisotope incorporation into the current nanocarrier design, the synthesis of an additional amphiphilic unit was undertaken to facilitate micelle radiolabeling. This strategy will also allow detailed investigation of the pharmacokinetics and biodistribution of the system, which will be addressed in the following chapter.

Chapter II: Gold Nanoparticles encapsulated in perfluorinated micelles radiolabeled with ^{177}Lu for Internal Radiotherapy

I. Objectives of the chapter

The ^{177}Lu radioisotope has emerged as a key player in the field of radionuclide therapy due to its favorable nuclear, chemical and biological properties. One major advantage lies in its relatively straightforward production in nuclear reactors. ^{177}Lu can be produced *via* direct irradiation of a ^{176}Lu target (carrier-added pathway), which offers high neutron capture cross-section and good specific activity, making it a simple and cost-effective method. In contrast, the indirect (non-carrier-added) pathway using ^{176}Yb gives higher specific activity but requires complex and costly separation of trace ^{177}Lu from the bulk Yb. The carrier-added pathway is the most popular as it allows to reach the required specific activity for clinical applications.

Another important feature is the week-long half-life of ^{177}Lu that enables complex radiolabeling, purification, and distribution to distant clinical centers with minimal activity loss. Furthermore, this half-life aligns well with the pharmacokinetics of many biomolecules[124] used in nuclear medicine, which often require several hours to reach their target tissues. This compatibility enhances the therapeutic index by ensuring the radiation is delivered mostly at the tumor site and minimizing the irradiation of healthy tissues.

^{177}Lu can be considered as a theranostic isotope due to its dual emission of γ photons and β^- particles. The medium-energy β^- particles, with short tissue penetration, induce DNA damage in the tumor area while limiting exposure of normal surrounding tissues. In parallel, low-energy photons are suitable for real-time imaging with SPECT/CT or gamma-cameras. This dual emission allows both therapy and imaging with a single radiopharmaceutical, which is of interest for personalized medicine. As a result, ^{177}Lu has been extensively studied and translated into clinical use. To date, two ^{177}Lu-labelled radiopharmaceuticals have been approved by FDA and EMA: ^{177}Lu-DOTA-TATE (Lutathera®) for neuroendocrine tumors and ^{177}Lu-PSMA-617 (Pluvicto™) for prostate cancer. These approvals have catalyzed a rise in the clinical exploration of ^{177}Lu for different applications in oncology.

In order to locally enhance the radiotherapeutic effect of ^{177}Lu, its combination with gold nanoparticles for radio-enhancement was explored in the literature[125]. When combined with ^{177}Lu, gold nanoparticles can amplify the radiation-induced cytotoxicity within the tumor environment, offering a synergistic effect that could allow the use of lower radiation doses and thus reduce toxic effects in non-targeted healthy tissues. Preclinical studies have demonstrated this synergistic potential, improving tumor-cell killing and tumor control on animal models when ^{177}Lu is co-delivered with gold nanoparticles.

---

[124] Yong, W., S. Zhang, Z. Zhang, Z. Li, Y. Qin, X. Qi, D. Wang, Y. Zhang, J. Li, Z. Liu, R. Zhu, H. Li, G. Wang *Journal of Medicinal Chemistry* **2025** 68 17794-17807.

[125] Ponchelle, M., M. Pruszyński, E. Gravel, E. Doris *Small Science* **2025** 5 2400550.

Despite the growing number of studies based on ^{177}Lu, the integration of perfluorocarbons into the formulation remains unexplored. Combination of ^{177}Lu with our previously described perfluorinated micelles represents a novel strategy that may offer several advantages. The micellar structure can serve as an effective carrier for the radioisotope, improve the pharmacokinetic profile and facilitate drug delivery. Moreover, the combined radiosensitizing effects of perfluorinated micelles (carriers of oxygen) and gold nanoparticles could address some of the current limitations of radiotherapy, particularly in solid tumors known for their poor vascularization, low oxygenation (hypoxia) and resistance to radiation.

Context

II. ^{177}Lu, characteristics and production of the isotope

II. A. Properties

Lutetium is a lanthanide that has various isotopes, including ^{175}Lu, a stable isotope and the most abundant on earth (97%) and ^{176}Lu, a natural radioactive isotope considered stable due to its very long half-life of 4×10^{10} years. On the other hand, ^{177}Lu is an artificial isotope ($t_{1/2} = 6.65$ days) produced in nuclear reactors, it decays through β^- and γ emissions useful in both therapy and diagnosis[126].

In the context of nuclear medicine, ^{177}Lu exhibits different key properties that make it useful for therapeutic applications thanks to its medium-energy β^- emission (498 keV) and average penetration range of 670 µm (up to 1 mm) in soft tissues[127]. This feature makes it ideal for delivering ionizing radiation within a relatively small volume, thus increasing toxicity to cancer cells while limiting damage to healthy tissues. Since ^{177}Lu also emits low-energy γ photons at 208 keV (10 % abundance) and 113 keV (6 % abundance), radiopharmaceuticals labelled with ^{177}Lu can also be imaged *in vivo* for their drug biodistribution and pharmacokinetics, using the same preparation as for therapy. This dual beta/gamma emission makes ^{177}Lu a theranostic isotope. Moreover, the moderate-energy of β^--particles and low-energy of gamma photons result in a relatively low radiation dose, which allows higher activity levels of ^{177}Lu to be used both in the preparation of a drug and in its administration to a patient.

Additionally, ^{177}Lu exists primarily in the +3-oxidation state, which is the most stable and prevents any reduction-oxidation changes during formulation or after administration to a patient. This property allows the radiolabeling of a large variety of molecules, from small molecules to biomolecules. Most of the ^{177}Lu radiolabeling is realized through the incorporation of a multifunctional chelating agent, the most popular being 1,4,7,10-tetraazacyclododecane-1,4,7,10-tetraacetic acid (DOTA) and its various bifunctional derivatives[128]. The half-life of ^{177}Lu is advantageous because it gives more time for preparing a radiopharmaceutical, enabling more elaborate procedures and quality control

II. B. Production

It is rather difficult to evaluate the worldwide demand for ^{177}Lu. According to Novartis' financial results and sale of Lutathera® radiopharmaceutical (^{177}Lu-DOTA-TATE used for

---

[126] Niu, T., M. Fan, B. Lin, F. Gao, B. Tan, X. Du *Experimental and Therapeutic Medicine* **2024** 27 225.

[127] Trejtnar, F., P. Bárta, J. Kozempel, M. Vlk, A. Ďurinová, M. Kuchařová, P. Pávek *Nuclear Medicine and Biology* **2025** 144-145 108998.

[128] Hunt, W.W., M. Long, U. Kamil, S. Kellapatha, W. Noonan, P.D. Roselt, B. Emmerson, M.S. Hofman, M.B. Haskali *Nature Protocols* **2025** .

neuroendocrine tumors treatment) it is possible to estimate that approximately 10,000 to 15,000 doses of 7.4 GBq of Lutathera® are administered yearly[129]. However, there are other producers of the ^{177}Lu radioisotope, as well as other radiopharmaceuticals labelled with it. The annual demand for ^{177}Lu continues to rise, driven not only by the growing number of patients eligible for treatment with ^{177}Lu-based radiopharmaceuticals, but also by ongoing research and development efforts aimed at creating novel radiopharmaceuticals incorporating this radionuclide[130].

The production of ^{177}Lu takes place in nuclear reactors through neutron irradiation of a target with a high flux of neutrons. There are currently two ways to produce ^{177}Lu: the indirect pathway, also called a non-carried-added, and the direct way named as a carrier added.

The objective of radionuclides production for medical applications is to reach the highest specific activity possible in order to administer a smaller amount of the pharmaceutical to the patient, while keeping the expected radiobiological effect. It was calculated that the theoretical highest specific activity possible for ^{177}Lu is 4103 GBq mg^{-1} if the sample is composed only of the expected radionuclide; however, such high specific activity was never actually reached[131].

II. B. 1. Indirect production pathway [^{176}Yb(n,γ)^{177}Yb $\beta^- \rightarrow$ ^{177}Lu]

The indirect production pathway, also called non-carrier-added[132], consists in irradiating a ^{176}Yb target to produce ^{177}Yb that quickly decays ($t_{1/2}$ < 2 h) to ^{177}Lu *via* β^- emissions (Equation 1). ^{177}Lu is chemically separated from the target to obtain the highest possible specific activity and purity. Generally speaking, SA > 3000 GBq mg^{-1} are required for medical applications[133]. Since ^{177}Lu is not directly obtained from irradiation of a target, the specific activity of the final product is independent of the neutron flux. However, this parameter is very important for the production yield. The probability of ^{176}Yb(n,γ)^{177}Yb nuclear reaction is relatively low because the neutron absorption cross-section of ^{176}Yb is ~ 2.85 barns. Therefore, the use of higher neutron flux (> 10^{14} n cm^{-2} s^{-1}) increases the yield and shortens the time of the reaction. Still, a large amount of target material (about 1 g) is needed to produce 50 clinical doses of ^{177}Lu[134]. To increase the amount of ^{177}Yb, and thus indirectly of ^{177}Lu, the target must be enriched in ^{176}Yb (up to 99%) to achieve a satisfactory reaction yield. This is however costly, as enriched target materials are quite expensive. As a consequence, unreacted ^{176}Yb has to be recovered after each cycle of irradiation and

---

[129] Vogel, W.V., S.C. Van Der Marck, M.W.J. Versleijen *European Journal of Nuclear Medicine and Molecular Imaging* **2021** 48 2329-2335.

[130] Zhang, S., X. Wang, X. Gao, X. Chen, L. Li, G. Li, C. Liu, Y. Miao, R. Wang, K. Hu *Signal Transduction and Targeted Therapy* **2025** 10 .

[131] Dash, A., M.R.A. Pillai, F.F. Knapp *Nuclear Medicine and Molecular Imaging* **2015** 49 85-107.

[132] Hashimoto, K., H. Matsuoka, S. Uchida *Journal of Radioanalytical and Nuclear Chemistry* **2003** 255, 575–579.

[133] Di Iorio, V., S. Boschi, C. Cuni, M. Monti, S. Severi, G. Paganelli, C. Masini *Molecules* **2022** 27 4143.

[134] Dash, A., M.R.A. Pillai, F.F. Knapp *Nuclear Medicine and Molecular Imaging* **2015** 49 85-107.

production of ^{177}Lu and again transformed into enriched target material ready for the next production.

Equation 1: Nuclear reaction of ^{177}Lu production through the indirect production pathway

$$^{176}Yb + n \rightarrow \gamma + {}^{177}Yb \xrightarrow{\beta^-} {}^{177}Lu$$

The key step in this indirect pathway is the purification procedure. It consists in the separation of micro amounts of ^{177}Lu from much larger amounts of ^{176}Yb, a challenging procedure since the two elements are lanthanides with +3 oxidation states and have close properties[135]. Therefore, advanced separation methods, e.g., extraction chromatography, solvent extraction, or the most widely used cation exchange chromatography, are used to reach an appropriate purity level. These sophisticated strategies also increase the production cost. Furthermore, the overall production setup is associated with the drawback of generating considerable quantities of radioactive waste. As a result, the indirect pathway remains the most expensive approach. Nonetheless, ongoing research is directed toward enhancing this method, with particular emphasis on optimizing the purification stage and improving the recovery and recycling of irradiated target materials[136].

II. B. 2. Direct production pathway [^{176}Lu(n,γ)^{177}Lu]

The direct production pathway is also known as carrier-added. It consists in irradiating a target made of lutetium-176 to give ^{177}Lu (Equation 2). After irradiation, the radiochemical process involves the production of [^{177}Lu]$LuCl_3$ through the dissolution of the irradiated target material in diluted mineral acids. This makes the overall production process relatively straightforward to implement[137]. Since ^{177}Lu is produced directly thanks to irradiation, the yield of the reaction and the final specific activity depend directly on the flux of neutrons.

Equation 2: Nuclear reaction of ^{177}Lu production through the direct production pathway

$$^{176}Lu + n \rightarrow {}^{177}Lu + \gamma$$

To enhance the yield of nuclear reactions and avoid the formation of unwanted radionuclides, the target is enriched up to 80 % with ^{176}Lu that possesses a high neutron capture cross-section (~2100 barns). The [^{176}Lu]Lu_2O_3 target is stable under the irradiation conditions, and its post-irradiation processing is relatively easy and fast. In comparison to the non-carrier-added pathway, with this method, only 1 mg of the target material is needed to produce approximately 50 clinical doses of ^{177}Lu with an acceptable specific activity[138]. Generally, it is easy to adjust the production depending on the requirement by simply adjusting the target size.

---

[135] Park, U.J., J.-S. Lee, K.H. Choi, S.S. Nam, K.H. Yu *Applied Radiation and Isotopes* **2016** 115 8-12.

[136] Morris, A.A., T. Wei, Z. Wang, Y. Xia, M. Han, Y. Lu *EJNMMI radiopharmacy and chemistry* **2025** 10 56.

[137] Chakravarty, R., S. Chakraborty *Am. J. Nucl. Med. Mol. Imaging* **2021** 11 443-475.

[138] Dash, A., M.R.A. Pillai, F.F. Knapp *Nuclear Medicine and Molecular Imaging* **2015** 49 85-107.

The obtained ^{177}Lu usually shows specific activities around 740–1110 GBq mg^{-1}, so approximately 25% of the theoretical maximum value, meaning that 75% of the atoms in the sample are stable isotopes[139]. This value is still suitable for biomedical applications, but because of the natural decay of ^{177}Lu, the specific activity of the sample also decays through time, and it might be lower when the sample reaches the patient.

During irradiation, a side reaction can occur and lead to the metastable isotope ^{177m}Lu that will follow a β-decay with a half-life of 160 days[140]. This long half-life can create waste management problems. Fortunately, the low neutron absorption cross-section and the low activity level of this isotope compared to ^{177}Lu make it insignificant at clinical doses.

Despite some limitations, the direct production pathway is preferred by hospitals since it is the most cost-effective synthesis to produce ^{177}Lu of good quality and with high availability.

III. State of the art on application of ^{177}Lu for radiotherapy

Among various radioisotopes available for biomedical applications, ^{177}Lu is becoming more popular, especially after approval of the first lutetium-based anticancer drugs [^{177}Lu]Lu-DOTA-TATE and [^{177}Lu]Lu-PSMA-617, both for targeted radionuclide therapy. Due to ^{177}Lu physicochemical and decay properties it is the most represented theranostic radionuclide in clinical trials with 168 trials, mostly phase I and II, currently underway[141].

In addition, many other studies at less advanced stages explore the possibilities given by this isotope in cancer treatment. In 2020, Mackenzie *et al.* studied the effect of combining radioimmunotherapy and immunotherapy on melanoma in mice[142]. The study aimed to enhance tumoricidal effects of treatments using a humanized anti-melanin antibody h8C3 radiolabeled with ^{177}Lu and ^{225}Ac (α-emitter, $t_{1/2}$ = 9.9 days) as medium-long half-life therapeutic agents together with an immune checkpoint blockade (ICB) agent called anti-PD-1. In this study, two activities of ^{177}Lu (3.7 and 7.4 MBq) were administered to mice and are defined as “low” and “high” doses, respectively. Doses were either injected once or three times depending on the group and with or without the anti-PD-1 ICB.

Injections of different radiolabeled formulations showed only a moderate effect with no significant differences between low and high doses. The results obtained with ICB alone are also moderate but significant compared to the control, with an extension of the overall survival of mice. It is worth mentioning that severe toxic effects on mice were observed (weight loss and a decrease in the number of red and white blood cells without recovery) at

---

[139] Dash, A., M.R.A. Pillai, F.F. Knapp *Nuclear Medicine and Molecular Imaging* **2015** 49 85-107.

[140] Canella, L., M.L. Bonardi, F. Groppi, E. Persico, C. Zona, E. Menapace, Z.B. Alfassi, M. Chinol, S. Papi, G. Tosi *Journal of Radioanalytical and Nuclear Chemistry* **2008** 276 813-818.

[141] Tran, H.H., A. Yamaguchi, H.C. Manning *European Journal of Nuclear Medicine and Molecular Imaging* **2025** 52 2685-2709.

[142] Malo, M.E., *et al., International Journal of Molecular Sciences* **2020** 21 8721.

higher dose of ^{177}Lu radiolabeled antibody. However, combination of anti-PD-1 ICB and low-dose of ^{177}Lu radioimmunotherapy led to reduced tumor growth and an increase in survival of mice up to 46 days, highlighting a significant synergistic effect. This study shows the potential application of ^{177}Lu-radiolabelled antibodies for radioimmunotherapy combined with classical immunotherapy.

Another strategy to locally enhance radiotoxicity of ^{177}Lu is to combine it with a radiosensitizing agent, especially gold nanoparticles. One of the first applications of a ^{177}Lu-gold nanohybrid in cancer radiotherapy was reported in 2012 by Ferro-Flores and colleagues[143]. They developed a multimeric platform consisting of ^{177}Lu-labeled gold nanoparticles (AuNPs) conjugated to cyclic RGD peptides which specifically bind to $\alpha_v\beta_3$ integrins, proteins frequently overexpressed in various carcinomas. The nanoparticle surface was functionalized with thiol-containing RGD peptides for tumor targeting and cysteine-DOTA for lutetium chelation. This ^{177}Lu-AuNP-RGD nanohybrid was administered *via* intraperitoneal injection in mice bearing U87MG tumors and demonstrated some degree of tumor targeting (Figure 27). Although radioenhancement effect was not explicitly investigated, the absorbed radiation dose delivered to the tumor was measured at 0.35 Gy per MBq of injected activity.

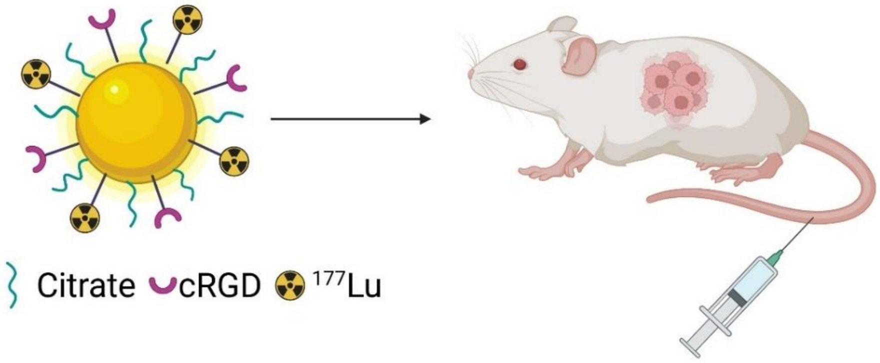

Figure 27: Combination of AuNP and ^{177}Lu for internal radiotherapy

Later, Reilly and colleagues investigated ^{177}Lu-AuNP nanohybrids as a neoadjuvant approach for radiotherapy of locally advanced breast cancer[144]. In this context, neoadjuvant brachytherapy refers to use of brachytherapy as the initial treatment, followed by locoregional therapy based on the extent of residual tumors. The gold nanoparticles were functionalized with polyethylene glycol (PEG) chains functionalized with terminal DOTA for ^{177}Lu chelation, and with panitumumab, a monoclonal antibody targeting the epidermal growth factor receptor (EGFR). To ensure colloidal stability and prevent aggregation, a saturating amount of simple 2 kDa PEG molecules was necessary for surface coating. The ^{177}Lu-AuNP-panitumumab constructs were administered *via* intratumoral injection in mice

---

[143] Hao, G., X. Sun, Q.N. Do, B. Ocampo-García, A. Vilchis-Juárez, G. Ferro-Flores, L.M. De León-Rodríguez *Dalton Transactions* **2012** 41 14051.

[144] Yook, S., Z. Cai, Y. Lu, M.A. Winnik, J.-P. Pignol, R.M. Reilly *Journal of Nuclear Medicine* **2016** 57 936-942.

bearing subcutaneous EGFR-positive MDA-MB-468 human breast cancer cells. Biodistribution and SPECT/CT imaging were used to assess tumor versus normal tissue localization. The targeted nanohybrid was compared to a non-targeted counterpart lacking panitumumab. Tumor radioactivity levels were high at 1-hour post-injection but declined two- to three-fold within 48 hours. Uptake in non-target organs was minimal, except for liver and spleen, and no signs of toxicity were observed (local radiation doses < 1 Gy). A treatment dose of 4.5 MBq (equivalent to 6×10^{11} gold nanoparticles) resulted in sustained tumor growth arrest for over 90 days and extended survival up to 120 days. The corresponding radiation-absorbed dose to the tumor ranged between 20 and 30 Gy. Previous *in vitro* studies by the same group showed that targeted nanohybrids exhibited strong EGFR binding, efficient cellular internalization, and pronounced cytotoxicity in EGFR-overexpressing breast cancer cells, with limited efficacy in low-EGFR cells[145]. However, *in vivo*, EGFR targeting did not translate into improved tumor retention or enhanced radiation dose delivery, as both targeted and non-targeted ^{177}Lu-AuNPs were similarly effective in treating breast cancer xenografts. These findings suggest that, for intratumoral injection, simpler, non-targeted nanohybrids could be broadly applicable to a wider range of breast cancer phenotypes, challenging the added value of EGFR-targeting and offering a more clinically feasible alternative.

Reilly and colleagues also investigated ^{177}Lu-labelled gold nanoparticles as a neoadjuvant therapy for HER2-positive breast cancer[146]. In this study, trastuzumab, a monoclonal antibody targeting the human epidermal growth factor receptor 2 (HER2), was conjugated to ^{177}Lu-AuNPs, forming a hybrid nanoconstruct similar to their earlier EGFR-targeted designs. *In vitro* assays demonstrated that ^{177}Lu-AuNP-trastuzumab selectively interacted with HER2-positive MDA-MB-361 cells and was approximately 2.5 times more effective than non-targeted ^{177}Lu-AuNPs in reducing clonogenic survival and inducing DNA double-strand breaks following exposure to 20 $\mathrm{MBq\,mg^{-1}}$ Au. The therapeutic potential of these nanohybrids was further evaluated *in vivo* by intratumoral injection in mice bearing MDA-MB-361 xenografts. Each animal received a single dose of 3 MBq (equivalent to 0.15 mg AuNPs or 5.5×10^{11} particles), and tumor growth was monitored over 16 days. The tumor growth index in the group treated with ^{177}Lu-AuNP-trastuzumab was significantly reduced by 1.7- and 2.2-fold compared to animals treated with non-targeted ^{177}Lu-AuNPs or left untreated, respectively. Unlike previous studies involving panitumumab-functionalized nanohybrids for EGFR-positive tumors, these trastuzumab-conjugated constructs did not achieve complete tumor growth inhibition. Nonetheless, the presence of the targeting antibody enhanced the therapeutic index, showing superior *in vivo* efficacy compared to non-targeted nanohybrids.

---

[145] Yook, S., Z. Cai, Y. Lu, M.A. Winnik, J.-P. Pignol, R.M. Reilly *Molecular Pharmaceutics* **2015** 12 3963-3972.

[146] Cai, Z., *et al.*, *Pharmaceutical Research* **2017** 34 579-590.

Based on the known association between resistance to HER2-targeted therapies and compensatory upregulation of EGFR, the group further developed a dual-targeting ^{177}Lu-AuNP nanomedicine[147]. These constructs were functionalized with both trastuzumab (for HER2) and panitumumab (for EGFR), and tested *in vitro* on breast cancer cell lines overexpressing either HER2, EGFR, or both receptors. As expected, single-antibody-conjugated ^{177}Lu-AuNPs bound selectively to cells expressing the corresponding target receptor. In contrast, the dual-antibody ^{177}Lu-AuNP-trastuzumab-panitumumab hybrid demonstrated effective binding across all cell types, including those co-expressing HER2 and EGFR. Notably, this dual-targeted system was more efficient at delivering high radiation doses to the nuclei of HER2/EGFR co-expressing cells, outperforming both single-receptor-targeted hybrids and the non-targeted counterpart.

Based on the above short overview, it seems that ^{177}Lu is a promising radioisotope that can be combined with different carriers depending on the desired application. The association of ^{177}Lu with gold nanoparticles shows some potential but could still be improved, particularly to simultaneously counteract hypoxia. Therefore, combination of therapeutic properties of ^{177}Lu with the characteristics of our gold nanoparticle-loaded perfluorinated micelles represents an innovative strategy for enhanced targeted radionuclide therapy. This approach may provide multiple benefits, including radioenhancement and radiosensitization effects, improved tumor re-oxygenation, particularly in hypoxic environments, and at the end of the day a potential synergistic therapeutic effect.

---

[147] Yook, S., *et al.*, *Molecular Pharmaceutics* **2020** 17 1226-1236.

Results

IV. Introduction of the radioisotope to the micelles

IV. A. Synthesis of a new amphiphilic unit

The previously described PFTD-PEG micellar assembly (see chapter 1) does not allow radiolabeling with ^{177}Lu. The introduction of a chelating agent such as DOTA is needed for the complexation of lutetium ions. DOTA was chosen as it is known to form very stable lanthanide complexes[148]. To introduce this moiety at the surface of the micelles, the synthesis of a new amphiphilic unit was developed, with DOTA as the hydrophilic head while keeping the perfluorinated tail to maintain the structural integrity and self-assembly characteristics of the micellar formulation (Scheme 2). This amphiphile will be used in mixed-formulations together with the micelle-structuring PFTD-PEG amphiphile.

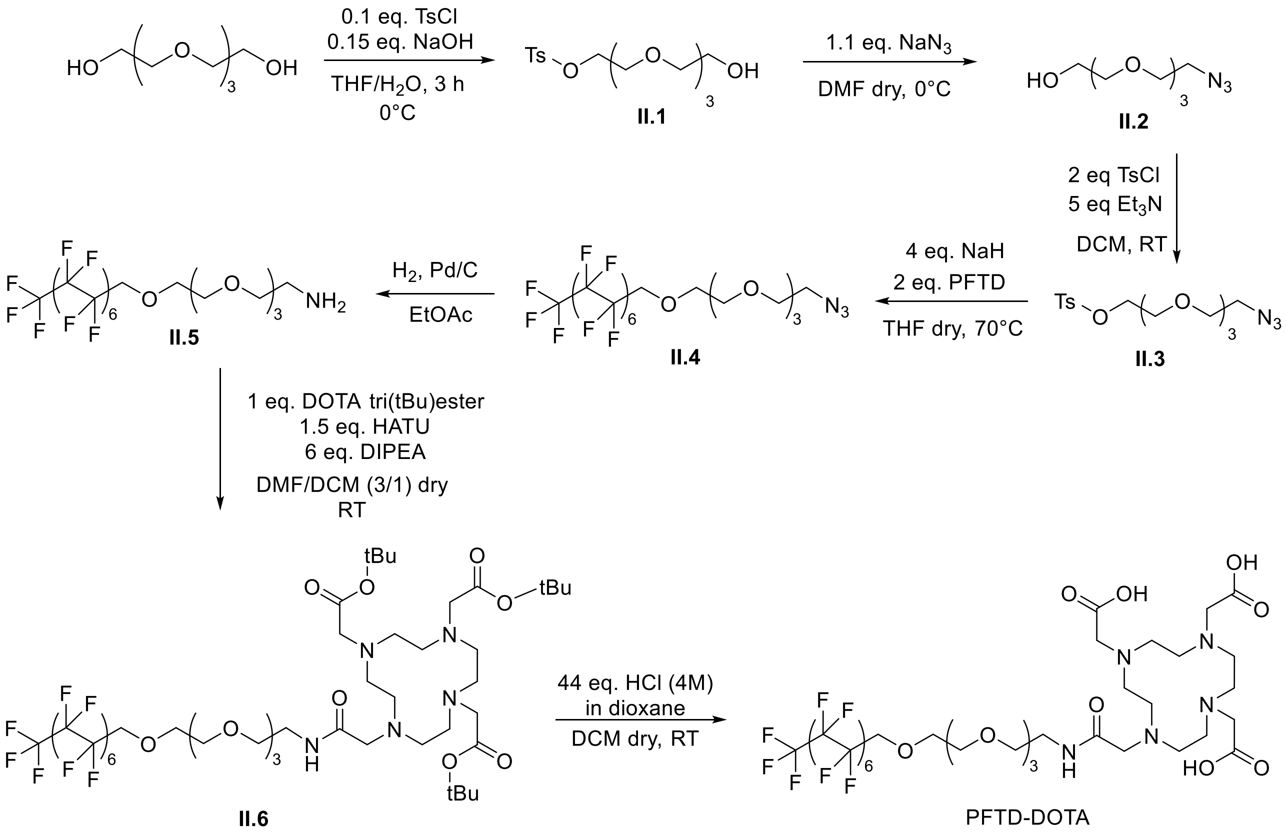

Scheme 2: Synthesis of PFTD-DOTA amphiphilic unit

The first steps of the synthesis consist in the activation of one (out of two) of the hydroxyl groups of tetra(ethylene glycol) as a tosylate (compound **II.1**), and treatment with NaN_3 to introduce an azido group. Activation of the remaining alcohol as a tosylate (compound **II.2**), followed by nucleophilic substitution with perfluorotetradecanol under basic conditions,

---

[148] Häussinger, D., J. Huang, S. Grzesiek *Journal of the American Chemical Society* **2009** 131 14761-14767.

leads to compound **II.4**. The azide group of **II.4** was then reduced under hydrogenation conditions, affording amine **II.5** that was subsequently involved in a pseudo-peptidic coupling with tri-*tert*butyl-protected DOTA ester to give product **II.6**. Finally, deprotection of the carboxylic groups of **II.6** under acidic conditions led to formation of the expected PFTD-DOTA amphiphilic unit. After synthesis, the amphiphilic unit was purified on NAP25 exclusion chromatography column with ultrapure water as eluent to remove the salts formed during the deprotection step. The PFTD-DOTA amphiphile was collected and lyophilized to obtain the compound as a solid form.

Following the synthesis of the DOTA-functionalized amphiphilic unit, a formulation study with PFTD-PEG micelles was performed. The two amphiphilic components, as solid powder, were combined in a 9:1 PFTD-PEG/PFTD-DOTA ratio, dispersed in ultrapure water, and subjected to ultrasonic treatment (ultrasonic tip 40% power, 3 min) to produce mixed PFTD-PEG/PFTD-DOTA micelles. Dynamic light scattering (DLS) analysis demonstrated that the incorporation of the PFTD-DOTA unit did not alter micelle size relative to simple PFTD-PEG micelles, indicating that the modification does not interfere with micellar dimensions that were measured at 11 nm. Moreover, the mixed micelles could also be reproducibly prepared within 15 min using an ultrasonic bath, a practical advantage when handling radioactive solutions, as it minimizes the risk of contamination. The availability of the DOTA-functionalized unit enabled us to further investigate the radiolabeling of micelles with ^{177}Lu**.**

IV. B. Radiolabeling of the fluorinated micelles with ^{177}Lu

IV. B. 1. Radiolabeling with ^{177}Lu and micelles formulation

The complexation of a lanthanide with DOTA at room temperature is a lengthy process that can take up to weeks to create the thermodynamically stable complex. In 2004, Aplincourt *et al.* described the three-phase mechanism of this reaction (Figure 28)[149]. The first step is the formation of the so-called “out-of-cage” complex $[LnH_2(DOTA)]^+$ at the very beginning of the reaction. This is a relatively fast process. In this complex, two protons are on two opposite nitrogen atoms and pointed towards the center of the cavity, while the Ln^{3+} ion is bound to the four oxygen atoms of the carboxylic groups, outside of the cage. At this point, the Ln^{3+} is not yet inserted into the macrocyclic cavity. To reach the lanthanide coordination number, five water molecules are involved in the complex (not shown).

---

[149] Moreau, J., E. Guillon, J. Pierrard, J. Rimbault, M. Port, M. Aplincourt *Chemistry – A European Journal* **2004** 10 5218-5232.

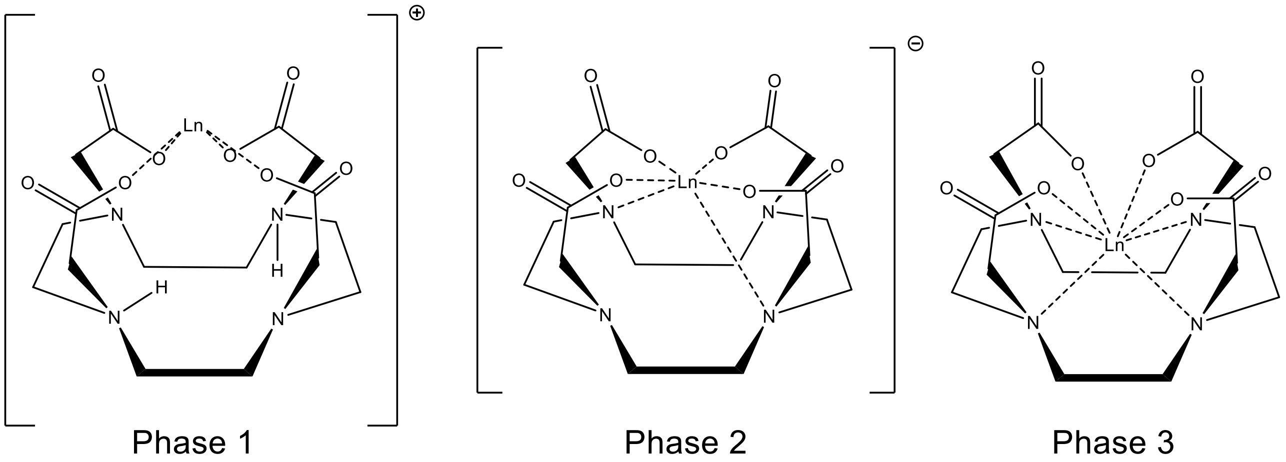

Figure 28: The three phases of the complexation of a lanthanide with DOTA

During the second phase, a concerted mechanism is observed: the simultaneous migration of two protons from nitrogen to carboxylate, where they become more accessible for a base (OH^-) to be removed from the complex. At the same time, two Ln-N bonds are formed by exchange of two water molecules and the lanthanide slowly enters the complexing cage. In the end, the lanthanide is still bound with four oxygen atoms of the carboxylate groups, three water molecules, and two new bonds with nitrogen atoms are formed in the $[Ln(DOTA)]^-$ complex. This is the slowest part of the complexation in which temperature and pH have a strong influence on the rate of reaction. Heating of the reaction speeds-up this step. Finally, the third step consists in a concerted rearrangement to form the last two Ln-N bonds with the release of two water molecules from the complex, leaving only one water molecule to complete the coordination sphere of the lanthanide. This step is faster than the second step but still slower than the first, and is crucial as it determines the final kinetic inertness and stability of the complex.

Since the kinetics of the reaction at room temperature is slow, most procedures for lanthanide radiolabeling often involve heating up to 80 °C for at least 30 min and using a pH 5 buffer to accelerate the formation of a thermodynamically stable complex[150].

IV. B. 2. Complexation of ^{177}Lu to PFTD-DOTA

All the radiolabeling studies presented thereafter were done at the NCBJ institute, in Poland, where the ^{177}Lu source is produced in the Maria Reactor through the carrier-added pathway. ^{177}Lu is provided as $[^{177}Lu]LuCl_3$ in diluted hydrochloric acid solutions (0.05 M), with an average specific activity of 850 GBq mg^{-1}.

For the labeling of our micelles with lutetium-177, we mainly have two options: either labeling of the PFTD-DOTA amphiphile and further assembly into micelle, or direct labeling of the preformed micelle containing a mixture of simple and complexing amphiphiles. Direct

---

[150] Häussinger, D., J. Huang, S. Grzesiek *Journal of the American Chemical Society* **2009** 131 14761-14767.

labelling with ^{177}Lu of the preformed micelle made of a 9:1 PFTD-PEG/PFTD-DOTA ratio under thermally activated conditions was not conclusive as we observed a sluggish reaction that could not be readily purified. It was therefore decided to investigate in depth the radiolabeling of the PFTD-DOTA amphiphilic unit itself before its assembly into micelles.

With the objective of finding the best reaction conditions and to ensure optimal attachment of ^{177}Lu to the DOTA complexing unit of the amphiphile, a set of reactions was implemented with fixed lutetium activity levels (20, 100 or 300 MBq) but with increasing equivalents of PFTD-DOTA ranging from 1 to 200 equiv. Briefly, [^{177}Lu]LuCl$_3$ was diluted in pH 5 acetate buffer and the PFTD-DOTA amphiphilic unit was added to the mixture. The resulting solution was heated up to 80 °C for 30 min before being allowed to cool down to room temperature and further analyzed.

The radiochemical yields (RCY) were determined by instant thin layer chromatography (iTLC). The curve representing RCY against the number of added equivalents of PFTD-DOTA was plotted (Figure 29). For example, for 30 equiv. of the PFTD-DOTA amphiphile, we observed that 20 MBq activity provided 45% RCY while the use of 100 and 300 MBq permitted to reach better (ca. 70%) RCY. The effect of added activity becomes negligible beyond 50 equiv. of PFTD-DOTA, as indicated by the plateau observed from this point onward and the steady radiochemical yields of approximately 90%.

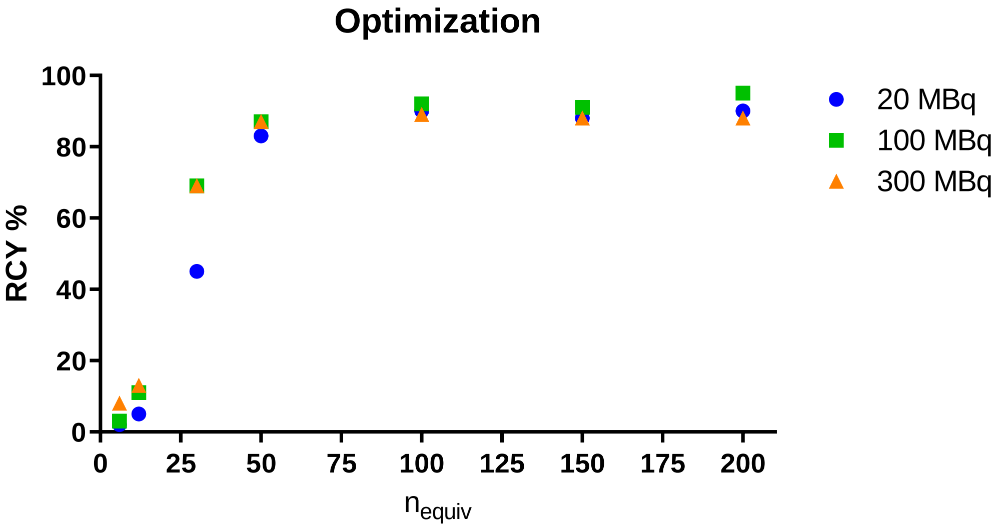

Figure 29: Optimization of the radiolabeling

Since the best RCY were obtained using 50 equiv. of PFTD-DOTA (*vs.* ^{177}Lu), these conditions were kept for the rest of the study for the preparation of larger-scale samples. The high yield observed in this reaction is consistent with the literature[151].

---

[151] Sharma, A.K., R. Sharma, K. Vats, H.D. Sarma, A. Mukherjee, T. Das, D. Satpati *Scientific Reports* **2022** 12 1572; Aslani, A., G.M. Snowdon, D.L. Bailey, G.P. Schembri, E.A. Bailey, N. Pavlakis, P.J. Roach *J Nucl Med Biol*. **2015** 3 107-15.

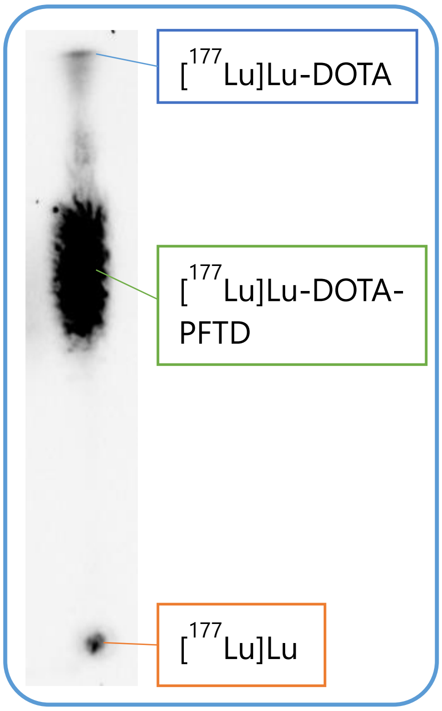

Figure 30: iTLC of PFTD-DOTA radiolabeling with ^{177}Lu

While analyzing the ^{177}Lu-labeled PFTD-DOTA amphiphile using a mixture of 5% NaCl/25% NH_3/MeOH (1:1:3) as the eluent solution for iTLC (Figure 30), we found out that the crude reaction mixture showed 3 spots:

1. a minor spot at the starting point of the iTLC (R_f = 0.0) that corresponds to traces of free [^{177}Lu]$LuCl_3$ which was hydrolyzed under basic ammonia conditions.
2. a major spot with R_f = 0.6 corresponding to the radiolabeled amphiphilic unit [^{177}Lu]Lu-DOTA-PFTD.
3. a minor spot, at R_f = 0.9, corresponding to $^{177}Lu^{3+}$ that is complexed by free DOTA (no longer attached to the PFTD unit)

The presence of free DOTA in the sample is surprising but could be explained by either remaining trace amounts of DOTA from the initial synthesis of the amphiphilic unit or by radiolysis of the amide bond of the PFTD-DOTA amphiphile under our complexation reaction conditions, releasing free DOTA and compound **II.5** (Figure 31).

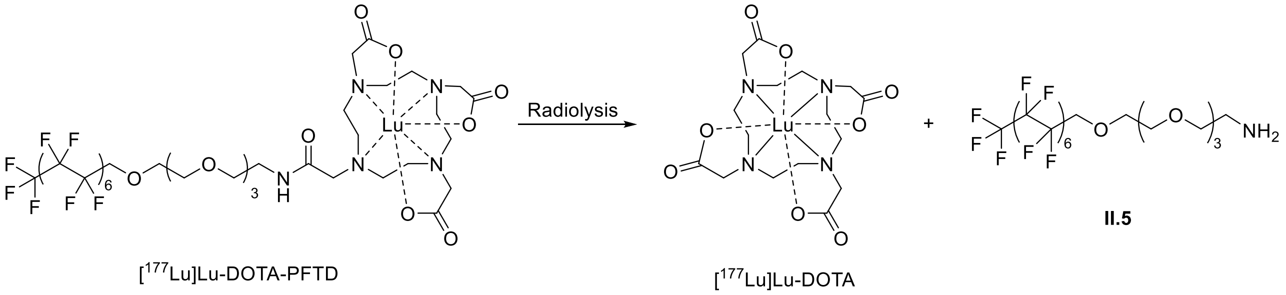

Figure 31: Proposed structure of the radiolysis products

The radiolabeled amphiphilic units were purified on a NAP25 exclusion chromatography column to remove free ^{177}Lu and its complex with DOTA. The purification profile of the amphiphiles appears to be reproducible and allows their separation from impurities. However, since the amphiphilic units are tailing on the column, not all the product could be collected with a satisfying purity since free [^{177}Lu]Lu-DOTA always ends up co-eluting with some fractions of the amphiphilic unit. Therefore, for each purification, only the fractions with a radiochemical purity (RCP) higher than 95 % were collected to be used further.

Post-radiolabeling of PFTD-DOTA, mixed micelles were readily formulated by sonication of structuring PFTD-PEG and labelled [^{177}Lu]Lu-DOTA-PFTD for 20 min in water, and in variable amounts, depending on the required activity of the [^{177}Lu]Micelle samples.

A closely related procedure was used to produce ^{177}Lu-labelled micelles containing gold nanoparticles ([^{177}Lu]AuNP@Micelles) by sonication in water of gold nanoparticles (already encapsulated in PFTD-PEG micelles) in the presence of [^{177}Lu]Lu-DOTA-PFTD. Before any biological evaluation of the nanometric carriers, the radiological stability of the supramolecular structure was tested.

IV. B. 3. Stability study of the radiolabeled micelles

The stability of the constructs was assessed using [^{177}Lu]Micelles in different media, including ultrapure water, phosphate-buffered saline (PBS), fetal bovine serum (FBS), and cell culture medium, at both room temperature and 37 °C. Stability was monitored by iTLC through measurement of the radiochemical purity (RCP) at various time points over a 10-day period of time. An activity of 10 MBq was selected as it represents a standard level for cellular studies. To investigate the effect of higher radioactivity on stability, an additional set of samples was prepared at 35 MBq activity. The study was conducted on purified [^{177}Lu]Lu-DOTA-PFTD samples, which were formulated with PFTD-PEG to generate [^{177}Lu]-labelled micelles. The resulting data provided curves illustrating the evolution of radiochemical purity over time (Figure 32).

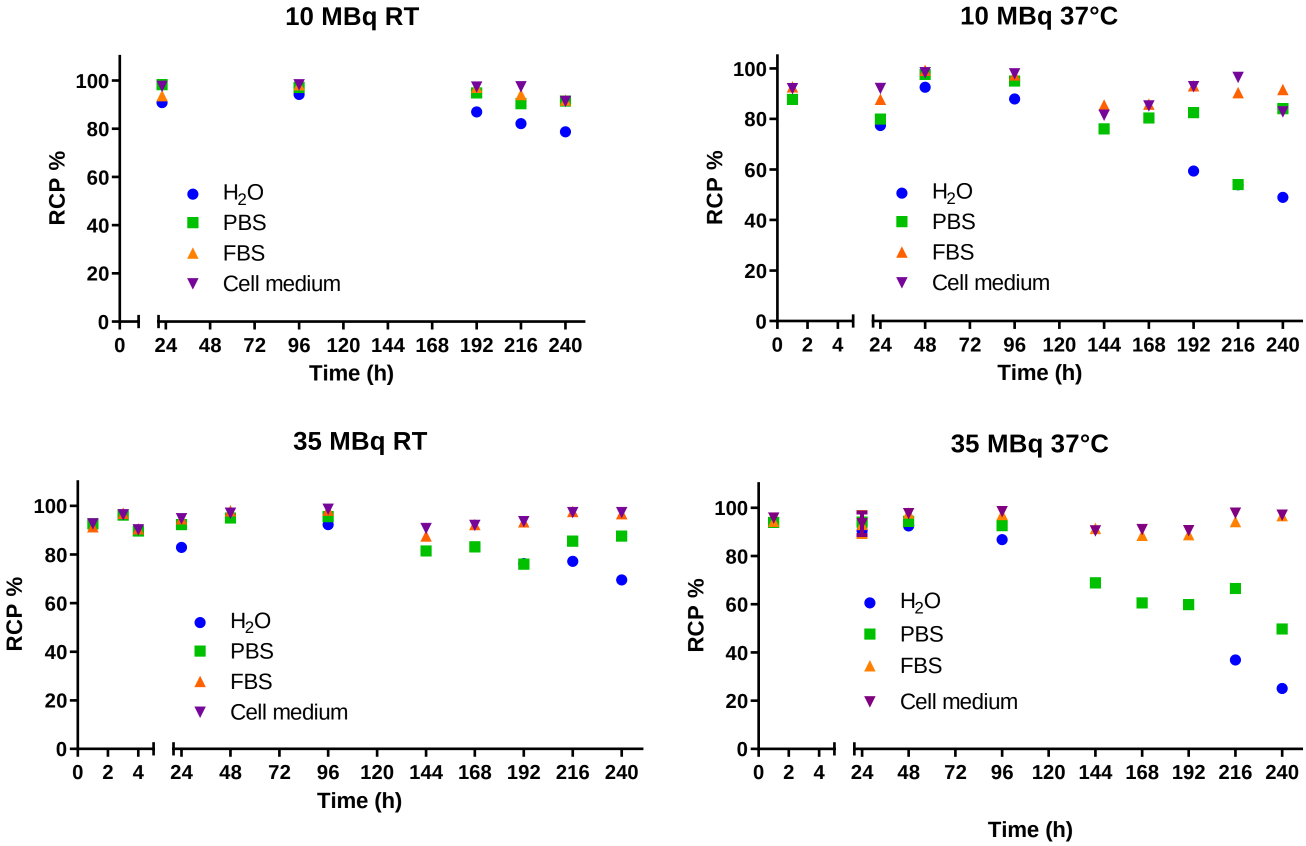

Figure 32: Stability study of [^{177}Lu]Micelles

At 10 MBq, the samples remain stable across all four media for up to 4 days (96 h), after which some degradation becomes noticeable, particularly in those incubated at 37 °C. A faster decrease in radiochemical purity was observed in water and PBS, likely due to ongoing radiolysis in these media. In contrast, degradation was less pronounced in FBS and cell culture medium, which can be attributed to the presence of proteins, albumins, and amino acids that act as scavengers, mitigating radiation-induced radical formation and thereby protecting the integrity of the amphiphilic units within the micelles. iTLC analysis further revealed a time-dependent decrease in the fraction of radioactivity associated with micelles, accompanied by an increase in detached [^{177}Lu]Lu-DOTA. This finding supports the hypothesis that radiolysis contributes to the gradual release of radiolabeled DOTA in solution. Notably, the release of free ^{177}Lu was minimal compared to [^{177}Lu]Lu-DOTA, confirming the high stability of the Lu-DOTA complex.

At 35 MBq, the samples also remained stable for up to four days. However, after this time point degradation occurred more rapidly in water and PBS, likely due to the increased radiation dose within the solution. Across both activity levels, temperature showed a pronounced effect on stability: for 10 MBq samples, degradation in water and PBS was below 30% at room temperature but exceeded 40% at 37 °C after 10 days.

Overall, these data confirm that the formulations remain stable for up to four days under the tested conditions. The minimal degradation observed in FBS and cell culture medium at 37 °C further supports the suitability of this formulation for subsequent biological evaluations, beginning with cytotoxicity studies.

IV. C. Toxicity studies of the radiolabeled micelles

As for the external irradiation experiment, cell studies were conducted on two cell lines, B16F10 and SKBR3, by MTS assay at three time points: 24, 48 and 72 h. A fresh batch of [^{177}Lu]Micelles and [^{177}Lu]AuNP@Micelles was produced for every test. We previously demonstrated that the non-radiolabeled samples (*i.e.,* Micelles and AuNP@Micelles) did not show any toxicity at all tested concentrations (0.004–1 mg mL^{-1}). The latter were used as negative controls. Comparisons of the cytotoxicity of [^{177}Lu]Micelles and [^{177}Lu]AuNP@Micelles with that of their respective non-labelled counterparts are presented in Annex 7 for B16F10 cell line, and Annex 8 for SKBR3.

Radioactive samples were prepared by serial dilution of a stock solution in the same manner as before for non-radioactive samples. With this method, the radioactivity level decreases with the concentration of micelles. The concentration range was chosen to match that of Micelles and AuNP@Micelles previously investigated and to have samples above and below the CMC of 0.06 mg mL^{-1}. The radioactivity range was selected to reach the maximum activity used for *in vitro* applications (*i.e.,*10 MBq), which is higher than the activity typically used on mice for *in vivo* studies (~5 MBq). Statistical analyses were done using a two-way ANOVA test.

IV. C. 1. Chronic radiotoxicity study on B16F10

In these experiments, the colloidal suspension was incubated with cells in a 96-well plate and cell survival was measured by the MTS assay at different time points. Of note, non-labelled Micelles and AuNP@Micelles exhibited no cytotoxicity in the range of concentrations studied. Also, B16F10 is a radioresistant cell line.

At 24 h, a slight radiotoxicity could already be seen for the two radiolabeled objects starting at 0.03 mg mL^{-1} in micelle concentration (Figure 33). A systematic additional effect of gold nanoparticles in [^{177}Lu]AuNP@Micelles could be detected, which, however, becomes less pronounced at higher concentrations and higher radioactivity levels.

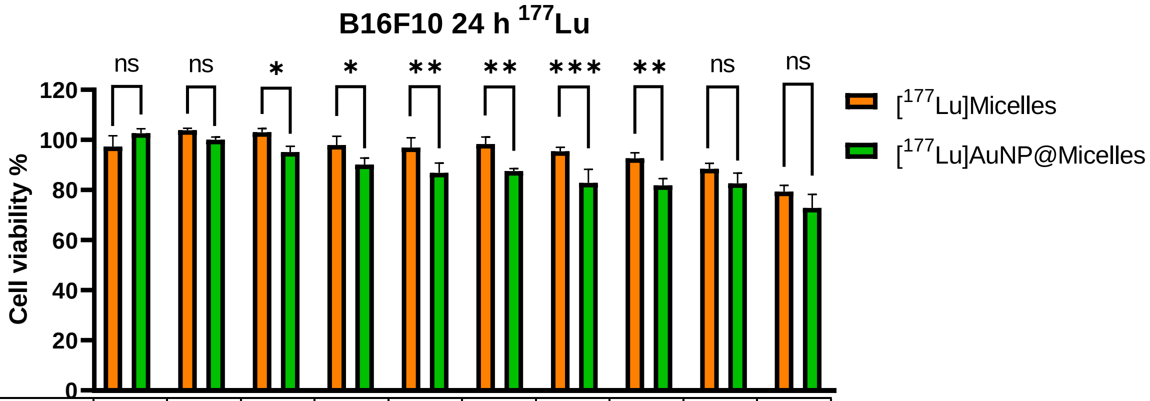

Micelles (mg/mL)	-	0.004	0.008	0.015	0.031	0.063	0.125	0.25	0.5	1
Au (µM)	-	-	-	-	-	-	-	-	-	-
	-	0.04	0.08	0.15	0.31	0.625	1.25	2.5	5	10
A (MBq)	-	0.04	0.08	0.15	0.31	0.625	1.25	2.5	5	10
	-	0.04	0.08	0.15	0.31	0.625	1.25	2.5	5	10

*Figure 33: B16F10 cell viability after 24 h incubation with [^{177}Lu]Micelles or [^{177}Lu]AuNP@Micelles, ns = non-significant * $p < 0.05$, ** $p < 0.01$, *** $p < 0.001$, **** $p < 0.0001$ (2-way ANOVA test), Results are plotted as mean ± SD*

At 48 h, cellular viability decreased more sharply for the two samples (Figure 34). This tendency is more important for concentrations higher than 0.063 mg mL^{-1}, where the micelles are fully assembled. Interestingly, [^{177}Lu]AuNP@Micelles are significantly more toxic than the [^{177}Lu]Micelles alone for all tested samples. The toxicity gap between both samples confirms the added value of gold in potentiating radiocytotoxicity. Cellular viability decreases with increasing radioactivity, leading to viability below 50% for both constructs at 10 MBq (1 mg mL^{-1}).

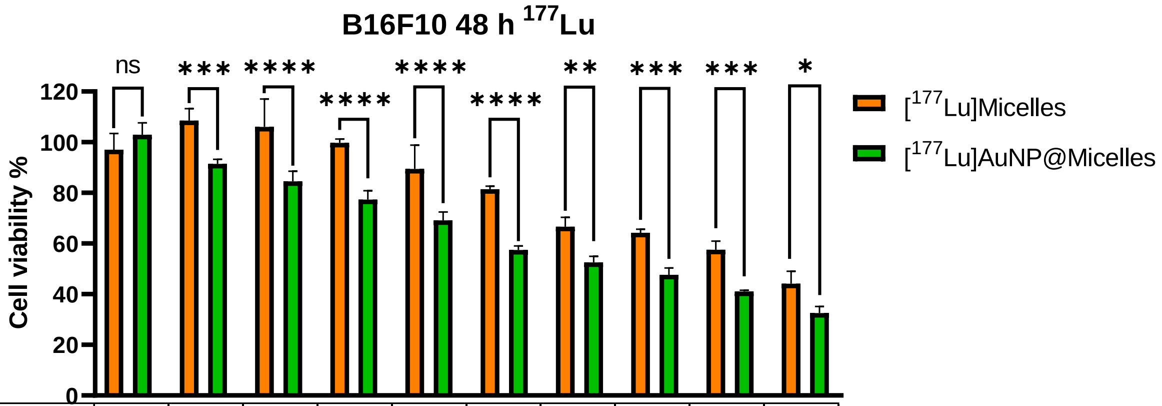

Micelles (mg/mL)	-	0.004	0.008	0.015	0.031	0.063	0.125	0.25	0.5	1
Au (µM)	-	-	-	-	-	-	-	-	-	-
	-	0.04	0.08	0.15	0.31	0.625	1.25	2.5	5	10
A (MBq)	-	0.04	0.08	0.15	0.31	0.625	1.25	2.5	5	10
	-	0.04	0.08	0.15	0.31	0.625	1.25	2.5	5	10

*Figure 34: B16F10 cell viability after 48 h incubation with, [^{177}Lu]Micelles or [^{177}Lu]AuNP@Micelles, ns = non-significant * $p < 0.05$, ** $p < 0.01$, *** $p < 0.001$, **** $p < 0.0001$ (2-way ANOVA test), Results are plotted as mean ± SD*

At 72 h, we observed nearly the same trend as for the 48 h experiments, with no additional radiotoxic effects on the cells, as cellular viabilities are in the same range for the two time points (Figure 35). This observation suggests that cells might have developed some advanced defense mechanisms, such as DNA repair, which could restore cell viability and counteract the effect of ^{177}Lu irradiation associated with nanometric carriers. However, [^{177}Lu]AuNP@Micelles are always more potent than [^{177}Lu]Micelles, suggesting a synergistic effect.

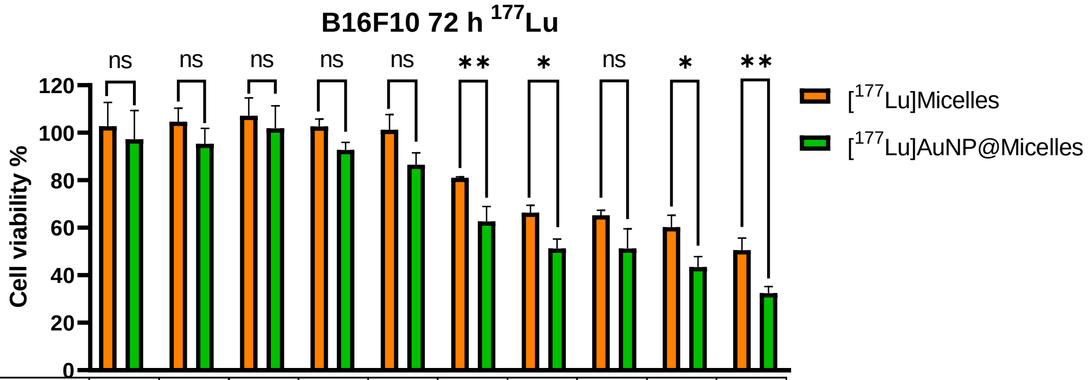

Micelles (mg/mL)	-	0.004	0.008	0.015	0.031	0.063	0.125	0.25	0.5	1
Au (µM)	-	-	-	-	-	-	-	-	-	-
	-	0.04	0.08	0.15	0.31	0.625	1.25	2.5	5	10
A (MBq)	-	0.04	0.08	0.15	0.31	0.625	1.25	2.5	5	10
	-	0.04	0.08	0.15	0.31	0.625	1.25	2.5	5	10

*Figure 35: B16F10 cell viability after 72 h incubation with [^{177}Lu]Micelles or [^{177}Lu]AuNP@Micelles, ns = non-significant * $p < 0.05$, ** $p < 0.01$, *** $p < 0.001$, **** $p < 0.0001$ (2-way ANOVA test), Results are plotted as mean ± SD*

In addition to the chronic radiotoxicity investigated above, acute effects were also looked on the B16F10 cell line.

IV. C. 2. Acute radiotoxicity study on B16F10

In these experiments, cells were incubated with radiolabeled nanocarriers in a 96-well plate for 24 h before the medium was removed and replaced with fresh cell culture medium. Cells were then further incubated and radiotoxicity (cell survival was measured by the MTS assay) was assessed 24 and 48 h (total exposure time 48 and 72 h, respectively). Of note, non-labelled Micelles and AuNP@Micelles exhibited no cytotoxicity in the range of concentrations studied.

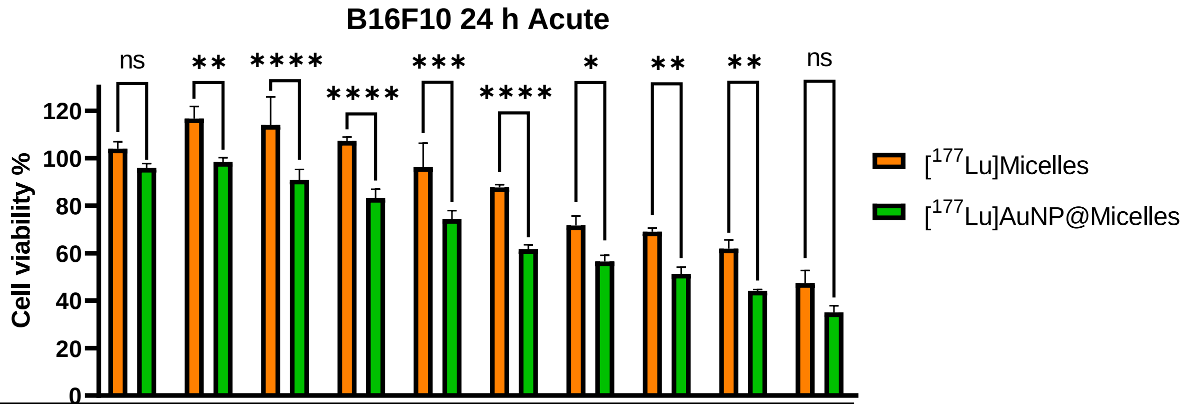

Micelles (mg/mL)	-	0.004	0.008	0.015	0.031	0.063	0.125	0.25	0.5	1
Au (µM)	-	-	-	-	-	-	-	-	-	-
	-	0.04	0.08	0.15	0.31	0.625	1.25	2.5	5	10
A (MBq)	-	0.04	0.08	0.15	0.31	0.625	1.25	2.5	5	10
	-	0.04	0.08	0.15	0.31	0.625	1.25	2.5	5	10

*Figure 36: B16F10 cell viability in acute toxicity after 24 h from removal of [^{177}Lu]Micelles or [1^{77}Lu]AuNP@Micelles, ns = non-significant * $p < 0.05$, ** $p < 0.01$, *** $p < 0.001$, **** $p < 0.0001$ (2-way ANOVA test), Results are plotted as mean ± SD*

At 24 h (corresponding to 48 h total exposure time, Figure 36), and 48 h (corresponding to 72 h total exposure time, Figure 37), no significant differences in radiocytotoxicity profiles could be detected in comparison with chronic exposure at the same time points (*i.e.*, 48 and 72 h). Levels of toxicity are in the same range for each of the concentrations/activities studied. Yet, [^{177}Lu]AuNP@Micelles are always more potent than [^{177}Lu]Micelles. The above observations on the lack of differentiated responses in chronic/acute exposures suggest that the active fraction of the nanometric carriers is the one that has been internalized in the intracellular compartment, and not the nanocarriers that remained outside of the cells in the medium. Therefore, the radiocytotoxic effect triggered by ^{177}Lu is only potent when in close contact with the cellular machinery. This could represent an advantage over more altering irradiation sources, as only the specific targeted area will undergo radiotherapeutic treatment, with little to no effect on non-targeted healthy areas.

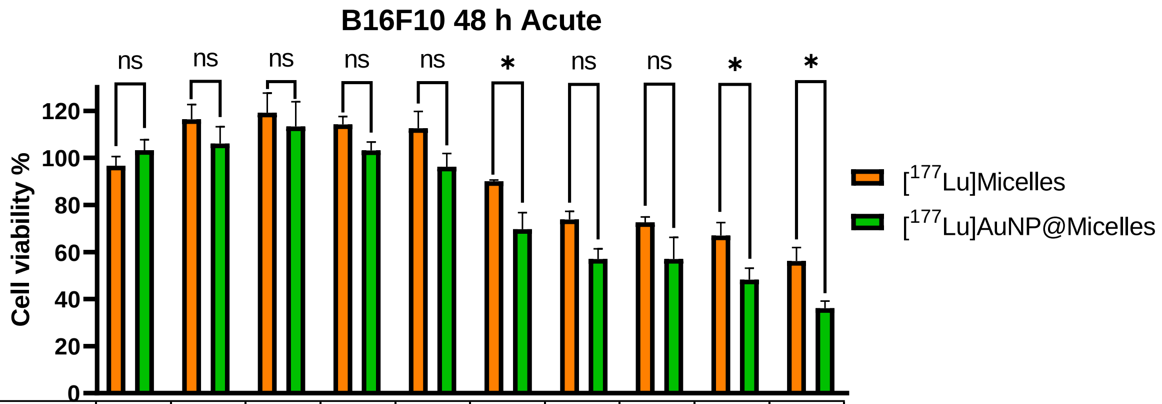

Micelles (mg/mL)	-	0.004	0.008	0.015	0.031	0.063	0.125	0.25	0.5	1
Au (µM)	-	-	-	-	-	-	-	-	-	-
	-	0.04	0.08	0.15	0.31	0.625	1.25	2.5	5	10
A (MBq)	-	0.04	0.08	0.15	0.31	0.625	1.25	2.5	5	10
	-	0.04	0.08	0.15	0.31	0.625	1.25	2.5	5	10

*Figure 37: B16F10 cell viability in acute toxicity after 48 h from removal of [^{177}Lu]Micelles or [^{177}Lu]AuNP@Micelles, ns = non-significant * $p < 0.05$, ** $p < 0.01$, *** $p < 0.001$, **** $p < 0.0001$ (2-way ANOVA test), Results are plotted as mean ± SD*

In addition to the radioresistant B16F10 cell line, radiocytotoxicity investigations were also conducted on the less radioresistant SKBR3 cell line under chronic exposure, as we demonstrated that the acute exposure does not bring any additional effects.

IV. C. 3. Chronic radiotoxicity study on SKBR3

The chronic radiotoxicity experiment on SKBR3 cells was performed through a procedure similar to that used for B16F10 cells. Briefly, the colloidal suspension was simply incubated with cells in a 96-well plate and cell viability was read at different time points. After the first 24 h, almost no toxicity was observed for [^{177}Lu]Micelles even at the highest activity level studied (Figure 39). However, [^{177}Lu]AuNP@Micelles exhibited some toxicity starting at low micelle concentration/lutetium activity (*i.e.*, 0.004 mg·mL^{-1}/0.04 MBq). Of note, large standard deviations were detected, especially for [^{177}Lu]AuNP@Micelles, which impacts statistical analysis.

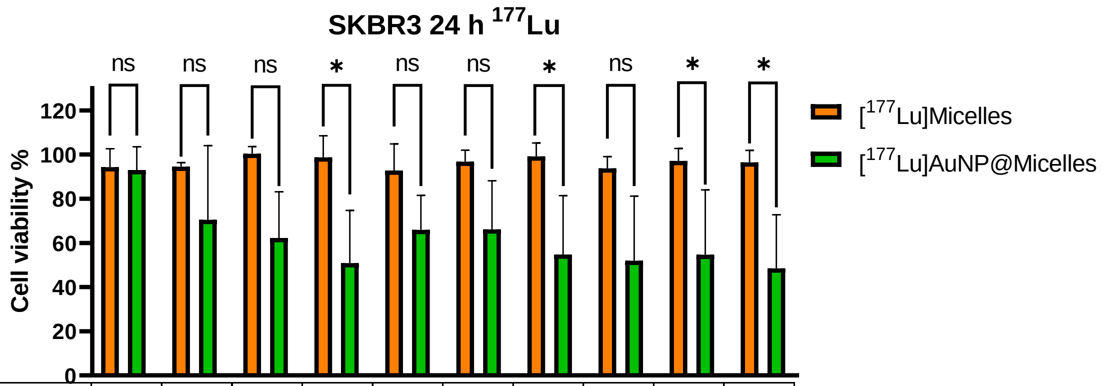

Micelles (mg/mL)	-	0.004	0.008	0.015	0.031	0.063	0.125	0.25	0.5	1
Au (µM)	-	-	-	-	-	-	-	-	-	-
	-	0.04	0.08	0.15	0.31	0.625	1.25	2.5	5	10
A (MBq)	-	0.04	0.08	0.15	0.31	0.625	1.25	2.5	5	10
	-	0.04	0.08	0.15	0.31	0.625	1.25	2.5	5	10

*Figure 38: SKBR3 cell viability after 24 h incubation with [^{177}Lu]Micelles or [^{177}Lu]AuNP@Micelles, ns = non-significant * $p < 0.05$, ** $p < 0.01$, *** $p < 0.001$, **** $p < 0.0001$ (2-way ANOVA test), Results are plotted as mean ± SD*

Surprisingly, the moderate radiotoxic effects observed at 24 h seem attenuated at 48 h, although a slight toxicity is observed for [^{177}Lu]Micelles at the highest concentration and activity levels (Figure 39). In fact, a more drastic effect was anticipated due to the less radioresistant nature of this cell line. Yet, the effect was recovered at 72 h with a more convincing dose-dependent response (Figure 40). [^{177}Lu]AuNP@Micelles were more potent than [^{177}Lu]Micelles with a three-fold superior effect at 1 mg mL^{-1}/10 MBq, and overall 90% decrease in cell viability, compared to controls without ^{177}Lu.

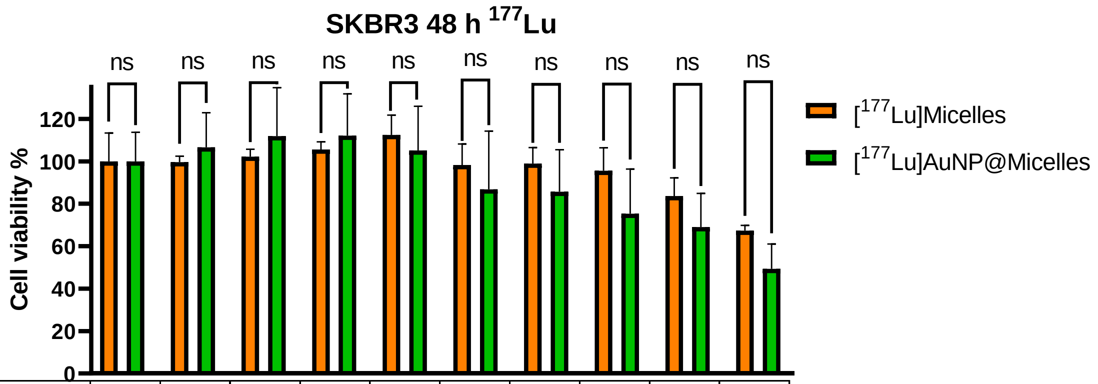

Micelles (mg/mL)	-	0.004	0.008	0.015	0.031	0.063	0.125	0.25	0.5	1
Au (µM)	-	-	-	-	-	-	-	-	-	-
	-	0.04	0.08	0.15	0.31	0.625	1.25	2.5	5	10
A (MBq)	-	0.04	0.08	0.15	0.31	0.625	1.25	2.5	5	10
	-	0.04	0.08	0.15	0.31	0.625	1.25	2.5	5	10

*Figure 39: SKBR3 cell viability after 48 h incubation with [^{177}Lu]Micelles or [^{177}Lu]AuNP@Micelles, ns = non-significant * $p < 0.05$, ** $p < 0.01$, *** $p < 0.001$, **** $p < 0.0001$ (2-way ANOVA test), Results are plotted as mean ± SD*

Taken together, the above results point out the radioenhancement effect of gold nanoparticles when associated to ^{177}Lu. The radiotoxicity studies conducted on both cell lines show a similar trend concerning the relative toxic effect of the two nanometric formulations. Gold nanoparticles could allow lower ^{177}Lu-radioactivity levels to produce a similar radiotoxic effect, compared to micelles. In order to evaluate the efficiency of both [^{177}Lu]Micelles and [^{177}Lu]AuNP@Micelles, their inhibitory concentration was calculated.

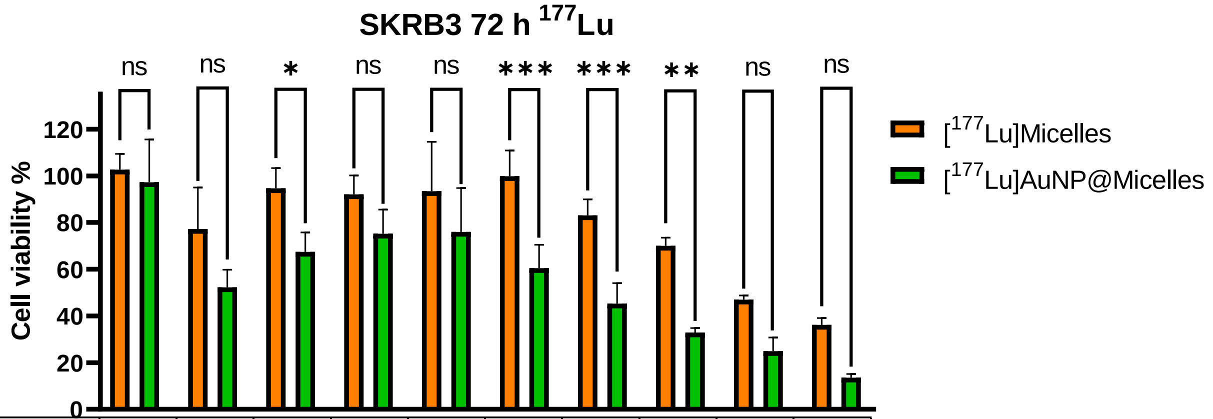

Micelles (mg/mL)		-	0.004	0.008	0.015	0.031	0.063	0.125	0.25	0.5	1
Au (µM)		-	-	-	-	-	-	-	-	-	-
		-	0.04	0.08	0.15	0.31	0.625	1.25	2.5	5	10
A (MBq)		-	0.04	0.08	0.15	0.31	0.625	1.25	2.5	5	10
		-	0.04	0.08	0.15	0.31	0.625	1.25	2.5	5	10

*Figure 40: SKBR3 cell viability after 72 h incubation with [^{177}Lu]Micelles or [^{177}Lu]AuNP@Micelles, ns = non-significant * $p < 0.05$, ** $p < 0.01$, *** $p < 0.001$, **** $p < 0.0001$ (2-way ANOVA test), Results are plotted as mean ± SD*

IV. C. 4. Half maximal inhibitory concentration determination

The half maximal inhibitory concentration (IC_{50}) is a pharmacological parameter that expresses the concentration of a compound required to achieve 50% of biological inhibition compared to an untreated negative control. This parameter is typically used in inhibition or cytotoxicity studies. Therefore, IC_{50} highlights the efficacy of a compound: the lower IC_{50} value, the more potent the compound. The determination of the IC_{50} value is based on the relationship between the concentration of the tested substance and the measured biological response which can typically be modelled using a nonlinear regression (Figure 41). Since the IC_{50} depends on many factors, including exposure time, cell type, and detection technique, it is a comparative parameter that must always be considered within a specific context.

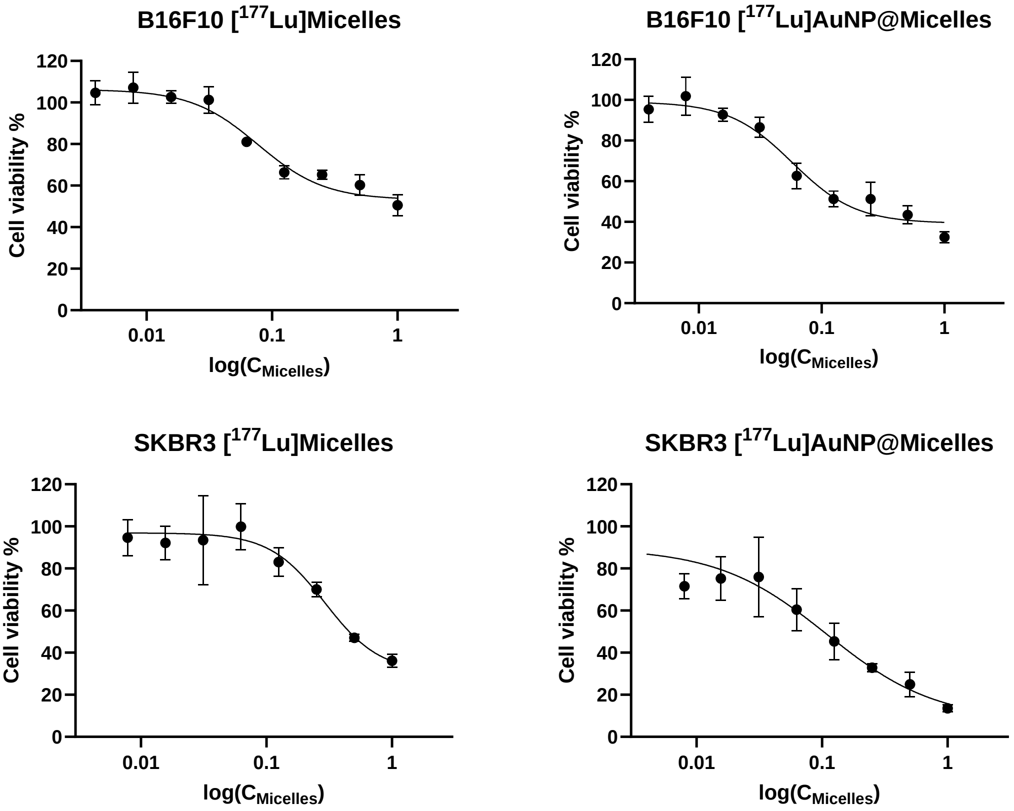

Figure 41: IC$_{50}$ determination for [^{177}Lu]Micelles and [^{177}Lu]AuNP@Micelles on B16F10 and SKBR3 cell lines after 72 h of incubation

We previously showed that unlabeled micelles and AuNP@Micelles are non-toxic to B16F10 and SKBR3 cell lines, in the entire concentration range investigated (*i.e.*, 0.004–1 mg mL^{-1}). However, their ^{177}Lu-radiolabeled counterparts significantly decrease cell viability, especially when combined with gold nanoparticles. The IC$_{50}$ of [^{177}Lu]Micelles and [^{177}Lu]AuNP@Micelles was calculated after 72 h of incubation with the two cell lines.

The IC$_{50}$ value was initially determined based on micelle concentrations, as this parameter is common to all samples. From these values, the corresponding radioactivity level and gold concentration were subsequently derived. In this study, however, defining a single IC$_{50}$ in terms of either activity or concentration alone is challenging. Instead, the IC$_{50}$ appears to be more representative of the overall formulation - comprising micelles, gold nanoparticles, and radioactive ^{177}Lu in fixed proportions - rather than of a single parameter such as radioactivity. All three values are thus reported in Table 6, with emphasis placed on the low radioactivity level associated with the IC$_{50}$.

For the B16F10 cell line, it was not possible to determine an IC$_{50}$ value for [^{177}Lu]Micelles, as the lowest cell viability reached was 50.5% at the highest tested micelle concentration/activity (1 mg mL^{-1}/10 MBq). Therefore, the IC$_{50}$ for this condition can only be assumed to exceed these values.

Table 6: IC$_{50}$ values for [^{177}Lu]Micelles and [^{177}Lu]AuNP@Micelles on B16F10 and SKBR3 cell lines

		B16F10	**SKBR3**
[^{177}Lu]Micelles	IC$_{50}$ [micelle]	> 1 mg mL^{-1}	0.48 mg mL^{-1}
	IC$_{50}$ [Au]	/	/
	Activity	**> 10 MBq**	**4.829 MBq**
[^{177}Lu]AuNP@Micelles	IC$_{50}$ [micelle]	0.14 mg mL^{-1}	0.10 mg mL^{-1}
	IC$_{50}$ [Au]	1.4 μM	1.0 μM
	Activity	**1.466 MBq**	**1.091 MBq**

The lower IC$_{50}$ values observed for [^{177}Lu]AuNP@Micelles in both cell lines highlight the synergistic radio-enhancement effect of gold in combination with the internal radiation emitted by the ^{177}Lu isotope. For example, in SKBR3 cells, the IC$_{50}$ of [^{177}Lu]AuNP@Micelles was 4.4-fold lower than that of [^{177}Lu]Micelles as regards MBq activity, and the difference between the two formulations was even more pronounced in B16F10 cells (6.8-fold). The more radioresistant nature of B16F10 cells, compared to SKBR3, could also be evidenced from this data set. For [^{177}Lu]Micelles, the SKBR3 cell line required at least two times lower activity levels (4.8 MBq) to produce the same radiotoxic effect as on B16F10 (> 10 MBq). For [^{177}Lu]AuNP@Micelles, this difference in activity was 1.4 times.

We can thus conclude that the incorporation of ^{177}Lu produced the expected cytotoxic effect with a clear radioenhancing contribution of gold nanoparticles. Based on these encouraging *in vitro* results, subsequent *in vivo* studies were carried out in mice using the radiolabeled micellar carriers.

IV. D. Biodistribution study on C57Bl/6 mice

In order to evaluate the pharmacokinetic parameters of our micelles containing gold nanoparticles, a biodistribution study was conducted on healthy C57Bl/6 mice. Since a previous biodistribution study was already performed by our group on empty PFTD-PEG micelles (radiolabeled with ^{89}Zr)[152], only the pharmacokinetics/biodistribution study of [^{177}Lu]AuNP@Micelles was conducted here. For this experiment, a fresh batch of [^{177}Lu]AuNP@Micelles was produced and injected on the same day to mice. Animal experiments were realized in collaboration with Agnieszka Kulesza, from POLATOM.

Animals were randomized into seven groups of 5 mice each. 100 μL of a micellar saline solution (10 mg mL^{-1}), corresponding to 6.02 MBq of activity, was intravenously injected in the tail vein. At chosen time points, *i.e.,* 1, 4, 8, 24, 48, 72 and 168 hours post-injection, animals were euthanized by cervical dislocation and dissected. Selected organs were resected, weighed and counted for their radioactivity. Accumulation of

---

[152] Godel-Pastre, S., E. Porcel, G. Pinna, M. Vandamme, C. Denis, C. Leterrier, E. Doris, C. Truillet, E. Gravel *ACS Applied Materials & Interfaces* **2024** 16 21557-21570.

[^{177}Lu]AuNP@Micelles in the different organs was expressed as the percentage of administered radioactivity per gram of tissue (%ID g^{-1}) (Figure 42).

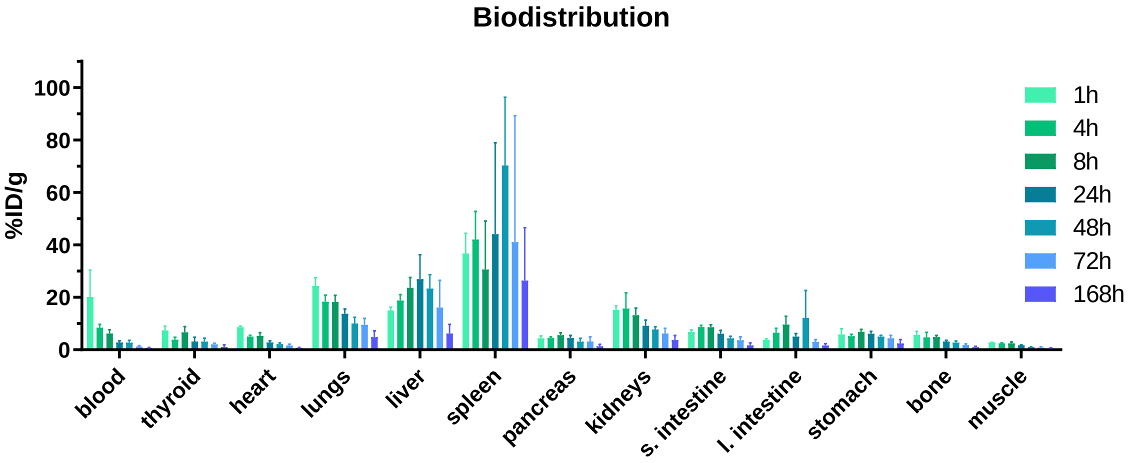

Figure 42: Biodistribution study of [^{177}Lu]AuNP@Micelles on C57Bl/6 mice

[^{177}Lu]AuNP@Micelles accumulated mainly in the liver and the spleen. If we consider the percentage of the injected dose per gram of tissue, the highest accumulation was found in the spleen which peaked at 48 h with 70.22 ± 26.06 %ID g^{-1}, before dropping to ca. 26 %ID g^{-1} at 168 h. A similar pattern was observed for the liver, however with a lower accumulated activity 23.31 ± 5.31 %ID g^{-1} at 48 h and ca. 6.20 %ID g^{-1} at 168 h. Accumulation in the liver area is classically observed with most nanometric carrier systems, as one of the physiological functions of the liver is to capture and eliminate particles for further clearance. Accumulation was transient and the level of radioactivity decreased with time and became negligible at 168 h (except for the spleen). In fact, hepatobiliary excretion was demonstrated by collecting the feces which revealed 21.36 ± 10.95 %ID at 24 h, and 25.02 ± 7.82 %ID at 48 h (see Annex 9).

For other organs and tissues, the level of accumulation was more moderate and decreased rapidly with time. Of note, we also detected some activity in the kidneys (15.21 ± 1.59 %ID g^{-1} at 1 h, decreasing to ca. 3.70 %ID g^{-1} at 168 h), suggesting urinary excretion of the nanoparticles. In fact, while negligible radioactivity was observed in urine immediately after administration, we observed a gradual and steady increase in cumulative urinary excretion over time. At 4 h post-injection, approximately 12% of the injected dose had been excreted, indicating the onset of renal clearance. The percentage of the compound excreted in the urine continued to rise, reaching approximately 40% at 72 h and 75.33 ± 12.59 %ID at 168 h (Annex 9). As the full nanoconstruct size is 16 nm, which is larger than the glomerular cut-off in kidneys, it is most likely that partial dissociation of the assembly is taking place. This led to the release of free amphiphilic units that could have been excreted though the urinary pathway.

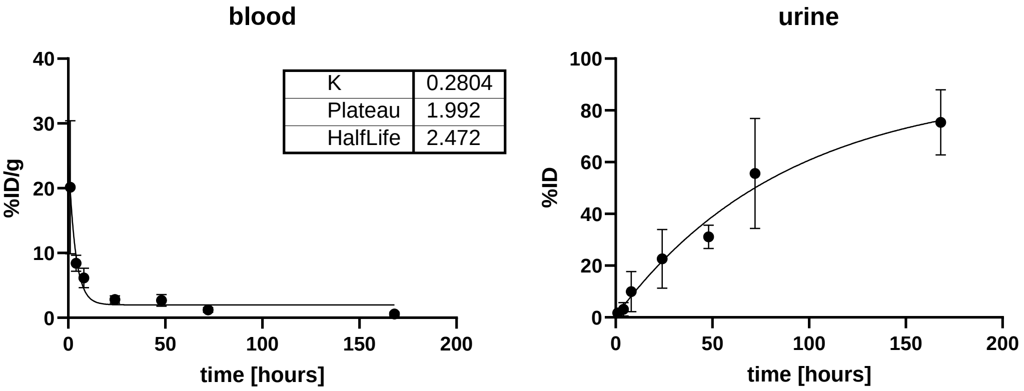

Figure 43: Blood clearance (right) and urine elimination (left) of [^{177}Lu]AuNP@Micelles

The pharmacokinetic parameters were determined using a one-phase exponential decay mode (Figure 43). At time zero, the compound reaches its highest concentration in the bloodstream and the radioactivity level detected in blood 1 h post-injection was 20.16 ± 10.27 %ID g^{-1}, which reflects systemic circulation of the radiolabeled micelles. However, a rapid decrease was observed over time, reaching 8.40 ± 1.24 %ID g^{-1} at 4 h. This initial drop is likely due to the rapid distribution of the [^{177}Lu]AuNP@Micelles to peripheral tissues and/or uptake by the mononuclear phagocyte system. Following this initial phase, the activity in the blood stabilizes, forming a plateau at approximately 2 %ID g^{-1}. This plateau suggests that a fraction of the compound remains in circulation, potentially due to slow release from tissue depots or continued equilibrium with peripheral compartments.

The half-life of the compound, calculated from the data, is approximately 2.5 h. This value indicates that half of the compound is cleared from the bloodstream within this timeframe, reflecting a relatively rapid elimination. The elimination rate constant (K) is 0.3 h^{-1}, further confirming the swift reduction in blood concentration during the initial phase.

Overall, the nanomicellar formulation demonstrated rapid clearance from blood circulation and accumulation in the liver and spleen, consistent with uptake by the reticuloendothelial system. Additional distribution to the lungs, kidneys, and gastrointestinal tract was also observed, with dual elimination *via* renal and hepatobiliary pathways. These results highlight the biphasic pharmacokinetic profile of the investigated compound: a rapid initial clearance from the bloodstream, followed by a much slower elimination phase. This behavior is characteristic of nanoparticle-based systems, which commonly undergo an initial distribution phase to organs such as the liver and spleen, subsequently followed by a more sustained circulation profile.

These observations are in slight contrast with those of “empty” PFTD-PEG micelles that were previously labeled with ^{89}Zr and studied by our group using PET imaging. The measured half-life of [^{89}Zr]PFTD-PEG micelles was 4.53 ± 1.18 h and the excretion pathway was mostly hepatobiliary. The different *in vivo* behavior of our gold containing micelles ([^{177}Lu]AuNP@Micelles) is therefore attributed to the presence of gold which can affect the size of the nanoconstruct, its density, and colloidal stability.

If one wants to achieve passive targeting of tumors using the EPR effect, that is the diffusion through leaky endothelium junctions of tumor blood vessels, prolonged circulation is needed to allow sufficient time for the carrier to reach its therapeutic target; however, this was not satisfactorily met in the present case. Also, the transient accumulation of [^{177}Lu]AuNP@Micelles in the spleen and liver after systemic administration could be problematic from a radiotoxic point of view. Given the pharmacokinetics and biodistribution of the micellar platform which was not fully optimal, we chose to implement direct intratumoral injection (nanobrachytherapy) as administration mode, rather than intravenous injection.

IV. E. Tumor retention in C57Bl/6 mice

By directly injecting micelles into the tumor, nanobrachytherapy allows to by-pass reticuloendothelial capture by macrophages. Moreover, the small size of the micellar platforms should facilitate their local diffusion within the tumor, promoting a uniform distribution of the radiation dose[153].

^{177}Lu-radiolabeled micelles were injected intratumorally to C57BL mice bearing subcutaneous syngeneic B16F10 tumors. Two different types of nanohybrid micelles were administered, either "empty" [^{177}Lu]Micelles (control group) or the same micelles but loaded with gold nanoparticles radioenhancers ([^{177}Lu]AuNP@Micelles). 30 µL of a concentrated colloidal suspension of the micelles (10 mg mL^{-1}), corresponding to 6 MBq ^{177}Lu activity, was injected directly in the tumor. Animals were monitored over 7 days at 24, 72 and 168 h. After each time point a few animals were sacrificed and the organs were collected for *ex vivo* analysis and counting. Results are expressed as the percentage of the injected dose. Results expressed in injected dose per mass of tissues can be found in Annex 10.

Key organs (tumor, liver, spleen) are also to be further analyzed soon by ICP-MS to check the co-localization of gold and the carrier amphiphiles after complete decay of the latter. To date, this analysis has not been possible due to the remaining contamination of the samples by radioactive materials.

The [^{177}Lu]Micelles exhibited high initial tumor retention at 24 and 72 h post-injection (69.8% and 65.8% of the injected dose (%ID), respectively) (Figure 44). However, tumor retention dropped significantly at 168 h post-injection, with only 26.3 %ID remaining in the tumor. The decrease of activity measured after intratumoral injection suggests that micelles are diffusing out of the tumor area and are entering the systemic circulation. In fact, we detected a concomitant accumulation of the micelles in peripheral organs such as the liver, which was the main organ in which micelles gathered after leaching out from the tumor.

---

[153] Terracciano, R., Y. Carcamo-Bahena, A.L.R. Royal, L. Messina, J. Delk, E.B. Butler, D. Demarchi, A. Grattoni, Z. Wang, V. Cristini, P. Dogra, C.S. Filgueira *Langmuir* **2022** 38 13983-13994.

In contrast, while [^{177}Lu]AuNP@Micelles demonstrated similar retention in the tumor at 72h (69 %ID), better long-term retention was measured at 168 h with 37.4 %ID. This value is significantly higher than in the [^{177}Lu]Micelles group (26.2 %ID). These findings suggest that gold nanoparticle encapsulation enhances the formulation robustness within the tumor microenvironment and delays its washout, potentially improving therapeutic efficacy.

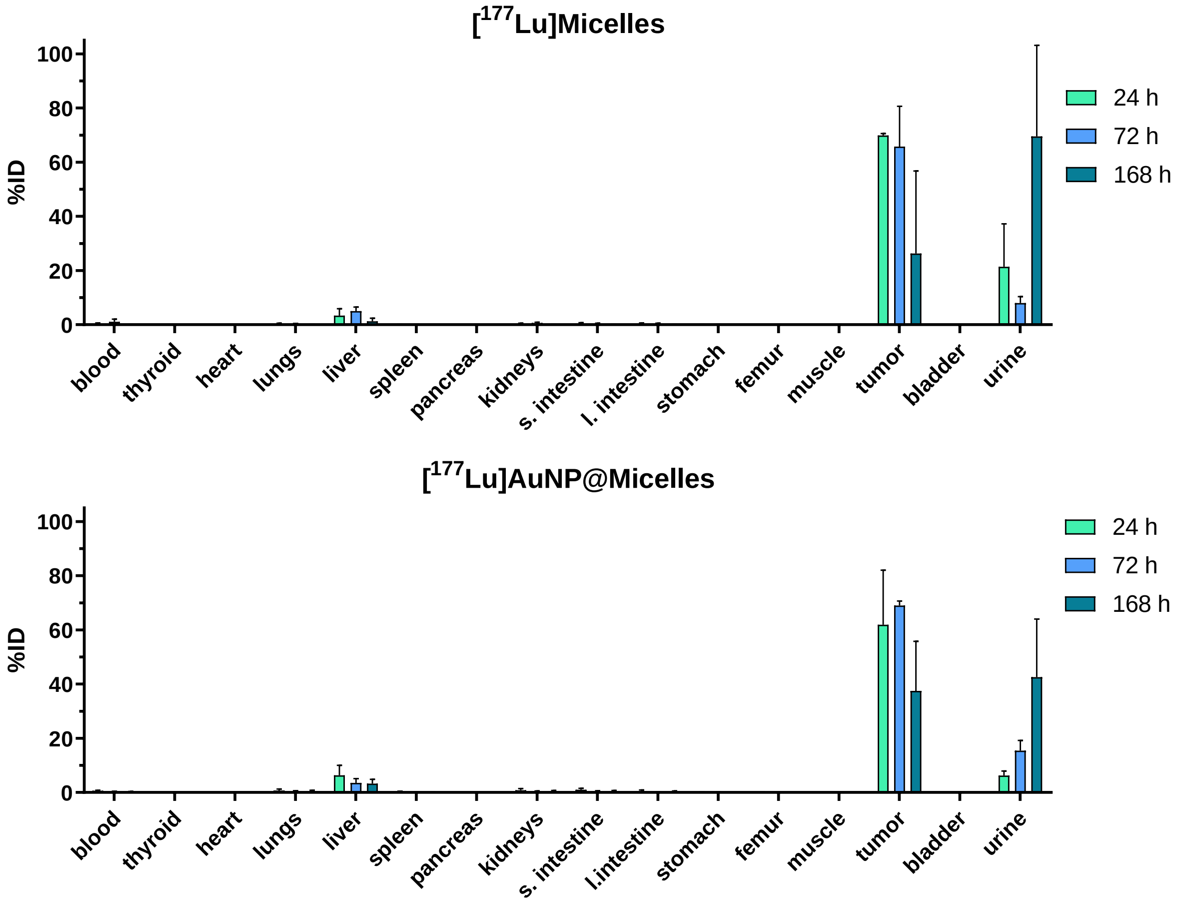

Figure 44: Tumor retention of [^{177}Lu]Micelles and [^{177}Lu]AuNP@Micelles on C57Bl/6 mice with melanoma B16F10 xenografts

The fraction of [^{177}Lu]Micelles or [^{177}Lu]AuNP@Micelles that are entering systemic circulation from the tumor area could then distribute classically in the different organs, with roughly the same pattern as for intravenously injected formulations, albeit to a lesser extent. Again, liver, spleen and lungs were the main targeted organs. Yet, accumulation is transient as we observed a steady decrease over time. Of note, some activity was detected in the urine, suggesting partial dissociation of the micelle and release of some free amphiphilic units.

IV. F. Evaluation of the tumor regression

The volume of the tumors was monitored to evaluate their growth over 7 days. The length and the width of the tumors were measured with a caliper to calculate their volumes after treatment with either [^{177}Lu]Micelles or [^{177}Lu]AuNP@Micelles. For ethical reasons, a control group of untreated mice could not be implemented as the growth of the tumors was very fast and would have led to giant tumoral masses in the untreated group. Tumor growth is expressed as the volume of the tumor at the considered time point minus the initial volume of the tumor and divided by the initial volume of the tumor. Percentages as a function of time are presented in Figure 45.

$$Tumor\ growth\ \% = \frac{Volume\ tumor_t - Volume\ tumor_{t0}}{Volume\ tumor_{t0}}$$

While we observed mostly no differences in the tumor growth percentage (ca. 20%) for the two groups at 24 h, a slight difference was detected at 72 h, and a more marked difference in favor of [^{177}Lu]AuNP@Micelles at 168 h. At this time point, the mean tumor growth percentage was 76.6% for [^{177}Lu]Micelles and only 62.7% for [^{177}Lu]AuNP@Micelles. Although non-statistical, these results highlight the likely contribution of gold in making the micellar formulation of lutetium-177 more potent *in vivo* by better inhibiting tumor growth compared to "empty" [^{177}Lu]Micelles.

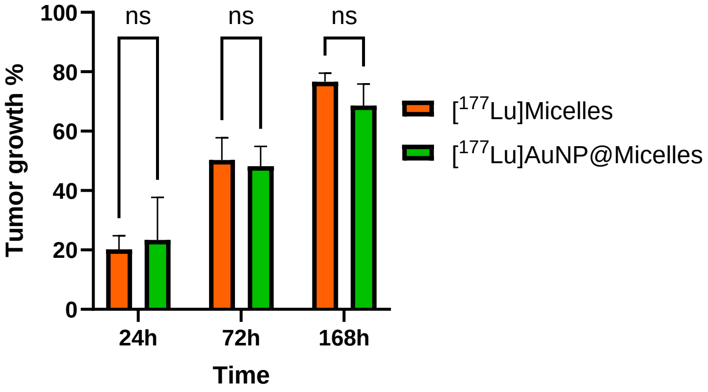

Figure 45: Tumor growth evolution on C57Bl/6 mice treated with [^{177}Lu]Micelles and [^{177}Lu]AuNP@Micelles, ns = non-significant (Student T-test)

In the above *in vivo* study, the behavior of [^{177}Lu]Micelles and that of [^{177}Lu]AuNP@Micelles were investigated following intratumoral injection. Although some leaching out of the tumor was observed at advanced time points, tumor retention was mostly achieved, in particular for [^{177}Lu]AuNP@Micelles which was better retained than [^{177}Lu]Micelles. Such enhanced retention enables delivery of a higher radiation dose within the tumor, which may translate into improved therapeutic efficacy.

Moreover, a preliminary comparison of tumor growth between mice treated with [^{177}Lu]AuNP@Micelles and those treated with [^{177}Lu]Micelles (acting as a negative control) suggests a synergistic radiosensitizing effect of the gold nanoparticles. Nevertheless, a more comprehensive study is required to confirm these preliminary findings.

V. Conclusion of the chapter

In this chapter, the previously developed perfluorinated micelles encapsulating gold nanoparticles were adapted for applications in internal radiotherapy. To achieve this objective, a new amphiphilic unit was synthesized and combined with PFTD-PEG to formulate mixed fluorinated micelles incorporating a DOTA complexing group for ^{177}Lu bonding. Radiolabeling of the amphiphilic units was successfully achieved with a radiochemical yield of 95%. The radiolabeled amphiphiles were subsequently used in the preparation of two formulations: [^{177}Lu]Micelles and [^{177}Lu]AuNP@Micelles.

Stability assessments demonstrated that both formulations remained stable for at least four days in various dispersants at room temperature and at 37 °C. Their cytotoxicity was then evaluated in two cancer cell lines, where both formulations exhibited the expected cytotoxic effect. Importantly, the presence of gold nanoparticles enhanced cytotoxicity, particularly at higher concentrations and radioactivity levels of ^{177}Lu.

Encouraged by these *in vitro* results, a pharmacokinetic study of the micelles was conducted *in vivo*. A first biodistribution study, performed in healthy mice with intravenously injected [^{177}Lu]AuNP@Micelles revealed the half-life of the micelle in the blood, which was approximately 2.5 h, which was not satisfactory. The distribution pattern in different organs is consistent with that of other nanometric carriers, and excretion pathways were both urinary and hepatobiliary.

Finally, tumor retention was evaluated in melanoma-bearing mice after intratumoral injection. Both formulations exhibited favorable early tumor localization, while [^{177}Lu]AuNP@Micelles displayed superior long-term retention. Moreover, some reduction in tumor growth was observed in mice treated with [^{177}Lu]AuNP@Micelles. The latter observation suggested a synergistic radio-enhancement effect gold in potentiating the effect of ^{177}Lu. These preliminary *in vivo* results support further investigation into the therapeutic potential of [^{177}Lu]AuNP@Micelles using nanobrachytherapy.

General conclusion

In the first chapter, we described the synthesis of a fluorinated amphiphile that was used to formulate perfluorinated micelles, applied to radiosensitization of tumors. The PFTD-PEG amphiphilic unit consisted of a perfluorinated chain linked to a PEGylated hydrophilic head, for oxygen transport and stealthiness properties, respectively. The monomers exhibited low critical micelle concentration (0.056 $mg \cdot mL^{-1}$) and were self-assembled into micelles of 11 nm of diameter.

The oxygen loading properties of the nanometric carrier were evaluated using the paramagnetic resonance enhancement (PRE) effect induced by oxygen on the NMR signals of the micelles. Higher PRE was measured for the fluorinated chains, compared to the PEGylated head or the surrounding water, confirming effective encapsulation of O_2 in PFTD-PEG micelles and its preferential localization in the perfluorinated core of the carrier.

In addition to their oxygen carrier capacity, micelles were designed to incorporate gold nanoparticles for radioenhancement properties. Gold nanoparticles coated with fluorinated ligands were synthesized and successfully encapsulated in the perfluorinated micelles. The resulting micelles were found to be intrinsically non-cytotoxic at all tested concentrations.

An external irradiation study under electron beam activation was conducted to evaluate the radiosensitizing properties of both empty micelles and micelles encapsulating gold nanoparticles. The study was performed on two cell lines, *i.e.*, murine melanoma (B16F10) and human breast cancer (SKBR3). The different assays showed that the two systems had, under electron beam activation, an effect on cellular viability, with AuNP@Micelles being more potent than PFTD-PEG micelles. A sensitizer enhancement ratio (SER) of 1.225 was calculated for AuNP@Micelles and 1.128 for empty micelles. Of note, a more pronounced effect was observed on the SKBR3 cell line. These promising results led us to apply our micelles to internal radiotherapy approaches.

In the second chapter, lutetium-177 was integrated to the micellar systems for internal radiotherapy applications. A new amphiphile, based on the same fluorinated PFTD backbone as that of PFTD-PEG, was coupled to a macrocyclic DOTA (dodecane tetraacetic acid) for the complexation of lutetium.

PFTD-DOTA amphiphiles could be radiolabeled with ^{177}Lu, achieving high radiochemical yields up to 95%. Hybrid micelles were then assembled from a mixture of PFTD-PEG and [^{177}Lu]PFTD-DOTA amphiphiles in variable amounts. Two types of micelles were prepared, either empty [^{177}Lu]Micelles or gold-containing [^{177}Lu]AuNP@Micelles. ^{177}Lu-labelled micelles were tested in vitro for their radiotoxicity against B16F10 and SKBR3 cancer cell lines, using non-radiolabeled analogs as a negative control.

We observed a more potent radiotoxic effect on the two cell lines, with increasing ^{177}Lu activity. [^{177}Lu]AuNP@Micelles were more active than simple [^{177}Lu]Micelles, highlighting the radioenhancement effect of gold nanoparticles. This trend was confirmed by determining the half maximal inhibitory concentration (IC50) values which were between 5 to 10 times lower than those of [^{177}Lu]Micelles.

A preliminary biodistribution study was conducted on healthy C57Bl/6 mice to determine the pharmacokinetic parameters of [^{177}Lu]AuNP@Micelles after intravenous injection. The circulatory half-life of the micelles was found to be 2.5 hours and the main organs in which they accumulated were the liver and the spleen. Radioactivity was also detected both in the feces and the urine, suggesting concomitant hepatobiliary and renal excretion, respectively.

As the transient accumulation of micelles in the spleen and liver after systemic administration could be problematic from a radiotoxic point of view, and given the pharmacokinetics and biodistribution of the micellar platform, which was not fully optimal, we chose in the final part of this work to implement direct intratumoral injection (nanobrachytherapy) as administration mode, rather than intravenous injection.

The study was again conducted on C57Bl/6 mice but bearing subcutaneous syngeneic B16F10 tumors. Mice were intratumorally injected with either [^{177}Lu]AuNP@Micelles of [^{177}Lu]Micelles as a negative control. Although retention in the tumor was mainly observed with both formulations, a slow decrease of activity was measured, suggesting that micelles were diffusing out of the tumor and entering systemic circulation. In fact, we detected a concomitant accumulation of the micelles in the liver, which was the main organ in which micelles gathered. Yet, better retention was observed for [^{177}Lu]AuNP@Micelles, compared to [^{177}Lu]Micelles.

Measuring of tumor sizes over time showed that gold nanoparticles had a beneficial effect on the performances of ^{177}Lu in inhibiting tumor growth. While we observed no difference in the tumor growth percentage (ca. 20%) for the two groups at 24 h, a marked difference in favor of [177Lu]AuNP@Micelles was detected at 168 h. At this time point, the mean tumor growth percentage was 76.6% for [^{177}Lu]Micelles and 62.7% only for [^{177}Lu]AuNP@Micelles, highlighting the contribution of gold.

Yet, further studies are needed to evaluate the full potential of [^{177}Lu]AuNP@Micelles for in vivo therapeutic applications.

Bibliography

Hanahan, D., R.A. Weinberg *Cell* **2011** 144 646-674.

Hanahan, D., R.A. Weinberg *Cell* **2000** 100 57-70.

Pulumati, A., A. Pulumati, B.S. Dwarakanath, A. Verma, R.V.L. Papineni *Cancer Reports* **2023** 6 1-17.

Institut National du Cancer **2021** 1-19.

Frey, K.A., H.D. Royal, M.F. Di Carli, G.L. Dillehay, L. Gordon, D.A. Mankoff, J. O'Malley, L. Ramanna, E. Rohren, G.M. Segall, B.L. Shulkin, J.W. Wallis, H.A. Ziessman *Journal of Nuclear Medicine* **2011** 52 994-997.

Zhang, S., X. Wang, X. Gao, X. Chen, L. Li, G. Li, C. Liu, Y. Miao, R. Wang, K. Hu *Signal Transduction and Targeted Therapy* **2025** 10 .

Knoll, G.F. **2000** .

Agency, I.A.E. *Manual for Reactor Produced Radioisotopes* **2003** 1-262.

Humphries, S., D.E. Young *Physics Today* **1988** 41 98-99.

Bockisch, A., L.S. Freudenberg, D. Schmidt, T. Kuwert *Seminars in Nuclear Medicine* **2009** 39 276-289.

Cheng, Z., P. Chen, J. Yan *EJNMMI Physics* **2025** 12 9.

Liu, Z., M. Niu, Z. Kuang, N. Ren, S. Wu, L. Cong, X. Wang, Z. Sang, C. Williams, Y. Yang *EJNMMI Physics* **2022** 9 29.

Katal, S., L.S. Eibschutz, B. Saboury, A. Gholamrezanezhad, A. Alavi *Diagnostics* **2022** 12 .

Surti, S. *Journal of Nuclear Medicine* **2015** 56 98-105.

Cherry, S.R., R.D. Badawi, J.S. Karp, W.W. Moses, P. Price, T. Jones *Science Translational Medicine* **2017** 9 .

Wang, J., Z. Wang, S. Chen, R. Wang, K. Chen, J. Lu, J. Xin, Y. Huang, M. Wang, F. Xie, W. Cheng, T. Yen, C.M. Wischik, M. Cui, C. Zuo, Q. Zhao, Y. Wang, J. Yu *Alzheimer's & Dementia* **2025** 21 e70563.

Wang, T., Q. Yang, W. Huang, X. Sun, Y. Lei, H. Xu, L. Song, X. Duan, F. Liu, W. Wang, Z. Bao, J. Gao, F. Wang, L. Kang *Journal of Medicinal Chemistry* **2025** 68 14843-14858.

N'Guessan, É., S. Bacot, F. Raes, J. Leenhardt, T. Guenard, L. Dumas, C. Ghezzi, D. Fagret, C. Lombardi, A. Broisat, M. Ahmadi *EJNMMI Radiopharmacy and Chemistry* **2025** 10 54.

Mark W. Groch, W.D.E. **2000** 233-244.

Ritt, P. *Seminars in Nuclear Medicine* **2022** 52 276-285.

Li, C., X. Li, Y. Wang, Z. Bai, Y. Wang, R. Gao, B. Jia *ACS Pharmacology & Translational Science* **2025** 8 2673-2682.

Giraudet, A.L. *Cancer/Radiotherapie* **2023** 27 754-758.

Choi, W.H., J. Cho *Journal of Korean Medical Science* **2016** 31 S75.

Ciurlia, E., B. Santo, M.C. Barba, E. Cavalera, P. De Franco, S. De Matteis, G. Di Paola, A. Leone, A. Papaleo, D. Rubini, D. Russo, G. Rubini, A. Sardaro *Frontiers in Oncology* **2025** 14 1525926.

Gudkov, S., N. Shilyagina, V. Vodeneev, A. Zvyagin *International Journal of Molecular Sciences* **2015** 17 33.

Arnoldo Piccardo 1, Martina Ugolini 2, Vania Altrinetti 2, Sergio Righi 3, Francesco Fiz 4, Luca Foppiani 5, L.G. 6 *Q J Nucl Med Mol Imaging* **2021** 65 132-137.

Das, S., T. Al-Toubah, G. El-Haddad, J. Strosberg *Expert Review of Gastroenterology & Hepatology* **2019** 13 1023-1031.

Volkert, W.A., W.F. Goeckeler, G.J. Ehrhardt, A.R. Ketring *J Nucl Med*. **1991** 32 174-85..

Staudacher, A.H., E. Bezak, A. Borysenko, M.P. Brown *Nuclear Medicine Communications* **2014** 35 1284-1290.

Dorso, L., E. Bigot-Corbel, J. Abadie, M. Diab, S. Gouard, F. Bruchertseifer, A. Morgenstern, C. Maurel, M. Chérel, F. Davodeau *PLOS ONE* **2016** 11 e0151330.

Chinn, P., G. Braslawsky, C. White, N. Hanna *Cancer Immunology, Immunotherapy* **2003** 52 257-280.

Ehlerding, E.B., P. Grodzinski, W. Cai, C.H. Liu *ACS Nano* **2018** 12 2106-2121.

Tinganelli, W., M. Durante *Cancers* **2020** 12 3022.

Aghevlian, S., A.J. Boyle, R.M. Reilly *Advanced Drug Delivery Reviews* **2017** 109 102-118.

Lomax, M.E., L.K. Folkes, P. O'Neill *Clinical Oncology* **2013** 25 578-585.

Breen, A.P., J.A. Murphy *Free Radical Biology and Medicine* **1995** 18 1033-1077.

El-Nachef, L., J. Al-Choboq, J. Restier-Verlet, A. Granzotto, E. Berthel, L. Sonzogni, M.L. Ferlazzo, A. Bouchet, P. Leblond, P. Combemale, S. Pinson, M. Bourguignon, N. Foray *International Journal of Molecular Sciences* **2021** 22 7158.

Pawlik, T.M., K. Keyomarsi *International Journal of Radiation Oncology*Biology*Physics* **2004** 59 928-942.

Hennequin, C., S. Guillerm, L. Quero *Cancer/Radiothérapie* **2019** 23 500-502.

Withers, H.R. *Advances in Radiation Biology* **1975** 5 241-271.

Genet, S.C., Y. Fujii, J. Maeda, M. Kaneko, M.D. Genet, K. Miyagawa, T.A. Kato *Journal of Cellular Physiology* **2013** 228 1473-1481.

Thoday, J.M., J. Read *Nature* **1947** 160 608-608.

Liu, C., Q. Lin, Z. Yun *Radiation research* **2015** 183 487-496.

Rockwell, S., I. Dobrucki, E. Kim, S. Marrison, V. Vu *Current Molecular Medicine* **2009** 9 442-458.

Richard P. Hill, PhD,*,‡,§ Robert G. Bristow, MD, P., P. Anthony Fyles, MD,†,§ Marianne Koritzinsky, P. Michael Milosevic, MD,†,§ and Bradly G. Wouters *Seminars in Radiation Oncology* **2015** 25 260-272.

Patel, K.D., R.K. Singh, H.-W. Kim *Materials Horizons* **2019** 6 434-469.

M. Pérez, E., N. Martín *Chemical Society Reviews* **2015** 44 6425-6433.

Gobre, V.V., A. Tkatchenko *Nature Communications* **2013** 4 2341.

Mitragotri, S., S. Patrick *MRS Bulletin* **2014** 39 219-223.

Farokhzad, O.C., R. Langer *ACS Nano* **2009** 3 16-20.

Lin, G., M. Zhang *Accounts of Chemical Research* **2023** 56 1578-1590.

M. Christopher, A.M.L.S. *Physiology & behavior* **2016** 176 100-106.

Hoshyar, N., S. Gray, H. Han, G. Bao *Nanomedicine* **2016** 11 673-692.

Sonavane, G., K. Tomoda, K. Makino *Colloids and Surfaces B: Biointerfaces* **2008** 66 274-280.

Wu, J. *Journal of Personalized Medicine* **2021** 11 .

Hashizume, H., P. Baluk, S. Morikawa, J.W. McLean, G. Thurston, S. Roberge, R.K. Jain, D.M. McDonald *American Journal of Pathology* **2000** 156 1363-1380.

Maeda, H. *Proceedings of the Japan Academy Series B: Physical and Biological Sciences* **2012** 88 53-71.

Liu, W., B. Chen, H. Zheng, Y. Xing, G. Chen, P. Zhou, L. Qian, Y. Min *Pharmaceutics* **2021** 13 1-31.

Ancira-Cortez, A., G. Ferro-Flores, N. Jiménez-Mancilla, E. Morales-Avila, D. Trujillo-Benítez, B. Ocampo-García, C. Santos-Cuevas, A. Escudero-Castellanos, M. Luna-Gutiérrez *Materials Science and Engineering C* **2020** 117 111335.

Luna-Gutiérrez, M., G. Ferro-Flores, B.E. Ocampo-García, C.L. Santos-Cuevas, N. Jiménez-Mancilla, L.M. De León-Rodríguez, E. Azorín-Vega, K. Isaac-Olivé *Journal of the Mexican Chemical Society* **2013** 57 212-219.

Yook, S., Z. Cai, J.J. Jeong, Y. Lu, M.A. Winnik, J.-P. Pignol, R.M. Reilly *Molecular Pharmaceutics* **2020** 17 1226-1236.

Li, C., L. Li, A.C. Keates *Oncotarget* **2012** 3 365-370.

Kwatra, D., A. Venugopal, S. Anant *Translational Cancer Research* **2013** 2 330-342.

Ghezzi, M., S. Pescina, C. Padula, P. Santi, E. Del Favero, L. Cantù, S. Nicoli *Journal of Controlled Release* **2021** 332 312-336.

Shuai, X., T. Merdan, A.K. Schaper, F. Xi, T. Kissel *Bioconjugate Chemistry* **2004** 15 441-448.

Hoffman, H. *Berichte der Bunsengesellschaft für physikalische Chemie* **1978** 82 988-1001.

Kosswig, K. *Ullmann's Encyclopedia of Industrial Chemistry* **2000** a25_747.

Santos, M.S., F.W. Tavares, E.C. Biscaia Jr *Brazilian Journal of Chemical Engineering* **2016** 33 515-523.

Nagarajan, R., E. Ruckenstein *Langmuir* **1991** 7 2934-2969.

Kim, K.S., W. Park, J. Hu, Y.H. Bae, K. Na *Biomaterials* **2014** 35 337-343.

Sonali, null, P. Agrawal, R.P. Singh, C.V. Rajesh, S. Singh, M.R. Vijayakumar, B.L. Pandey, M.S. Muthu *Drug Delivery* **2016** 23 1788-1798.

De Caro, L., T. Stoll, A. Grandeury, F. Gozzo, C. Giannini *Pharmaceutics* **2024** 16 604.

Paruchuri, V.K., A.V. Nguyen, J.D. Miller *Colloids and Surfaces A: Physicochemical and Engineering Aspects* **2004** 250 519-526.

Pang, Z., A. Al-Mahrouki, M. Berezovski, S.N. Krylov *ELECTROPHORESIS* **2006** 27 1489-1494.

Yamamoto, Y., Y. Nagasaki, Y. Kato, Y. Sugiyama, K. Kataoka *Journal of Controlled Release* **2001** 77 27-38.

Zhang, P., D. Chen, L. Li, K. Sun *Journal of Nanobiotechnology* **2022** 20 31.

Deng, H., X. Zhao, J. Liu, L. Deng, J. Zhang, J. Liu, A. Dong *Journal of Materials Chemistry B* **2015** 3 9397-9408.

Seredyuk, V., E. Alami, M. Nydén, K. Holmberg, A.V. Peresypkin, F.M. Menger *Langmuir* **2001** 17 5160-5165.

Almajidi, Y.Q., M.M. Kadhim, F. Alsaikhan, A. Turki Jalil, N. Hassan Sayyid, A. Alexis Ramírez-Coronel, Z. Hassan Jawhar, J. Gupta, N. Nabavi, W. Yu, Y.N. Ertas *Environmental Research* **2023** 227 115722.

Gravel, E., J. Ogier, T. Arnauld, N. Mackiewicz, F. Ducongé, E. Doris *Chemistry – A European Journal* **2012** 18 400-408.

Fang, Y., J. Xue, S. Gao, A. Lu, D. Yang, H. Jiang, Y. He, K. Shi *Drug Delivery* **2017** 24 22-32.

Talelli, M., M. Barz, C.J.F. Rijcken, F. Kiessling, W.E. Hennink, T. Lammers *Nano Today* **2015** 10 93-117.

Kalinova, R.G., I.V. Dimitrov, D.I. Ivanova, Y.E. Ilieva, A.N. Tashev, M.M. Zaharieva, G. Angelov, H.M. Najdenski *Journal of Functional Biomaterials* **2024** 15 53.

Srinivas, U.S., B.W.Q. Tan, B.A. Vellayappan, A.D. Jeyasekharan *Redox Biology* **2018** 25 101084.

Wang, Q., J.-M. Li, H. Yu, K. Deng, W. Zhou, C.-X. Wang, Y. Zhang, K.-H. Li, R.-X. Zhuo, S.-W. Huang *Biomaterials Science* **2018** 6 3096-3107.

Kirsch, P. **2004** .

Jägers, J., A. Wrobeln, K.B. Ferenz *Pflügers Archiv - European Journal of Physiology* **2021** 473 139-150.

Krafft, M.P., J.G. Riess *Advances in Colloid and Interface Science* **2021** 294 102407.

Zhou, Z., B. Zhang, H. Wang, A. Yuan, Y. Hu, J. Wu *Theranostics* **2018** 8 4898-4911.

Shen, Y., L. Liang, S. Zhang, D. Huang, J. Zhang, S. Xu, C. Liang, W. Xu *Nanoscale* **2018** 10 1622-1630.

Song, G., C. Ji, C. Liang, X. Song, X. Yi, Z. Dong, K. Yang, Z. Liu *Biomaterials* **2017** 112 257-263.

Krafft, M. *Advanced Drug Delivery Reviews* **2001** 47 209-228.

Godel-Pastre, S., E. Porcel, G. Pinna, M. Vandamme, C. Denis, C. Leterrier, E. Doris, C. Truillet, E. Gravel *ACS Applied Materials & Interfaces* **2024** 16 21557-21570.

Huang, X., P.K. Jain, I.H. El-Sayed, M.A. El-Sayed *Nanomedicine* **2007** 2 681-693.

Liu, X.-Y., J.-Q. Wang, C.R. Ashby, L. Zeng, Y.-F. Fan, Z.-S. Chen *Drug Discovery Today* **2021** 26 1284-1292.

Li, W., X. Chen *Nanomedicine* **2015** 10 299-320.

Riley, R.S., E.S. Day *WIREs Nanomedicine and Nanobiotechnology* **2017** 9 .

Her, S., D.A. Jaffray, C. Allen *Advanced Drug Delivery Reviews* **2017** 109 84-101.

Loscertales, E., R. López-Méndez, J. Mateo, L.M. Fraile, J.M. Udias, A. Espinosa, S. España *Nanoscale Advances* **2025** 7 1204-1214.

Hainfeld, J.F., D.N. Slatkin, H.M. Smilowitz *Physics in Medicine and Biology* **2004** 49 N309-N315.

Jain, S., J.A. Coulter, K.T. Butterworth, A.R. Hounsell, S.J. McMahon, W.B. Hyland, M.F. Muir, G.R. Dickson, K.M. Prise, F.J. Currell, D.G. Hirst, J.M. O'Sullivan *Radiotherapy and Oncology* **2014** 110 342-347.

Tudda, A., E. Donzelli, G. Nicolini, S. Semperboni, M. Bossi, G. Cavaletti, R. Castriconi, P. Mangili, A.D. Vecchio, A. Sarno, G. Mettivier, P. Russo *Medical Physics* **2022** 49 568-578.

Cerqueira, P., J. Noro, S. Moura, D. Guimarães, C. Silva, A. Cavaco-Paulo, A. Loureiro *International Journal of Pharmaceutics* **2019** 566 282-290.

Padday, J.F., A.R. Pitt, R.M. Pashley *Journal of the Chemical Society, Faraday Transactions 1: Physical Chemistry in Condensed Phases* **1975** 71 1919.

Lenard, A.J., F.A.A. Mulder, T. Madl *Progress in Nuclear Magnetic Resonance Spectroscopy* **2022** 132-133 113-139.

Woźniak, A., A. Malankowska, G. Nowaczyk, B.F. Grześkowiak, K. Tuśnio, R. Słomski, A. Zaleska-Medynska, S. Jurga *Journal of Materials Science: Materials in Medicine* **2017** 28 .

Park, J.-W., J.S. Shumaker-Parry *ACS Nano* **2015** 9 1665-1682.

Wang, A., Y.R. Perera, M.B. Davidson, N.C. Fitzkee *The Journal of Physical Chemistry C* **2016** 120 24231-24239.

Ul-Islam, M., K.F. Alabbosh, S. Manan, S. Khan, F. Ahmad, M.W. Ullah *Advanced Industrial and Engineering Polymer Research* **2024** 7 79-99.

Yang, W., L. Zhang, S. Wang, A.D. White, S. Jiang *Biomaterials* **2009** 30 5617-5621.

Brust, M., M. Walker, D. Bethell, D.J. Schiffrin, R. Whyman *J. Chem. Soc., Chem. Commun.* **1994** 0 801-802.

Booth, S.G., A. Uehara, S.-Y. Chang, C.L. Fontaine, T. Fujii, Y. Okamoto, T. Imai, S.L.M. Schroeder, R. a. W. Dryfe *Chemical Science* **2017** 8 7954-7962.

Zhu, L., C. Zhang, C. Guo, X. Wang, P. Sun, D. Zhou, W. Chen, G. Xue *The Journal of Physical Chemistry C* **2013** 117 11399-11405.

Zhang, Y., B. Newton, E. Lewis, P.P. Fu, R. Kafoury, P.C. Ray, H. Yu *Toxicology in Vitro* **2015** 29 762-768.

Dong, J., P.L. Carpinone, G. Pyrgiotakis, P. Demokritou, B.M. Moudgil *KONA Powder and Particle Journal* **2020** 37 224-232.

Sivaraman, S.K., S. Kumar, V. Santhanam *Journal of Colloid and Interface Science* **2011** 361 543-547.

He, Y.Q., S.P. Liu, L. Kong, Z.F. Liu *Spectrochimica Acta Part A: Molecular and Biomolecular Spectroscopy* **2005** 61 2861-2866.

Uzun, O., Y. Hu, A. Verma, S. Chen, A. Centrone, F. Stellacci *Chem. Commun.* **2008** 196-198.

Alcaraz, M., A. Olivares, M. Andreu-Gálvez, D.G. Achel, A.M. Mercado, M. Alcaraz-Saura *Antioxidants* **2022** 11 2166.

Wang, L., C. Yuan, K. Lv, S. Xie, P. Fu, X. Liu, Y. Chen, C. Qin, W. Deng, W. Hu *PLoS ONE* **2013** 8 e67373.

Roach, M.C., J.D. Bradley, C.G. Robinson *Journal of Thoracic Disease* **2018** 10 .

Subiel, A., R. Ashmore, G. Schettino *Theranostics* **2016** 6 1651-1671.

Detappe, A., S. Kunjachan, J. Rottmann, J. Robar, P. Tsiamas, H. Korideck, O. Tillement, R. Berbeco *Cancer Nanotechnology* **2015** 6 4.

Chang, M.-Y., A.-L. Shiau, Y.-H. Chen, C.-J. Chang, H.H.-W. Chen, C.-L. Wu *Cancer Science* **2008** 99 1479-1484.

Yong, W., S. Zhang, Z. Zhang, Z. Li, Y. Qin, X. Qi, D. Wang, Y. Zhang, J. Li, Z. Liu, R. Zhu, H. Li, G. Wang *Journal of Medicinal Chemistry* **2025** 68 17794-17807.

Ponchelle, M., M. Pruszyński, E. Gravel, E. Doris *Small Science* **2025** 5 2400550.

Niu, T., M. Fan, B. Lin, F. Gao, B. Tan, X. Du *Experimental and Therapeutic Medicine* **2024** 27 225.

Trejtnar, F., P. Bárta, J. Kozempel, M. Vlk, A. Ďurinová, M. Kuchařová, P. Pávek *Nuclear Medicine and Biology* **2025** 144-145 108998.

Hunt, W.W., M. Long, U. Kamil, S. Kellapatha, W. Noonan, P.D. Roselt, B. Emmerson, M.S. Hofman, M.B. Haskali *Nature Protocols* **2025** .

Vogel, W.V., S.C. Van Der Marck, M.W.J. Versleijen *European Journal of Nuclear Medicine and Molecular Imaging* **2021** 48 2329-2335.

Zhang, S., X. Wang, X. Gao, X. Chen, L. Li, G. Li, C. Liu, Y. Miao, R. Wang, K. Hu *Signal Transduction and Targeted Therapy* **2025** 10 .

Dash, A., M.R.A. Pillai, F.F. Knapp *Nuclear Medicine and Molecular Imaging* **2015** 49 85-107.

Hashimoto, K., H. Matsuoka, S. Uchida .

Di Iorio, V., S. Boschi, C. Cuni, M. Monti, S. Severi, G. Paganelli, C. Masini *Molecules* **2022** 27 4143.

Park, U.J., J.-S. Lee, K.H. Choi, S.S. Nam, K.H. Yu *Applied Radiation and Isotopes* **2016** 115 8-12.

Morris, A.A., T. Wei, Z. Wang, Y. Xia, M. Han, Y. Lu *EJNMMI radiopharmacy and chemistry* **2025** 10 56.

Chakravarty, R., S. Chakraborty *American Journal of Nuclear Medicine and Molecular Imaging* **2021** 11 443-475.

Dash, A., M.R.A. Pillai, F.F. Knapp *Nuclear Medicine and Molecular Imaging* **2015** 49 85-107.

Canella, L., M.L. Bonardi, F. Groppi, E. Persico, C. Zona, E. Menapace, Z.B. Alfassi, M. Chinol, S. Papi, G. Tosi *Journal of Radioanalytical and Nuclear Chemistry* **2008** 276 813-818.

Tran, H.H., A. Yamaguchi, H.C. Manning *European Journal of Nuclear Medicine and Molecular Imaging* **2025** 52 2685-2709.

Malo, M.E., K.J.H. Allen, R. Jiao, C. Frank, D. Rickles, E. Dadachova *International Journal of Molecular Sciences* **2020** 21 8721.

Hao, G., X. Sun, Q.N. Do, B. Ocampo-García, A. Vilchis-Juárez, G. Ferro-Flores, L.M. De León-Rodríguez *Dalton Transactions* **2012** 41 14051.

Yook, S., Z. Cai, Y. Lu, M.A. Winnik, J.-P. Pignol, R.M. Reilly *Journal of Nuclear Medicine* **2016** 57 936-942.

Yook, S., Z. Cai, Y. Lu, M.A. Winnik, J.-P. Pignol, R.M. Reilly *Molecular Pharmaceutics* **2015** 12 3963-3972.

Cai, Z., S. Yook, Y. Lu, D. Bergstrom, M.A. Winnik, J.-P. Pignol, R.M. Reilly *Pharmaceutical Research* **2017** 34 579-590.

Yook, S., Z. Cai, J.J. Jeong, Y. Lu, M.A. Winnik, J.-P. Pignol, R.M. Reilly *Molecular Pharmaceutics* **2020** 17 1226-1236.

Häussinger, D., J. Huang, S. Grzesiek *Journal of the American Chemical Society* **2009** 131 14761-14767.

Moreau, J., E. Guillon, J. Pierrard, J. Rimbault, M. Port, M. Aplincourt *Chemistry – A European Journal* **2004** 10 5218-5232.

Sharma, A.K., R. Sharma, K. Vats, H.D. Sarma, A. Mukherjee, T. Das, D. Satpati *Scientific Reports* **2022** 12 15720.

Bibliography

Aslani, A., G.M. Snowdon, D.L. Bailey, G.P. Schembri, E.A. Bailey, N. Pavlakis, P.J. Roach *J Nucl Med Biol*. **2015** 3 107-15..

Godel-Pastre, S., E. Porcel, G. Pinna, M. Vandamme, C. Denis, C. Leterrier, E. Doris, C. Truillet, E. Gravel *ACS Applied Materials & Interfaces* **2024** 16 21557-21570.

Terracciano, R., Y. Carcamo-Bahena, A.L.R. Royal, L. Messina, J. Delk, E.B. Butler, D. Demarchi, A. Grattoni, Z. Wang, V. Cristini, P. Dogra, C.S. Filgueira *Langmuir* **2022** 38 13983-13994.

List of Figures

List of Figures

Experimental Section

General procedure

All reagents were purchased from Sigma Aldrich, VWR, Fluorochem or Acros Organic and were used without further purification. Dry DMF was purchased in anhydrous form and used without further purification. THF was dried over sodium and benzophenone under N_2 atmosphere, and dichloromethane was dried over calcium hydride under N_2 atmosphere. $[^{177}Lu]LuCl_3$ was produced through neutron capture reaction carried out in Maria Nuclear Reactor, Swierk, Poland.

Reactions were monitored by TLC (Silica 230-240 mesh, 0,25 mm, Merck) and compounds were visualized with UV light (254 nm) and potassium permanganate as developing agent. Purifications by column chromatography were made with Silica Gel 60 (0.040–0.063 mm). Automated purifications were realized using CombiFlash Rf 150 (Teledyne Isco) using RediSepRf columns (particle size: 40-63 µm, irregular, Mesh size: 230-400, pore size: 60 Å).

^{1}H (400 MHz), ^{13}C (100 MHz), ^{19}F (376 MHz) NMR were performed on a Brucker Avance spectrometer. Chemical shift was expressed in part per million (ppm) downfield from residual solvent and coupling constants are expressed in Hz. Splitting patterns are described as singlet (s), doublet (d), triplet (t). Splitting patterns that could not be easily visualized or interpreted were described as multiplet (m). Spectra were analyzed using MestRenova software.

Ultra-Performance Liquid Chromatography-Mass Spectroscopy (UPLC-MS) analyses were performed using a Waters device equipped with an ELSD detector (SEDEX 100, SEDERE), a diode array detector (Acquity PDA eλ Detector) coupled with a simple quadrupole detector (SQ detector 2). Compounds were eluted through a BEH Xbridge C18 (50 x 2.1 mm, 1.7 µm) column or BEH Phenyl (50 x 2.1 mm x 1.7 µm 130 Å) column (Solvent A: MiliQ water + 0.1% HCO_2H; Solvent B: Acetonitrile + 0.1% HCO_2H). Mass spectra were recorded in positive and negative ion mode in a range of 100 – 2000 *m/z* and analyzed using MassLynx Software

Micelles were purified by NAP™-5, NAP™-25, and PD™-10 columns sold by GE Healthcare and Cytiva. Columns were packed with Sephadex™ G-25 DNA Grade resin and compounds were eluted with ultrapure water by gravity.

Assembly of the micelles was performed using a Branson sonifier 550 system with a 3 mm tapered microtip (300 ms pulse per second, output 40 %).

DLS measurements were realized using a VascoFlex device from Cordouan Technologies using a laser diode λ_{laser} = 450 nm at 20 °C. For gold nanoparticles, DLS analysis was realized on a Zetasizer Advance system from Malvern Panalytical using a laser diode λ_{laser} = 660 nm at 25 °C and analyzed with Malvern 7.11 Software. Zeta potential was measured with the same Zetasizer Advance device.

Transmission Electron Microscopy (TEM) was performed on a TECNAI 20 G2 FEI. microscope operated at 200 kV. Pictures were analyzed using ImageJ software.

ICP-MS analyses were performed on an iCap Q spectroscope from Thermo Scientific and data were analyzed with Qtegra software.

Thermogravimetric analyses were carried out on a Mettler-Toledo TGA 2 machine using the STARe software for result exploitation.

Instant Thin Layer Chromatography (iTLC) were developed using an Azure scanner and analyzed using Azure Spot Pro software.

Cell proliferation assays were performed on two cell lines (B16F10 and SKBR3). 24 h post-seeding in 96-well plates, cells were treated with [^{177}Lu]Micelles or [^{177}Lu]AuNP@Micelles in cell culture medium (or non-radiolabeled analogues) at the final indicated concentrations. Cells were incubated for the desired amount of time at 37 °C with 5% CO_2 in humid atmosphere. Then the supernatant was removed and the wells were washed two times with 100 µL PBS. 100 µL of cell culture medium and 20 µL of CellTiter 96® AQueous One Solution Reagent were added to the wells before stirring the plate at 1100 rpm for 5 min. Then the 96-well plate was put back in the incubator for 2 h. Before analysis, the plates were stirred again at 100 rpm for 5 min. Absorbance at λ = 490 nm was recorded using a Promega 96-well plate reader.

Statistical analysis was performed using GraphPad Prism (v10.5.0, GraphPad software). Cytotoxicity and biodistribution studies are represented as mean and SD. *In vitro* experiments were carried out in triplicate, while 5 repetitions were done for animal experiments. Student’s t-test or two-way ANOVA analysis of variance was used to determine statistical significance between two or more groups. The significance of difference was indicated as ns = non-significant, $p < 0.05$ (* $p < 0.05$, ** $p < 0.01$, *** $p < 0.001$, *** $p < 0.0001$).

Chapter I

Synthesis of compound **I.1**:

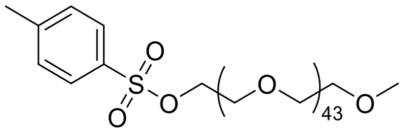

Chemical Formula: $C_{96}H_{186}O_{47}S$
Molecular Weight: 2124,56

Under N_2 atmosphere, to a solution of monomethyl ether PEG-2000 (3.15 g, 1.575 mmol, 1 equiv, CAS: 25322-68-3) in dry CH_2Cl_2 was added Et_3N (1.096 mL, 7.875 mmol, 5 equiv). The mixture was cooled down to 0 °C before the portion-wise addition of a solution of *p*-tosylchloride (1.4963 g, 7.875 mmol, 5 equiv) in dry CH_2Cl_2. The reaction mixture was allowed to warm up at room temperature overnight and the progress of the reaction was monitored by TLC (CH_2Cl_2/MeOH 9:1). Once complete, the reaction mixture was washed with saturated NH_4Cl solution, saturated $NaHCO_3$ solution and brine. The organic layer was dried over $MgSO_4$ then concentrated under vacuum. Purification was carried out by precipitation of the expected product in Et_2O at -20 °C for 2 h. Product **I.1** (3.16 g, 93 %) was obtained as a white solid.

^{1}H NMR (400 MHz, $CDCl_3$) δ 7.80 (d, J = 8.4 Hz, 1H), 7.34 (d, J = 8.0 Hz, 1H), 4.18 – 4.13 (m, 1H), 3.68 – 3.61 (m, 59H), 3.38 (s, 3H), 2.45 ppm (s, 3H).

^{13}C NMR (100 MHz, $CDCl_3$): δ 144.8, 133.1, 129.8, 128, 72, 70.6, 69.3, 68.7, 59, 29.7, 21.6 ppm.

Synthesis of **PFTD-PEG:**

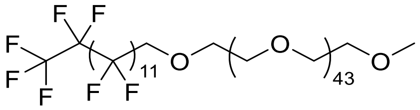

Chemical Formula: $C_{103}H_{181}F_{27}O_{45}$
Molecular Weight: 2652,49

Under N_2 atmosphere, to a solution of perfluorotetradecanol (1.4624 g, 2.089 mmol, 3 equiv, CAS: 15622-57-8) in dry THF was added NaH (111 mg, 60 % in oil, 2.786 mmol, 4 equiv). The reaction mixture was warmed up to 70 °C and stirred for 30 min before addition of compound **I.1** (1.5 g, 0.696 mmol, 1 equiv) dissolved in dry THF. The reaction mixture was stirred at 70 °C for 3 days. The reaction was monitored by NMR. Once completed, the reaction mixture was cooled down and concentrated under vacuum. The crude mixture was dissolved in CH_2Cl_2 and was filtered over Celite bed to remove the excess of perfluorotetradecanol. The filtrate was concentrated under reduced pressure. The expected product was purified by precipitation in Et_2O at -20 °C for 2 h. PFTD-PEG (1.276 g, 68 %) was obtained as a white solid.

^{1}H NMR (400 MHz, $CDCl_3$) *δ* 4.04 (t, *J* = 13.8 Hz, 2H), 3.68 – 3.60 (m, 143H), 3.37 ppm (s, 3H).

^{13}C NMR (100 MHz, $CDCl_3$) δ 72.5, 72.1, 70.7, 59.1 ppm.

^{19}F NMR (376 MHz, $CDCl_3$) δ −80.70 (t, J = 10.0 Hz), −119.71 (t, J = 14.6 Hz), −121.41 to −122.13 (m), −122.62 (s), −123.36 (s), −125.98 to −126.06 ppm (m).

Assembly of PFTD-PEG micelles and size measurement by DLS analysis:

PFTD-PEG (10 mg) was dissolved in ultrapure water (1 mL). The solution was sonicated using an ultrasound probe (300 ms pulse per second, output 40 %) for 10 min. The resulting solution was filtered over 0.2 µm nylon membrane. The mean hydrodynamic diameter was measured by DLS (λ_{laser} = 450 nm) at 20 °C.

Determination of ζ potential of PFTD-PEG micelles:

Zeta potential of PFTD-PEG micelles was measured in ultrapure water (C = 10 mg·mL^{-1}). Measurements were performed over 7 runs of 15 s. Raw data was analyzed with ZetaQ V1.7.9.24080 software and the mean value of zeta potential was displayed.

Determination of the critical micellar concentration (CMC):

CMC was determined by measuring the surface tension of the micellar colloids. Suspensions at different concentrations of amphiphilic units (0.0001 to 1 mg·mL^{-1}) were prepared and the surface tension was measured (in triplicate) using the du Noüy-Padday method. The CMC value was obtained at the intersection of the two lines (see graph fig. 11).

Oxygen level and PRE measurement:

A PFTD-PEG micelle solution (10 mg mL^{-1}– in D_2O) was transferred in an NMR tube equipped with a Teflon valve from Young Scientific Glassware Ltd. The solution was thoroughly degassed under vacuum at -196 °C. Then, O_2 (oxygen ultrapure, from Air Products) was gradually added (from 1 to 2.5 bar) above the solution via the Teflon valve. The tube was then vigorously shaken in order for O_2 to reach a thermodynamic equilibrium between the gas and liquid phases. For each O_2 pressure/dissolved O_2 concentration, relaxation rates R1 were measured by using the inversion-recovery sequence. For each R1 measurement, 8 to 16 spectra of 1 scan were recorded, with recovery delays rd chosen to span at least 0 – 5 times the reverse of R1. The pre-scan delay was equal to the longest recovery delay of the spectrum. Signals were integrated over the 4.8 ppm for water and 3.65 for PEG in proton nuclei and -80 ppm for the fluorine nucleus. Respectively, Integrals were fitted against the equation I(rd) = Iinf × (1−2A exp(−R1 rd)) with A, a factor mandatory to take into account imperfect inversion of signals by the p pulse.

Brust-Schiffrin gold nanoparticle synthesis and encapsulation in PFTD-PEG micelles:

Under vigorous stirring, to an aqueous solution of $HAuCl_4.3H_2O$ (0.075 mmol, 29.5 mg, 2.5 mL) was added TOAB in toluene (50 mM, 191 mg, 7 mL). After 20 min, an aqueous solution of $NaBH_4$ (0.75 M, 25 mg, 0.85 mL) was added dropwise to the medium and the resulting burgundy mixture was left to stir for 3 h. Afterwards, the toluene phase was extracted and 1H-1H-2H-2H-perfluorooctanethiol (7 µL, 0.025 mmol, 0.33 equiv.) was added to the toluene phase. Almost instant precipitation was observed. Several washing steps with toluene were needed to recover a dry black precipitate. Solubilization in perfluoromethylcyclohexane (PFMC, 0.5 mL) of this black precipitate yielded a dark red colloidal suspension of AuNP@PFS.

AuNP@PFS in suspension in PFMC (0.5 mL) were added to PFTD-PEG micellar suspension (2 mL, C = 10 mg·mL^{-1}) and the biphasic mixture was sonicated using an ultrasound probe (300 ms pulse per second, output 40 %) for 15 min. This step was repeated twice and after the third run, the solution was filtered over 0.2 µm nylon membrane. The mean hydrodynamic diameter was measured by DLS (λ_{laser} = 660 nm) at 20 °C

Stellacci gold nanoparticle synthesis and encapsulation in PFTD-PEG micelles:

To a solution of $HAuCl_4 \cdot 3H_2O$ in EtOH (0.025 mmol, 10 mg, 4mL), 1H-1H-2H-2H-perfluorooctanethiol (0.025 mmol, 7 µL, 1 equiv.) was added. Under vigorous stirring, a solution of $NaBH_4$ (0.3 mmol, 12 mg, 12 equiv.) was added dropwise to the medium and the resulting dark brown mixture was stirred at room temperature for 2 h. Afterwards, the crude mixture was purified over LH20 Sephadex using ultrapure water as eluent. The resulting suspension of AuNP@PFS in EtOH was mixed with PFTD-PEG micelles (10 mg·mL^{-1}) in a 1/1 v/v ratio and sonicated using an ultrasound probe (300 ms pulse per second, output 40 %) for 15 min. This step was repeated twice and after the third run, the solution was filtered over 0.2 µm nylon membrane. The mean hydrodynamic diameter was measured by dynamic light scattering (λ_{laser} = 660 nm) at 20 °C

TEM analysis of AuNP@PFTD-PEG:

Liquid samples (5 µL) were deposited on carbon grids and were analyzed after overnight drying at room temperature.

ICPMS quantification:

AuNP@PFTD-PEG (50 µL) were digested in 1 mL *aqua regia* (HCl / HNO_3 3:1 v/v) overnight and diluted up to 5 mL. The resulting solution was analyzed by ICPMS.

External irradiation experiment – Chronic toxicity:

B16F10 and SKBR3 were seeded in a 96-well plate and left to adhere for 24 h in cell culture medium at 37 °C in a humidified 5 % CO_2 atmosphere. Then cells were treated with Micelles of AuNP@Micelles at the desired concentration and incubated for another 24 h. Cells were irradiated with an electron beam source (9 MV, 10 Gy·min^{-1}) at different doses (1, 2 and 4 Gy) in NCBJ, Swierk, Poland. After irradiation, cells were kept at 37 °C in a humidified incubator for the desired amount of time. Cell viability was assessed by MTS assay.

External irradiation experiment – Acute toxicity:

B16F10 and SKBR3 were seeded in a 96-well plate and left to adhere for 24 h in cell culture medium at 37 °C in a humidified 5 % CO_2 atmosphere. Then cells were treated with Micelles of AuNP@Micelles at the desired concentration and incubated for another 24 h. After treatment, the medium was discarded and replaced by fresh medium. Cells were irradiated with an electron beam source (9 MV, 10 Gy·min^{-1}) at different doses (1, 2 and 4 Gy) in NCBJ, Swierk, Poland. After irradiation, cells were kept at 37 °C in a humidified incubator for the desired amount of time. Cell viability was assessed by MTS assay.

Chapter II

Synthesis of compound **II.1**:

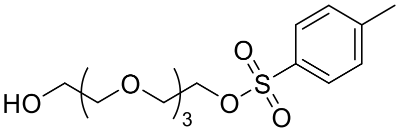

Chemical Formula: $C_{15}H_{24}O_7S$
Molecular Weight: 348,41

To a solution of tetraethylene glycol (40 g, 206.2 mmol, 1 equiv) in THF (10 mL) sodium hydroxide (1.234 g, 30.928 mmol, 0.15 equiv) in 16 mL of H_2O was added, this mixture was cooled down to 0 °C. To this mixture, *p*-tosylchloride (3.918 g, 20.619 mmol, 0.1 equiv) in THF (15 mL) was added using a syringe pump over 2 h. The reaction mixture was stirred for one more hour after completion of the addition. Ice was added to the solution, and the solution was extracted with CH_2Cl_2, washed with water and dried over $MgSO_4$. The solvent was evaporated under vacuum to obtain the compound **II.1** (6.45 g, 90 %) as a pale-yellow oil.

^{1}H NMR (400 MHz, $CDCl_3$) *δ* 7.80 (d, *J* = 8.3 Hz, 2H), 7.34 (d, *J* = 8.0 Hz, 2H), 4.19 – 4.13 (m, 2H), 4.19 – 4.15 (m, 2H), 3.76 – 3.59 (m, 26H), 2.45 ppm (s, 3H).

^{13}C NMR (100 MHz, $CDCl_3$) δ 144.9, 132.8, 129.8, 72.6, 70.5, 70.4, 70.3, 70.2, 69.8, 69.2, 68.5, 21.6 ppm.

Synthesis of compound **II.2**:

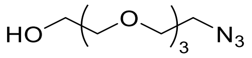

Chemical Formula: $C_8H_{17}N_3O_4$
Molecular Weight: 219,24

Under N_2 atmosphere, to a solution of sodium azide (0.668 g, 10.273 mmol, 1.1 equiv) in dry DMF (10 mL), a solution of compounds **II.1** (3.25 g, 9.339 mmol, 1 equiv.) in dry DMF (10 mL) was added at 0 °C. The reaction mixture was stirred at room temperature overnight. The progress of the reaction was monitored by LC-MS. Once completed, the solvent was evaporated under vacuum and the crude mixture was dissolved in CH_2Cl_2 and washed with water and brine, then dried with $MgSO_4$. The crude product was concentrated under vacuum and compound **II.2** (1.386 g, 61 %) is obtained as an orange oil.

^{1}H NMR (400 MHz, $CDCl_3$) δ 3.76 – 3.59 (m, 15H), 3.44 – 3.37 ppm (m, 2H).

^{13}C NMR (100 MHz, $CDCl_3$) δ 72.6, 70.8, 70.8, 70.7, 70.5, 70.2, 61.9, 50.8 ppm

Synthesis of compound **II.3**:

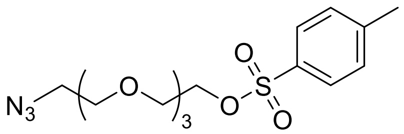

Chemical Formula: $C_{15}H_{23}N_3O_6S$
Molecular Weight: 373,42

Under N_2 atmosphere, to a solution of compound **II.2** (1.04 g, 4.749 mmol, 1 equiv) in dry CH_2Cl_2 (5 mL) was added Et_3N (3.155 mL, 23.744 mmol, 5 equiv). To the resulting mixture, a solution of *p*-tosylchloride (1.805 g, 9.498 mmol, 2 equiv) in dry CH_2Cl_2 (6 mL) was added. The resulting solution was stirred at room temperature overnight. The progress of the reaction was monitored by TLC (cyclohexane / EtOAc 7:3). Once the reaction was completed, the crude mixture was diluted in CH_2Cl_2. The solution was washed with water and brine. The crude mixture is concentrated under vacuum. Purification was carried out by silica gel chromatography using cyclohexane / EtOAc (7:3) as eluent. Product **II.3** (1.28 g, 72 %) was obtained as a translucent oil.

^{1}H NMR (400 MHz, $CDCl_3$) δ 7.80 (d, J = 8.3 Hz, 2H), 7.34 (d, J = 8.0 Hz, 2H), 4.19 – 4.14 (m, 2H), 3.71 – 3.58 (m, 12H), 3.42 – 3.35 (m, 2H), 2.45 ppm (s, 3H).

^{13}C NMR (100 MHz, $CDCl_3$) δ 144.7, 132.7, 129.7, 127.7, 70.5, 70.4, 70.4, 70.3, 69.8, 69.2, 68.4, 50.4, 30.7, 21.4 ppm.

Synthesis of compound **II.4**:

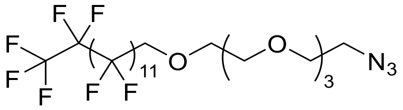

Chemical Formula: $C_{22}H_{18}F_{27}N_3O_4$
Molecular Weight: 901,36

Under N_2 atmosphere, to a solution of perfluorotetradecanol (5.029 g, 7.185 mmol, 2 equiv CAS: 15622-57-8) in dry THF (20 mL) was added NaH (0.575 g, 14.370 mmol, 4 equiv.). The resulting mixture was heated up to 70 °C and stirred for 30 min before addition of compound **II.3** (1.34 g, 3.592 mmol, 1 equiv) in solution in dry THF (20 mL). The resulting solution was stirred at 70 °C for 3 days. Progress of the reaction was monitored by LC-MS. Once the reaction completed, the reaction mixture was cooled down to room temperature and concentrated under vacuum. The crude mixture was solubilized in CH_2Cl_2 and filtered over a Celite bed to remove the excess of perfluorotetradecanol. The filtrate was concentrated under reduced pressure. Purification was carried out with silica gel chromatography using cyclohexane / EtOAc (7:3) as eluent. Compound **II.4** (1.256 g, 39 %) was obtained as a white solid.

^{1}H NMR (400 MHz, $CDCl_3$) δ 4.05 (t, J = 14.1 Hz, 2H), 3.82 – 3.76 (m, 2H), 3.71 – 3.63 (m, 10H), 3.42 – 3.36 ppm (m, 2H).

^{13}C NMR (100 MHz, $CDCl_3$) δ 73.0, 72.5, 70.9, 70.8, 70.8, 70.7, 70.4, 68.7, 68.4, 68.2, 50.2 ppm

^{19}F NMR (376 MHz, $CDCl_3$) δ −80.70 (t, J = 10.0 Hz), −119.73 (t, J = 12 Hz), −121.52 to −122.09 (m), −122.66 (s), −123.38 (s), −126.02 to −126.14 ppm (m).

Synthesis of compound **II.5**:

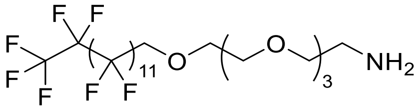

Chemical Formula: $C_{22}H_{20}F_{27}NO_4$
Molecular Weight: 875,36

Under N_2 atmosphere, a solution of compound **II.4** (0.861 g, 0.956 mmol) in EtOAc (30 mL) was degassed with N_2 for 5 min. A spatula tip of Pd/C is added to the mixture and the N_2 atmosphere was removed under vacuum. The reaction mixture was put under H_2 atmosphere and was stirred at room temperature overnight. Progress of the reaction was monitored by LC-MS. Once completed, the H_2 atmosphere was removed under vacuum and the solution was put under N_2 atmosphere. The reaction mixture was filtered out over a Celite pad to remove Pd/C, which was covered by Celite to avoid any fire. The Celite pad was washed several times with EtOAc and the filtrate was concentrated under vacuum. Compound **II.5** (0.788 g, 94 %) was obtained as a white solid.

^{1}H NMR (400 MHz, $CDCl_3$) *δ* 4.05 (t, *J* = 13.8 Hz, 2H), 3.82 – 3.76 (m, 2H), 3.71 – 3.59 (m, 7H), 3.51 (t, *J* = 5.3 Hz, 2H), 2.87 ppm (t, *J* = 5.2 Hz, 1H).

^{13}C NMR (100 MHz, $CDCl_3$) δ 73.0, 72.5, 70.9, 70.8, 70.8, 70.7, 70.4, 68.7, 68.4, 68.2, 41.6 ppm

^{19}F NMR (376 MHz, $CDCl_3$) δ −80.70 (t, J = 10.0 Hz), −119.73 (t, J = 12 Hz), −121.52 to −122.09 (m), −122.66 (s), −123.38 (s), −126.02 to −126.14 ppm (m).

Synthesis of compound **II.6**:

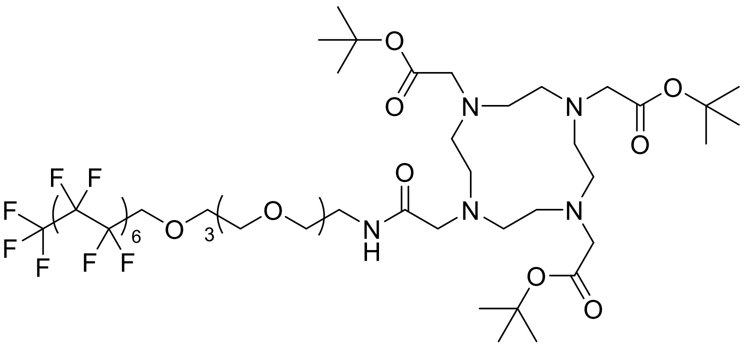

Chemical Formula: $C_{50}H_{70}F_{27}N_5O_{11}$
Molecular Weight: 1430,09

Under N_2 atmosphere, compound **II.5** (0.188 g, 0.215 mmol, 1 equiv) was dissolved in DMF/CH_2Cl_2 (6 mL, 3:1). To the resulting solution, Hexafluorophosphate Azabenzotriazole Tetramethyl Uronium (HATU 0.1225 g, 0.322 mmol, 1.5 equiv, CAS: 148893-10-1), 2-(4,7,10-tris(2-(tert-butoxy)-2-oxoethyl)-1,4,7,10-tetraazacyclododecan-1-yl)acetic acid (DOTA, 0.123 g, 0.215 mmol, 1 equiv, CAS: 137076-54-1).and Et_3N (0.171 mL, 1.289 mmol, 6 equiv) were added. The resulting mixture was stirred at room temperature overnight. Progress of the reaction was monitored by LC-MS. Once completed, the reaction mixture was concentrated under vacuum. Purification was carried out with silica gel chromatography using CH_2Cl_2 / MeOH (gradient to 9:1) as eluent. Product **II.6** (0.063 g, 20 %) was obtained as a white solid.

^{1}H NMR (400 MHz, $CDCl_3$) δ 4.05 (t, *J* = 13.8 Hz, 2H), 3.82 – 3.76 (m, 2H), 3.71 – 3.59 (m, 7H), 3.51 (t, *J* = 5.3 Hz, 2H), 3.32 (s, 8H), 2.87 ppm (t, *J* = 5.2 Hz, 1H), 2.46 (m, 16H).

^{13}C NMR (100 MHz, $CDCl_3$) δ 170.2, 81.8, 73.0, 72.5, 70.9, 70.8, 70.8, 70.7, 70.4, 68.7, 68.4, 68.2, 58.2, 55.5, 41.6, 28.7 ppm

^{19}F NMR (376 MHz, $CDCl_3$) δ −80.70 (t, J = 10.0 Hz), −119.73 (t, J = 12 Hz), −121.52 to −122.09 (m), −122.66 (s), −123.38 (s), −126.02 to −126.14 ppm (m).

Synthesis of **PFTD-DOTA:**

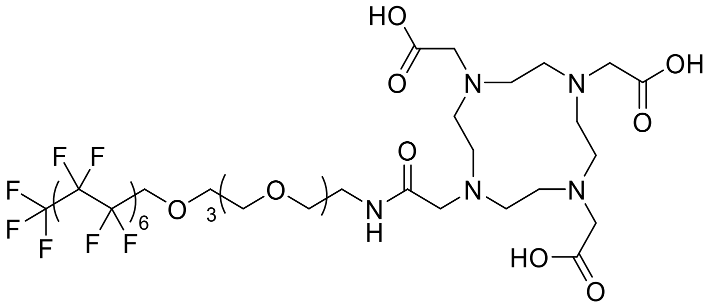

Chemical Formula: $C_{38}H_{46}F_{27}N_5O_{11}$
Molecular Weight: 1261,77

Under N_2 atmosphere, compound **II.6** (0.063 g, 0.044 mmol, 1 equiv), was dissolved in dry CH_2Cl_2. Hydrochloric acid in dioxane (4 M, 0.5 mL) was added and the reaction mixture was stirred at room temperature overnight. Progress of the reaction was monitored by LC-MS. Once completed, the solvent was evaporated under vacuum. Purification was carried out by steric exclusion chromatography (NAP25 column) using water as eluent. PFTD-DOTA (0.042 g, 95 %) was obtained as a white solid.

^{1}H NMR (400 MHz, $CDCl_3$) δ 4.05 (t, *J* = 13.8 Hz, 2H), 3.82 – 3.76 (m, 2H), 3.71 – 3.59 (m, 7H), 3.51 (t, *J* = 5.3 Hz, 2H), 3.32 (s, 8H), 2.87 ppm (t, *J* = 5.2 Hz, 1H), 2.46 (m, 16H).

^{13}C NMR (100 MHz, $CDCl_3$) δ 170.2, 73.0, 72.5, 70.9, 70.8, 70.8, 70.7, 70.4, 68.7, 68.4, 68.2, 58.2, 55.5, 41.6 ppm

^{19}F NMR (376 MHz, $CDCl_3$) δ −80.70 (t, J = 10.0 Hz), −119.73 (t, J = 12 Hz), −121.52 to −122.09 (m), −122.66 (s), −123.38 (s), −126.02 to −126.14 ppm (m).

PFTD-DOTA radiolabeling with ^{177}Lu:

[^{177}Lu]LuCl$_3$ (2040 MBq, 860 GBq·mg^{-1}, 1 equiv.) in hydrochloric acid (0.05 M) was diluted in 300 µL of sodium acetate buffer (pH 5). PFTD-DOTA (0.431 mg, 0.341 mmol, 50 equiv., 10 mg·mL^{-1}) in ultrapure water was added, and the solution was filled up to 1 mL with sodium acetate buffer. The mixture was stirred with the pipette twice. Then the reaction mixture was heated up to 80 °C for 30 min. After incubation, the reaction was allowed to cool down to room temperature and the radiochemical yield was evaluated by iTLC (RCP: 90 %). Purification was carried out by steric exclusion chromatography (NAP column) using ultrapure water as eluent to get the radiolabeled [^{177}Lu]Lu-DOTA-PFTD (1 mL, 1215 MBq, RCY 60 %, RCP 95 %).

Assembly of [^{177}Lu]Lu-Micelles:

[^{177}Lu]Lu-DOTA-PFTD (735 µL, 96.3 MBq) in ultrapure water was mixed with PFTD-PEG (43 µL, 50 mg·mL^{-1}) in ultrapure water and the resulting solution was filled up to 2.2 mL ($C_{micelles}$ = 1 mg·mL^{-1}). The colloid solution was sonicated with an ultrasound bath for 20 min.

Assembly of [^{177}Lu]Lu-AuNP@Micelles:

[^{177}Lu]Lu-DOTA-PFTD (735 µL, 99 MBq) in ultrapure water was mixed with AuNP@PFTD-PEG (216 µL, 10 mg·mL^{-1}) in ultrapure water and the resulting solution was filled up to 2.2 mL ($C_{micelles}$ = 1 mg·mL^{-1}). The colloid suspension was sonicated with an ultrasound bath for 20 min.

Stability study of [^{177}Lu]Lu-Micelles:

[^{177}Lu]LuMicelles suspensions in the different tested media (ultrapure water, PBS, FBS cell culture medium) were prepared to reach the desired activity and a final micelles concentration of 5 mg·mL^{-1}. Samples were stored in lead shields at room temperature under a ventilated fumehood or inside a cell incubator at 37 °C in a humidified 5 % CO$_2$ atmosphere. Radiochemical purity was assessed by iTLC.

Animal model:

5-10 weeks old C57Bl/6 mice, were obtained from M. Mossakowski Institute of Experimental and Clinical Medicine, Polish Academy of Sciences in Warsaw (Poland). Mice were housed under pathogen-free conditions with food and water ad libitum, and a 12-12 hours light-dark cycle. Veterinarian staff and investigators observed the mice daily to ensure animal welfare and determine if humane endpoints (e.g., hunched and ruffled appearance, apathy, ulceration, severe weight loss) were reached.

Studies were conducted at POLATOM (Swierk, Poland) following the guidelines approved on March 18, 2025, by the National Ethical Committee, Poland (the authorization number 1668/2025) and was carried out in accordance with the national legislation regarding laboratory animals' protection and the principles of good laboratory practice.

Biodistribution study:

For the experiment, thirty-five female mice were intravenously injected with [^{177}Lu]AuNP@Micelles (0.1 mL, 10 mg·mL^{-1}, 6.02 MBq) and randomized into seven groups. At 1, 4, 8, 24, 48, 72 and 168 h after injection, the animals were euthanized by cervical dislocation and dissected. Selected organs and tissues were assayed for their radioactivity and weighed. Their radioactivity was measured using the RUM-2 POLON-ALFA radiometer immediately after dissection. The physiological distribution was then calculated and expressed in the percentage of administered radioactivity found in each of the selected organs or tissues per gram (% ID·g^{-1}) with suitable standards of the injected dose.

Tumor retention study:

For the experiment, thirty female mice were subcutaneously injected in the interscapular region with 1 million murine melanoma cells (B16F10 cell line) suspended in 0.2 mL of a Matrigel + PBS (1:1) solution. The animals were monitored regularly for tumor development and progression. After 14 days, mice were randomized into two groups and received intratumoral injections of [^{177}Lu]Micelles or [^{177}Lu]AuNP@Micelles (0.03 mL, 10 mg·mL^{-1}, 6.02 MBq). At 24, 72 and 168 h after injection, the animals were euthanized by cervical dislocation and dissected. Selected organs and tissues were assayed for their radioactivity and weighed. Their radioactivity was measured using the RUM-2 POLON-ALFA radiometer immediately after dissection. The physiological distribution was then calculated and expressed in the percentage of administered radioactivity found in each of the selected organs or tissues per gram (% ID·g^{-1}) with suitable standards of the injected dose.

Annexes

Annex 1: TGA analysis of AuNP@PFS (a) and PFTD-PEG (b)

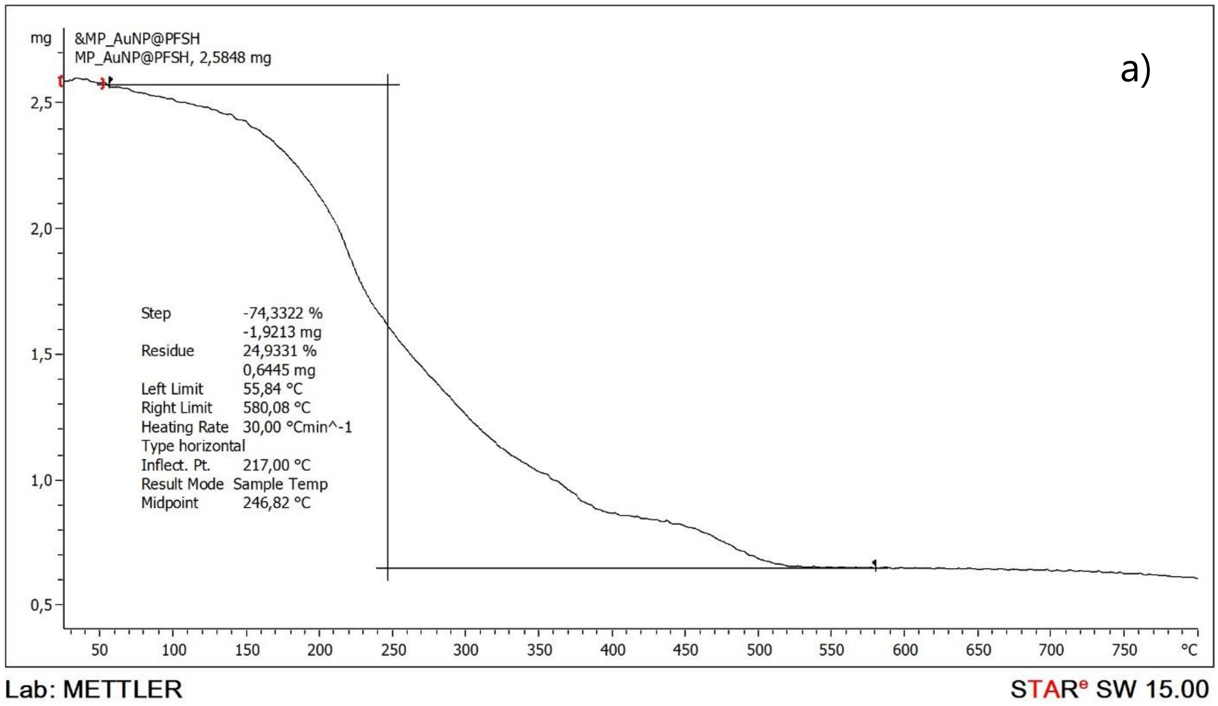

Step	-74,3322 % -1,9213 mg
Residue	24,9331 % 0,6445 mg
Left Limit	55,84 °C
Right Limit	580,08 °C
Heating Rate	30,00 °Cmin^-1
Type horizontal	
Inflect. Pt.	217,00 °C
Result Mode	Sample Temp
Midpoint	246,82 °C

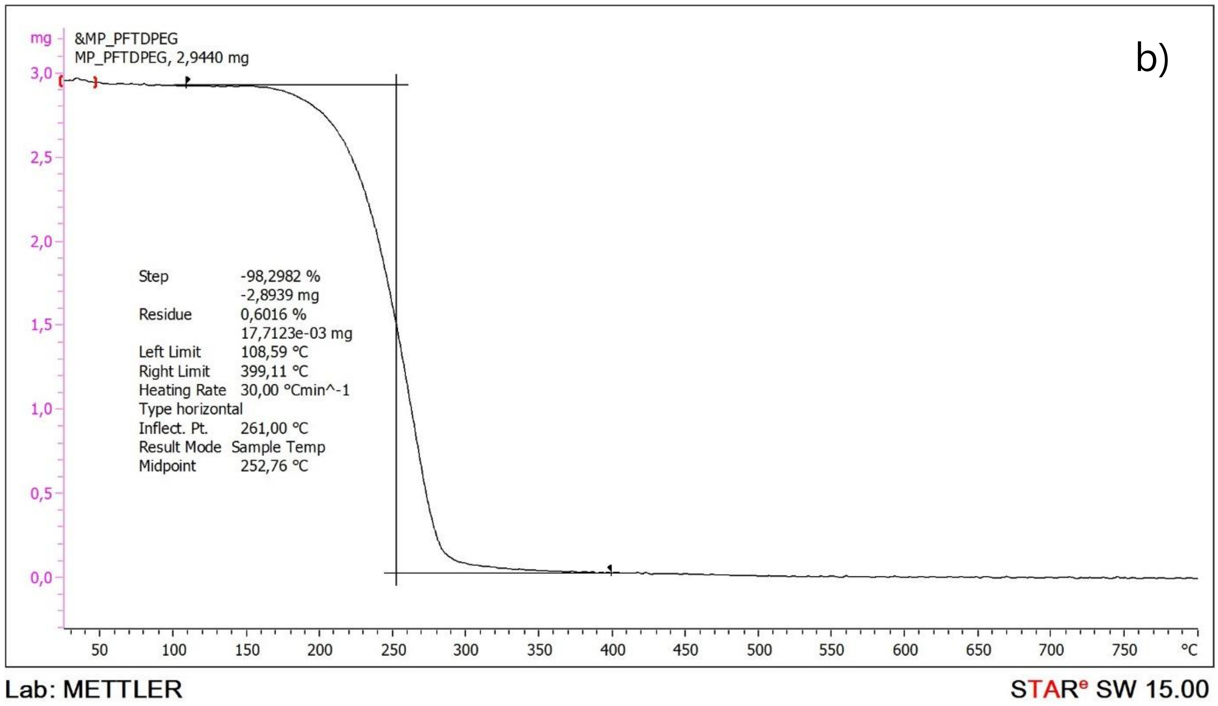

Step	-98,2982 % -2,8939 mg
Residue	0,6016 % 17,7123e-03 mg
Left Limit	108,59 °C
Right Limit	399,11 °C
Heating Rate	30,00 °Cmin^-1
Type horizontal	
Inflect. Pt.	261,00 °C
Result Mode	Sample Temp
Midpoint	252,76 °C

Annex 2: Chronic toxicity study on B16F10 at 0.01 and 0.1 mg·mL^{-1}, ns = non-significant, * p < 0.05, ** p < 0.01, *** p < 0.001, **** p < 0.0001 (two-way ANOVA), results shown as mean ± SD

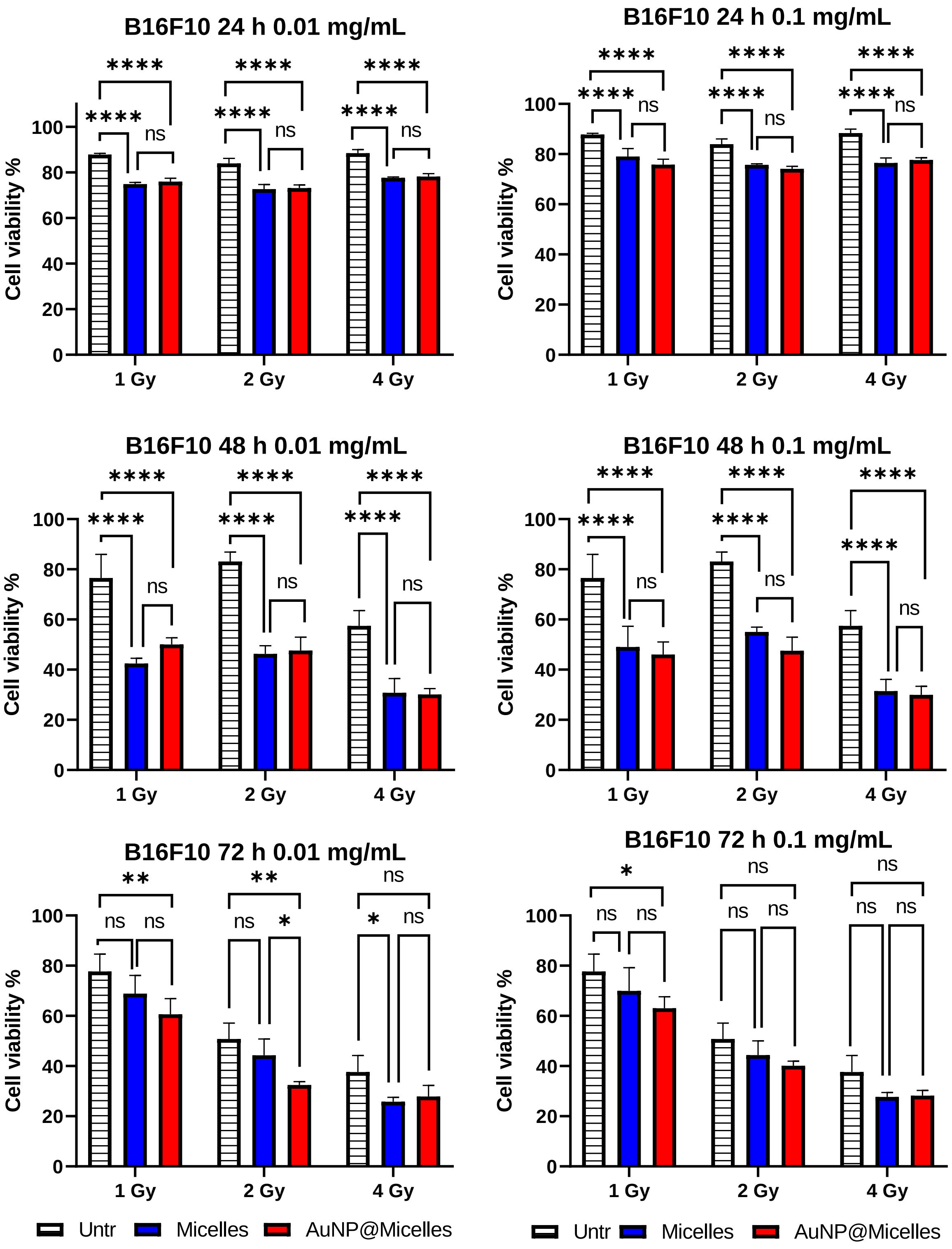

Annex 3: Chronic toxicity on SKBR3 cells at 0.01 and 0.1 $mg \cdot mL^{-1}$, ns = non-significant, * $p < 0.05$, ** $p < 0.01$, *** $p < 0.001$, **** $p < 0.0001$ (two-way ANOVA), results shown as mean ± SD

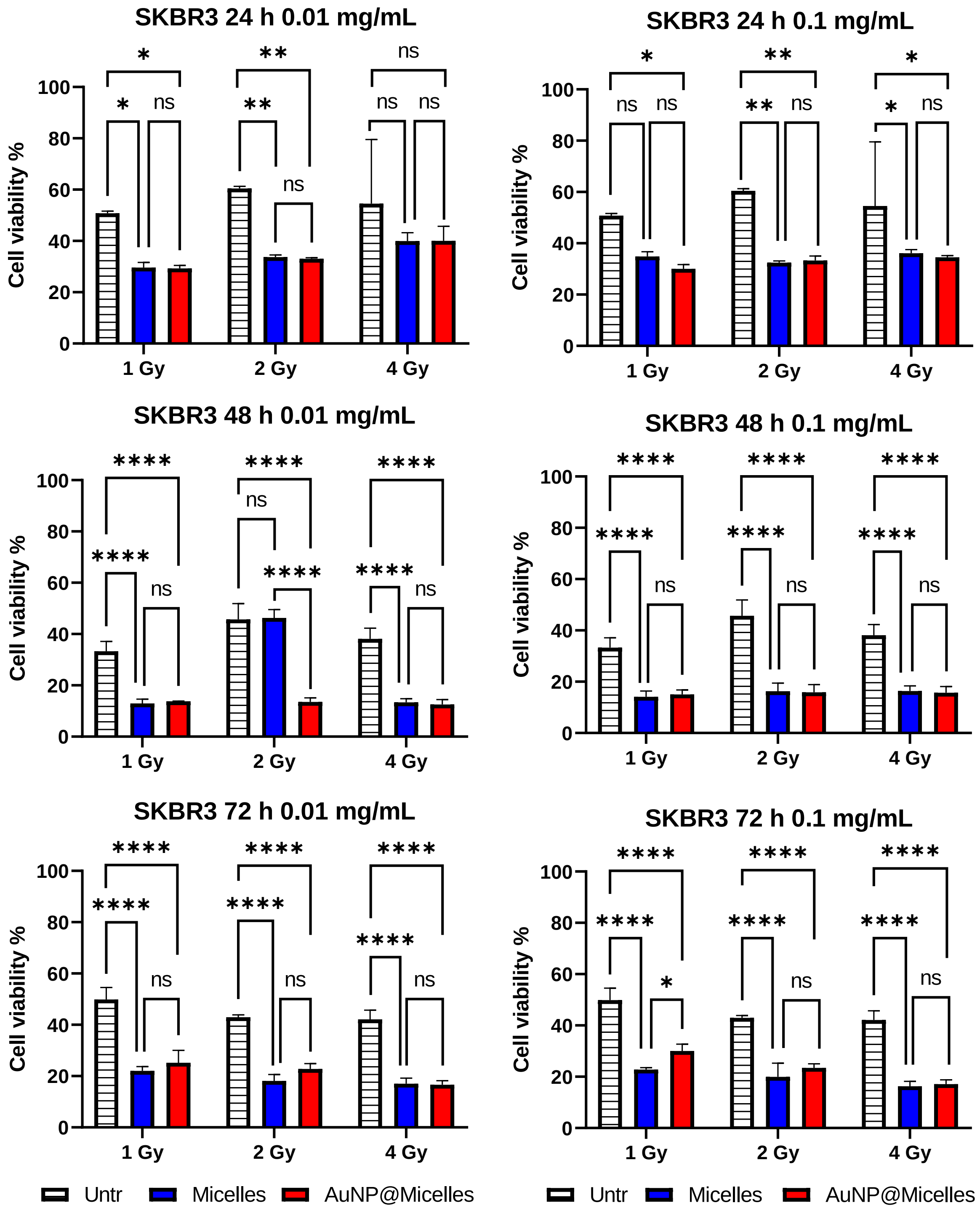

Annex 4: Determination of the radiosensitizing parameters of PFTD-PEG micelles and AuNP@Micelles (1 mg·mL^{-1}) on B16F10 and SKBR3 cell lines after 72 h incubation

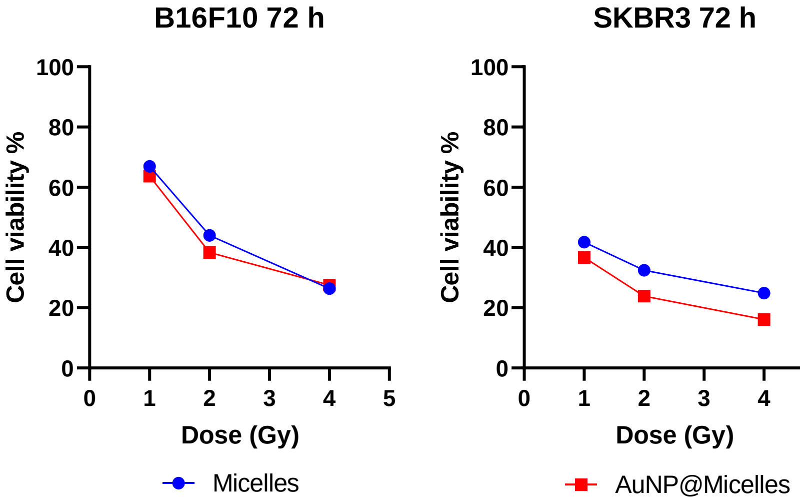

Annex 5: Acute toxicity on B16F10 at 0.01 and 0.1 mg·mL^{-1}, ns = non-significant, * $p < 0.05$, ** $p < 0.01$, *** $p < 0.001$, **** $p < 0.0001$ (two-way ANOVA), results shown as mean ± SD

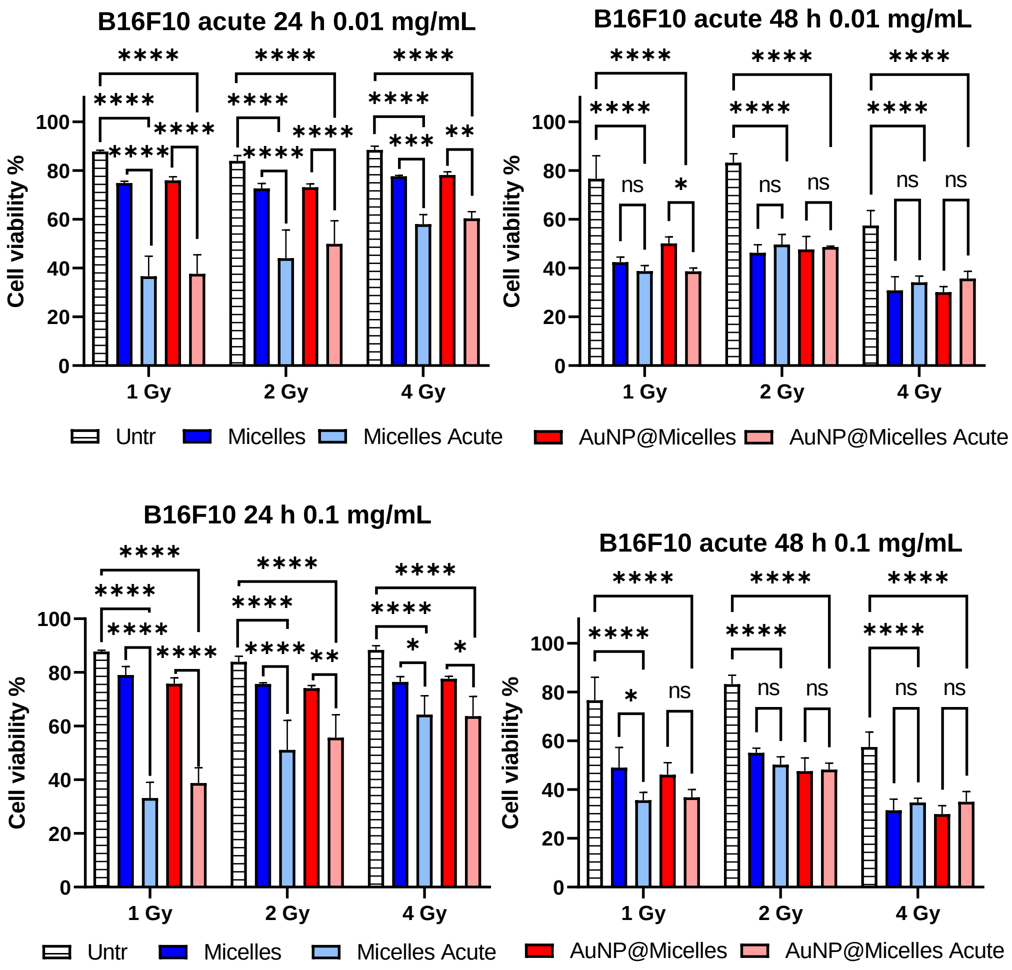

Annex 6: Acute toxicity on SKBR3 at 0.01 and 0.1 mg·mL^{-1}, ns = non-significant, * $p < 0.05$, ** $p < 0.01$, *** $p < 0.001$, **** $p < 0.0001$ (two-way ANOVA), results shown as mean ± SD

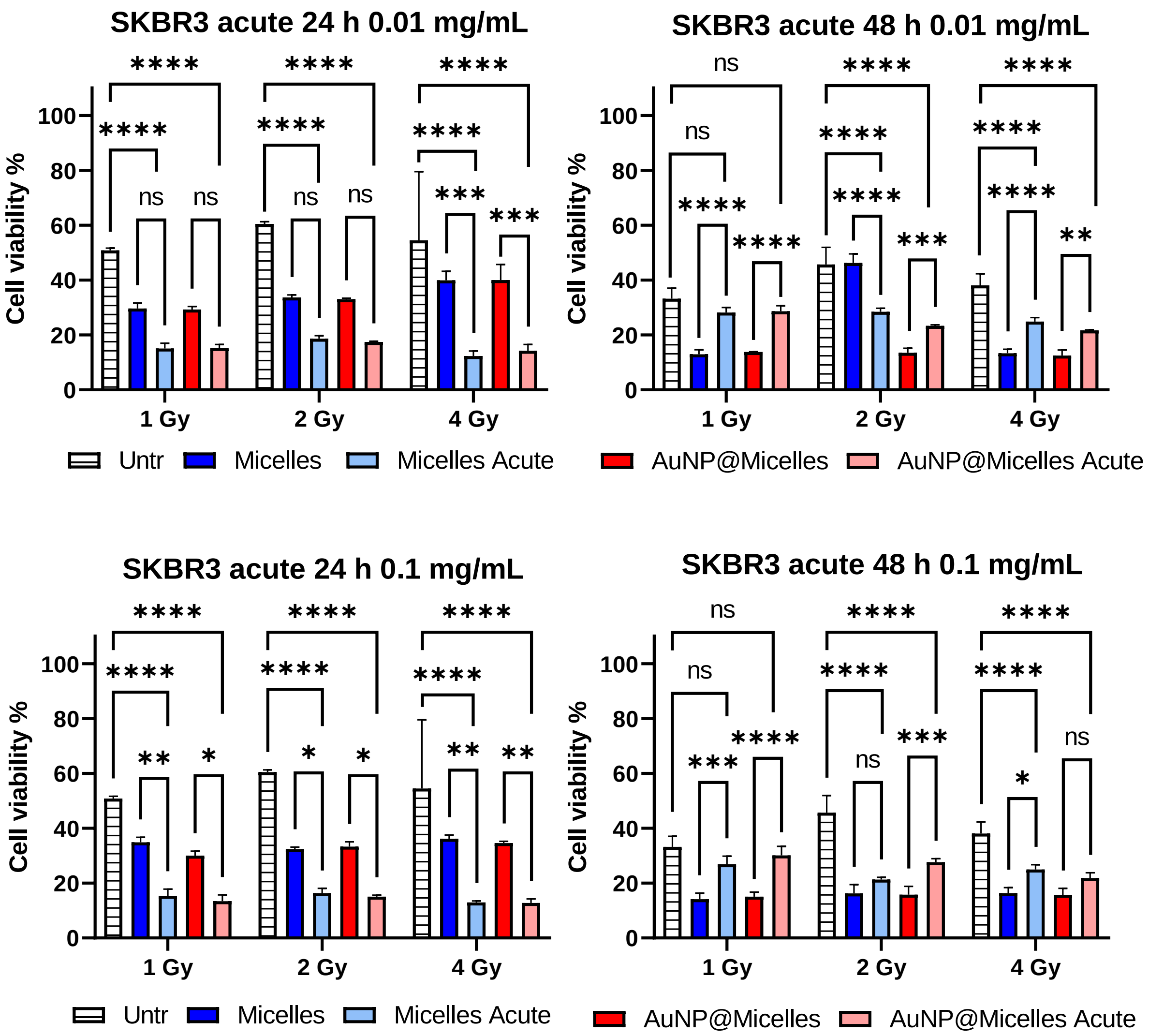

Annex 7: B16F10 cell viability after 24, 48 and 72 h incubation with Micelles, AuNP@Micelles, [^{177}Lu]Micelles and [^{177}Lu]AuNP@Micelles, comparison with negative control, ns = non-significant * $p < 0.05$, ** $p < 0.01$, *** $p < 0.001$, **** $p < 0.0001$ (2-way ANOVA test), Results are plotted as mean ± SD

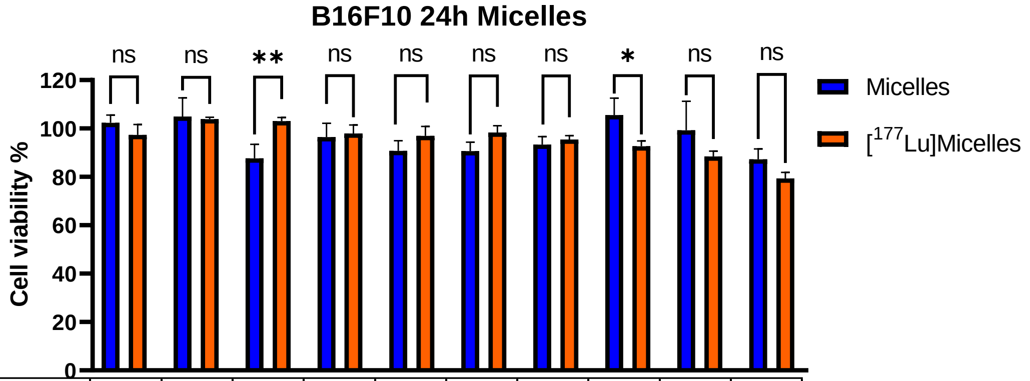

Micelles (mg/mL)	-	0.004	0.008	0.015	0.031	0.063	0.125	0.25	0.5	1
A (MBq)	-	-	-	-	-	-	-	-	-	-
	-	0.04	0.08	0.15	0.31	0.625	1.25	2.5	5	10

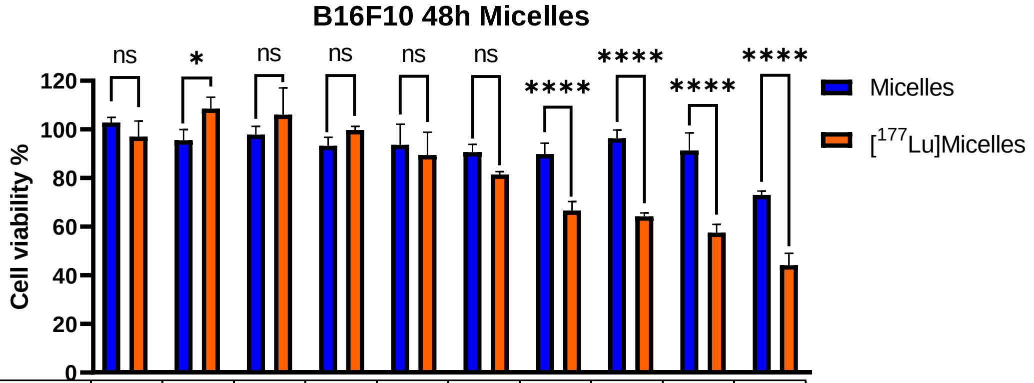

Micelles (mg/mL)	-	0.004	0.008	0.015	0.031	0.063	0.125	0.25	0.5	1
A (MBq)	-	-	-	-	-	-	-	-	-	-
	-	0.04	0.08	0.15	0.31	0.625	1.25	2.5	5	10

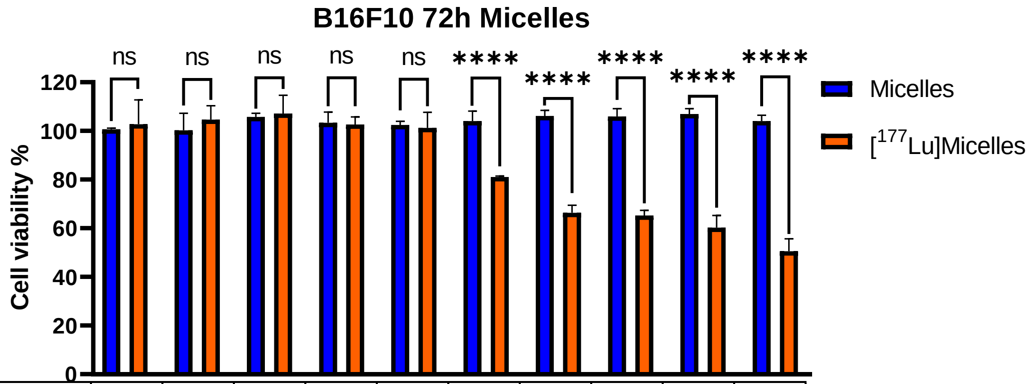

Micelles (mg/mL)	-	0.004	0.008	0.015	0.031	0.063	0.125	0.25	0.5	1
A (MBq)	-	-	-	-	-	-	-	-	-	-
	-	0.04	0.08	0.15	0.31	0.625	1.25	2.5	5	10

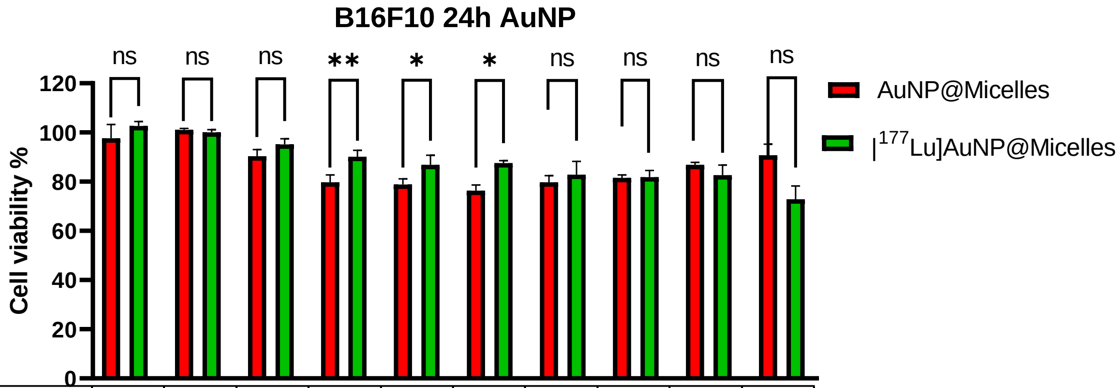

Micelles (mg/mL)	-	0.004	0.008	0.015	0.031	0.063	0.125	0.25	0.5	1
Au (µM)	-	0.04	0.08	0.15	0.31	0.625	1.25	2.5	5	10
	-	0.04	0.08	0.15	0.31	0.625	1.25	2.5	5	10
A (MBq)	-	-	-	-	-	-	-	-	-	-
	-	0.04	0.08	0.15	0.31	0.625	1.25	2.5	5	10

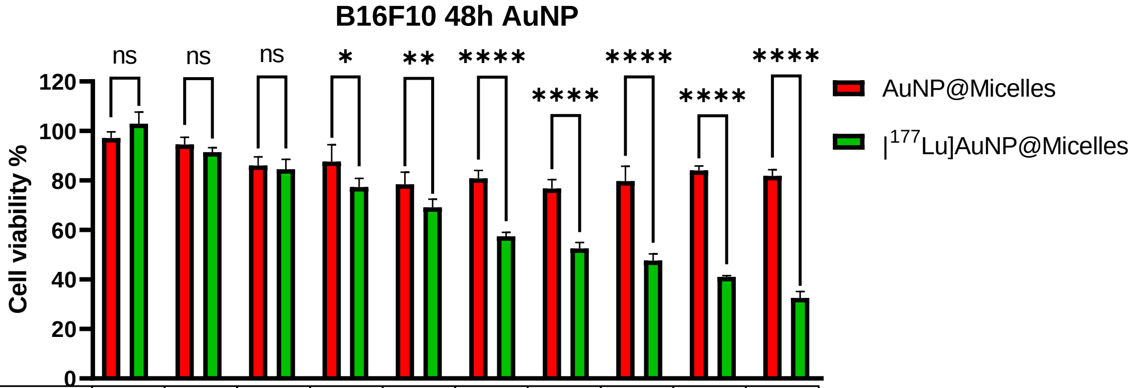

Micelles (mg/mL)	-	0.004	0.008	0.015	0.031	0.063	0.125	0.25	0.5	1
Au (µM)	-	0.04	0.08	0.15	0.31	0.625	1.25	2.5	5	10
	-	0.04	0.08	0.15	0.31	0.625	1.25	2.5	5	10
A (MBq)	-	-	-	-	-	-	-	-	-	-
	-	0.04	0.08	0.15	0.31	0.625	1.25	2.5	5	10

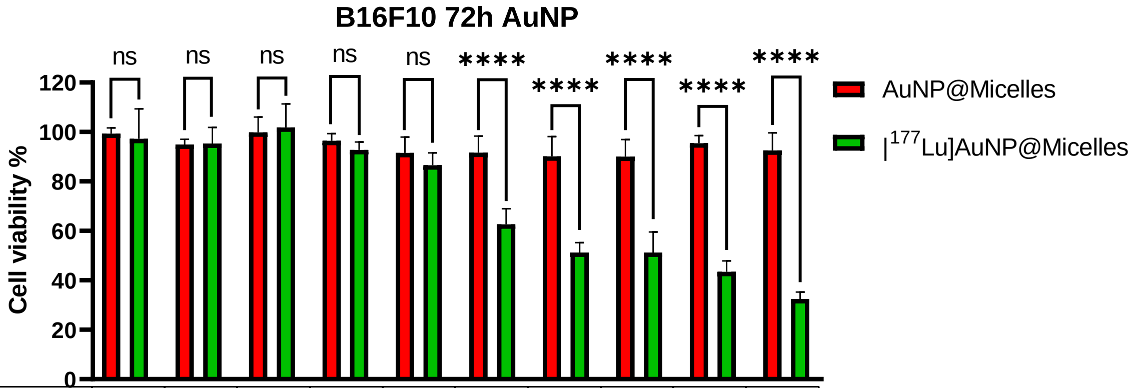

Micelles (mg/mL)	-	0.004	0.008	0.015	0.031	0.063	0.125	0.25	0.5	1
Au (µM)	-	0.04	0.08	0.15	0.31	0.625	1.25	2.5	5	10
	-	0.04	0.08	0.15	0.31	0.625	1.25	2.5	5	10
A (MBq)	-	-	-	-	-	-	-	-	-	-
	-	0.04	0.08	0.15	0.31	0.625	1.25	2.5	5	10

Annex 8: SKBR3 cell viability after 24, 48 and 72 h incubation with Micelles, AuNP@Micelles, [^{177}Lu]Micelles or [^{177}Lu]AuNP@Micelles, comparison with negative control, ns = non-significant * $p < 0.05$, ** $p < 0.01$, *** $p < 0.001$, **** $p < 0.0001$ (2-way ANOVA test), Results are plotted as mean ± SD

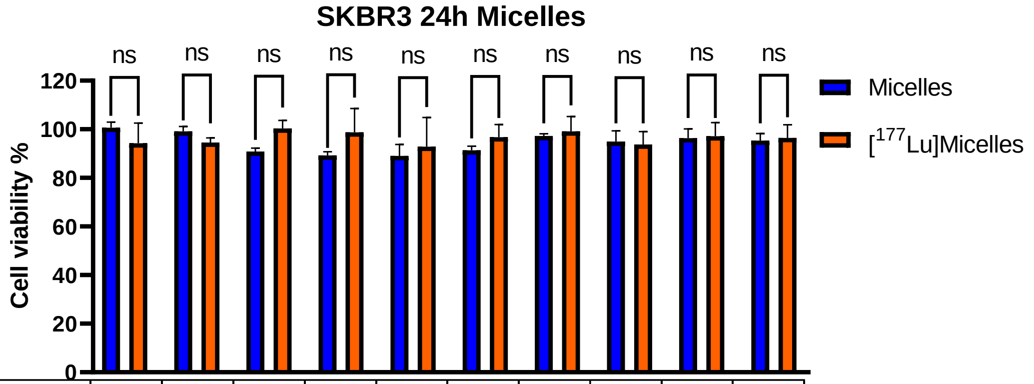
SKBR3 24h Micelles

Micelles (mg/mL)	-	0.004	0.008	0.015	0.031	0.063	0.125	0.25	0.5	1
A (MBq)	-	-	-	-	-	-	-	-	-	-
	-	0.04	0.08	0.15	0.31	0.625	1.25	2.5	5	10

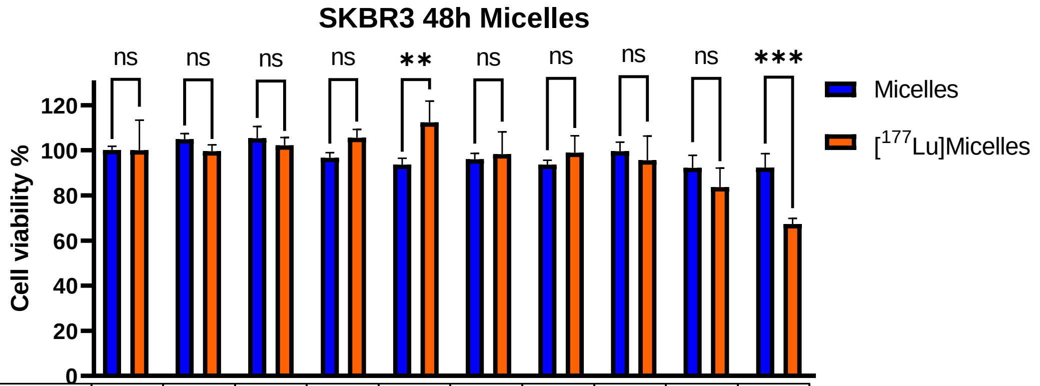
SKBR3 48h Micelles

Micelles (mg/mL)	-	0.004	0.008	0.015	0.031	0.063	0.125	0.25	0.5	1
A (MBq)	-	-	-	-	-	-	-	-	-	-
	-	0.04	0.08	0.15	0.31	0.625	1.25	2.5	5	10

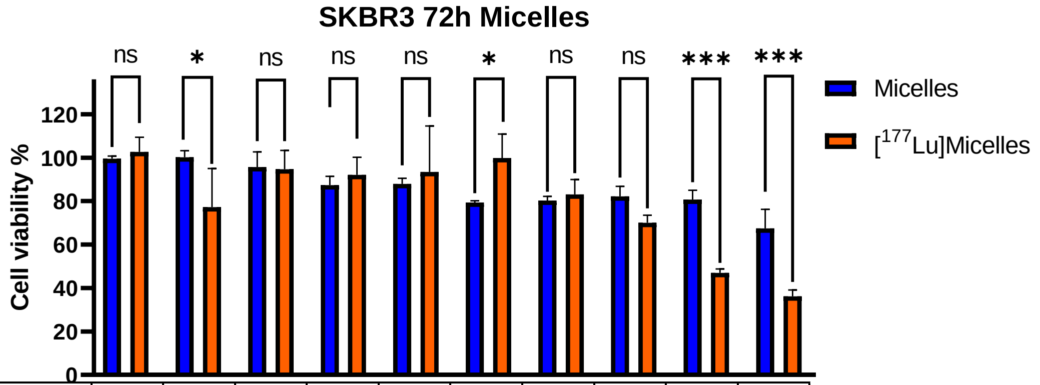
SKBR3 72h Micelles

Micelles (mg/mL)	-	0.004	0.008	0.015	0.031	0.063	0.125	0.25	0.5	1
A (MBq)	-	-	-	-	-	-	-	-	-	-
	-	0.04	0.08	0.15	0.31	0.625	1.25	2.5	5	10

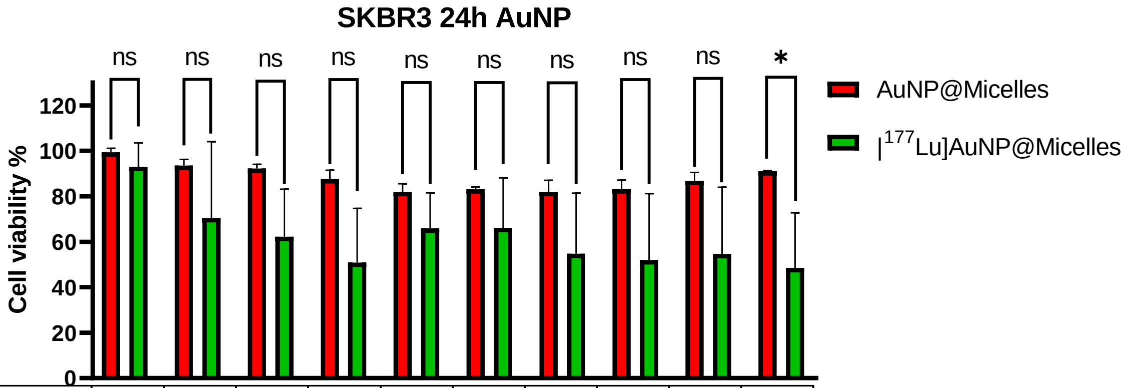

Micelles (mg/mL)	-	0.004	0.008	0.015	0.031	0.063	0.125	0.25	0.5	1
Au (µM)	-	0.04	0.08	0.15	0.31	0.625	1.25	2.5	5	10
	-	0.04	0.08	0.15	0.31	0.625	1.25	2.5	5	10
A (MBq)	-	-	-	-	-	-	-	-	-	-
	-	0.04	0.08	0.15	0.31	0.625	1.25	2.5	5	10

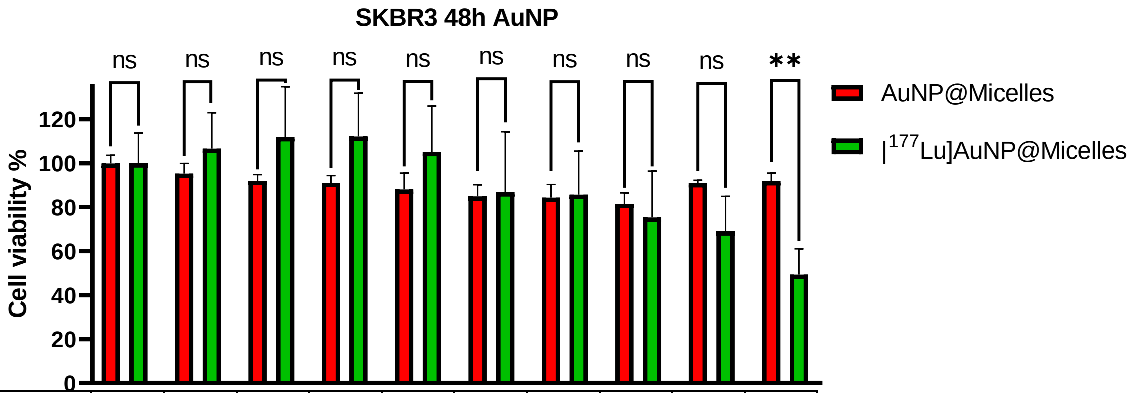

Micelles (mg/mL)	-	0.004	0.008	0.015	0.031	0.063	0.125	0.25	0.5	1
Au (µM)	-	0.04	0.08	0.15	0.31	0.625	1.25	2.5	5	10
	-	0.04	0.08	0.15	0.31	0.625	1.25	2.5	5	10
A (MBq)	-	-	-	-	-	-	-	-	-	-
	-	0.04	0.08	0.15	0.31	0.625	1.25	2.5	5	10

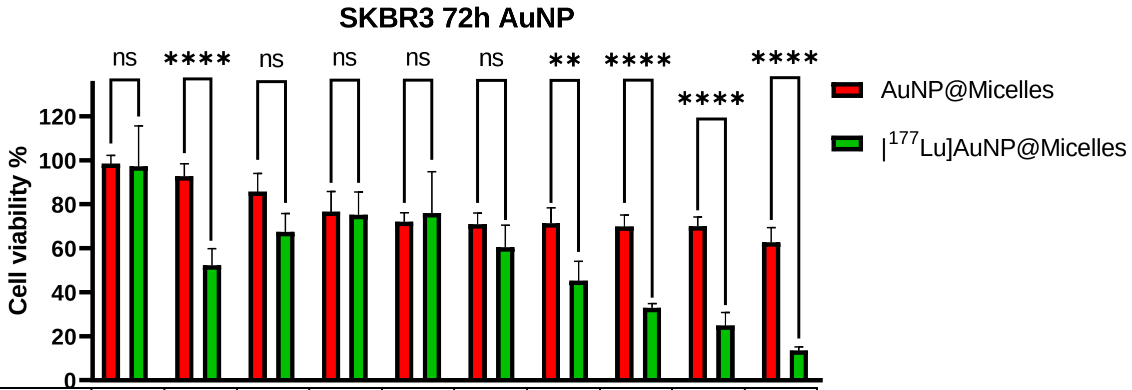

Micelles (mg/mL)	-	0.004	0.008	0.015	0.031	0.063	0.125	0.25	0.5	1
Au (µM)	-	0.04	0.08	0.15	0.31	0.625	1.25	2.5	5	10
	-	0.04	0.08	0.15	0.31	0.625	1.25	2.5	5	10
A (MBq)	-	-	-	-	-	-	-	-	-	-
	-	0.04	0.08	0.15	0.31	0.625	1.25	2.5	5	10

Annex 9: Biodistribution study of [^{177}Lu]AuNP@Micelles on C57Bl/6 mice, results plot in %ID, mean ± SD

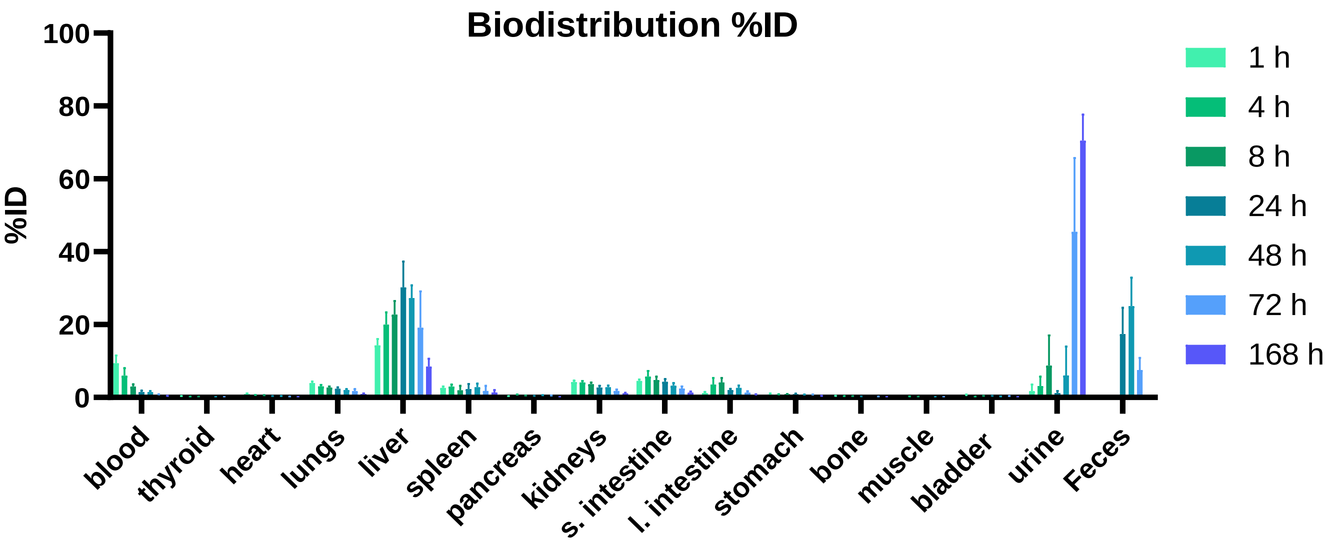

Annex 10: Tumor retention of [^{177}Lu]Micelles and [^{177}Lu]AuNP@Micelles on C57Bl/6 mice with melanoma B16F10 xenografts, results plot in %ID/g, mean ± SD

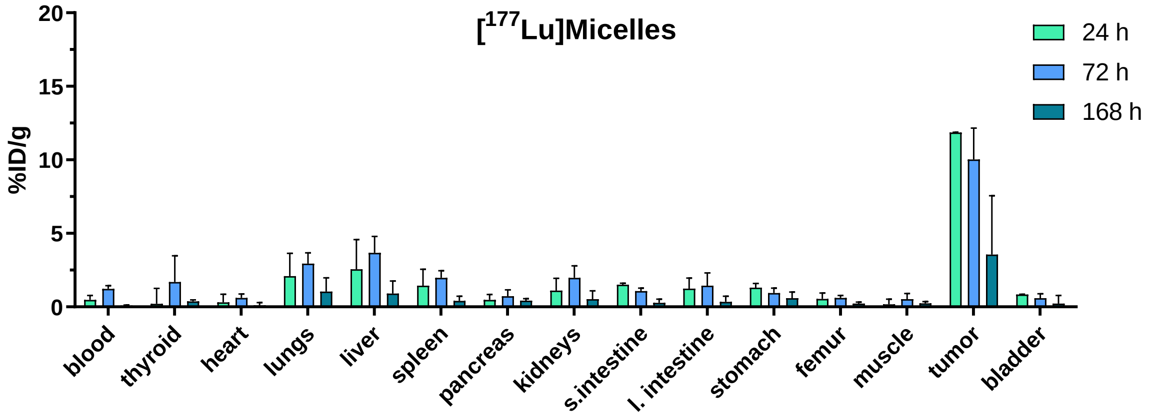

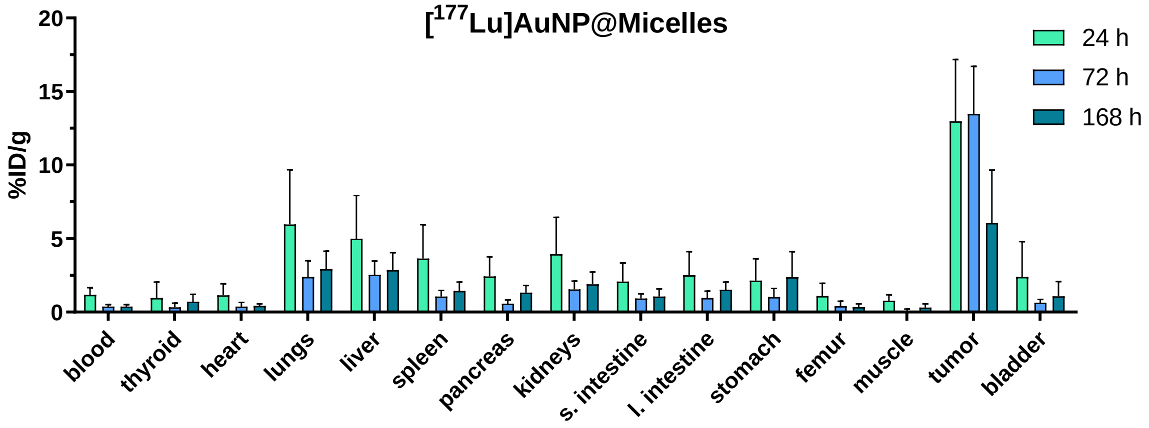

Résumé

Parmi les approches actuelles utilisées pour le traitement du cancer, deux axes thérapeutiques connaissent un intérêt croissant : la médecine nucléaire et la nanomédecine. Cette dernière exploite les propriétés uniques des nanostructures, notamment leur capacité à s'accumuler dans les tumeurs pour l'administration ciblée de médicaments. La médecine nucléaire, quant à elle, repose sur l'utilisation des rayonnements ionisants à des fins diagnostiques ou thérapeutiques. En cancérologie, la radiothérapie interne se distingue par son aptitude à cibler les tissus profonds. Son objectif principal est de mettre au point des radiopharmaceutiques capables de détruire sélectivement les cellules tumorales tout en préservant les tissus sains afin de limiter les effets secondaires. Cependant, divers mécanismes de radiorésistance, notamment liés à l'hypoxie, peuvent réduire son efficacité. Le développement d'agents favorisant la réoxygénation tumorale constitue donc une voie prometteuse.

Mon travail de thèse s'inscrit dans cette perspective, avec pour objectif la conception de nanovecteurs micellaires destinés à la radiothérapie interne. Le vecteur développé doit combiner plusieurs fonctions : ciblage tumoral, administration de radionucléides, apport d'oxygène et radiosensibilisation. Pour cela, une unité amphiphile fluorée a été conçue, permettant la formation de micelles perfluorées capables de solubiliser de l'oxygène (pour renforcer la sensibilité des cellules aux rayonnements) et d'encapsuler des nanoparticules d'or (pour amplifier l'effet des rayonnements). En absence de rayonnements, les deux formulations, micelles et micelles chargées en or, se sont révélées être non cytotoxiques à toutes les concentrations testées.

Une évaluation in vitro des micelles a été réalisée sous rayonnements, par irradiation externe (faisceaux d'électrons) sur des lignées de mélanome murin (B16F10) et de cancer du sein humain (SKBR3). Les résultats obtenus ont mis en évidence les propriétés radio-sensibilisantes des micelles simples et de celles contenant de l'or, avec un effet particulièrement marqué sur les cellules SKBR3 plus radiosensibles. L'effet de radio-amplification induit par l'or a également pu être démontré sur ces lignées.

Dans un second temps, le radionucléide ^{177}Lu a été incorporé aux formulations micellaires pour de la radiothérapie interne. Des tests de cytotoxicité sur des cellules B16F10 et SKBR3 ont montré une radiotoxicité dose-dépendante du ^{177}Lu, avec un effet supérieur pour les micelles qui incorporent à la fois de l'or et du ^{177}Lu, par rapport aux micelles n'incorporant que du ^{177}Lu.

Les micelles ^{177}Lu/or ont ensuite été injectées par voie intraveineuse à des souris saines pour une étude de biodistribution avec une demi-vie circulatoire des

micelles de 2,5 h. Une accumulation essentiellement dans le foie et la rate a été détectée, avec la mise en place d'une voie d'excrétion hépatobiliaire et rénale. En raison de ce profil pharmacocinétique peu optimal et du risque de radiotoxicité sur les organes périphériques sains, l'administration intra-tumorale (nanobrachythérapie) des micelles a par la suite été privilégiée.

Un protocole de nanobrachythérapie a été mis en place chez des souris porteuses de tumeurs. Les vecteurs micellaires ^{177}Lu et ^{177}Lu/or ont été injectés directement dans la tumeur. Les micelles présentent une bonne rétention dans la zone tumorale avec une néanmoins une diffusion progressive mais lente vers la circulation systémique. Le suivi de la croissance tumorale a confirmé l'effet radio-sensibilisant de l'or, avec une inhibition marquée 7 jours après le début du traitement avec les micelles ^{177}Lu/or.

Les résultats que nous avons obtenus au cours de ce travail soulignent le potentiel thérapeutique des nanovecteurs micellaires qui combinent du lutetium-177, des nanoparticules d'or et de l'oxygène embarqué à des fins de radiosensibilisation et de radio-amplification. Des études complémentaires devront cependant être conduites pour confirmer ces résultats préliminaires.

Abstract

Among current approaches to cancer treatment, two therapeutic avenues are attracting growing interest: nuclear medicine and nanomedicine. The latter exploits the unique properties of nanostructures, particularly their ability to accumulate in tumors for targeted drug delivery. Nuclear medicine, on the other hand, relies on the use of ionizing radiation for diagnostic or therapeutic purposes. In oncology, internal radiotherapy stands out for its ability to target deep tissues. Its main objective is to develop radiopharmaceuticals capable of selectively destroying tumor cells while sparing healthy tissues, thereby limiting side effects. However, various mechanisms of radioresistance, particularly those linked to hypoxia, can reduce its effectiveness. The development of systems that promote tumor reoxygenation therefore, represents a promising strategy.

My doctoral work was carried out within this context, with the aim of designing micellar nanocarriers for internal radiotherapy. The developed nanocarrier was intended to combine multiple functions: tumor targeting, radionuclide delivery, oxygen supply, and radiosensitization. To this end, a fluorinated amphiphilic unit was designed, enabling the formation of perfluorinated micelles capable of solubilizing oxygen (to enhance cellular radiosensitivity) and encapsulating gold nanoparticles (to amplify radiation effects). In the absence of irradiation, both formulations—plain micelles and gold-loaded micelles—proved non-cytotoxic at all tested concentrations.

The micelles were then evaluated in vitro under irradiation, using external electron beams on murine melanoma (B16F10) and human breast cancer (SKBR3) cell lines. Results highlighted the radiosensitizing properties of both simple and gold-containing micelles, with a particularly marked effect on the more radiosensitive SKBR3 cells. The radio-enhancement effect of gold was also clearly demonstrated on these cell lines.

Subsequently, the radionuclide ^{177}Lu was incorporated into the micellar formulations for internal radiotherapy. Cytotoxicity assays on B16F10 and SKBR3 cells revealed a dose-dependent radiotoxicity of ^{177}Lu, with greater effects observed for micelles combining both gold and ^{177}Lu compared to those containing ^{177}Lu alone.

The ^{177}Lu/gold micelles were then intravenously injected into healthy mice for a biodistribution study, which showed a circulatory half-life of 2.5 h. Accumulation occurred mainly in the liver and spleen, with both hepatobiliary and renal excretion pathways identified. Due to this suboptimal pharmacokinetic profile and the risk of radiotoxicity in healthy peripheral organs, intratumoral administration (nanobrachytherapy) was then prioritized.

A nanobrachytherapy protocol was implemented in tumor-bearing mice. Both ^{177}Lu micelles and ^{177}Lu/gold micelles were injected directly into the tumor. The micelles exhibited good tumor retention, although a slow diffusion into systemic circulation was observed. Tumor growth monitoring confirmed the radiosensitizing effect of gold, with marked inhibition observed seven days after treatment with ^{177}Lu/gold micelles.

The results obtained in this work highlight the therapeutic potential of micellar nanovectors combining lutetium-177, gold nanoparticles, and encapsulated oxygen to achieve radiosensitization and radio-enhancement. However, further studies are required to confirm these preliminary findings.

Streszczenie

Wśród różnych strategii dostępnych obecnie w leczeniu nowotworów, dwa obszary badań cieszą się ponownym zainteresowaniem: nanomedycyna i medycyna nuklearna. Nanomedycyna koncentruje się na wyjątkowych właściwościach osiąganych w skali nano, które pozwalają cząsteczkom pasywnie dotrzeć do obszaru guza dzięki efektowi zwiększonej przepuszczalności i retencji (EPR). Duża różnorodność nanocząstek oferuje liczne możliwości w zakresie opracowywania nowych strategii diagnostycznych i terapeutycznych w leczeniu nowotworów. Obecnie nanocząstki z pustą wnęką, takie jak micele, są wykorzystywane jako supramolekularne nośniki do dostarczania leków.

Medycyna nuklearna koncentruje się na wykorzystaniu promieniowania jonizującego do leczenia lub diagnostyki. W kontekście leczenia nowotworów radioterapia wewnętrzna wykazuje obiecujące właściwości, w tym możliwość selektywnego oddziaływania na głębokie tkanki. Głównym celem radioterapii jest opracowanie radiofarmaceutyku, który skutecznie zabija komórki nowotworowe, oszczędzając zdrowe tkanki, aby ograniczyć skutki uboczne. Niedawne zatwierdzenie różnych radiofarmaceutyków jako środków terapeutycznych potwierdza ponowne zainteresowanie radioterapią wewnętrzną. Jednak różne mechanizmy radiooporności mogą utrudniać i ograniczać skuteczność radioterapii. Ponieważ niedotlenienie jest źródłem różnych zjawisk radiooporności, bardzo pożądane jest opracowanie środków terapeutycznych, które mogą przywrócić perfuzję tlenową.

Celem mojej pracy doktorskiej było opracowanie preparatu nanonośnika micelarnego do stosowania w radioterapii wewnętrznej. Zaprojektowany nośnik miał łączyć wiele funkcji, w tym kumulowanie się w guzie, dostarczanie radionuklidów terapeutycznych, wzmacnianie działania promieniowania i ponowne natlenianie. Przede wszystkim zaprojektowano fluorowaną jednostkę amfifilową w celu wytworzenia miceli perfluorowanych, które rozpuszczają tlen i nadają właściwości radiouczulające. Oprócz zdolności do przenoszenia tlenu, micele zostały zaprojektowane tak, aby zawierały nanocząsteczki złota (AuNP) w celu uzyskania właściwości wzmacniających działanie promieniowania. Obie formuły, zarówno same micele (Micelles), jak i micele zawierające AuNP (AuNP@Micelles), okazały się nietoksyczne we wszystkich badanych stężeniach.

Przeprowadzono badanie napromieniowania zewnętrznego w celu oceny właściwości radiouczulających preparatów Micelles i AuNP@Micelles. Badanie przeprowadzono na dwóch liniach komórkowych, mysim czerniaku (B16F10) i ludzkim raku piersi (SKBR3), poddanych napromieniowaniu wiązką elektronów. Właściwości radiouczulające miceli potwierdzono w obu liniach komórkowych, a były one szczególnie znaczące w komórkach SKBR3. Ponadto wykazano efekt

wzmocnienia promieniowania przez nanocząsteczki złota w obu liniach komórkowych.

Druga część pracy polegała na przyłączeniu radionuklidu ^{177}Lu do preparatów Micelles i AuNP@Micelles w celu oceny ich potencjalnego zastosowania w radioterapii wewnętrznej. Następnie zbadano toksyczność tych zawiesin w stosunku do nowotworowych linii komórkowych B16F10 i SKBR3, stosując analogi nieradioaktywnie jako kontrole negatywne. Spodziewana radiotoksyczność ^{177}Lu została zaobserwowana w obu liniach komórkowych, a toksyczność wzrastała wraz z wyższym poziomem aktywności. [^{177}Lu]AuNP@Micelles wykazywały wyższą toksyczność w porównaniu z [^{177}Lu]Micelles, zwłaszcza przy wyższych stężeniach i dodanej aktywności radionuklidu, co podkreśla synergiczny wpływ nanocząstek złota na efekt wzmocnienia działania promieniowania.

Zachęceni wynikami z badań *in vitro*, przeprowadzono wstępne badania *in vivo* w celu określenia profilu farmakokinetycznego i biodystrybucji preparatu micelarnego w różnych narządach i tkankach u zdrowych myszy C57Bl/6. W drugim badaniu *in vivo* oceniano retencję preparatów w guzach u myszy C57Bl/6 z przeszczepami mysiego czerniaka (B16F10). Oba doświadczenia wykazały, że opracowane nanonośniki charakteryzują się zachowaniem biologicznym zbliżonym do opisywanego dla innych nanocząstek, z wyraźną akumulacją w wątrobie i śledzionie. Uzyskane wyniki potwierdzają, że podanie bezpośrednio do guza może prowadzić do bardziej efektywnego efektu terapeutycznego. Konieczne są dalsze badania *in vitro* i *in vivo*, ze szczególnym uwzględnieniem oceny skuteczności terapeutycznej [^{177}Lu]AuNP@Micelles jako wielofunkcyjnych nanonośników.

universite PARIS-SACLAY

ÉCOLE DOCTORALE
Sciences Chimiques : Molécules,
Matériaux, Instrumentation
et Biosystèmes (2MIB)

Tytuł: Projektowanie i synteza nanononików micelarnych do radioterapii wewnętrznej

Słowa kluczowe: synteza organiczna, nanomedycyna, połączenia supramolekularne

Streszczenie : .Radioterapia stała się skuteczną strategią terapeutyczną w walce z rakiem. Jednak jej skuteczność jest ograniczona przez zjawiska radioopornoci. Wśród różnych mechanizmów przyczyniających się do radioresistencji kluczową rolę odgrywa przewlekła hipoksja.

Celem niniejszej pracy doktorskiej było opracowanie oryginalnych nanometrycznych nośników łączących właściwości transportu tlenu w celu przywrócenia normoksji oraz właściwości radiouczulajce w celu wzmocnienia działania promieniowania, przy jednoczesnym oszczędzaniu zdrowych tkanek.

Opracowano micele perfluorowane (do transportu O_2) o właściwościach kierujących się do guzów i załadowano je nanocząstkami złota (w celu zwiększenia wrażliwości na promieniowanie). Micele zostały ocenione *in vitro* i *in vivo* pod kątem zastosowań w radioterapii zewnętrznej (wiązka elektronów) i wewnętrznej. W tym ostatnim podejściu micele zostały połączone z lutetem-177, a ich działanie oceniono w modelu mysim z nowotworem.

universite
PARIS-SACLAY

ÉCOLE DOCTORALE
Sciences Chimiques : Molécules,
Matériaux, Instrumentation
et Biosystèmes (2MIB)

Titre : Design et synthèse de nanovecteurs micellaires pour et la radiothérapie interne

Mots clés : synthèse organique, nanomédecine, assemblage supramoléculaire

Résumé : La radiothérapie s'est imposée comme une stratégie thérapeutique efficace contre le cancer. Cependant, son efficacité est limitée par des phénomènes de radiorésistance. Parmi les différents mécanismes contribuant à la radiorésistance, l'hypoxie chronique joue un rôle central.

L'objectif de ce travail de doctorat a été de développer des vecteurs nanométriques originaux combinant des propriétés de transport d'oxygène pour rétablir la normoxie et des propriétés radio-sensibilisantes pour accentuer l'impact des radiations, tout en épargnant les tissus sains.

Des micelles perfluorées (pour le transport de O_2) dotées de propriétés de ciblage des tumeurs ont été conçues et chargées de nanoparticules d'or (pour la radiosensibilisation). Les micelles ont été évaluées *in vitro* et *in vivo* pour des applications en radiothérapie externe (faisceau d'électrons) et interne. Dans cette dernière approche, les micelles ont été associées au lutétium-177 et leurs performances ont été évaluées dans un modèle murin porteur de tumeur.

Title: Design and synthesis of micellar nanocarriers for internal radiotherapy

Keywords: organic synthesis, nanomedicine, supramolecular assemblies

Abstract: Radiotherapy has been established as an effective treatment strategy against cancer. However, its effectiveness is limited by radioresistance phenomena. Among the various mechanisms contributing to radioresistance, chronic hypoxia plays a central role.

The objective of this PhD work was to develop original nanometric carrier systems combining oxygen transport properties to restore normoxia, and radiosensitizing properties to enhance the impact of radiations, while sparing healthy tissues.

Perfluorinated micelles (for O_2 transport) with tumor targeting properties were designed and loaded with gold nanoparticles (for radioenhancement). The micelles were *evaluated in vitro* and *in vivo* for applications in external (electron beam) and internal radiotherapy. In the latter approach, micelles were combined to lutetium-177 and their performances assessed in a tumor-bearing mice model.